



HAL
open science

New generations of boron-doped diamond structures by delta-doping technique for power electronics: CVD growth and characterization

Alexandre Fiori

► **To cite this version:**

Alexandre Fiori. New generations of boron-doped diamond structures by delta-doping technique for power electronics: CVD growth and characterization. Electronics. Université de Grenoble, 2012. English. NNT: 2012GRENI018 . tel-00967208v2

HAL Id: tel-00967208

<https://theses.hal.science/tel-00967208v2>

Submitted on 28 Jun 2017

HAL is a multi-disciplinary open access archive for the deposit and dissemination of scientific research documents, whether they are published or not. The documents may come from teaching and research institutions in France or abroad, or from public or private research centers.

L'archive ouverte pluridisciplinaire **HAL**, est destinée au dépôt et à la diffusion de documents scientifiques de niveau recherche, publiés ou non, émanant des établissements d'enseignement et de recherche français ou étrangers, des laboratoires publics ou privés.

THÈSE

Pour obtenir le grade de

DOCTEUR DE L'UNIVERSITÉ DE GRENOBLE

Spécialité : **Matériaux, Mécanique, Génie civil, Electrochimie**

Arrêté ministériel : 7 août 2006

Présentée par

Alexandre FIORI

Thèse dirigée par **Franck Omnès** et
codirigée par **Julien Pernot**

préparée au sein de l'**institut Néel** au CNRS à Grenoble
dans l'**École Doctorale I-MEP2 : Ingénierie – Matériaux,
mécanique, Environnement, Energétique, Procédés,
Production**

**Nouvelles générations de structures en diamant
dopé au bore par technique de delta-dopage pour
l'électronique de puissance : croissance par CVD
et caractérisation**

Thèse soutenue publiquement le **24 octobre 2012**,
devant le jury composé de :

M. Christophe VALLEE

Professeur, Université de Grenoble, Président

M. Ken HAENEN

Professeur, Université de Hasselt, Rapporteur

M. Jocelyn ACHARD

Professeur, Université Paris XIII, Rapporteur

M. Gilles PRUDON

Maître de Conférences, INSA Lyon, Examineur

M. Jean-Charles ARNAULT

Directeur de recherche, CEA Saclay, Examineur

M. Etienne BUSTARRET

Directeur de recherche, CNRS Institut Néel, Examineur

M. Franck OMNES

Chargé de recherche (HDR), CNRS - Institut Néel, Directeur de thèse

M. Tokuyuki TERAJI

Senior researcher, NIMS, Japon, Invité



ACKNOWLEDGMENTS

I want to express my sincere thanks to all the people who helped during the work on my PhD project. These in particular:

Franck Omnès, who accepted the direction of this PhD project at the CNRS Grenoble. His expertise on the plasma-enhanced chemical vapor deposition was indispensable for the success of this thesis. He gave me the possibility to work on this interesting and nice topic.

Julien Pernot, who guided me during this PhD project and accepted the co-direction of this thesis. His expertise on semiconductor physics and electronic power devices was important too.

Etienne Bustarret, the project manager, who was always present to guide, help and encourage me throughout this work.

Tokuyuki Teraji, my main supervisor during my six months internship at NIMS, Tsukuba in Japan, who gave me the opportunity to experiment lateral and isotopic carbon source diamond growth, which were fundamental for the accomplishment of this work. He always took time to discuss with me about diamond growth and life in Japan. With **Satoshi Koizumi**, they strongly contributed to my knowledge of diamond growth mechanisms, associate defects and doping. **Yasuo Koide**, who gave me the possibility to work in the Wide Bandgap Materials Group, at NIMS and also **Yiuri Garrino** for his experimental help and his sympathy.

Ken Haenen and **Jocelyn Achard**, who kindly accepted to render their expert opinion for this PhD thesis, and **Christophe Vallée**, **Gilles Prudon** and **Jean-Charles Arnault** who also accepted to took part of the examining jury.

All the members of my group at the Institut Néel – CNRS Grenoble. **Etienne Gheeraert** (group leader), **David Eon** (plasma), **Pierre Muret** (DLTS) for their true interest in my daily work, and for their very efficient help.

Yasuo Koide, who gave me the possibility to work in the Wide Bandgap Materials Group, at NIMS and also all members: **Masataka Imura**, **Yoshihiro Irokawa**, **Meiyong Liao**, **Masatomo Sumiya**. It was a great pleasure to join the group again.

All my precious collaborators to this study: **Francois Jomard** (GEMaC, France) for SIMS, **Maria de la Paz Alegre Salguero**, **José Carlos Piñero Charlo** and **Daniel Araújo** (Cádiz, Spain) for TEM, **Edith Bellet-Amalric** (INAC, Grenoble) and **Eric Mossang** (Inst. Néel, Grenoble) for XRD.

And friendlier, I want to thanks some nice people who helped me and encourage me in the PhD work. These in particular:

Japanese researchers: **Hisao Kanda**, **Takashi Taniguchi**, group leaders of Ultra-High Pressure Processes Group at NIMS, **Kenji Watanabe**, principal researcher at the Optoelectronic Materials Group at NIMS, and **Hiromitsu Kato**, researcher at the Diamond Research Center at AIST. I gained a lot of experience from my time with them.

Plus librement, je remercie :

Les étudiants doctorant de passage dans l'équipe : **Pierre-Nicolas VOLPE**, **Sébastien RUFFINATTO**, **Clément HEBERT**, **Stéphane BROCHEN**, **Hasan-al MEHEDI**, **Gauthier CHICOT**, **Aboulaye TRAORE**, **Jessica BOUSQUET**, **Pierre TCHOULFIAN**, **Aurélien MARECHAL**, **Rafael FILLON**, ainsi que les stagiaires : **Jean-Baptiste FAY** et **Ilias JALAL**.

Le personnel technique et administratif de l'institut Néel, des personnes remarquables, que l'on ne retrouve nulle part ailleurs :

Philippe DAVID	Julien JARREAU	Eric MOSSANG
Pierre GIROUX	Denis MAILLARD	Christophe BOUCHARD
David BARRAL	Fabrice BRUNOUD	Stephanie KODJIKIAN
Richard HAETTEL	Isabelle CROS-JOUVIN	Sébastien PAIRIS
Graziella KAVAKLIAN	Nicolas SCARLATA	Emmanuel VERLOOP
Valérie GUISSET	Véronique FAUVEL	Frédéric GAY
Valérie REITA	Sabine GADAL	Jacques MARCUS
Fabrice DONATINI	Mireille DUBOIS	Philippe PLAINDOUX
Thierry FOURNIER	Laurence GRITTI	Edouard WAGNER
Bruno FERNANDEZ	Caroline BARTOLI	Sylvain DUMONT
Sébastien DUFRESNES	Louise INFUSO	Daniel LEPOITTEVIN
Didier DUFEU	Marielle LARDATO	Bernard MAIRE-AMIOT
Laurent DEL-REY	Mathilde MAURO	Patrick BELMAIN
Yves DESCHANELS	Carmela MELI	Laurent JOUBERT
Eric EYRAUD	Christine ZAMPAOLO	Julien MICHEL

Je remercie ma famille, pour l'aide logistique, culinaire et financier du pot de thèse.

CONTENTS

ACKNOWLEDGMENTS	5
CONTENTS	7
GENERAL INTRODUCTION	11
INTRODUCTION GÉNÉRALE.....	13
CHAPTER 1. INTRODUCTION TO BORON-DELTA-DOPING OF DIAMOND	15
I. DIAMOND DEVICES FOR POWER ELECTRONICS AND HIGH FREQUENCY APPLICATION.....	18
I.1. Physical properties of diamond	18
I.2. Challenges in power electronics	20
I.3. Devices.....	22
II. PROBLEMS RELATED TO DOPING.....	23
II.1. n-type doping.....	24
II.2. p-type doping – Boron doping	26
III. DELTA DOPING IN SEMICONDUCTORS.....	28
III.1. History of diamond boron delta-doping	29
III.2. Theory of delta-doping	29
III.3. Basic theory of electronic delta-doped structure	30
III.4. Simulation of diamond boron delta-doping.....	31
IV. CHALLENGES & STRATEGIES.....	36
IV.1. From heavy to light boron doping and vice versa	36
IV.2. Thickness	36
IV.3. Interface	37
V. SUMMARY	37
VI. RÉSUMÉ DU CHAPITRE 1.....	39
CHAPTER 2. ENGINEERING OF THE MPCVD DIAMOND GROWTH TECHNIQUE	45
I. PRESENTATION OF ENGINEERING PROJECTS.....	47
II. NIRIM-TYPE DIAMOND GROWTH REACTOR ENGINEERING	48
II.1. MPCVD reactor: the starting point	48
II.2. Design and optimization	51
III. IN SITU CHARACTERIZATION ENGINEERING	60
III.1. Surface temperature measurement	60
III.2. IR interference - Temperature oscillation.....	61
III.3. Sample position effect	64
III.4. In-situ gas phase composition monitoring - Mass spectrometry.....	65
IV. CONCLUSION	68
V. RÉSUMÉ DU CHAPITRE 2.....	69
CHAPTER 3. CHARACTERIZATION TECHNIQUES.....	73
I. SURFACE MORPHOLOGY ANALYSIS	75
I.1. Reflected light microscopy.....	76
I.2. Optical profile	80
I.3. In-lens Secondary Electron Detector	82
II. CATHODOLUMINESCENCE SPECTROSCOPY.....	84
II.1. Theory.....	84
II.2. Experimental setup.....	85
II.3. Cathodoluminescence of diamond	86
III. TRANSMISSION ELECTRON MICROSCOPY	88
III.1. Imaging methods	88

III.2. Sample preparation	94
IV. SECONDARY ION MASS SPECTROSCOPY	95
IV.1. De-convolution and profile reconstruction	96
IV.2. Ion implantation and recoiling.....	97
IV.3. Mixing-Roughness-Information model (MRI)	99
V. HIGH RESOLUTION X-RAY DIFFRACTION	100
V.1. Diffractometer system.....	100
V.2. Diffraction peaks in diamond.....	101
V.3. Relaxation/strain, composition and tilt	101
VI. CONCLUSION	103
VII. RÉSUMÉ DU CHAPITRE 3	104
CHAPTER 4. DIAMOND SUBSTRATES PROPERTIES	109
I. INTRODUCTION.....	111
II. GENERALITY ABOUT SYNTHETIC DIAMOND GROWTH.....	111
II.1. Ἀδάμας – Adámas – Unbreakable.....	111
II.2. Diamond synthesis.....	111
II.3. Development in CVD growth	113
II.4. Plasma-enhanced CVD methods.....	115
II.5. Mechanisms of CVD diamond growth	115
III. DIAMOND TYPE CLASSIFICATION	119
IV. GROWTH SECTORS IN HPHT.....	121
IV.1. Definition	121
IV.2. Polishing steps induced by growth sectors.....	122
IV.3. Impurity distribution in growth sectors.....	122
V. VOLUME IMPERFECTIONS IN TYPE I AND II DIAMOND	124
VI. SURFACE IMPERFECTION ON TYPE I AND II DIAMOND	126
VI.1. Surface polishing.....	126
VI.2. ISO 25178-2: Geometric Product Specifications (GPS) – Surface texture parameters	126
VI.3. Comparison CVD / HPHT substrates	127
VI.4. Ultimate polishing.....	128
VII. DEFINITION OF SURFACE DEFECTS	129
VIII. CONCLUSION	131
IX. RÉSUMÉ DU CHAPITRE 4	132
CHAPTER 5. HEAVY AND LIGHT BORON DOPING – LATERAL GROWTH.....	137
I. INTRODUCTION.....	139
II. INFLUENCE OF THE SAMPLE POSITION IN THE PLASMA ON THE GROWTH	140
II.1. Definition of plasma/sample contact modes.....	140
II.2. Growth uniformity	141
II.3. Plasma density and doping efficiency.....	143
II.4. Boron incorporation mechanisms: a short tentative discussion	143
III. HEAVILY BORON DOPING OF DIAMOND UNDER SLOW GROWTH CONDITIONS.....	146
III.1. On the reference growth conditions for heavily boron doped diamond layers growth.....	147
III.2. Measurements of high boron concentration in the solid phase.....	148
III.3. Discussion on heavily boron doping efficiency	150
III.4. Effects of the boron concentration in the gas phase on the diamond growth rate	152
III.5. Effects of the total gas flow on the growth rate and on the boron incorporation	153
IV. LOW BORON DOPING AND LATERAL GROWTH	156
IV.1. Origin of the roughness	157
IV.2. Effect of lateral growth on surface defects height reduction.....	160
IV.3. Determination of growth anisotropy parameters	163

IV.4. Influence of growth sectors	167
V. CONCLUSION	169
VI. RÉSUMÉ DU CHAPITRE 5	170
CHAPTER 6. OPTIMIZATION OF P--/P++/P-- INTERFACES, APPLIED TO DELTA-STRUCTURES	175
I. INTRODUCTION	177
II. SIMS ION MIXING EFFECT ON ULTRA-THIN LAYER.....	177
II.1. Effects on the thickness determinations in thin layers.....	178
II.2. Thickness effects on peak concentration values	181
II.3. SIMS memory effects	183
III. OPTIMIZATION OF INTERFACES SHARPNESS	184
III.1. Diamond growth conditions properties on p++ layer interfaces.....	185
III.2. Optimization of the rising interface	186
III.3. Optimization of the falling interface.....	187
IV. INTERFACE CHARACTERIZATION BY STEM.....	192
IV.1. HAADF contrast	192
IV.2. From contrast to boron doping	194
IV.3. Extrapolation on interface sharpness.....	196
IV.4. H-TEM on delta-layers	197
V. X-RAY DIFFRACTION OF BORON-DOPED P++ STRUCTURES AND SUPERLATTICE	199
V.1. HRXRD on P++ layers	199
V.2. HRXRD on p++/p-- superlattice.....	201
VI. COMPARISON WITH OTHER MPCVD TECHNIQUES FOR DELTA-DOPING IN (100) DIAMOND	202
VII. CONCLUSION	203
VIII. RÉSUMÉ DU CHAPITRE 6.....	204
GENERAL CONCLUSION	209
CONCLUSION GÉNÉRALE	210
REFERENCES.....	213
ANNEXES	225
I. FLUID MECHANICS	225
I.1. Correction of the gas density.....	225
I.2. Correction of the gas flow.....	225
I.3. Reynolds number for a pipe.....	225
I.4. Position on Moody chart: turbulences regime	226
II. MASS-SPECTROMETRY	227
III. LOW BORON DOPING MEASUREMENT	228
III.1. By CL.....	228
III.2. By Capacitance-Voltage (C(V)).....	229
IV. SURFACE CONTAMINATION DURING P-- GROWTH	230
IV.1. UC	230
IV.2. Micro-masking	231
V. STRUCTURES ON SAMPLE GROWTH STUDIED	232
VI. SUMMARY OF COLOR-PRODUCING DIAMOND DEFECTS NOT RELATED TO DIAMOND TYPE	233
ABSTRACT.....	235
RESUME.....	235

GENERAL INTRODUCTION

Diamond is the ultimate gemstone, having many strengths and few weaknesses. Boron-doped diamond is a promising semiconductor which can be the base of the future electronic. However its weaknesses impose new development and research in term of structure, packaging... The design of a field effect transistor for high power, high frequency electric applications in diamond, relies on delta-doping, which consist in a 2D doping in order to create a quantum well and a 2D carrier gas, increasing the conductivity. During the design stage of the device, not only the thickness of the boron-doped diamond layer (a few nanometers) but the sharpness of the interface between doped and undoped diamond is a key question, due to the influence of this transition on the properties of the quantum well.

During this PhD project, the chemical vapor deposition growth and the characterization of boron-delta-doped diamond structures were investigated. This work was made under the pathway of a national project (ANR Deltadiam) started in 2009, with the aim to fabricate a diamond delta-field effect transistor for high power, high frequency electric applications. Delta-doping required good knowledge in the diamond growth process and in the boron incorporation mechanisms. This thesis is organized as follow:

In the chapter 1, the motivation to use diamond, a wide band gap semiconductor, for the fabrication of high power, high frequency electric devices will be discussed. Then, operation of a delta field effect transistor will be reviewed. Main functional parameters will be listed and the scope statement will be draft.

The chapter 2 highlights the engineering part of the PhD project. In order to elaborate delta-doping, an original diamond chemical vapor deposition reactor has been designed and fabricated indeed with many home-made customized options (fast gas feeding and switching system for the reaction chamber, sample motion and precise positional setting ...). In parallel, a new technique based on infrared emission allows the in-situ measure of the thickness deposition and gas monitoring allows to follow in real time immediate changes in the gas mixture composition during the growth.

In the chapter 3, characterization techniques used in the diamond surface morphology determination (reflected light microscope, optical profile, secondary electron microscopy) and bulk analysis (cathodoluminescence spectroscopy, transmission electron microscopy, secondary ion mass spectroscopy and X-ray diffraction) will be described.

In the chapter 4, the principal synthetic diamond growth techniques will be reviewed in a relationship with the properties related to diamond substrate (surface and volume imperfections). The aim of this chapter is to classify substrates in terms of applications

(destructive analysis, electric and optical measurements) and to list the main associated defect types.

The chapter 5 discusses the presentation of optimization processes in homoepitaxial boron doped diamond growth by microwave assisted plasma enhanced chemical vapor deposition. The study was made in two times: improvements in the heavy boron doping deposition in thin films first, and then in the low boron doping in both conventional (100)-oriented and novel lateral growth modes.

The chapter 6 focuses on the growth and characterization of thin diamond films, with a special attention brought on the boron doping interface sharpness between heavy and light boron-doped layers. SIMS limitations in the analysis of boron profile on thin diamond films will be discussed. In doing so, alternative characterization techniques, notably SIMS and TEM, were employed in the interfaces study.

INTRODUCTION GENERALE

Le diamant est une pierre précieuse qui possède de nombreux atouts et quelques points faibles. Le diamant dopé au bore est un semi-conducteur prometteur qui peut être la base de l'électronique du futur. Cependant ses faiblesses imposent une recherche et un développement de nouvelles structures, assemblages... La conception d'un transistor à effet de champ pour les applications électriques de puissances élevées, à haute fréquence dans le diamant, repose sur le delta-dopage, qui consiste en un dopage 2D afin de créer un puits quantique et un gaz de porteur de charge 2D, ce qui augmente la conductivité. Au cours de la phase de conception du dispositif, non seulement l'épaisseur de la couche de diamant dopé au bore (quelques nanomètres), mais la raideur de l'interface entre le diamant dopé et le non dopé est une question clé, en raison de l'influence de cette transition sur les propriétés du puits quantique.

Au cours de ce projet de thèse, nous avons étudié la croissance par dépôt chimique en phase vapeur (CVD) et la caractérisation de structures de diamant dopé au bore par technique de delta-dopage. Ce travail a été effectué sous l'égide d'un projet national (ANR Deltadiam) commencé en 2009, ayant pour but de fabriquer un transistor effet de champ en diamant delta-dopé au bore pour les applications électriques de haute puissance et de haute fréquence. La technique de delta-dopage requière de bonnes connaissances dans le processus de croissance du diamant et dans les mécanismes d'incorporation du bore.

Ce manuscrit de thèse s'organise de la façon suivante :

Le chapitre 1 explique l'intérêt du diamant, semi-conducteur à large bande interdite, pour la fabrication de composants électriques de haute puissance et haute fréquence. Puis le fonctionnement d'un transistor delta à effet de champ est étudié en détail afin de déterminer quels paramètres sont à retenir dans le cahier des charges.

Le chapitre 2 traite de la partie ingénierie du projet de thèse. En effet, un réacteur CVD pour la croissance du diamant a été spécialement conçu et fabriqué avec de nombreuses options personnelles (alimentation en gaz rapide et système de commutation pour la chambre de réaction, déplacement précis de l'échantillon et réglage de sa position ...). En parallèle, une nouvelle technique basée sur l'émission infrarouge a été mise au point pour la mesure *in situ* de l'épaisseur du dépôt, et une autre technique permet de suivre en temps réel les changements rapides dans la composition du mélange gazeux au cours de la croissance.

Dans le chapitre 3, il s'agit de passer en revue les techniques de caractérisation utilisées dans la détermination de l'état de surface du diamant (microscope en lumière réfléchie, profilomètre optique, la microscopie à balayage d'électrons secondaires) et l'analyse en volume (spectroscopie de cathodoluminescence, microscopie électronique à transmission, spectroscopie de masse d'ions secondaires et diffraction de rayons X).

Le chapitre 4 fait le point sur les principales techniques de croissance de diamant de synthèse. Par la suite les substrats de diamant sont classés en fonction de leur mode d'élaboration et des principaux types de défauts se trouvant en surface et en volume.

Le chapitre 5 traite des processus d'optimisation de la croissance homoépitaxiale (100) du diamant dopé au bore par CVD assisté par plasma micro-ondes. L'étude a été réalisée en deux temps: amélioration du dépôt de diamant à fort dopage au bore en couches minces, puis croissance du diamant faiblement dopé sous forme conventionnelle et sur de nouveaux modes de croissance latérales.

Le chapitre 6 est axé sur la croissance et la caractérisation de couches minces en diamant. Une attention particulière est portée sur la raideur des interfaces de dopage entre les couches de dopage lourd et faible au bore. Les limites de résolution du profil géométrique du dopage au bore (films minces de diamant delta-dopés) sont discutés. Des techniques de caractérisation alternatives à la spectrométrie de masse à ionisation secondaire (SIMS) ont été employées pour étudier ces interfaces, notamment la microscopie électronique en transmission (MET).

Chapter 1.
**INTRODUCTION TO BORON-
DELTA-DOPING OF DIAMOND**

Nowadays, electricity is the lifeblood of human civilization. All over the world, it is an essential and a vital resource for all economic sectors (production, manufactures and services). World electrical power generation rose at an average annual rate of 3.6% from 1971 to 2009, greater than the 2.1% growth in total primary energy supply. As example, the production of electricity in 2009 was 20053 TWh*, which was 11% of the solar energy the earth receives in one hour (174000 TWh).

Needs in terms of voltage, power density, frequency of use, reliability, or working temperature are becoming more stringent; energy losses must be reduced and performance enhanced. Progress in recent decades in the field of power electronics are due to the introduction of innovative architectures, on the one hand, and to the evolution of composition of devices, on the other. Today progress is hindered by the inherent limitations of silicon; the vast majority of power electronics components commercially available are silicon components. A change of base material for the design of power electronics components must be considered.

Wide band gap semiconductors have properties particularly suited to managing high voltages, high frequencies, in hot environment. Silicon carbide (SiC), gallium nitride (GaN) and diamond are the most prominent materials expected to supersede silicon. Among them, diamond has the physical and electronic properties most suitable to power electronics components. Progress since the 80's in the chemical vapor deposition of diamond films makes it now possible to fabricate good crystalline quality and purity samples, sufficient to develop, in spite of their small size, electronic power devices.

In this chapter, the ability of diamond to respond to the requirements of power electronics will be reviewed from material theoretical points. A set of intrinsic limitations of diamond will be underlined. Then a solution based on delta-doping of diamond will be presented. Finally, the challenges and strategies associated to delta-doping in the case of diamond growth will be presented and discussed.

* [OECD, iLibrary Factbook 2011-2012: Economic, Environmental and Social Statistics](#)

I. DIAMOND DEVICES FOR POWER ELECTRONICS AND HIGH FREQUENCY APPLICATION

The current electrical applications have growing needs in terms of power or operating frequency. In this chapter, we review how the use of wide band gap semiconductors would improve the operating range of power electronic devices

I.1. Physical properties of diamond

The use of wide band gap semiconductors in power electronics has been seriously considered since the 80s (Baliga, 1982). Table 1-1 lists the main electronic characteristics of silicon, diamond and two other wide band gap materials: silicon carbide (4H-SiC) and gallium nitride (GaN). In addition to its well-known optical and mechanical properties, diamond has exceptional electronic proprieties.

The maximum voltage difference that can be applied across the material before the insulator breaks down and conducts is related to their band gap energy (Kyuregyan & Yurkov, 1989), (Chow & Tyagi, 1994). The wide band gap semiconductor properties offer exceptional breakdown voltage. In addition, a wide band gap induces a low intrinsic carrier density, which allows to use devices at higher temperatures without disturbing the properties of the semiconductor material. The excellent mobility of electrons and holes in diamond allows high current densities (which are an important parameter because of the current increase in power) and its high thermal conductivity facilitates the heat dissipation. Finally, the wide band gap ensures greater immunity to radiation, which can be useful in space and nuclear applications, for example. Among the semiconductor considered, the diamond has the widest band gap. The combination of these properties makes diamond an ideal candidate for the manufacture of components for power electronics (Schneider, et al., 2005).

The maximal operating temperature is difficult to determine. In the case of silicon, the temperature of use is mainly limited by the increase of intrinsic carrier densities with the temperature. The law describing the variation of the intrinsic carrier density as a function of temperature can be written as: $n_i^2 = n \cdot p = \sqrt{N_C \cdot N_V} \cdot \exp^{-E_G/kT}$. *Equ.: 1-1*

The maximum operating temperature shown in table 1-1 is the temperature at which the calculated intrinsic carrier concentration is 10^{13} cm^{-3} . Such intrinsic carrier concentration is not negligible compared with the carrier concentration induced by the low doping of the drift zone of power devices. The values presented are indicative: it is possible, for example, to design silicon components operating at higher temperature. However, if the intrinsic carrier density restricted the use of wide band gap semiconductors at high temperatures, the limitation comes from the environment rather than components that must be adapted to the constraints, including thermo-mechanical.

The comparison of different suitable candidate materials used in electronics is often done through the calculation of figures of merit. The different figures of merit established over time reflect a specific type of application. Among the figures of merit commonly used in electronics include the Johnson's figure of merit (JFM) (Johnson, 1965) or that of Keyes (KFM) (Keyes, 1972). They are calculated in table 1-1, with the Baliga's figure of merit (BFM) (Baliga, 1982), and their value were normalized from silicon, which allows an easiest comparison.

Property	Symbol (unit)	Si	4H-SiC	GaN	Diam.
Band gap	E_G (ev)	1.12	3.23	3.39	5.45
Breakdown voltage	E_C ($\times 10^6$ V.cm ⁻¹)	0.3	3	3	10
Electrons mobility	μ_e (cm ² .v ⁻¹ .s ⁻¹)	1500	980	1250	1000
Holes mobility	μ_h (cm ² .v ⁻¹ .s ⁻¹)	480	100	200	2000
Thermal conductivity	λ (W.cm ⁻¹ .K ⁻¹)	1.5	5	1.5	22 [†]
Relative permittivity	ϵ_r	11.8	9.7	10.4	5.7
Saturated drift velocity	($\times 10^7$ cm ² .s ⁻¹)	1.0	2.0	2.2	1.1
Maximal temperature	T_{max} (K)	140	760	800	1350
Normalized JFM	Si = 1	1	400	484	8100
Normalized KFM	Si = 1	1	8.5	2.3	60.8
Normalized BFM	Si = 1	1	13.7	20.4	183

Table 1-1 : comparative properties of silicon and major wide band gap materials used in power electronics and associated figures of merit. JFM - Johnson figure of merit, KFM - Keyes figure of merit, BFM - Baliga figure of merit.

The Johnson's figure of merit involves the breakdown field and the saturation rate of the carriers in the numerator. It reflects the possibilities of producing a low voltage transistor using a semiconductor given in terms power/frequency: $JFM = \frac{E_C^2 \cdot v_S^2}{4\pi^2}$. The Keyes figure of merit illustrates the potential of a semiconductor for the fabrication of high frequency switches. It introduces the thermal conductivity to deal with the heat dissipation: $KFM = \lambda \cdot \sqrt{\frac{c \cdot v_S}{4\pi \cdot \epsilon}}$. The Baliga's figure of merit illustrates the capacity of the material for the manufacture of components through their compromise unipolar voltage strength/resistance response: $BFM = \epsilon_r \cdot \mu \cdot E_C^3$. For all figures of merit considered, diamond got higher values than other materials, which explains the interest it has generated in recent years.

[†] Increase with the ¹²C-enrichement (Anthony, et al., 1989)

I.2. Challenges in power electronics

There is a compromise in electronic devices between the commuted power (product of maximum blocking voltage times the maximum current in the “on” state) and their maximum working frequency. The research on power electronics components therefore aims at improving the trade-off. These two properties depend on both the intrinsic characteristics of the semiconductor and the device architecture. In addition, the compromise must take into account the cooling capabilities of the system. Increasing the operating frequency or the power switched tends to increase the power dissipated by the system. For a particular cooling capacity, one may increase the frequency, but this involves the reduction of switching power, or increase the switching power, at the cost of lowering the system frequency.

I.2.1. At the heart of the power components, the drift

In the OFF state, the space charge extends mainly in the n -region (case of p-n junction) or where the doping is low, often called drift zone or epitaxy area. The breakdown voltage is determined on the one hand by the architecture, doping and thickness of the drift zone and on the other hand by the characteristics of the material (field maximum value which does not trigger the avalanche phenomenon by carrier multiplication). The increase in the breakdown voltage of the device requires an increase in the thickness of the n -region and/or lowering of the doping.

In the ON state, the n -region and/or the low doping region (p-) has a great influence on the voltage drop in the component. Indeed, the resistivity is determined by doping and electron mobility. In the case of bipolar conduction, holes are injected into the n -area. The voltage drop is determined by the mobility and lifetime of the two types of carriers. Bipolar conduction provides better conduction characteristics. If unipolar devices are widely used in low voltage (<500V), at higher voltage, the necessarily thick drift zone induces a very large resistance in the conducting state, which results in very high dissipated power. This is why bipolar components are preferably used.

However, when switching from ON to OFF state, in the case of the bipolar devices, the holes in the n -region must recombine to be effective for blocking. The time required is called recovery time and constitutes the major handicap in bipolar components. In the case of unipolar devices, the time required to switch from ON to OFF state is very short. Switching times result in losing a significant electrical power (switching losses). For high frequency operation, it is thus preferable to use unipolar components.

I.2.2. Increasing the power switched

High power electrical applications, such as railway traction, for example, require larger and larger powers. Transportation of electric energy, from its production site to its place of use, is made at high voltages. Indeed, the electrical power delivered is equal to the product of voltage in the line times the current flowing in the line. Because electrical losses in the line are due to the Joule effect, it is desirable to increase the voltage of power lines, and so, to reduce the current. The increase in the power spent by the load at constant supply voltage consists, for the power component, to provide a higher current. It can be achieved by increasing the voltage or the current rating of power components.

A. Increase in current

The increase in current driven by the converter can be obtained in several ways: by the manufacture of electronic components capable of flowing increasingly important currents, or by the parallel connection of elementary power modules, to add the contribution of different modules. The parallelization of a large number of modules leads to a high cost and volume. So, it is desirable to develop components capable of passing a lot of current. However, the increase in current is limited by thermal effects of power dissipation. The diamond transistor discussed in this study is a solution.

B. Increase in breakdown voltage

The increase in breakdown voltage can be achieved by the serial connection of a large number of elementary modules to divide the voltage between the different modules. As in the case of the parallel modules, this has a cost in terms of number of electronic components and volume. More complex driver circuits will be required. The best option could be to design individual modules capable of holding higher voltages in order to minimize the number of modules in series. The diamond device presented in this study was not developed to increase breakdown voltage.

I.2.3. Increasing the frequency

Increasing the working frequency in power electronics components can have an interesting impact on their environment. Indeed, inside a power electronics module, the value of passive elements surrounding the active components varies inversely with the frequency of operation. An increase in operating frequency induces a decrease in the value of capacitors and inductors used, which results in a decrease in the volume occupied by the various coils and capacitors. It can induce thermal effects that influence the compromise between the operating frequency and the quantity of losses dissipated by the components. The diamond transistor presented in this study has the function to work at high frequency with low thermal losses.

1.2.4. Thermal limitation

There are two types of losses in power switches: conduction losses and switching losses. The share of switching losses compared to conduction losses is determined by the operating frequency. The energy dissipated due to conduction losses and switching induced heating of the components. The temperature increased in junction may impair their functioning, or lead to their destruction; the dissipated energy must be extracted by cooling systems. The evacuation of the power emitted by the component is made through the assembly of the various layers (solders, metallization, electrical insulation ...) to the cooling fluid (generally air or water at room temperature). Each of these layers is associated with a thermal resistance that limits the power extracted. In order to reach a thermal equilibrium, the power extracted must be equal to the power dissipated by the component. Increasing power densities, which is central to the development of power components, runs into the limits of cooling systems.

There are several ways to resolve this issue. First, with cooling systems, which minimize the thermal resistance between the component and the coolant. This would allow a higher density of power dissipated by the components without an increase of their operating temperature. Second, from a research conducted on the components (in order to limit power thermal losses by conduction or switching). Finally, in devices able to operate at higher temperature (to overcome requirements in terms of cooling).

1.3. Devices

Silicon is still the dominant material used in electronics, even for high voltage and high power applications. Silicon is a mature, low cost and widely available technology. However, it has significant limitations coming from its moderate thermal conductivity and its small band gap. Thus its operation is limited at 200°C and a breakdown appears at relatively low electric field. The use of silicon in high power application is followed by relatively high losses and heavy cooling requirements, leading to major costs, space and weight. This is a big disadvantage in key applications such as power conversion, power distribution and transportation.

Several groups, either industrial or academic, mainly in Europe, Japan and USA, have recognized and begun to use the huge potentialities of synthetic diamond for implementing electronic devices. If electronic, thermal and chemical inertness properties of diamond were simultaneously utilized, unprecedented performances would result. Recent progress of epitaxial growth, high boron doping level, surface treatment and improved crystalline quality and availability of synthetic diamond substrates make a solid background for enhancing the development of diamond based applications in several fields like fast and

power electronics (Balmer, et al., 2008), sensors both in biological media (Nebel, et al., 2007) and harsh environment (Brambilla, et al., 2001), monitoring systems in high radiation beams (Morse, et al., 2007), etc... Such perspectives have motivated growing industrial developments in England (Element Six Company), Ireland (Diamond Microwave Devices Ltd) and USA (sp³ Diamond Technologies; Appolo Diamond). Recent advances in manufacturing and enlarging synthetic crystalline diamond substrates open a practicable route for growing epitaxially all the layers necessary for building electronic devices. The possibility of *p*-type doping from traces close to ppb boron concentration up to above one percent, and *n*-type doping with phosphorus, offers the opportunity of relying only on diamond for elaborating all functionalities.

Diamond electronics holds a fantastic promise. A 10 kV diamond Schottky diode has been reported (Volpe, et al., 2010). Such device exploits the high mobility and power handling properties of diamond. These characteristics would enable individual power devices capable of switching voltage of several kV and kA at temperature beyond 300°C. Kato and co-workers reported a diamond bipolar junction transistor device with phosphorus-doped diamond base layer with a current amplification ratio of around 10 in (111)-oriented diamond at room temperature by utilizing optimized device geometry (Kato, et al., 2012). Field Effect Transistors for high frequency and high power applications are still in development. Structures as hydrogen-terminated diamond FET exhibited a drain-current approaching 80 mA.mm⁻¹, with a trans-conductance of 12 mS.mm⁻¹, but were unstable at high temperature (Moran, et al., 2011). A development hetero-junction field effect transistor (HFET) is designed to work at higher temperature. However, a maximum trans-conductance of 0.45 mS.mm⁻¹ was reported with AlN/diamond (Imura, et al., 2012). Using high-quality polycrystalline diamond, MESFET exhibits a maximum transition frequency of 45 GHz, a drain-current density of 550 mA.mm⁻¹ and a maximum trans-conductance of 143 mS.mm⁻¹ (Ueda, et al., 2006). Another kind of transistor, solution gate field effect transistors used the biocompatibility and high frequency properties. Edgington et al. shows a maximum gain and a trans-conductance of 3 and 200 μ S.mm⁻¹ respectively (Edgington, et al., 2012(a)). Technological developments were carried out in order to improve the low contact resistance, surface passivation and doping homogeneity.

II. PROBLEMS RELATED TO DOPING

In contrast with silicon manufacture and with other more common semiconductors, the high compacity of the diamond lattice offers a very small volume to allow impurities to substitute carbon atoms. Few candidates are suitable for diamond doping; principal dopant atoms found are boron, nitrogen, phosphorous, silicon, nickel and sulphur. By ion-implantation

techniques, other impurities can be introduced but the compensation resulting from crystal damage is not negligible and required complex annealing techniques.

If diamond *p*-type doping is available from traces close to ppb boron concentration up to above one percent, and *n*-type doping with phosphorus too, some intrinsic problems occur to get high conductive layers. The success of the doping resides in the diamond ability to receive the dopant (depends of crystal orientation), in the compensation ratio (depends of the doping technique and the crystal orientation) and in the ability to incorporate on substitutional sites where the dopant will be active (acceptor and donor ratio).

II.1. n-type doping

n-type diamond has not been found in nature yet. Since the CVD growth technique exists there have been quite a few attempts to dope diamond *n*-type. Nitrogen is a natural dopant but it doesn't yield any shallow donor (Kajihara, et al., 1993). In theory phosphorus is a good candidate and recently some investigations have been even made on BH complexes (Teukam, et al., 2003).

II.1.1. Nitrogen doping

Nitrogen is the natural candidate for the *n*-type doping of diamond due to its covalent radius (0.079 nm) close to that of carbon (0.077 nm). From this point of view, it should fit easily in substitution site dopant. Nevertheless nitrogen in substitutional site distorts the lattice, increasing its ionization energy up to 1700 meV (Kajihara, et al., 1991). This too deep level makes *n*-type doping with nitrogen unsuitable for the production of devices.

II.1.2. BD₂ complex

In 2003, Teukam et al. discovered the possibility to get *n*-type material using boron-doped diamond after deuterium plasma diffusion (Teukam, et al., 2003). The authors proposed that boron-deuterium complexes could provide a shallow donor level with ionization energy in the 230 - 370 meV range. *Ab initio* calculations were performed and concluded that shallow donor levels close to the conduction band were not induced by such BD₂ complex (Kumar, et al., 2008). Several BD₂-doped diamond samples were measured by Hall Effect and capacitance-voltage spectroscopy. The final conclusion of these investigations is the presence of neutral complexes in *p*-type diamond (Kumar, et al., 2011), but no donor level.

II.1.3. Phosphorus doping

The large covalent radius (0.117 nm) of phosphorus (carbon is 0.077 nm) makes its incorporation difficult and more effective on diamond substrate (111)-oriented than (100).

This donor has an ionization energy near 570 meV (Katagiri, et al., 2004), (Kato, et al., 2005(a)).

n-type doping of diamond by phosphorus on (111)-oriented faces has been shown for the first time at the National Institute for Research in Inorganic Materials (NIRIM, actually called NIMS) in 1997 (Koizumi, et al., 1997). This result was reproduced in other laboratories, as example: at Institut Néel (laboratoire d'études des propriétés électroniques des solides (LEPES) at that time) (Casanova, et al., 2002) and at the groupe d'études de la matière condensée (GEMaC) (Kociniewski, et al., 2006) in France, at the Instituut voor Materiaalonderzoek (IMO) in Belgium (Nesládek, et al., 2003), at the National Institute of Advanced Industrial Science and Technology (AIST) (Kato, et al., 2004) in Japan... It was obtained by microwave plasma-assisted CVD from a gas precursor: the phosphine (chemical formula: PH_3), or from a liquid precursor: the *t*-Butylphosphine (or written TBP, chemical formula: $\text{C}_4\text{H}_{11}\text{P}$) as doping source (Kato, et al., 2004). The first diamond bipolar devices reported in the world was a p-n diode made at NIMS by Koizumi and it was emitting in the UV light (Koizumi, et al., 2001). In 2005, a team of AIST (Kato, et al., 2005(a)) (Kato, et al., 2005(b)) has succeed in the *n*-type doping of diamond with phosphorus on (100)-oriented faces and an ultraviolet emission from a p-n junction was produced (Makino, et al., 2005). This is a major advance because it eliminates a restriction on the substrate orientation which was a hindrance to the development of electronic components based on diamond.

However, the elevated ionization energy of dopant results in a low carrier concentration at room temperature (about 1 electron for 1'000'000 phosphorus donor). Most of donor atoms are neutral at temperature lower than a few hundred of Kelvin (depending on the doping concentration). This low electron density in *n*-type diamond layers provides a large sheet resistance. Currently, no metal-to-insulator transition has been reported on *n*-type diamond. The maximal phosphorus doping reach is around 2×10^{20} at.cm⁻³ regardless of whether the substrate orientation is (001) or (111) and shows no change of the low conductivity at low temperature (Kato, et al., 2005(a)), (Kato, et al., 2009).

II.2. p-type doping – Boron doping

The first clear demonstration of the feasibility of the boron doping of diamond layer was made by Collins et al. in 1971 (Collins & Williams, 1971). Initially, aluminum was supposed to be the main acceptor in *p*-type diamond (Chrenko, 1973), but it has been shown, in response to electrical characterizations that boron is in fact the only the *p*-type dopant that can be incorporated with high reproducibility and with an activation energy of 368.5 ± 1.5 meV (Lagrange, et al., 1998). The first known studies on boron-doped diamond (Field, 1979) in 1950s were performed on IIB-type* natural and synthetic substrates. The main difficulties encountered in these studies were related to the problem of lack of reproducibility of boron doping over several batches of crystals. However, it was commonly assumed that acceptors "boron" of the atoms is perfectly capable of providing *p*-type conduction inside the diamond layers because their covalent radius (0.088 nm) and carbon (0.077 nm) are close enough to allow the incorporation of boron into substitutional sites.

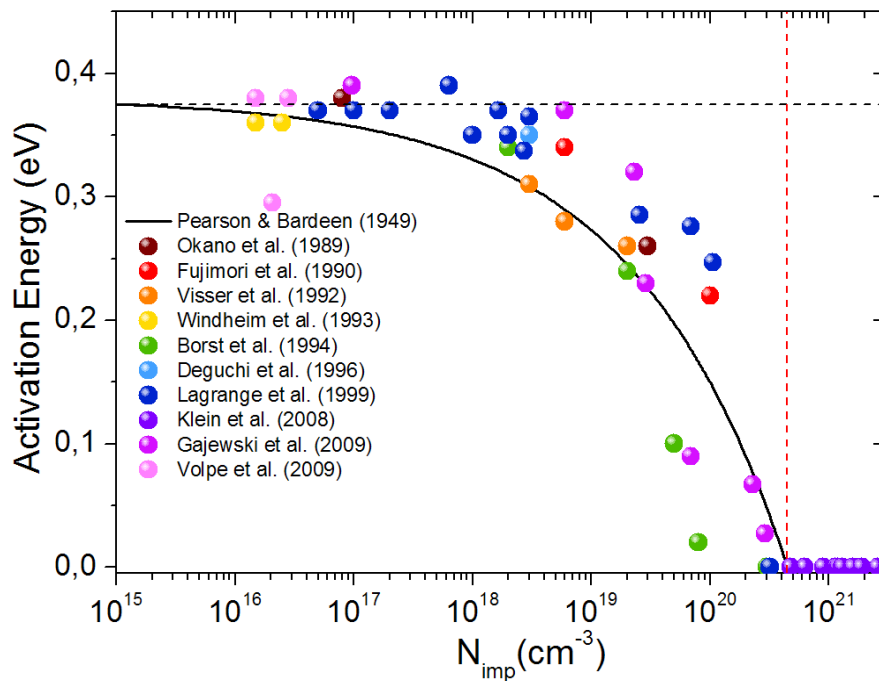


Figure 1-1 : Value of activation energy as a function of boron incorporation reported in the literature. Pearson-Barden fitting model: $E_a = E_{a0} - a \times N_a^{1/3}$, $E_{a0} = 0.38$ eV, $a = 4.7877 \times 10^{-8}$ eV.cm.

Initially, the first attempts of boron doping from the gas phase were performed using diborane (B_2H_6) which, upon decomposition, allows an intake of boron atoms in the gas mixture and thus a possible reintroduction of these in the solid phase (Fujimori, et al., 1986). Subsequently, other attempts at *p*-doping diamond from the gas phase have been initiated from various other gaseous precursors: Tri-methylborate ($\text{B}(\text{OCH}_3)_3$) (Chen, et al., 1994), Tri-methylboron (TMB, $\text{B}(\text{CH}_3)_3$ higher thermal stability compare to diborane) (Cifre,

* See Chapter 4. III. , definition of diamond types.

et al., 1994), Tri-ethylbore ($B(C_2H_5)_3$) (Haubner, et al., 1999), or solid: boron powder (Borst & Weis, 1995), but also liquid (Show, et al., 2000). Currently, p -doping from the gas phase is done only using gaseous precursors which are diborane and TMB. With diborane, one can achieve a range of doping concentrations from a few 10^{14} at.cm $^{-3}$ (Volpe, et al., 2010) up to 10^{22} at.cm $^{-3}$ (Bustarret, et al., 2008), and this on both monocrystalline and polycrystalline layers (Takano, et al., 2005). For boron concentration lower than 2×10^{17} at.cm $^{-3}$, the activation energy is around 370 meV. Then at higher boron concentration (figure 1-1), the activation energy is decreasing near the formation of a boron impurity band which supplies an additional near neighbor hopping conduction at low temperature. At a boron concentration equal to 4.5×10^{20} at.cm $^{-3}$, a metallic conduction on the boron impurity band is observed (Klein, et al., 2007), (Kawano, et al., 2010). At room temperature the phonon scattering mechanism governs the carriers' mobility (figure 1-2a, b) (Pernot, et al., 2010). In theory (when the compensation is neglected), the value of the intrinsic hole mobility is around $2000 \text{ cm}^2.V^{-1}.s^{-1}$. Up to 10^{17} at.cm $^{-3}$ doping level, this scattering mechanism is the only one limiting the carriers' mobility. The maximal experimental achievable hole mobility for p -type diamond is $2000 \text{ cm}^2.V^{-1}.s^{-1}$ (figure 1-2c), as reported by (Yamanaka, et al., 1998), (Teraji, et al., 2006), (Mortet, et al., 2008), (Volpe, et al., 2009). In the case of doping levels superior to 10^{17} at.cm $^{-3}$, the scattering induced by the ionized impurities become the dominant mechanism for the mobility limitation. At high doping level (figure 1-2c), the slope of ionized impurity scattering increases, because the ionization energy decreases quickly at doping levels above 10^{18} at.cm $^{-3}$.

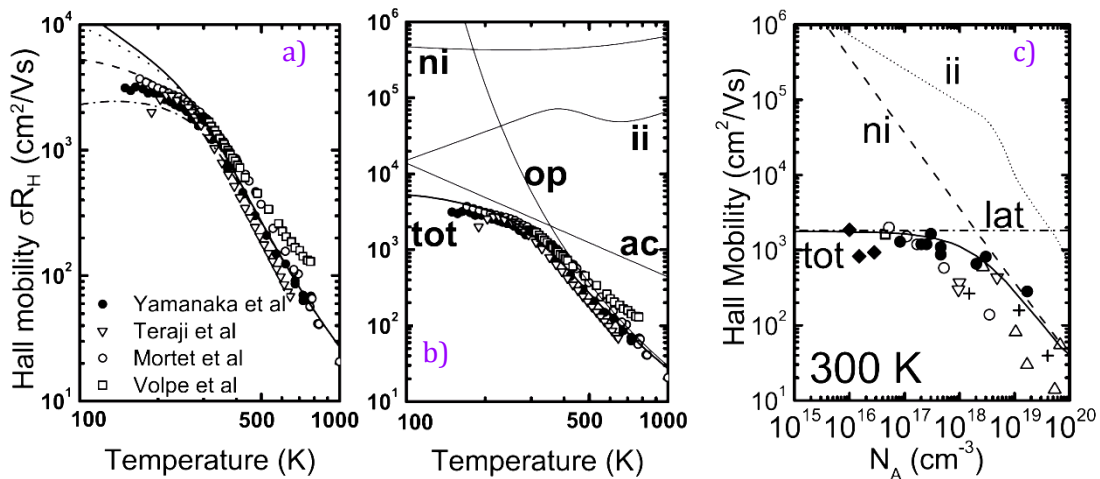


Figure 1-2 : From (Pernot, et al., 2010) (a, b) temperature dependence of the Hall mobility, (c) hole Hall mobility as a function of doping level in homoepitaxial diamond at 300K. (a, b) Experimental data are illustrated by symbols : \bullet — (Yamanaka, et al., 1998), ∇ — (Teraji, et al., 2006), \circ — (Mortet, et al., 2008), \square — (Volpe, et al., 2009). (a) The lines show the calculated mobility with $N_A = 10^{16}$ cm $^{-3}$ and different compensation densities: $N_D = 0$ — solid line, $N_D = 10^{14}$ cm $^{-3}$ — dotted line, $N_D = 10^{15}$ cm $^{-3}$ — dashed line and $N_D = 5 \times 10^{15}$ cm $^{-3}$ — dashed-dotted line. (b) The solid lines show the theoretical contribution of various scattering modes and the total mobility (tot) with $N_A = 10^{16}$ cm $^{-3}$ and $N_D = 10^{15}$ cm $^{-3}$. (b, c) The scattering mechanisms are ii, ni, ac, and op. (c) The theoretical contribution of various scattering modes are illustrated by dashed and dotted line for lattice (lat = ac + op), dotted line for ii mode and dashed line for ni mode. \blacklozenge — (Volpe, et al., 2009), \bullet — (Tsukioka & Okushi, 2006), \square — (Teraji, et al., 2006), \circ — (Mortet, et al., 2008), ∇ — (Gabrysch, et al., 2008), \triangle — (Werner, et al., 1997), $+$ — (Thonke, 2003).

III. DELTA DOPING IN SEMICONDUCTORS

Delta-doping consists of a nanoscale metallic conducting channel (heavily boron-doped diamond), where the mobility is enhanced by quantum effects. In theory, thin delta-doped layers result in the formation of a V-shaped potential well and a 2D hole gas around the boron-doped region, which allows the partial delocalization of holes into the surrounding high mobility intrinsic diamond; leading to the fully activated holes having a higher mobility. In order to achieve a high fraction of delocalized hole, the delta-doped region must follow certain specifications, reviewed and discussed in this paragraph.

At first, the delta-doped layer must be substantially thinner than the de-Broglie wavelength of holes in diamond and have an abrupt box-shaped boron profile with boron concentration transitions shorter than the Debye length in diamond in order to allow the formation of a 2D hole gas. Secondly, the boron concentration (hole concentration) must be sufficiently dense (over the MIT) so that its charge distribution forms a deep V-shaped potential well within which its carriers can populate more delocalized states with higher mobility. Finally, the hole concentration must not be too dense (limitation in the carrier sheet density) to be controllable by a field effect resulting from applying gate voltages not exceeding diamond's breakdown voltage.

In a δ -FET (Field Effect Transistor) a very thin heavily doped diamond film (the delta layer, doped at typ. $5 \times 10^{20} \text{ at.cm}^{-3}$) is buried under a low-doped diamond layer (the cap layer, typ. $10^{15} \text{ at.cm}^{-3}$). The quantum confinement into the delta layer induces a 2D hole gas weakly localized around it with a very high mobility and thus a low ON resistance of the transistor. A positive voltage applied on the top gate will reduce the hole concentration in the 2D channel and create an OFF state.

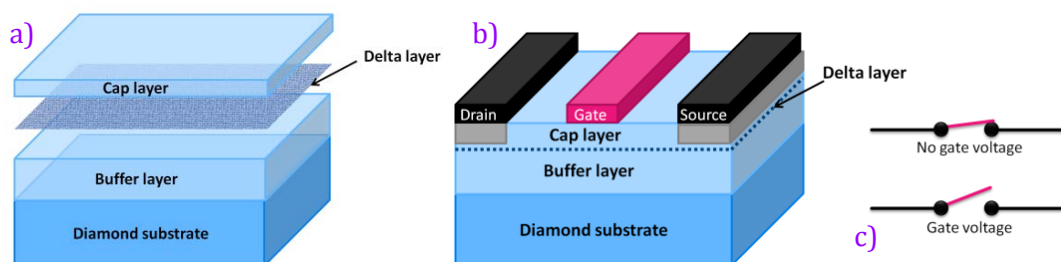


Figure 1-3 : Boron-delta-doped structure (a) and transistor (b). (b) source and drain are ohmic contact, the gate is a Schottky contact. (c) the transistor is normally ON and turn OFF by applying a positive voltage on the gate.

For a maximum blocking gate voltage of 15 V, a holes sheet density of $2 \times 10^{13} \text{ cm}^{-2}$ would be reached with a 25 nm undoped gate thickness and a 0.6 MV/cm electric field under zero drain-source voltage.

III.1. History of diamond boron delta-doping

In 1994, Kobayashi (Osaka univ.) published analytical studies on multiple delta doping in diamond thin films for efficient hole excitation and conductivity enhancement (Kobayashi, et al., 1994). He concluded that most of the holes were propagating in non-doped layers. These areas showed higher mobility, and compared with conventional structures for the same boron concentration, the conductivity in delta-doped diamond appeared 20 times higher. In 1995, Shiomi (Sumitomo Electric) reported a boron pulse-doping leading to p-type conducting channel ($116 \mu\text{S}\cdot\text{mm}^{-1}$) in diamond metal-semiconductor field-effect transistor (MESFET) (Shiomi, 1995). In 1997 another pulse-doped diamond MESFET was presented by Vescan (Univ. of Ulm) with a carrier sheet density of $8 \times 10^{12} \text{ cm}^{-2}$ modulation ($220 \mu\text{S}\cdot\text{mm}^{-1}$) (Vescan, 1997).

In 1999, Kunze (Univ. of Ulm) and co-workers performed a 6 nm FWHM boron delta-doping in diamond with solid boron-rod in ASTEX-type MPCVD reactor (Kunze, et al., 1999), and diamond junction FETs based on delta-doped channels has been fabricated (Aleksov, et al., 1999). In 2005 Element Six claimed a patent on MESFET for RF included a boron “delta doped” layer (Scarsbrook, et al., 2006). In 2008 a collaboration between Element Six, Univ. of Ulm, University of Uppsala and University College London improved delta-FET properties (Balmer, et al., 2008), (El-Hajj, et al., 2008(b)). The doping pulsed technique provides ranging 1.1 to 2.5 nm delta FWHM, and a maximal doping of $1 \times 10^{21} \text{ at}\cdot\text{cm}^{-3}$ (El-Hajj, et al., 2008(a)). The delta-thickness was reduced by 0.9 nm in FWHM, typ. doped at $7 \times 10^{20} \text{ at}\cdot\text{cm}^{-3}$ (Liu, et al., 2010) and most of applications were shifted from MESFET to solution gate field effect transistors (SGFET) ($\approx 200 \mu\text{S}\cdot\text{mm}^{-1}$) biosensors (Edgington, et al., 2012(a)).

III.2. Theory of delta-doping

In theory, the narrowest 1D doping profile is archived if doping atoms are confined to a single atomic layer in the host material. The two parameters characterizing a delta-doping profile are the location of the dopant sheet and the density of doping atoms in the sheet. In practice, dopants in delta-doped semiconductors may not be confined to a single atomic layer but may be distributed over more than a single layer. Surface roughness and other processes (diffusion, drifts, segregation...) may contribute to the doping redistribution. In order to quantify the spread of dopant in delta-doped semiconductor, a top-hat distribution is often considered. But for all well-behaved doping profiles such as a Gaussian or a triangular doping distribution introduces a doping width (Δz_d), larger than the lattice parameter and a standard deviation σ . In order to be considered as a delta-function like, the value of Δz_d must be compared to other relevant length scales such as the screening length, free carrier diffusion length, depletion length, free carrier wavelength... the distribution width Δz_d must be smaller than the shortest of length scales. The typical shortest length scale is the free-carrier de Broglie wavelength. The free-carrier de Broglie wavelength

decrease with increasing the effective mass and the carrier kinetic energy. In general the scale of the length is 2.5 nm. In consequent all doping profiles with a distribution width of ionized impurities satisfying $\Delta z_d \leq 2.5$ nm can be considered as a delta-function-like.

The first truly delta-doped semiconductor structure with clear evidence for a narrow doping profile was reported by Schubert et al. (Schubert, et al., 1984). Capacitance-voltage (CV) measurement on molecular-beam-epitaxy grown GaAs sample revealed a half-width of 2 nm (Schubert & Ploog, 1985). Assuming their profile are symmetric, they deduced a full profile width of 4 nm from the CV measurement. This profile was the first truly delta-doped semiconductor. In the same publication, reported the first field-effect transistor (FET) using a delta-doped GaAs. The delta-doping technique has been used by Schubert and co-workers in a number of MBE-grown semiconductor devices, as example: the heterojunction FET, the high-mobility heterojunction FET...

III.3. Basic theory of electronic delta-doped structure

The free-carrier diffusion depends on the distribution of ionized impurities in semiconductor. In the case of semiconductor with “traditional” smooth changes of doping concentration, the free-carrier profile follows the doping profile with a good approximation. Delta-doped semiconductors exhibits large doping concentration over very short distance, the free-carrier distribution is spread out much further than the doping distribution. Assuming that all impurities are ionized in a very narrow ($\Delta z_d = 0.36$ nm) doping distribution (500 nm of low B-doped diamond, typ. 10^{15} at.cm⁻³, then 0.36 nm of heavily B-doped diamond, typ. 5×10^{20} at.cm⁻³, and finally 500 nm of low B-doped diamond, figure 1-4a), the electrostatic potential created by the impurities ions can be calculated using Poisson – Schrödinger equations.

The resulting potential is V-shaped, symmetric to the center position of the delta-layer (zoom on +/-10 nm on figure 1-4b). Ideally the free-carrier density equals the ionized dopant concentration. The contribution of the free carriers to band-bending cannot be neglected and the potential well will no long be strictly V-shaped. Whereas still not V-shaped in the vicinity of the notch of the potential, the edges become flat sufficiently far away from the doping sheet. The entire dopant-free-carrier system is neutral and as consequence, the band edges are flat at larges distance from the dopant sheet (at 500 nm from the delta layer, the potential is flat. Not visible on figure 1-4b).

The self-consistent solution of spatial and energetic structure of the delta-doped semiconductors requires simultaneous solution of Schrödinger and Poisson equation. The solution is usually done in an iterative way. Initially, a “reasonable” free-carrier distribution is assumed (ground-state wavefunction) from which, using Poisson’s equation, a potential is

deduced. A new set of wavefunctions is calculated from the potential using the Schrödinger equation. A second iteration of the potential is the calculated using the new free-carrier distribution. This procedure is continuous until the calculation converges, that is the wavefunction and the potential do lower change than a convergence criteria with further iterations of the calculation. The result of such structure calculated by *Nextnano*³ code from the Walter Schottky Institute (Institute, 2012) is given on figure 1-4c, where the ground energy and 4 excited states corresponding to heavy holes is represented inverted (maximum of presence on $-Y$ axis).

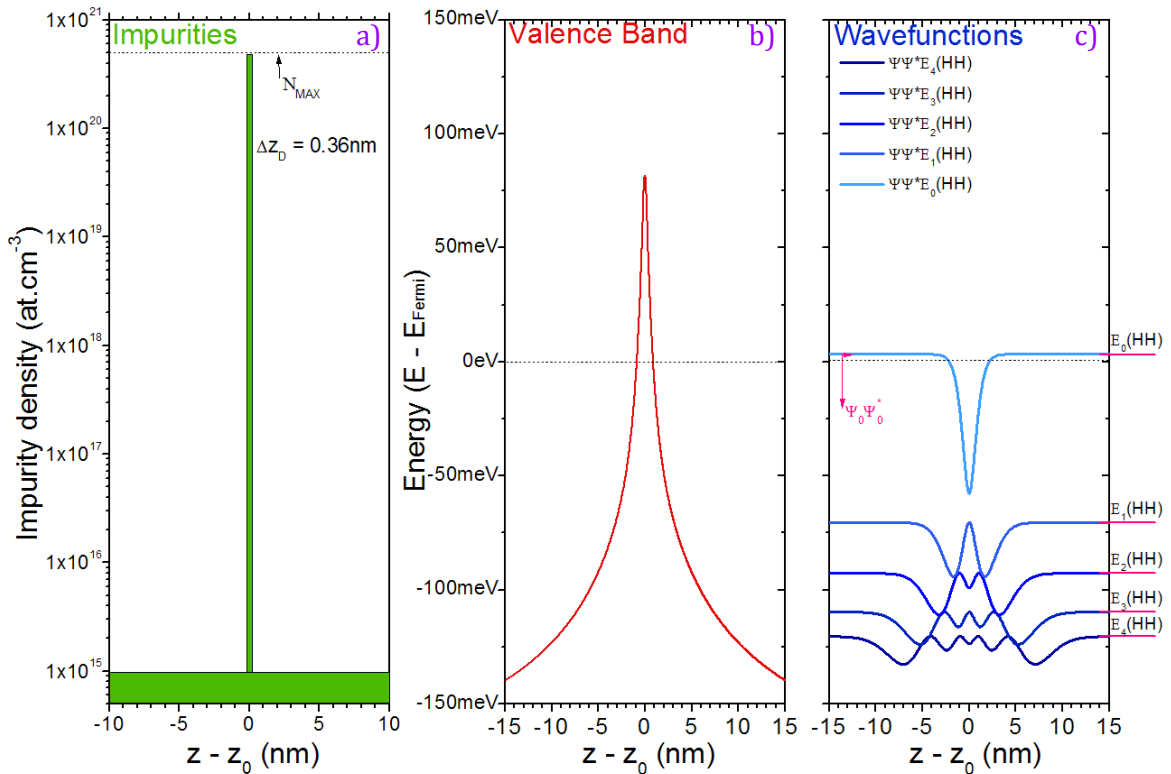


Figure 1-4 : (a) Boron top-hat profile located in the centre of a 1 μm tick diamond with a maximum 3D boron density $N_{MAX} = 5 \times 10^{20}$ at.cm⁻³ and a width of 0.36 nm. (b) Self-consistent calculated heavy holes valence band diagram at 300 K corresponding to boron profile (a). (c) Detail on wave function of five first states of corresponding free-carrier distribution densities, represented inverted (maximum of presence on $-Y$ axis). Distribution densities are shifted according to their relative energies. Energy levels are pointed out on the right side; only the E_0 energy lies above the Fermi level.

III.4. Simulation of diamond boron delta-doping

The goal of this section is to determine roughly the critical parameters to get a 2D hole gas in diamond, in particular the doping level and the delta-layer thickness, based on calculation of hole wave-functions localizations within the envelope-function formalism, without transport consideration.

III.4.1. Computational details

Diamond structures were simulated in 1D mode in order to simplify calculations; we suppose the system is homogenous in the plan X-Y. Diamond crystal was considered with a low boron concentration of $[B] = 1 \times 10^{16} \text{ at.cm}^{-3}$ and with a thin ($\delta = \Delta z_d$) heavily boron-doped 2D diamond layer, called “delta-layer”, imbedded at $z = z_0$ (Fiori, et al., 2010). In order to avoid a boron concentration discontinuity boundaries at $\pm\delta/2$, Gaussian type boron concentration gradients, with a standard deviation σ equal to 0.36 nm were added, composing delta-layer interfaces. The electronic structure is represented within the multi-band effective-mass function approximation. The carrier density (heavy holes (HH), light holes (LH) and spin-orbit splitted holes (SO)), wave-function, energy spectrum and band-edges along the device depth were calculated as a function of delta-layer thickness, boron concentration and device structure at room temperature (300 K).

Heavy holes masse	0.588 m_0
Light holes masse	0.303 m_0
Spin-orbit split holes masse	0.394 m_0
Spin-orbit split-off energy	0.006 eV

Table 1-2 : Holes effective masses and other input data used for diamond simulation.

Hole concentration, energy and localization were deduced from the simulations. In particular, densities of carriers located outside of the delta-layer, i.e. in the high mobility region, were calculated in each case. The parameters used for diamond are summarized in table 1. The hole effective masses of the three valence sub bands are considered isotropic using the density of state masses described in (Pernot, et al., 2010) from the *ab initio* calculated in (Willatzen, et al., 1994). The spin orbit split-off energy comes from (Rauch, 1962).

III.4.2. Efficiency in carriers delocalization

At first, simulation of boron delta doping in diamond were made without perturbations, the case was modeled infinite. This allows estimation of the dependency in the delta-layer thinness on the delocalized fraction of carriers. This efficiency to delocalized carriers is modified with the influence of Schottky barrier height; this is the way to close the channel of a delta-FET.

A. No perturbation – Infinite case

In the case of the infinite structure, the delta-layer lies on a symmetry axis. This symmetry acts on the valence band and on the presence probability density of holes, as already presented in figure 1-4 for heavy holes. *Nota bene* at 0 K only energy levels located above the Fermi level are “occupied” by holes. At room temperature, the 25 meV thermal energy allows some of the deeper energy levels to be partially filled.

Based on 2D densities of holes, fractions of holes located outside of the heavily-doped region (where the boron concentration is lower than $5 \times 10^{20} \text{ at.cm}^{-3}$), *i.e.* in the lightly doped and high mobility region, were estimated. It resulted from a rough integration of the probability density of holes in areas located just inside and outside the delta-layer in order to get the number of free holes located outside the delta-layer. The ratio of the holes outside of delta-layer to the total number of holes in the structure yielded the so-called delocalized holes fraction (considered at 0 K).

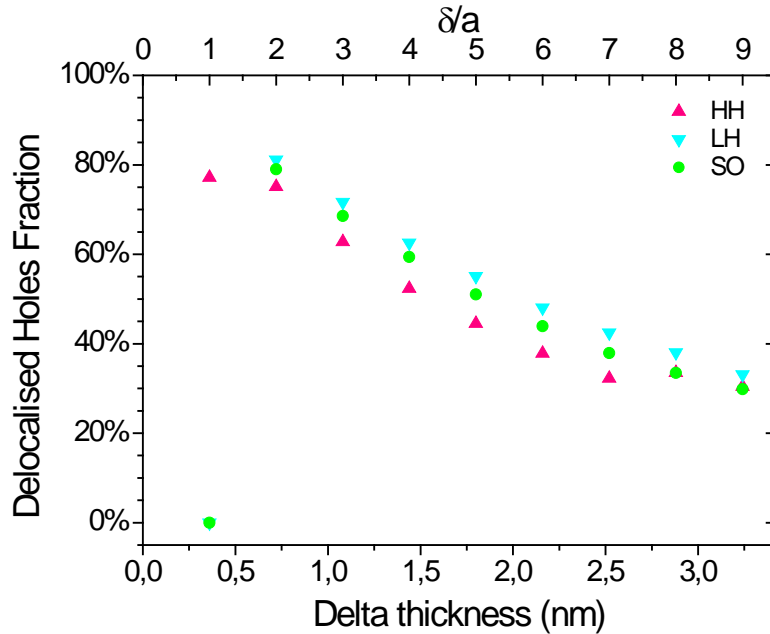


Figure 1-5 : Delocalized holes fraction evolution with δ thickness, $\sigma = 1 \text{ nm}$, in an infinite diamond structure with a boron concentration of $5 \times 10^{20} \text{ cm}^{-3}$.

For a delta-layer doped at $5 \times 10^{20} \text{ at.cm}^{-3}$, on one single atomic bilayer ($\delta = 0.36 \text{ nm}$) illustrated in figure 1-4, with an interface gradient $\sigma = 1 \text{ nm}$, only the ground energy level was fully occupied by heavy holes (see HH dot on figure 1-5). In this case, energy levels of spin-orbit (SO) and light holes (LH) are empty. For thicker delta-layers, 2 to 7 atomic bilayers, 3 energy levels were occupied by holes (heavy, spin-orbit and light holes). These energy levels correspond to the ground states of each kind of holes. Since ground state wave-functions are symmetric (s-type), the probability density reached a maximum in the middle of the delta-layer, and the delocalization ratio was low. For 8 atomic planes of delta-layer, $\delta = 2.9 \text{ nm}$, the first excited state of heavy holes became occupied. As its wave-function is anti-symmetric (p-type), probability density had 2 maxima located outside of the delta-layer, leading to a sharp increase in the fraction of delocalized holes (Figure 1-5). When the doping level raises $1 \times 10^{21} \text{ at.cm}^{-3}$ on one single atomic plane, the 3 ground levels were fully occupied by holes (heavy, split-orbit and light holes) at 0 K. When the delta thickness reaches 6 atomic planes, the first excited mode wave-function of heavy holes becomes fully occupied, and led to the step-like increase in the delocalized holes fraction because of the function asymmetry. At 9 atomic planes, the first excited mode wave-function of spin-orbit split holes becomes fully occupied too; the delocalized holes fraction increased again.

In summary, the fraction of delocalized holes is decreasing with the delta-layer thickness. For a 1 nm-thick delta-layer, around 60% of holes are delocalized, but only 30% are delocalized for a 2.5 nm-thick delta-layer. It has been previously reported in the literature (Anda, et al., 1995) that 95% holes were delocalized in the case of multiple diamond delta-layers at 500 K. This result cannot be compared directly to our work, because our structure is studied at 0 K, with the metal-to-insulator transition taken at 5×10^{20} at.cm⁻³ and is different than the “ideal computing” case of intrinsic-layer/ delta-layer/ intrinsic-layer because of the choice of sharp interfaces. In addition, in our case, the delta-layer corresponds to a boron concentration above the metal-to-insulator transition, not 5×10^{18} at.cm⁻³ as used before (Anda, et al., 1995). The sensitivity of the input parameter, especially the hole effective masses, has an effect on this final result. As described previously, with very thin layer, the hole effective mass has an effect on the contribution of different types of holes (energy levels occupied or empty, position of anti-symmetric wave-functions). However, it is possible to get an idea on this sensitivity, looking difference holes sub bands. For example, for an effective hole mass of $0.588 m_0$ (HH), the delocalized hole fraction is always smaller than for an effective hole mass of $0.303 m_0$ (LH) with a difference, at maximum gap of 9%.

Results show that the boron doping level has a minor effect on the fraction of delocalized holes, as soon as the doping level is high enough to ensure metallic conductivity. However the ratio between the doping and the thickness is pinned by the maximum sheet carrier density to fully deplete the delta-layer (OFF state of delta-FET) without overcome the breakdown voltage. The parameter σ (interface gradient) can be an additional problem by the addition of impurities.

B. Delta-layers interfaces

The parameter σ (standard deviation in the modeling of interface Gaussian gradient) has shown no critical effect on quantum properties at 0K, because no impurities are ionized in these areas. By increasing the temperature, impurities present at the delta-layers interface ionized, thus holes concentration profile is modified leading into both decrease of the sheet carrier density and the efficiency to delocalize holes.

C. Perturbation brought by a Schottky barrier

A Schottky barrier located at 25 nm from the delta-layer (barrier height ≈ 2 eV) is used to reproduce the effect of a gate on the surface of the diamond, as in the case of a FET. No tunneling to the metal surface is included. It introduces an asymmetry in the potential well, resulting in two different densities of holes outside of the delta-area.

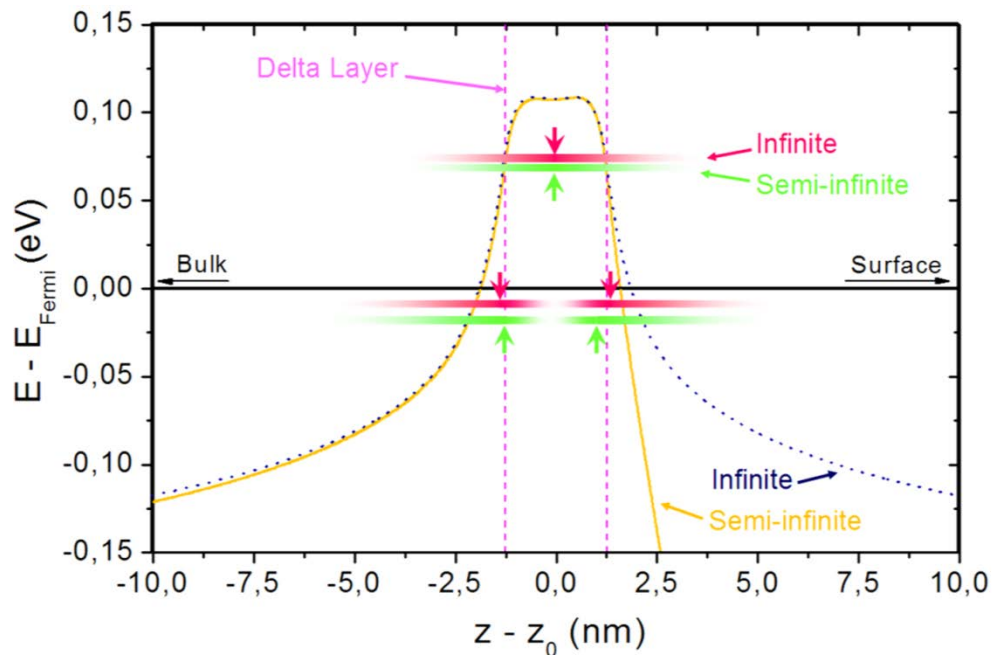


Figure 1-6 : Heavy holes probability density colored in pink for $\delta = 2.52$ nm in an infinite diamond structure (valence band potential is drawn in blue) and in green in the semi-infinite structure (valence band potential is drawn in gold). Peaks of heavy holes probability density are localized by wide arrows. The vertical position of the energy level indicates its energy, the horizontal position its spatial extension and the color contrast its probability density. The Fermi level is drawn in black. Only the ground state and first excited state are represented to simplify the drawing.

As seen in figure 1-6, the asymmetry caused by the Schottky contact induced a slight shift of wave-functions towards the bulk of the device. However, this spatial shift was accompanied by an energy shift towards lower energies. This is the indication of a channel modulation by the gate, as it will affect the occupation density. The fraction of delocalized holes was reduced by 3% in this case (2 eV Schottky barrier height) of $\delta = 2.5$ nm, $\sigma = 1$ nm and followed the above-described tendency when the delta-layer thickness was modified.

III.4.3. Conclusion on simulations

Preliminary calculations of the effect of quantum confinement of holes in diamond indicates that a 1 nm-thick delta-layer would induce the delocalization of 70% of the free holes outside of the doped region, provided that the doping level is high enough to ensure metallic conductivity. The difference between the case of a delta-layer deeply buried into the diamond, and a delta-layer near a Schottky barrier at the surface is a small reduction of the fraction of delocalized holes. The conductivity should be weakened and considering 25 nm of cap layer below the gate, 15 Volts would full depleted the channel. The maximal thinnest for the delta layer doped at 5×10^{20} at.cm⁻³ is 1nm, if the maximal electric is 0.6 MV.cm⁻¹. Then considering this value ($\delta = 1$ nm), the doping gradient doesn't exceed the MIT in order to not modify quantum properties and screening effect. If delta-layer is too smooth, then the path conduction becomes another problem. According to simulation, $\sigma = 1$ nm seems to be a good compromise.

IV. CHALLENGES & STRATEGIES

To fabricate sharp boron delta-doped profiles (< 2 nm in thickness) implies details knowledge on the influence as well as the exact control of the growth and doping parameters. From a technological point of view, this is a great challenge. Such a thin and heavily boron doped film embedded into a lightly doped diamond crystal with abrupt interfaces has never been grown at the Institut Néel. However, optimizing existing diamond growth reactors with specific conditions should allow us to meet the challenge and yield a powerful diamond FET. To do so, in this study we will investigate improvement of parameters such as the active gas dwelling and switching times in the growth chambers. On the one hand, reducing the chamber length and volume will shorten the dwell time of the gas. On the other hand, a new design of the gas cabinet of the machine in a way similar to MOCVD systems will be introduced, using special vent lines associated with a gas manifold equipped with vent-to-reactor valves located very close to the injection point on the reaction chamber. This latter technical feature will clearly give the possibility to both thoroughly reduce the diborane blend concentration transients and the switch ON/OFF time of the dopant to the growth chamber, thus giving much better chances to get an higher homogeneous boron concentration in the delta-doped layer together with more abrupt interfaces with the intrinsic diamond regions.

IV.1. From heavy to light boron doping and vice versa

The boron concentration must be very low in both buffer and cap layers (typ. $[B] < 1 \times 10^{15}$ at.cm⁻³). To do so, a strategy consist to add some oxygen in the gas phase to reduce drastically the boron contamination in the growth reactor (Volpe, et al., 2009) and to avoid any back-doping from the buried heavily boron-doped delta-layer. Heavily boron-doping layers have been reported above the metal-to-insulator transition, *i.e.* $[B] > 4.5 \times 10^{20}$ at.cm⁻³ (Bustarret, et al., 2008).

Key point to ensure a suitable boron-doping profile:

- Uniformity in the boron doping (same doping on 3×3 mm²);
- Constance in the boron doping with the time (flat box-shape).

IV.2. Thickness

The thickness of the delta layer is critical to get the suitable sheet carrier density. The thickness of the cap layer is important. If the cap layer is too thick, then modulation of channel conductivity will require higher voltage, which is limited by the breakdown voltage.

Key points to ensure a suitable thickness:

- Slow growth rate for both boron doping in order to control the deposited matter,
- Low surface roughness and as few defects as possible.

IV.3. Interface

The last challenge, and maybe the most difficult one, deals with the delta-layer interface. The 3D concentration of dopant located in these transition areas induces a decrease in the conductivity and reduce the ability to modulate/close the channel of delta-FET.

Key points to ensure a suitable sharpness of interface:

- Introduce plasma rinsing/etching steps;
- Working at high gas flow rate.

V. SUMMARY

Diamond has a large band gap (5.45eV) and as reported in figure 1-7; dopant impurity (boron and phosphorus) exhibit a quite large ionization energy in comparison with other semiconductors like Si or 4H-SiC.

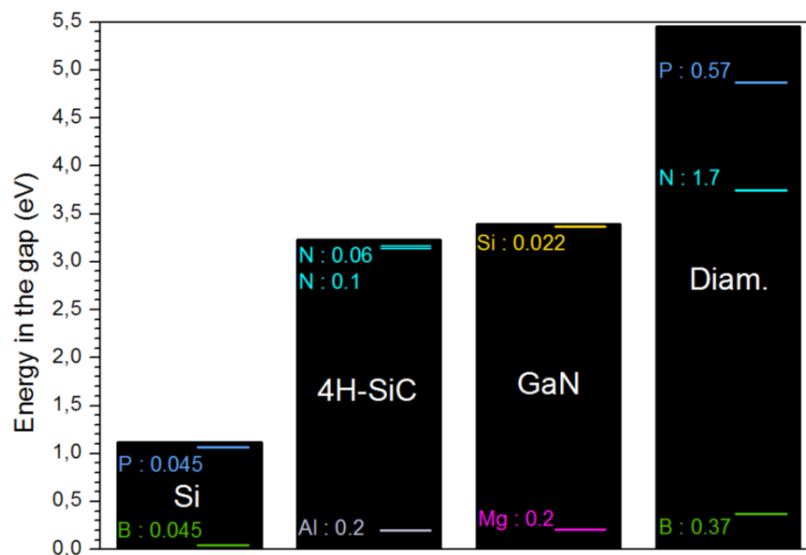


Figure 1-7 : Ionization energies of dopant impurities (eV) in Si, 4H-SiC, GaN and diamond.

The elevated ionization energy of dopant results in a low carrier concentration at room temperature (about 1 hole over 1000 boron acceptor and about 1/1000000 phosphorus donor). Most of acceptor or donor atoms are neutral at temperature lower than a few hundred of Kelvin (depending on the doping concentration and below the metal-to-insulator

transition). *n*-type diamond exhibits a large sheet resistance and no MIT has been reported yet, the doping level to achieve the MIT is large. *p*-type diamond exhibits a large sheet resistance but lower. Increasing the boron concentration reduces this activation energy, and at $4.5 \times 10^{20} \text{ at.cm}^{-3}$ the MIT occurs. Unfortunately, as the activation energy of holes decreases, because of the increased impurity scattering and the onset of a low-mobility, hopping-like conduction, the carrier mobility decreases. The resulting material has poor carrier mobility and sheet carrier densities exceed a value controlled by a typical field effect transistor. A potential solution to this problem of doping diamond is in the development of a delta-doped boron layer.

In a δ -FET (Field Effect Transistor) a very thin heavily boron doped diamond film (the delta layer, doped at typ. $5 \times 10^{20} \text{ at.cm}^{-3}$) is buried under a low-doped diamond layer (the cap layer, typ. $10^{15} \text{ at.cm}^{-3}$). The quantum confinement into the delta layer induces a 2D hole gas weakly localized around it with a very high mobility and thus a low ON resistance of the transistor. If the delta-layer thickness is below 1 nm, then a positive voltage applied on the top gate will reduce the hole concentration in the 2D channel and create an OFF state. The main challenge yields in the extreme sharpness of delta layer interfaces (from $10^{15} \text{ at.cm}^{-3}$ to $5 \times 10^{20} \text{ at.cm}^{-3}$ on less than 2.5nm).

VI. RÉSUMÉ DU CHAPITRE 1

De nos jours, l'électricité est une pierre angulaire de notre civilisation. C'est un élément essentiel et une ressource vitale pour tous les secteurs économiques (l'exploitation, la fabrication et les services). La production d'énergie électrique mondiale a augmenté avec un taux annuel moyen de 3,6% entre 1971 et 2009, ce qui est supérieur à la croissance de l'offre totale d'énergie primaire (2,1%). A titre d'exemple, la production d'électricité en 2009 était de 20053 TWh, ce qui représente 11% de l'énergie solaire que reçoit la terre en une heure (174000 TWh).

Les besoins en termes de tension, densité de puissance, fréquence d'utilisation, fiabilité ou température de travail sont de plus en plus exigeants. Les pertes d'énergie doivent être réduites et les performances améliorées. Les progrès de ces dernières décennies dans le domaine de l'électronique de puissance sont dus, d'une part, à la mise en place d'architectures innovantes, et d'autre part, à l'évolution de la composition des dispositifs. Aujourd'hui, le progrès est entravé par les limites inhérentes au silicium; la grande majorité des composants d'électroniques de puissance disponibles dans le commerce sont des composants en silicium. Un changement de matériau pour la conception des composants électroniques de puissance doit être pris en considération.

Les semi-conducteurs à large bande interdite ont des propriétés particulièrement adaptées à la gestion des hautes tensions, des fréquences élevées, au travail en environnement sévère. Le carbure de silicium (SiC), le nitrure de gallium (GaN) et le diamant sont les matériaux les plus prometteurs pour remplacer le silicium. Parmi eux, le diamant possède les propriétés physiques et électroniques les plus adaptées pour fournir des composants de puissances. Grâce aux progrès accomplis depuis les années 80 dans le dépôt par CVD de films de diamant, il est désormais possible de fabriquer des échantillons de bonne qualité cristalline, aux dopages contrôlés, et de développer, en dépit de leur petite taille, des composants d'électronique de puissance.

Ce chapitre fait le point sur les atouts théoriques du diamant pour répondre aux exigences de l'électronique de puissance et sur ses limitations intrinsèques. Une solution pour dépasser ces contraintes repose sur le delta-dopage du diamant. Les défis et les stratégies associés au delta-dopage dans le cas de la croissance du diamant sont discutés en fin de chapitre.

L'utilisation de semi-conducteurs à large bande interdite en électronique de puissance a été sérieusement envisagée depuis les années 80 (Baliga, 1982). Les propriétés issues de la large bande interdite du semi-conducteur offrent des tensions de claquage exceptionnelles. En outre, une large bande interdite induit une faible densité de porteurs intrinsèques, ce qui permet d'utiliser des dispositifs à haute température, sans perturber les propriétés du matériau semi-conducteur. L'excellente mobilité des électrons et des trous dans le diamant permet d'obtenir des densités de courant élevées (paramètre important en raison de l'augmentation actuelle de la puissance) et son importante conductivité thermique facilite la

dissipation de la chaleur. Enfin, la largeur de bande interdite assure une plus grande immunité aux rayonnements, ce qui peut être utile dans les applications spatiales et nucléaires. Parmi tous les semi-conducteurs, le diamant a le plus grand gap. La combinaison de ces propriétés fait du diamant un candidat idéal pour la fabrication de composants pour l'électronique de puissance (Schneider et al., 2005).

Certes, la filière du silicium est mature, de faible coût et largement disponible, mais le silicium a des limites importantes en raison de sa conductivité thermique modérée et de sa bande interdite de petite taille. Ainsi son fonctionnement est limité à 200°C et son champ de claquage est relativement faible. L'utilisation du silicium dans la gestion de fortes puissances génère des pertes relativement élevées et de lourdes exigences de refroidissement, ce qui implique des coûts importants, de l'espace et du poids. C'est un gros inconvénient dans les applications clés telles que la conversion, la distribution d'énergie et le transport (bus, train, avion...).

Plusieurs groupes industriels ou universitaires, basés en Europe, au Japon et aux USA, ont reconnu et ont commencé à utiliser les énormes potentialités du diamant synthétique pour la mise en œuvre de dispositifs électroniques. Si les propriétés électroniques, thermiques et chimiques du diamant étaient utilisées simultanément, des performances sans précédent en résulteraient. Les récents progrès de la croissance épitaxiale, du dopage, des traitements de surface, de l'amélioration de la qualité cristalline et de la disponibilité des substrats de diamant synthétique permettent le développement d'applications à base de diamant dans plusieurs domaines, comme l'électronique analogique rapide et l'électronique de puissance (Balmer et al., 2008), les capteurs à la fois dans les milieux biologiques (Nebel, et al., 2007) et l'environnement sévère (Brambilla et al., 2001), les systèmes de surveillance de faisceaux de rayon X (Morse et al., 2007), etc. De telles perspectives ont incité de plus en plus les industriels en Angleterre (Element Six), en Irlande (Diamond Microwave Devices Ltd) et aux USA (sp³ Diamond Technologies, Appolo diamant) à fournir de la matière première (substrats de diamant) et des efforts de recherche.

En 2010, une diode Schottky résistant à plus de 10 kV a été mesurée (Volpe et al., 2010). Ces caractéristiques permettraient à équipements électriques individuels de commuter une tension électrique de plusieurs kV et sous des kA à des températures dépassant de 300°C. Kato et ses collaborateurs ont mis au point un transistor à jonction bipolaire en diamant ayant un rapport d'amplification du courant de l'ordre de 10 à température ambiante avec un dopage au phosphore et au bore (Kato et al., 2012). Les transistors à effet de champ à haute fréquence et les applications de forte puissance sont encore en développement. Actuellement la surface hydrogénée utilisée comme canal de conduction dans des dispositifs de transistor montrent de bonnes caractéristiques à haute fréquence, mais sont instables à haute température (Moran et al., 2011). Un développement d'hétérojonctions (H-FET) conçu pour fonctionner à une température plus élevée est toujours à l'étude. Actuellement la recherche porte sur le dépôt de nitrure d'aluminium (Imura, et al., 2012).

De grands progrès technologiques ont été réalisés sur l'amélioration des résistances de contact, sur la passivation des surfaces et sur l'homogénéité du dopage.

Contrairement au silicium et aux autres semi-conducteurs les plus courants, la compacité du réseau atomique du diamant offre un volume très faible pour substituer des impuretés aux atomes de carbone. Peu de candidats sont aptes à doper le diamant : le bore, l'azote, le phosphore, le silicium, le nickel et le soufre. D'autres impuretés peuvent être introduites par implantation, mais les dommages résultant ne sont pas négligeables et impliquent de complexes techniques de recuit.

Le dopage du diamant de type p s'effectue avec du bore (un atome trivalent), et cela sur une gamme allant des traces de concentration (ppb) jusqu'au pourcentage. Le dopage de type n, lui, s'effectue avec du phosphore (un atome pentavalent) mais quelques problèmes intrinsèques persistent pour obtenir des couches conductrices. La réussite du dopage réside dans la capacité du diamant à accueillir le dopant, qui dépend de l'orientation cristalline, dans le rapport de la compensation (lacunes, atomes interstitiels...), qui dépend de la technique de dopage et l'orientation du cristal, et dans la capacité à intégrer des sites de substitution, là où le dopant sera actif (accepteur et donneur de porteur de charge).

Le diamant possède une largeur de bande interdite de 5.45 eV ce qui se traduit par des énergies d'ionisation des dopants (bore et phosphore) assez grandes en comparaison avec d'autres semi-conducteurs comme le silicium ou le carbure de silicium. Cette énergie d'ionisation élevée est à l'origine d'une faible concentration de porteurs à la température ambiante : environ 1 trou pour 1000 accepteurs (bore) et environ 1 électron pour 1000000 donneurs (phosphore). La plupart des accepteurs et des donneurs sont neutres pour à une température inférieure à quelques centaines de Kelvin (en dessous de la transition métal-isolant).

Le diamant de type n présente une résistance de couche importante et aucune transition métal-isolant n'a été rapportée pour l'instant, le niveau de dopage pour l'obtenir est trop grand. Le diamant de type p présente également une résistance de couche importante, mais inférieure au diamant de type n.

L'augmentation de la concentration en bore réduit l'énergie d'activation et dès les $4,5 \times 10^{20}$ at.cm⁻³, on dépasse la transition métal-isolant. Malheureusement, comme l'énergie d'activation des trous diminue, leur mobilité diminue également à cause des mécanismes de diffusions. Le matériau résultant possède une faible mobilité de porteurs et des densités surfaciques de charges qui dépassent leurs valeurs raisonnables à la commande d'un transistor à effet de champ caractéristique. Une solution à ce problème de dopage du diamant réside dans le développement d'une structure particulière avec une couche delta-dopée en bore.

Le delta-dopage consiste à réaliser un plan de conduction de taille nanométrique (un feuillet de diamant fortement dopé au bore, métallique), où la mobilité dans ce plan est renforcée par des effets quantiques. En théorie, le profil de dopage (type p) dans lequel les impuretés ionisées sont localisées sur un même plan (dopage 2D), induit la formation d'un puits de potentiel qui prend la forme d'un V et qui génère un gaz de porteurs 2D (trous) au voisinage de la région dopée. Ceci permet ainsi la délocalisation partielle des porteurs dans le diamant intrinsèque, matériau à haute mobilité, qui borde le plan de dopage. Le but est d'amener le

plus de porteurs de charges dans les régions de plus grande mobilité. Pour obtenir une fraction importante de trous délocalisés, le delta-dopage doit suivre certaines spécifications, dont nous allons faire l'état.

Dans un premier temps, la couche delta-dopée doit être sensiblement plus mince que la longueur d'onde de Broglie des trous dans le diamant et doit présenter un profil de bore abrupte en forme de créneau avec des transitions en concentration de bore plus courtes que la longueur de Debye dans le diamant, de telle manière à permettre la formation d'un gaz de trous 2D. D'autre part, la concentration en bore (concentration de trous) doit être suffisamment dense (pour dépasser la transition métal-isolant) de sorte que sa distribution de charge forme un puits de potentiel profond, dans lequel les porteurs peuvent peupler des états plus délocalisés, ayant une plus grande mobilité. Enfin, la concentration de trou ne doit pas être trop dense (limitation de la densité surfacique des porteurs) pour être modulée par un effet de champ résultant de l'application d'une tension de grille, qui ne doit pas dépasser la tension de claquage du matériau diamant.

Concrètement, dans un δ -FET (transistor à effet de champ delta-dopé) un film très mince de diamant fortement dopé (à $5 \times 10^{20} \text{ at.cm}^{-3}$) est homoépitaxié sur et sous une couche faiblement dopée diamant (dans les $10^{15} \text{ at.cm}^{-3}$). Le confinement quantique des trous dans la couche delta induit un gaz 2D qui s'éloigne des impuretés ionisées et qui gagne une très grande mobilité et par conséquent cela permet une faible résistance d'état passant du transistor. Une tension positive appliquée sur la grille en surface permet de réduire la concentration de trous dans le canal du transistor et d'arriver à un état bloqué.

Des calculs préliminaires de l'effet du confinement quantique des trous dans le diamant indiquent qu'une épaisseur de couche delta de 1 nm induirait la délocalisation de près de 70% des trous en dehors de la zone dopée. Cela à condition que le niveau de dopage soit suffisamment élevé pour garantir une conductivité métallique. La différence entre le cas théorique d'une couche delta enfouie dans le diamant (cas symétrique), et le cas d'une couche delta à proximité d'une barrière Schottky à la surface, présente une petite réduction dans la fraction des trous délocalisés en faveur du cas symétrique. La conductivité doit être maîtrisée et en tenant compte des 25 nm de couche de couverture sous la grille de commande. Dans ce cas, une tension de 15 Volts est nécessaire pour vider le canal totalement, pour couche delta dopée à $5 \times 10^{20} \text{ at.cm}^{-3}$. Le champ électrique maximal imposable de $0,6 \text{ MV.cm}^{-1}$, nous impose de ne pas dépasser 1 nm d'épaisseur (densité surfacique limite de trous). L'épaisseur ainsi fixée ($\delta = 1 \text{ nm}$), le gradient de dopage qui constitue les interfaces ne doit pas dépasser la MIT, afin de ne pas perturber le puits de potentiel et d'ajouter un effet d'écrantage. Si les interfaces de la couche delta sont trop molles, alors des canaux de conduction parallèles posent un autre problème. Selon des simulations, une raideur d'interface inférieure à 1 nm par ordre de grandeur ($\sigma = 1 \text{ nm}$) semble être un bon compromis.

La fabrication de profils de bore ultra minces ($< 2 \text{ nm}$ d'épaisseur) requière une connaissance approfondie sur l'influence des paramètres de croissance du diamant ainsi que le contrôle exact du dopage. D'un point de vue technologique, il s'agit d'un grand défi.

De tels films minces de diamant fortement dopés au bore intégrés dans un monocristal faiblement dopée avec des interfaces abruptes n'a pas de précédent à l'Institut Néel. Cependant, l'optimisation d'un réacteur de croissance de diamant existant et la mise en place de conditions spécifiques doivent nous permettre de relever le défi et aboutir à un δ -FET en diamant.

Pour ce faire, dans cette étude, nous allons étudier l'amélioration des paramètres tels que les temps de résidence des gaz actifs dans la chambre de croissance et les temps de commutation. D'une part, il est question de réduire la longueur de la chambre et son volume pour réduire le temps de séjour des gaz. D'autre part, une nouvelle conception des panneaux de gaz s'inspirant des systèmes MOCVD sera mise en place. Il utilise des lignes de mélange dédiées, associé à un système de vannes d'aiguillage situées très près du point d'injection de la chambre de réaction. Ces caractéristiques techniques apportent la possibilité de réduire les transitoires de dopage aux interfaces des couches et la concentration résiduelle en diborane du mélange, ce qui donne de bien meilleures chances d'obtenir une plus grande concentration de bore homogène dans la couche delta-dopée avec des interfaces abruptes aux régions intrinsèques.

Chapter 2.

ENGINEERING OF THE MPCVD DIAMOND GROWTH TECHNIQUE

I. PRESENTATION OF ENGINEERING PROJECTS

The Microwave Plasma-enhanced Chemical Vapor Deposition (MPCVD) diamond growth reactor dedicated for the boron doping was modified in order to fit with the delta-doping growth process (high gas flow, gas mixture prepared and stabilized before introduction...) and a higher number of operators using it (easy to use, fast initialization, safety with oxygen/hydrogen mixture and diborane gas...).

Following the development of the upgrade, optimization of peripheral systems was pursued. The observation of periodic variations in the apparent surface temperature has led us to setup a way to measure in situ the growth rate. Several methods have been tested to improve the reproducibility of the sample position in the plasma. A gas monitoring facility composed of a mass spectrometer and a differential vacuum system was also developed.

II. NIRIM-TYPE DIAMOND GROWTH REACTOR ENGINEERING

The equipment and procedure for loading and unloading diamond samples was totally renewed. A separate load-lock vessel and X-Y-Z sample in-situ manipulators were installed. The free volume and pumping time were drastically reduced. The original gas feeding was completely replaced by a 3 ways manifolds system inspired from MOCVD growth systems and pressure management was automated by PID controller. The safety was upgraded in accordance with present regulations and safety rules.

II.1. MPCVD reactor: the starting point

The initial MPCVD growth reactor was built up by E. Gheeraert (Gheeraert, 1992) and P. Gonon (Gonon, 1993), principally based on the model of a Japanese reactor used at NIRIM (National Institute for Research in Inorganic Materials, actually called NIMS) by Kamo et al. (Kamo, et al., 1983).

The growth chamber consists of an inner and an outer fused silica (quartz) tube, the sample holder is placed on the top of the inner quartz tube at the intersection with the waveguide. A microwave plasma generator (Metal Process model G2V2) operating at a standard frequency of 2.45 GHz supplies an adjustable microwave power in the range of 0 to 2000 Watt. The horizontal position of the plasma can be adjusted by the hollow-faced piston (standing wave tuning); the reflected power (water cooled with the isolator) can be minimized by adapting the impedance. The growth chamber is connected to a pump system underneath, consisting of a primary pump and a turbo molecular pump. While the primary pump is used for the circulation of the gas mixture, the secondary pump ensures a base pressure below 10^{-5} Torr before introduction of the gas mixture and therefore prevents incorporation of other impurities.

In time several features have been added to the growth chamber in order to improve the quality of the grown layers. From March 2004 on, a multistage dilution system (the dilutor) has been installed which allows to control the concentration of B_2H_6 in the gas mixture with a higher precision compared to the previous apparatus. This has significantly improved the reproducibility of the samples, and, furthermore, the three-stage dilution system is also suited to the growth of very weakly-doped layers with boron concentrations of the order of 10^{15} cm^{-3} . Safety in the feeding line was ensured by closing the inlet and outlet valves of the dilutor in case of any gas leakage detected by an independent multisensory fix gas detection central unit. In November 2005, a gas purifier was installed on the hydrogen line (N60). The purity of hydrogen (main gas source during growth) is better than 99.9999995% (N85) which limits considerably the presence of impurities like water and nitrogen. Methane and diborane are not filtered, but their purity is claimed by the supplier to be 99.9995% (N55).

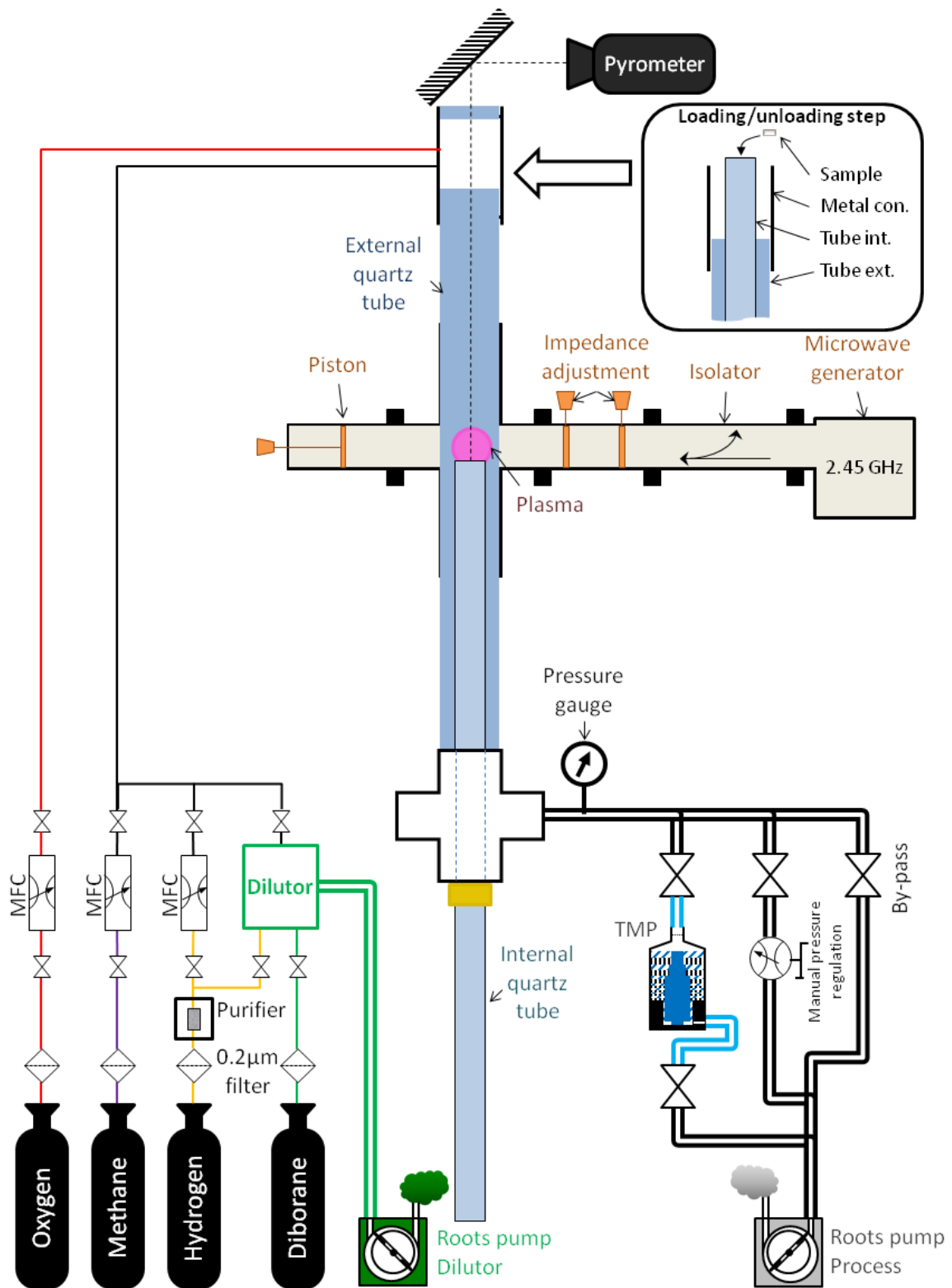


Figure 2-1 : Design of NIRIM-type MPCVD growth until May 2010.

The plasma ignites at the crossing of the metallic waveguide and the external quartz tube (see figure 2-2). The ignition is made under pure hydrogen gas flow. When the pressure in the vessel is stable around 4 Torr the microwave peak power is ramped up to 400 Watt. The

impedance of the microwave guide is adjusted to reduce the reflected power and the plasma ignites. The pressure is increased and the microwave power is adjusted with respect to the process step flow.

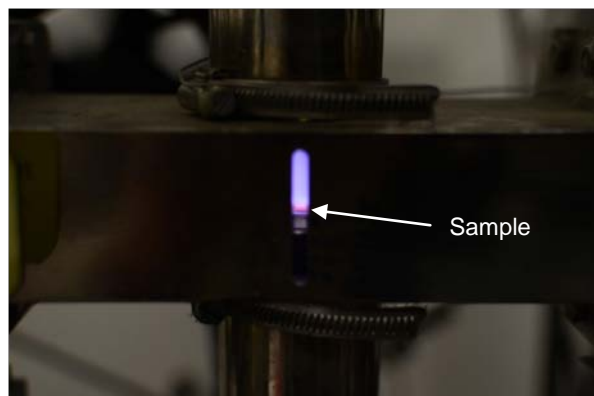


Figure 2-2 : Detail on the sample position inside the plasma.

The heat dissipated in the quartz and the wave guide is evacuated by air-cooling providing by 2 powerful fans. Usually the temperature of the waveguide (get by thermocouple K-type) is around 140°C under pure hydrogen plasma conditions. The diamond sample is located on the sample holder at the extremity of the internal quartz tube which ensures its electrical and thermal insulation. A single wavelength optical pyrometer is used for reading the sample surface temperature trough the window located at the top side of the vessel as illustrate on figure 2-1. The emission of the silicon substrate holder in the infrared, corrected by the transmission through the optical window, is collected by the pyrometer, using an effective emissivity of 0.4 (Gheeraert, 1992). The motion of the internal quartz tube is possible only form the back side when the vessel is vented (atmosphere pressure) by unscrewing the fixation made of brass. Top side of the vessel is uncapped and the internal tube is moving up by hand (like a screw) to reach the top side of the external tube (see detailed view on figure 2-1). This situation of unloading/loading is very critical:

- During moving up the internal tube can break and the hand is cut by the quartz;
- During moving up and down, the sample can fall down because of human vibration;
- The final position in the plasma area is not easily reproducible because of backlashes.

The sample holder consists of a 10×10 mm² silicon piece overgrown with non-intentionally doped polycrystalline diamond (in order to avoid incorporation of silicon from the sample holder as impurity during growth). After the growth, the surface of both internal and external tubes is dirty and contaminated with boron if diborane is introduced. The cleaning of both internal and external tubes is made by applying pure oxygen plasma. In this case, the plasma is cold, the pressure and microwave power are low (typically 160 mTorr and 220 Watt).

II.2. Design and optimization

II.2.1. Load lock vessel

Loading and unloading diamond samples used to be critical steps. When the sample fell down inside the reactor, it meant to open completely the reactor and to lose one day (pollution, large volume). In addition, the final vertical (Z) position of the diamond sample was not easy to reproduce from growth to growth because of mechanical backlash (internal quartz tube / metal sealing screw connection). The internal quartz tube was sometimes broken during sample unloading step and the person in charge of the tube motion (translation by hand) was injured (cut).

The idea was to totally modify this system by the installation of a load lock vessel and by X-Y-Z in-situ manipulator (see Figure 2-3). The load lock vessel ensures a vacuum insulation of the reaction chamber; during loading and unloading steps, the reaction chamber is maintained under secondary vacuum pumping (Turbo molecular pump, TMP) by closing a gate valve. The load lock vessel is connected to the primary pump via a chain of valve and throttle valve used to control the pressure during growth steps. It is connected to a dedicated turbo-molecular pump (via a dedicated valve) in order to minimize the loading time prior to open the gate valve of the reaction chamber (in order to transfer the sample). Of course, the load lock is equipped of pressure gauges for measuring primary and secondary vacuum, which can be insulated to reduce the free volume. With this system, the base pressure before plasma is better ($<1 \times 10^{-6}$ against 1×10^{-5} Torr) and the pumping time has been reduced at 50 minutes against 12 hours initially (Volpe, 2009 PhD thesis).

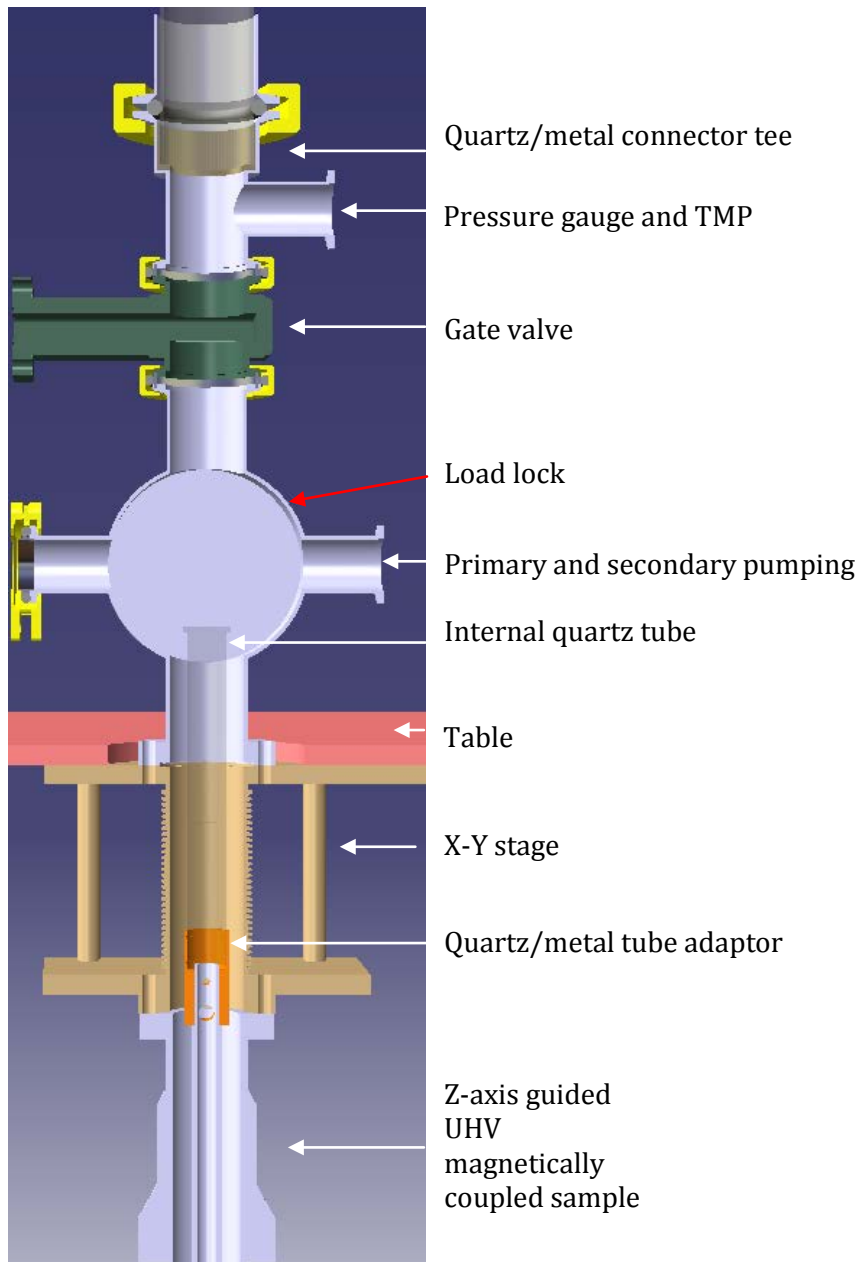


Figure 2-3 : Load lock position and vessel modifications designed by J.-B. Fay* and P. Giroux†

* Internship student at Institut Néel, 2009

† Assistant engineer, epitaxy & thin layers deposition at Institut Néel

The motion of the sample holder from the load lock vessel to the reaction chamber is ensured by a linear Z-axis guided UHV magnetically coupled metallic transporter fixed at the bottom part of a dual axis X-Y stage located below the load lock vessel. The vertical translation is guided by rods. An in-line 90 Vdc motor is used to precisely displace the diamond sample inside the plasma. A voltage regulation control panel allows to adjust the vertical displacement by tuning the voltage from 0 to ± 90 Vdc without any uncontrolled “vibrations” which might displace the diamond sample on the sample holder. The dual axis X-Y stage (figure 2-4) is manually micrometer driven and guided by cross roller bearing slides. Micrometer drivers have unique laser etched plus/minus scales that indicate positive and negative port displacement (“0” indicates the coaxially of both external and internal tubes) and provide precise motion and manipulation of the diamond sample inside vacuum and on plasma processes environments. This complete system has the huge advantage to allow the diamond sample motion inside the plasma when the plasma is ignited, along three directions in space (the horizontal plan X-Y and the vertical Z) and one rotation along Z.

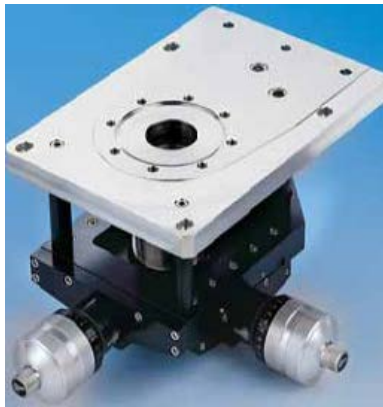
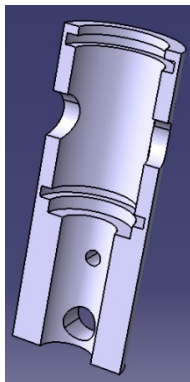


Figure 2-4 : Picture of the V-Plane® dual axis XY stage from Caburn MDC Europe Ltd.



The internal tube is connected with the vertical sample transporter by a metallic adaptor piece. This adaptor (Figure 2-5) is composed of two cylindrical coaxial cavities: at bottom side for the connection of the sample transporter, with clamping orifices to fix the adaptor at the extremity of the sample transporter, and at the top side to plug the internal quartz tube into two strained O-rings seals. This adaptor ensures the continuity of motions given by the sample transporter to the internal quartz tube.

Figure 2-5 : 3D cross-section view of quartz/metal tube adaptor designed by J.-B. Fay[‡] and P. Giroux[§]

[‡] Internship student at Institut Néel, 2009

[§] Assistant engineer, epitaxy & thin layers deposition at Institut Néel

II.2.2. MOCVD-like gas flow management

The original gas distribution (visible on figure 2-1) was completely replaced by a 3 ways manifolds, similar to those of MOCVD systems, connected to 3 independent Mixing Preparation Unit (MPU) blocks. These MPUs are responsible of the gas preparation (parallel mass flow controllers (MFC)) and gas stabilization (pressure regulation) feeding the plasma in the reaction chamber (see detailed view in figure 2-9). In these blocks, gas mixture has the possibility to flow in the direction of the reaction chamber or the event line, parallel to the reaction chamber, before to be evacuated by a primary (roots) pump. When the gas is flowing through event line, a pressure controller located after MFCs is responsible of the pressure balance order to keep a small overpressure between the MPU and the reaction chamber. This configuration allows gas mixtures to flow independently, in parallel, without any cross contamination. When the gas composition of the plasma has to be changed (by pressing a button on the main control panel) manifolds are switched over to send the gas mixture to the reactor or to event depending on the plasma mode selected (H₂, NiD, Dop).

The gas panel is divided into two platforms.

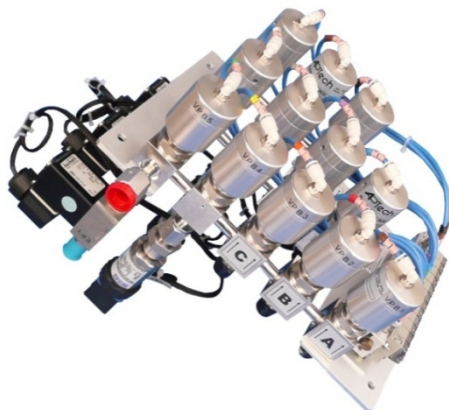


Figure 2-6 : Picture of the gas platform #B - Pressure controllers, manifolds and mixing valves.



Figure 2-7 : Picture of the gas platform #A - Mass flow controllers and insulating valves.

The platform #A composed the gas distribution and flow management. On this platform, hydrogen, methane and oxygen are conditioned (pressure and filtered) and are distributed to 3 Preparation Mixing Units (MPU). 8 mass flow controllers (AERA®) ensure an accurate mixture ratio in each unit. Prepared gases are sent to the platform #B which is located very close to the inlet point of the reaction chamber and at 1 meter of #A. The platform #B ensure the pressurization of mixing units, the final mixing point of gas species and the orientation of gas flow trough manifolds. This platform is very compact, and was easily integrated in the existing reactor configuration.

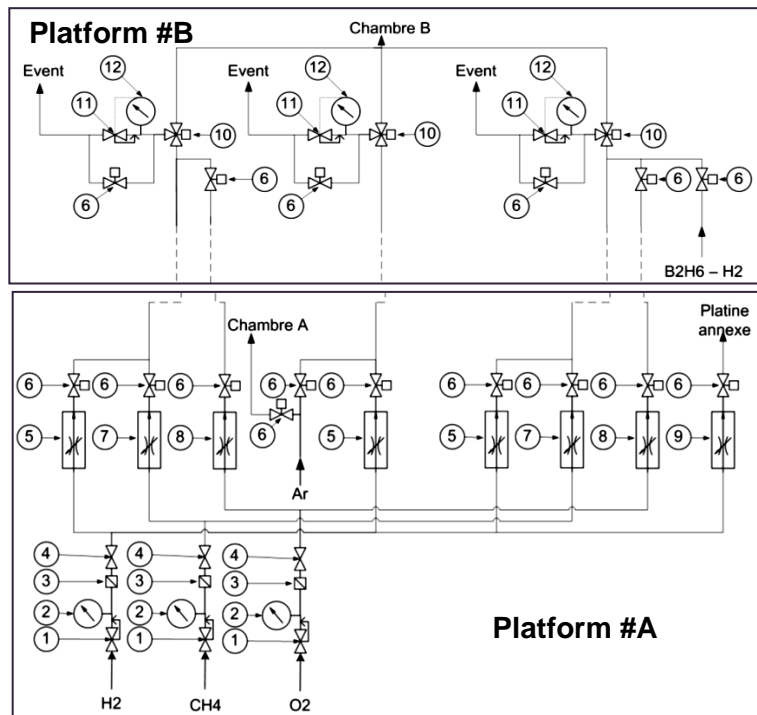


Figure 2-8 : New gas panels. (1) Pressure reducer. (2) Manometer. (3) 0.2 µm filter. (4) Manual insulation valve. (5) 2 sccm range H₂ MFC. (6) Pneumatic insulation valve. (7) 50 sccm range CH₄ MFC. (8) 10 sccm range O₂ MFC. (9) 200 sccm range H₂ MFC. (10) 3 way manifold. (11) Pressure controller. (12) Pressure sensor.

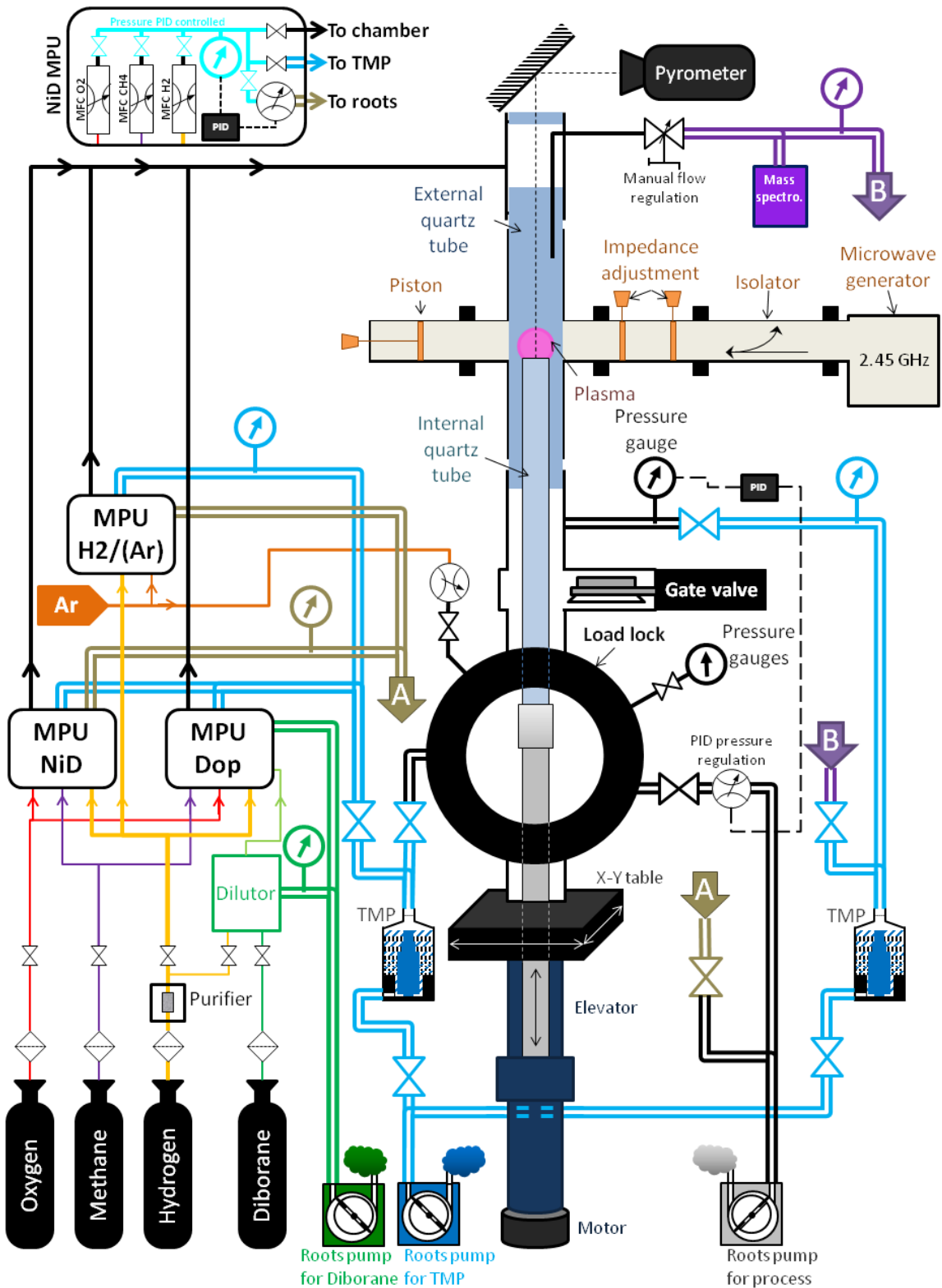


Figure 2-9 : New design of the MPCVD growth reactor for delta-doping process.

II.2.3. Pressure control

Initially, the pressure inside the reaction chamber was measured by a capacitance Baratron gauge and it was tuned by hand with a needle valve. At that time, the growth process was composed of one or two plasma steps; the manual pressure control was suitable enough to grow diamond with a small pressure derivation of 0.5 Torr per hour.

The delta-doping processes required several plasma steps using widely different plasma composition and total gas flows. As a consequence, the control of the pressure cannot be manual. This is the reason of the replacement of the needle valve by the throttle valve actuated by a PID pressure controller (MKS Type 651C). This equipment is very reactive to flow variations in order to keep a stable pressure. The same capacitance gauge (0.1 – 99.99 Torr) is used to measure the pressure

This pressure controller has five Set Points. Set Points are the combination of SETUP pressure, Lead and Gain. It means, we can regulate the pressure on five modes depending of the plasma step and composition.

Set Point	A	B	C	D	E
Pressure	4 Torr	33 Torr	50 Torr	2.5 Torr	9 Torr
Purpose	H ₂ plasma ignition	Growth mode low	Growth mode high	O ₂ plasma ignition	O ₂ plasma etching

Table 2-1 : Purpose of Set Points. Work made with Ilias Jalal*

A. Pressure stability

Lead and Gain value are two parameters which determined the pressure regulation efficiency according to the SETUP pressure. These parameters have to be adjusted in order to get a constant pressure corresponding to the SETUP pressure.

The determination of Lead and Gain was made under 1500 sccm of hydrogen gas without any plasma. The idea was to SET a pressure of 30 Torr and to tune both parameters to optimize the response stability and offset.

Gain (%)	Lead (sec)	Pressure measured (Torr)
100	0.5	Not stable : 22 – 32
75	1.25	Not stable : 21 – 25
75	0.5	Not stable : 28 – 32
30	0.5	Not stable : 26 – 33
10	0.5	Stable : 30.08
15	0.5	Stable : 30.01

Table 2-2 : Determination of Lead and Gain at 30 Torr under 1500 sccm of hydrogen (no plasma). Work made with Ilias Jalal*

* Internship student at Institut Néel, 2009

Gain 15% and Lead 0.5 seconds were used to check pressure stability at higher pressures and flows. The pressure stability was confirmed from 4 sccm to 2000 sccm.

B. Plasma stability

The next step was to check the plasma stability. The plasmas were ignited at 4 Torr and under different flows of hydrogen. The diagram on figure 2-10 shows the plasma stability when the flow is quickly modified by manifolds and that under different pressure.

Plasma conditions switches from 50 sccm to 6000 sccm, or from 4 Torr to 80 Torr, did not result in any plasma interruption.

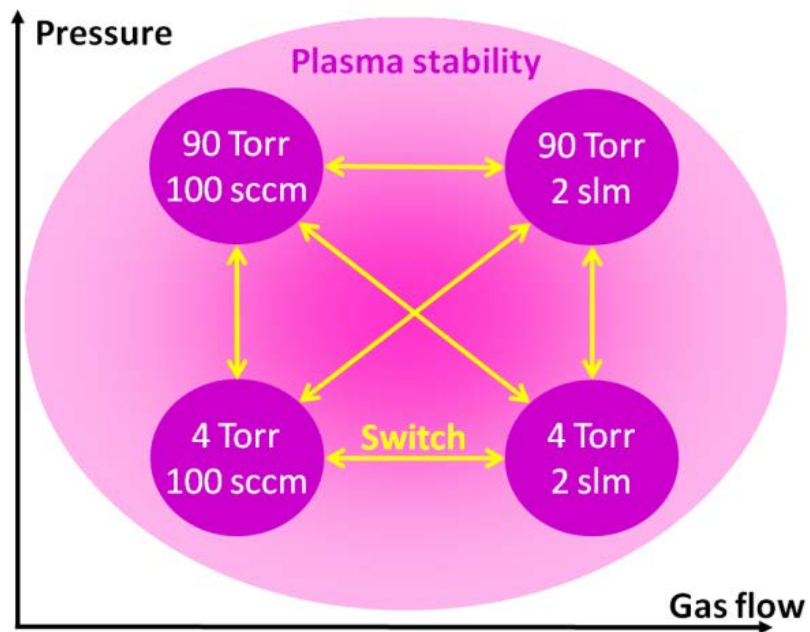


Figure 2-10 : Diagram of plasma stability.

II.2.4. Automation & Safety

At the same time the reactor was modified, the safety was improved. All valves are pneumatic and controlled under the supervision of an automaton (figure 2-11). This automaton is composed of three main parts: a safety controller, a production controller and a test controller.

The safety controller is checking on the external parameters of the reactor unit (fire detection, gas leakage detection, gas extraction, root pump energy failure) and on the inside of the reactor unit through a flow comparator O_2/H_2 , a water cooling flow control, a vessel overpressure detection and a plasma presence detection (deduced from a lower value in the surface sample temperature). The safety controller allows the production controller and the test controller to be operating or not, informs operators with light and sound alarms and with the gas feeding and cylinders manager unit. Production and test controllers are dialing with the microwave generator, valves, the gas flow, the pressure and the temperature.

If a problem appears, scenarios have been written to secure the reactor with respect to the nature of the problem. It provides a safety for both diamond and operators.

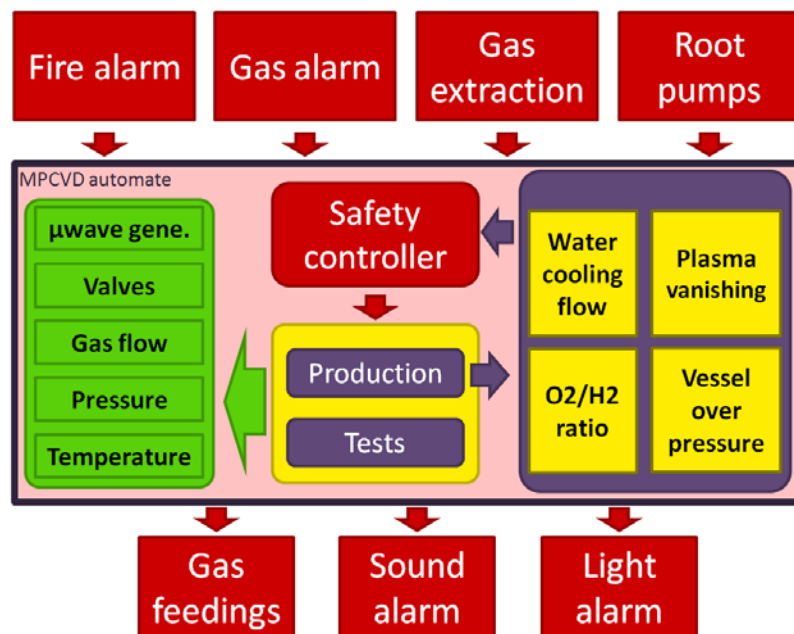


Figure 2-11 : Safety diagram

III. IN SITU CHARACTERIZATION ENGINEERING

III.1. Surface temperature measurement

Many possibilities exist for measuring a temperature but only a few are able to measure with a good accuracy the surface temperature of diamond during the growth. The measurement used is based on infrared emission. The optical system focuses on the thermal radiation onto the detector. The output signal of the detector (temperature T) is related to the thermal radiation or irradiance j^* of the target object through the Stefan–Boltzmann law, the constant of proportionality σ , called the Stefan-Boltzmann constant and the emissivity ϵ of the object, $j^* = \epsilon \sigma T^4$. The emissivity ϵ is the ratio of energy radiated by a particular material to energy radiated by a black body at the same temperature. A true black body would have an emissivity, $\epsilon = 1$, while any real object would have $\epsilon < 1$. Emissivity is a dimensionless quantity.

In our case, the pyrometer used is a single color pyrometer (960 nm) and the corrected ϵ is 0.40 because the infrared radiation is the sum of contributions from the diamond sample, the silicon of the sample holder and the polycrystalline diamond coating of the sample holder. Multiple infrared sources introduce a problem in the true determination of the sample surface temperature. Emissivity was found to change, often drastically, with surface roughness, bulk and surface composition, and even with the temperature itself.

Disappearing filament pyrometer is dependent on the emissivity of the object. If we look at the diamond through a disappearing filament pyrometer, in which comparison is made between a thin, heated filament superimposed over the object to be measured and rely on the operator's eye to detect when the filament vanished the bright object to determine temperature, it appears that the color is different inside the diamond, *i.e.* emissivity is different from a point to another in the same substrate (figure 2-12). This is especially true on HPHT diamond, the emissivity depends of growth sector and the bulk emissivity on CVD substrate is very low, the main emitted infrared coming from substrate edges.

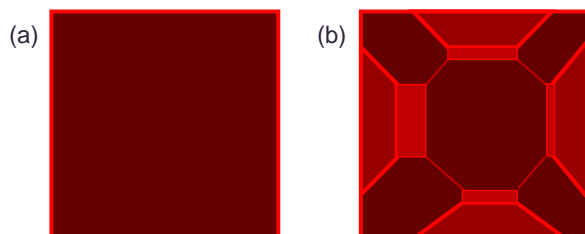


Figure 2-12 : Red color at 900°C of: (a) CVD diamond (bright edges), (b) HPHT diamond with growth sectors (arbitrary growth sector colors)

III.2. IR interference - Temperature oscillation

The temperature measured by the 980nm single-color pyrometer may oscillate with time when a light boron doping growth is made under particular situations. This phenomenon was clearly observed and recorded in the case of delta-cap-layer growth and p-- epitaxy* on p++ samples. After treatment of the signal, it is possible to determinate the growth rate and to follow by computer the deposited layer thickness *in situ*.

III.2.1. Interference phenomenon

Oscillations might be the consequence of optical interferences from a Fabry-Perot cavity within the growing p- - layer because the p++ layer underneath behaves as a mirror: its refractive index at 960 is affected by the presence of free carriers. In theory, from these temperature oscillations, it is possible to determine the thickness of the growing epilayer. The main limitations are the loss of interference intensity when the layer becomes too thick (>1 μm), or when the surface become rough, or when the difference in doping level is too small. The figure 2-13 illustrates this phenomenon in the case of p-- growths made on p++ metallic layer. All p-- layers have a similar thickness, 1.3 μm measured by SEM after MESA etching. For all samples, oscillations have a different time constant and might imply differences in growth rates. The variation in growth rates can be explained by differences in the surface temperature and the sample position in the plasma which was fixed with an error of 0.1 mm on the Z axis (see influence of Z in Chapter 5. II.).

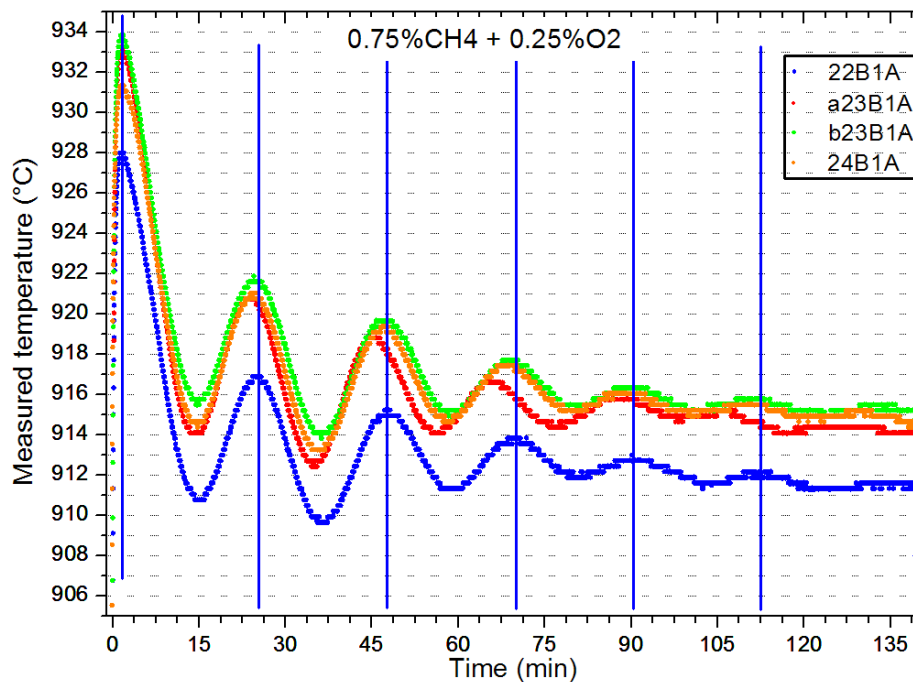


Figure 2-13 : Temperature time records for 4 p-- growth on p++ under the same plasma conditions.

* P-- is the name given to a light boron-doped layer. P++ is the name given to a heavily boron-doped layer above the metal-to-insulator transition. See Chapter 5.

III.2.2. Growth rate estimation for p-- growth by in-situ optical pyrometer monitoring growth temperature oscillation

Maximum transmission occurs when the optical path-length difference between each transmitted beam is an integer multiple of the wavelength (schematized on figure 2-14a) because transmitted beams are in phase; creating constructive interference. The minimum of transmission, occurs when the path-length difference is equal to half an odd multiple of the wavelength, beams are out-of-phase leading in destructive interference (figure 2-14c). During the growth the optical path-length difference increase and the transmitted IR light oscillates. In our case, the measured wavelength is 980nm, *i.e.* 306 THz.

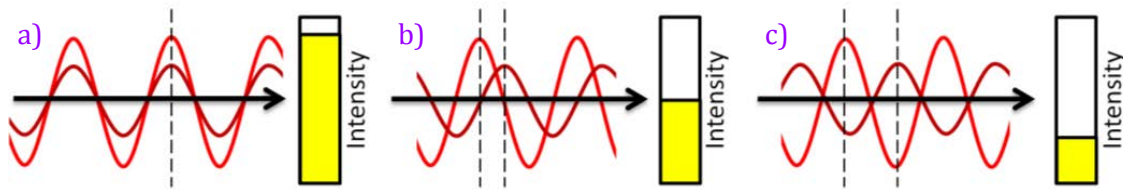


Figure 2-14 : Illustration of transmitted intensity with the phase shift. (a) beams are on phase, the intensity is maximal. (b) beams are in quadrature, the intensity is reduced. (c) beams are in opposition, the intensity is minimal.

Whether the multiply reflected beams are in phase or not depends on the wavelength (λ) of the light (in vacuum), the angle the light travels through the cavity (θ), the thickness of the cavity (ℓ) and the refractive index of the material between the reflecting surfaces (n). The phase difference between each succeeding reflection is given by: $\Delta\varphi(t) = \left(\frac{2\pi}{\lambda}\right) \cdot \delta(t)$ with $\delta(t) = 2 \cdot n \cdot \ell(t) \cos(\theta)$. The detector is measuring beams from the top side of the sample, *i.e.* $\cos(\theta) = 1$, and the aperture is very small; the phase difference observed is grouped.

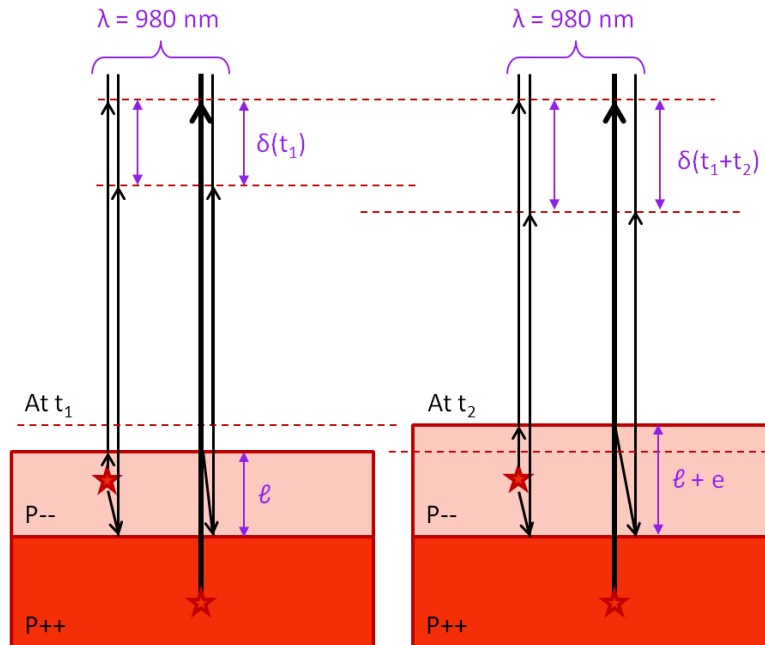


Figure 2-15 : Evolution of the phase difference during the p-- growth on p++. IR rays are emitted mainly from the p++ layer and the substrate. The low-doped epilayer on the p++ acts like a cavity. IR rays are reflected. The path-length difference (δ) increase with the deposited thickness (e).

At first, the signal (temperature) is normalized (-1 to +1) and the background (coming from intrinsic thermal response) is removed by a double exponential interpolation. The background was recorded during the same process applied on CVD substrate. The temperature increase after methane and oxygen introduction and then it slowly decrease to be constant.

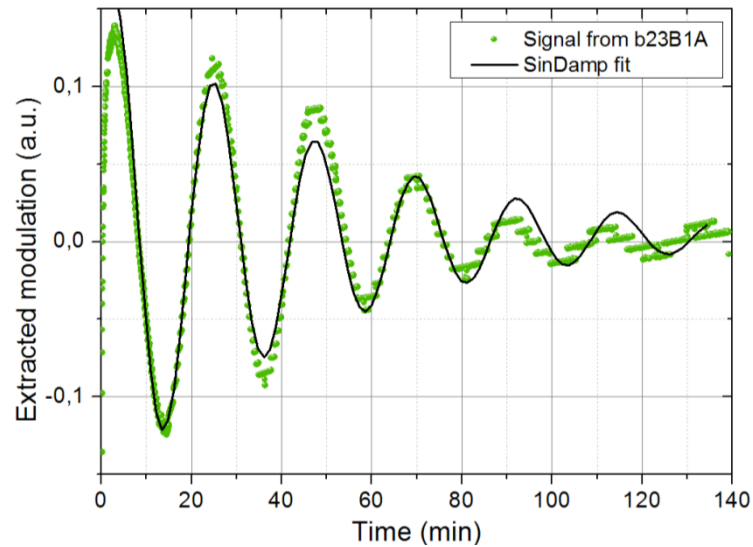


Figure 2-16 : Signal modulation extracted from temperature read-outs.

The extracted modulation is then interpolated by a sinus dampened function type $y = y_0 + A \cdot \exp\left(-\frac{x}{t_0}\right) \cdot \sin\left(\frac{\pi(x-x_c)}{w}\right)$. The extrapolation (figure 2-16) is made with content time dependence. The real signal is going faster at the end, so points are not fitted by the curve. A careful measurement of minima/maxima was converted into thickness. The extrapolation of the deposition rate shows some difference from a sample to another; the growth rate under these conditions (0.75% CH₄/H₂ and 0.25% O₂/H₂) was $9.6 \pm 0.2 \text{ nm}\cdot\text{min}^{-1}$. This could be explained by the difference of surface temperature which is related to a difference in sample position and microwave power.

III.3. Sample position effect

Several methods to measure the vertical position in the plasma where investigated: a linear resistance along the translator, motor steps counter, laser interference from the sample top side and laser diffraction pattern figures.

At first, the easiest way to measure the vertical position of the sample was to use a linear sensor composed of a 10 parts telescopic resistance. The linear resistivity is constant on the length and by measuring the resistance variation it is possible to get the position. The problem is the total length is too long, and the accuracy on the resistance variation was not good enough to be precise (± 0.1 mm).

It was also possible to count the number of rotations produced by the DC voltage motor. An embayed wheel was contacting the rotor axis and an optical system was used to count the number of rotation by a Labview program. The problem comes from the backlash in the mechanical transmission and the conversion from the motor to the translation by slewing drive system. As a consequence memory effects appeared each time the sample went up or down, it was not reliable to measure precisely the vertical position.

Next idea was to use a laser beam tilted from the normal plan to the surface directly positioned at the suitable vertical position and the measure the position of the reflected ray. The problem comes from the external quartz tube which is cylindrical. The tube diffracts the laser and the beam is wider; almost all the sample surface is reflective when the sample is in the suitable area (± 1 mm). The sample position cannot be precisely measured by this technique.

The last idea was to draw benefit from the laser diffraction problem. Because both external and internal quartz tubes are not perfectly cylindrical, by placing the laser in the horizontal plan, we observe a diffraction pattern very recognizable depending of the Z position but also depending of the relative position of both tubes in the plan XY as schematized on figure 2-17. The length where the diffraction is possible measure 15 cm from the sample holder.

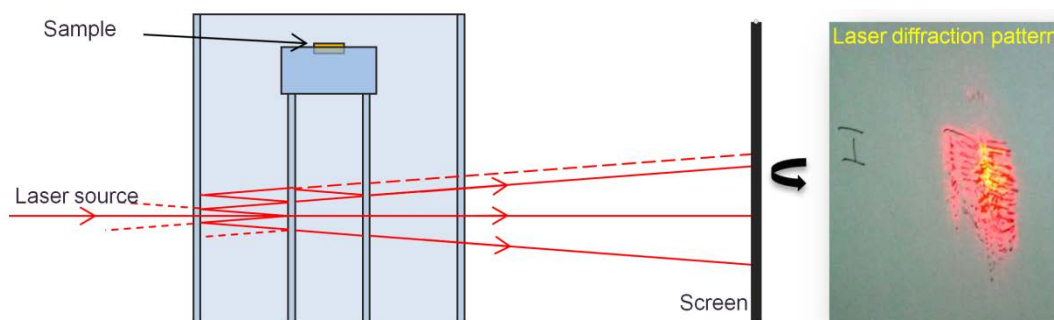


Figure 2-17 : Laser diffraction through quartz tubes.

Over a few μm on the vertical axis the diffraction pattern is totally different. The motion of the internal tube on X-Y axis moves the diffraction pattern on the vertical plane. The measured point is located 13.5 cm below the plasma ball; at this position, the diffraction is negligibly affected by heating of the plasma and soot deposition. The measure of the sample along three axes is very accurate (less than 0.1 mm) when diffraction pattern is drawn with enough details. As example, on Z axis it is as sensible as the motor step counter without the error introduced by the mechanical backlash. At low speed (24 Vdc on the motor), the vertical speed is around $1.3 \text{ mm}\cdot\text{min}^{-1}$. This technique was employed in multilayers growth with layers made at two Z values *i.e.* at different plasma contact modes.

III.4. In-situ gas phase composition monitoring - Mass spectrometry

The mass spectrometer gas analyzer is located in a secondary vacuum gas extractor system. A capillary pipe measuring 0.8 mm in diameter sampled the gas composition 2 cm above the plasma ball and this sampled gas is driven by a Macro Torr turbo-molecular high vacuum pump (Turbo-V70D from Varian co.) which ensure high pumping speed and good base pressure of 10^{-5} Torr when the vessel is pressurized at 50 Torr. This secondary vacuum stage ensures a good dynamic in gas sampling process.



Figure 2-18 : diagram of gas detection chain

The mass spectrometer used is composed of an ionization chamber and a quadrupole mass analyzer. Electrons are produced through thermionic emission by heating a wire filament that has electric current running through it. The electrons are accelerated to 70 eV in the region between the filament and the entrance to the ion source block. The accelerated electrons are then concentrated into a beam by being attracted to the trap electrode. The gas under investigation which contains the neutral molecules is introduced to the ion source in a perpendicular direction to the electron beam. Close passage of highly energetic electrons, referred to as a hard ionization source, causes large fluctuations in the electric field around the neutral molecules and induces ionization and fragmentation. At around 70 eV, the de Broglie wavelength of the electrons matches the length of typical bonds in organic molecules (about 0.14 nm) and energy transfer to organic gas sample molecules is maximized, leading to the strongest possible ionization and fragmentation. Under these conditions, about 1/1000 molecule is ionized. The products are then directed towards the mass analyzer by a repeller electrode. The ionization process often follows predictable cleavage reactions that give rise to fragment ions which, following detection and signal processing, convey structural information about the gas composition.

The quadrupole consists of four parallel metal rods. Each opposing rod pair is connected together electrically, and a radio frequency (RF) voltage is applied between one pair of rods and the other. A direct current voltage is then superimposed on the RF voltage. Ions travel down the quadrupole between the rods. Only ions of a certain mass-to-charge ratio (m/z) will reach the detector for a given ratio of voltages: other ions have unstable trajectories and will collide with the rods. This permits selection of an ion with a particular (m/z) or allows the operator to scan for a range of (m/z)-values by continuously varying the applied voltage.

Mass spectrometry data analysis is a complicated subject that is very specific to the type of experiment producing the data. Different types of ion source result in different arrays of fragments produced from the original molecules. An electron ionization source produces many fragments and mostly single-charged radicals (odd number of electrons). By understanding the origin of a sample, certain expectations can be assumed as to the component molecules of the sample and their fragmentations. In our case, gases sample from a diamond synthesis process will contain impurities chemically related to the methane, carbon oxides and boron oxides component.

Electron ionization mass spectra have several distinct sets of peaks: the molecular ion, isotope peaks, fragmentation peaks and metastable peaks. In the mass spectra the molecular ion peak is often most intense, but can be weak or missing. The molecular ion is a radical cation ($\bullet M^+$) as a result of removing one electron from the molecule. Identification of the molecular ion can be difficult. Examining organic compounds, the relative intensity of the molecular ion peak diminishes with branching and with increasing mass in a homologous series. In the spectrum for methane for example, the molecular ion peak is located at 16 (m/z) corresponding to its molecular mass. Molecular ion peaks are also preceded by a M-1 or M-2 peak resulting from loss of a hydrogen radical or di-hydrogen. The peak with the highest intensity is called the base peak which is not necessarily the molecular ion. More peaks may be visible with (m/z) ratios larger than the molecular ion peak due to isotope distributions, called isotope peaks. The value of 16 in the methane example corresponds to the mono-isotopic mass of a molecule of methane entirely composed of the most abundant isotopes (^1H and ^{12}C). The so-called M+1 peak corresponds to a fraction of the molecules with one higher isotope incorporated (^2H or ^{13}C) and the M+2 peak has two higher isotopes. The natural abundance of the higher isotopes is low for frequently encountered elements such as hydrogen, carbon and nitrogen and the intensity of isotope peaks subsequently low.

Peaks with mass less than the molecular ion are the result of fragmentation of the molecule. Many reaction pathways exist for fragmentation, but only newly formed cations will show up in the mass spectrum, not radical fragments or neutral fragments. Metastable peaks are broad peaks with low intensity at non-integer mass values. These peaks result from ions with lifetimes shorter than the time needed to traverse the distance between ionization chamber and the detector.

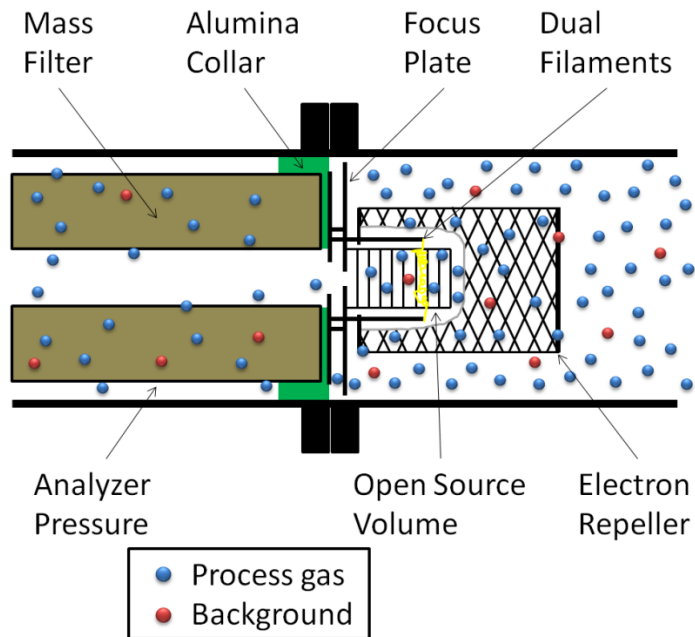


Figure 2-19: Diagram of mass spectrometer used.

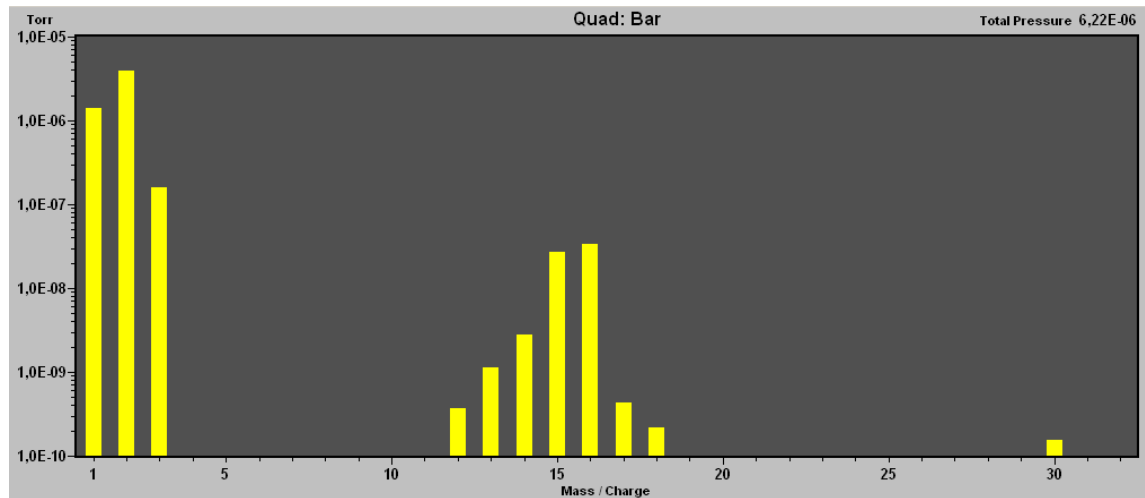


Figure 2-20: Bar mass/charge spectrum during a diamond growth with 1% (CH₄/H₂). Signals around 2 are attributed to H₂ with M+1 and M-1. Signals around 16 correspond to CH₄ and fractioned molecules, as CH₃...

IV. CONCLUSION

The MOCVD-like reactor allows the growth of delta-structures step by step without plasma stop. The gas flow rate has been increase up 2 slm per Mixing Preparation Units (MPU) and the free volume was reduced down to 2 liters ensuring a small time residence of species in the reaction chamber. The gas composition can be monitored by a mass spectrometer plugged trough a cascade differential vacuum, giving as example, the information on gas commutation time delay.

In addition, a new load lock associated with a new sample transfer system UHV compatible ensure a very low base pressure (10^{-7} Torr), a fastest loading time and the large advantage to adjust the position of the sample inside the ignited plasma, on the tree space dimensions. A diffracted laser beam is used the memorized the exact position the sample in the plasma.

A new program was created to estimate in real time the deposition thickness of lightly doped layer overgrown on metallic diamond from the IR intensity oscillations recorded by the single color pyrometer used to monitor the surface temperature. This was very useful in order to precisely control the cap layer thickness.

V. RÉSUMÉ DU CHAPITRE 2

Le premier réacteur de croissance du diamant par dépôt chimique en phase vapeur assisté par plasma micro-onde (MPCVD) pour le dopage au bore a été modifié afin de s'adapter au processus de croissance par delta-dopage (débit de gaz plus importants, mélanges de gaz préparés et stabilisés avant l'introduction dans la chambre de réaction...) et à l'environnement de travail (un nombre plus élevé des opérateurs qui l'utilisent). En parallèle, de nouvelles techniques de diagnostic ont été mise au point. L'observation des variations périodiques de la température de la surface apparente nous a permis de mesurer, *in situ*, la vitesse de croissance. Plusieurs méthodes ont été testées pour améliorer la reproductibilité de la position de l'échantillon dans le plasma. Une installation de détection de gaz composé d'un spectromètre de masse allié à un système de pompage différentiel a également été mise au point.

Le réacteur de croissance MPCVD original a été construit par E. Gheeraert (Gheeraert, 1992) et P. Gonon (Gonon, 1993), sur la base d'un réacteur japonais développé et utilisé au NIRIM (Institut national de recherche sur les matériaux inorganiques, appelé de nos jours NIMS) par Kamo et al. (Kamo et al., 1983). Dans ce type de réacteur, la chambre de croissance se compose d'un tube intérieur et d'un tube extérieur en quartz. Le porte-échantillon est placé sur la partie supérieure du tube en quartz intérieur, à l'intersection avec le guide d'ondes. Un générateur de plasma micro-onde fonctionnant à une fréquence standard de 2,45 GHz fournit une puissance réglable allant de 0 à 2000 Watts. La position horizontale du plasma peut être réglée par le piston en bout de guide (syntonisation d'onde stationnaire), la puissance réfléchie qui est redirigée sur une charge (refroidie à l'eau) peut être minimisée par l'adaptation de l'impédance. La chambre de croissance est connectée à un système de pompage, constitué d'une pompe primaire et une pompe turbo-moléculaire. La pompe primaire est utilisée pour la circulation du mélange de gaz et la pompe secondaire assure une pression inférieure à 10^{-5} Torr avant l'introduction du mélange de gaz, et qui empêche donc l'incorporation d'autres impuretés, non désirées (comme l'azote). Un système de dilution à plusieurs étages (le diluteur) permet de contrôler la concentration de diborane (B_2H_6) dans le mélange de gaz avec une grande précision. Il est responsable de l'obtention de couches très faiblement dopées en bore (10^{15} at.cm⁻³). Un purificateur de gaz a été installé sur la canalisation d'hydrogène (N60). La pureté de l'hydrogène (source principale de gaz pendant la croissance) est supérieure à 99,999995% (N85) ce qui limite considérablement la présence d'impuretés comme l'eau et l'azote. Le méthane et le diborane ne sont pas filtrés, mais leur pureté est qualifiée par le fournisseur comme étant 99,9995% (N55).

Le système de distribution des gaz (visible sur la figure 2.1) a été complètement remplacé par un système à 3 voies, semblable à ceux des systèmes MOCVD, comportant 3 Unités de Préparation de Mélange (MPU) indépendantes. Ces MPU sont responsables du dosage des

gaz (régulateurs de débit massique (MFC) parallèles) et de leur stabilisation (régulation de la pression) avant leur introduction dans la chambre de réaction (voir détail sur la figure 2.9). Dans ces unités, le mélange a la possibilité de s'écouler soit dans la chambre de réaction ou soit en parallèle de la chambre dans une ligne d'évent, avant d'être évacué par la pompe primaire. Lorsque le gaz s'écoule à travers l'évent, un régulateur de pression situé après les MFC est responsable de l'équilibrage des pressions afin de maintenir une légère surpression entre le MPU et la chambre de réaction. Cette configuration permet aux mélanges de gaz de s'écouler indépendamment, en parallèle, sans aucune contamination croisée. Lorsque la composition du gaz du plasma doit être changée, un système de vanne d'aiguillage envoie le mélange gazeux dans le réacteur ou dans l'évent en fonction du mode de plasma sélectionné (H₂, NiD, Dop) en appuyant sur un bouton sur le panneau de commande principal.

Le déplacement de l'échantillon à partir du SAS de chargement vers la chambre de réaction est assuré par un transporteur linéaire métallique (axe Z), à couplage magnétique, fixé sous une table micrométrique X-Y située sous le SAS de chargement. L'échantillon de diamant est positionné avec précision dans le plasma, grâce à un panneau de régulation de tension de commande de moteur permettant de d'agir sur la vitesse de déplacement vertical en réglant la tension de 0 à ±90Vcc sans vibration qui pourrai déplacer l'échantillon de diamant sur le porte-échantillon. Les axes X et Y (figure 2.4) sont manuels et se pilotent avec des verniers micrométriques. Le "0" indique l'alignement coaxial des tubes internes et externes). Ce système a l'énorme avantage de permettre le mouvement échantillon de diamant à l'intérieur du plasma lorsque le plasma est allumé, dans les trois directions de l'espace (plan horizontal XY et la vertical Z) et une rotation suivant l'axe Z.

La température mesurée par un pyromètre monochromatique (980 nm) peut osciller pendant la croissance de couches faiblement dopées au bore, réalisées dans des situations particulières. Ce phénomène a été clairement observé et enregistré dans le cas des croissances de couches de couverture du procédé delta et lors d'épitaxies faiblement dopées sur des échantillons fortement dopés. Après traitement du signal, il est possible de déterminer la vitesse de croissance et de suivre par ordinateur l'épaisseur de la couche déposée, *in situ*.

Les oscillations sont la conséquence d'interférences optiques à partir d'une cavité de Fabry-Perot à l'intérieur de la couche en croissance, car la sous-couche fortement dopée se comporte comme un miroir: son indice de réfraction à 960 nm est affectée par la présence de porteurs libres. En théorie, à partir de ces variations de la température, il est possible de déterminer l'épaisseur de la couche en croissance. Les principales contraintes sont la perte d'intensité d'interférences lorsque la couche devient trop épaisse (> 1 µm), lorsque la surface devient rugueuse, ou lorsque la différence de niveau de dopage est trop petite. La figure 2.13 illustre ce phénomène dans le cas de croissances faiblement dopées réalisées sur couches métalliques. Les couches ont une épaisseur comparable de 1,3 µm mesurée par MEB après gravure MESA. Il apparaît que les oscillations ont une constante de temps

différente et s'expliquent par des différences de vitesses de croissance. Ces variations de vitesses peuvent être expliquées par des différences de température de surface et de position d'échantillon dans le plasma (fixé avec une erreur de 0,1 mm sur l'axe Z).

Plusieurs méthodes pour mesurer la position verticale dans le plasma furent étudiées: par résistance linéaire le long du tube, compteur de pas de moteur, interférences laser à partir de la face supérieure de l'échantillon et motifs de diffraction laser traversant les tubes.

La dernière idée tire profit du fait que les deux tubes de quartz (externes et internes) ne sont pas parfaitement cylindriques, en plaçant le laser dans le plan horizontal, on observe un motif de diffraction très reconnaissable en fonction de la position verticale Z, mais aussi en fonction de la position relative des deux tubes dans le plan XY comme schématisé sur la figure 2.17. La mesure est possible sur 15 cm sous du porte-échantillon.

Au cours d'un déplacement de quelques microns sur l'axe vertical, la figure de diffraction est complètement modifiée. Le déplacement du tube intérieur sur plan XY déplace le motif de diffraction sur le plan vertical. Le point de mesure est situé 13,5 cm au-dessous de la boule de plasma; dans cette position, la diffraction est peu affectée par le chauffage du plasma et par le dépôt de suie. Cette mesure est très précise (moins de 0,1 mm) lorsque le motif de diffraction est établi avec suffisamment de détails (on relève les points singuliers comme sur une empreinte digitale). À basse vitesse (24 Vcc sur le moteur), le déplacement vertical est d'environ 1,3 mm par minute, ce qui permet de retrouver une position antérieure avec précision. Cette technique a été employée dans la croissance de multicouches où les couches sont faites à deux modes différents de contact plasma.

Un tube de 0,8 mm de diamètre est utilisé pour mesurer la composition du gaz se trouvant à 2 cm au-dessus de la boule de plasma. Ce gaz échantillonné est entraîné par une pompe turbo-moléculaire hybride macroTorr (Turbo-V70D de Varian Co.) qui assure une grande vitesse de pompage et un bon vide de base proche de 10^{-5} Torr alors que la chambre est mise sous pression à 50 Torr. Cette étape de vide secondaire assure une bonne dynamique dans le processus de prélèvement des gaz.

Chapter 3.
C H A R A C T E R I Z A T I O N
T E C H N I Q U E S

I. SURFACE MORPHOLOGY ANALYSIS

The good surface quality of diamond substrate is essential to grow defect-free epilayers. A particular attention was paid to the surface modifications after growth in order to understand growth mechanisms and defects origin. In the case of delta-doping, the surface has to be as flat as possible and it has to keep the same flatness after buffer, delta and cap layers growths. When the project involves electrical contacts (ohmic, Schottky or MOS) 3D defects have a strong effect on the deterioration of device's performance.

Diamond substrates and diamond growth were analyzed by microscopy techniques (optical microscope, scanning electron microscope) and profiling system (optical profile) in order to quantify the surface morphology (RMS, defect height). To do so, a systematic surface analysis approach has been developed. Characterization techniques will be reviewed in this chapter.

I.1. Reflected light microscopy

Several techniques are employed to introduce a contrast in reflected light microscopy. Most commonly used in our study are darkfield illumination (DF), polarized light (Pol), and differential interference contrast (DIC).

I.1.1. Techniques reviews

In reflected darkfield microscopy, which is an ideal method for exploring the surface morphology, wavefronts from the vertical illuminator are directed toward the objective using a specialized mirror assembly that contains an oval opening (figure 3-1). This light passes through an outer sleeve in the microscope objective and impacts on a ring-shaped concave mirror, which directs the wavefronts at a highly incident angle onto the specimen surface. In cases where the specimen acts as a mirror (no relief features on the surface), there is no light reflected back into the objective from the specimen and the image remains dark. Areas where relief contours exist, light goes back into the objective front lens and contours are observed as being bright features against a very dark background. Please note that in darkfield reflected light microscopy, the field and aperture diaphragms in the vertical illuminator should be fully opened so that the light beam illuminating the mirror assembly is not partially blocked.

Polarized reflected light microscopy is a suitable technique for examining surfaces containing structures that alter the state of polarization during the reflection process. For example, structural grains in samples and a number of metallic alloys and thin films can be readily examined using this method. In the optical configuration outlined in figure 3-1, the illuminating wavefronts encounter a polarizer that is placed in the vertical illuminator before the mirror unit that directs light into the objective. The linearly polarized light waves are focused onto the specimen surface and reflected back into the objective. After leaving the objective aperture as a parallel bundle of wavefronts, the light is then projected onto a second polarizer (the analyzer) oriented at 90 degrees with respect to the polarizer. Only the depolarized wavefronts are able to pass through the analyzer to reach the tube lens. An auxiliary lambda plate is inserted just prior to the analyzer in the optical train to examine the sign of birefringence (changing gray to color contrast). This method is referred to as sensitive tint.

One of the most powerful imaging techniques for introducing contrast into reflected light is differential interference contrast, which allows the visualization of minute elevation differences in surfaces. In the optical configuration (figure 3-1), a birefringent prism (also known as a Wollaston or Nomarski prism, depending upon design), is placed just above the objective and a polarizer is installed in the vertical illuminator (similar to polarized light). The prism splits the polarized light wavefronts into two orthogonal polarized beams on their way to the specimen. The interference of the two parts at recombination is sensitive to

their optical path difference (product of refractive index times the geometric path length). If the surface is completely flat, nothing is observed. However, if there is, for example, a small step (see figure 3-1) between the two wavefronts, one of the beams must travel a path that is longer and is assigned this path difference. Once the parallel beams have returned to the microscope after passing back through the objective and prism, they pass through a second polarizer (the analyzer) where interference produces an intermediate image where path differences are translated into gray values that can be seen by the eye. Similar to polarized light microscopy, a lambda plate is positioned beneath the analyzer to shift gray values into colored hues, emphasizing lines and edges providing a topographically accurate image.

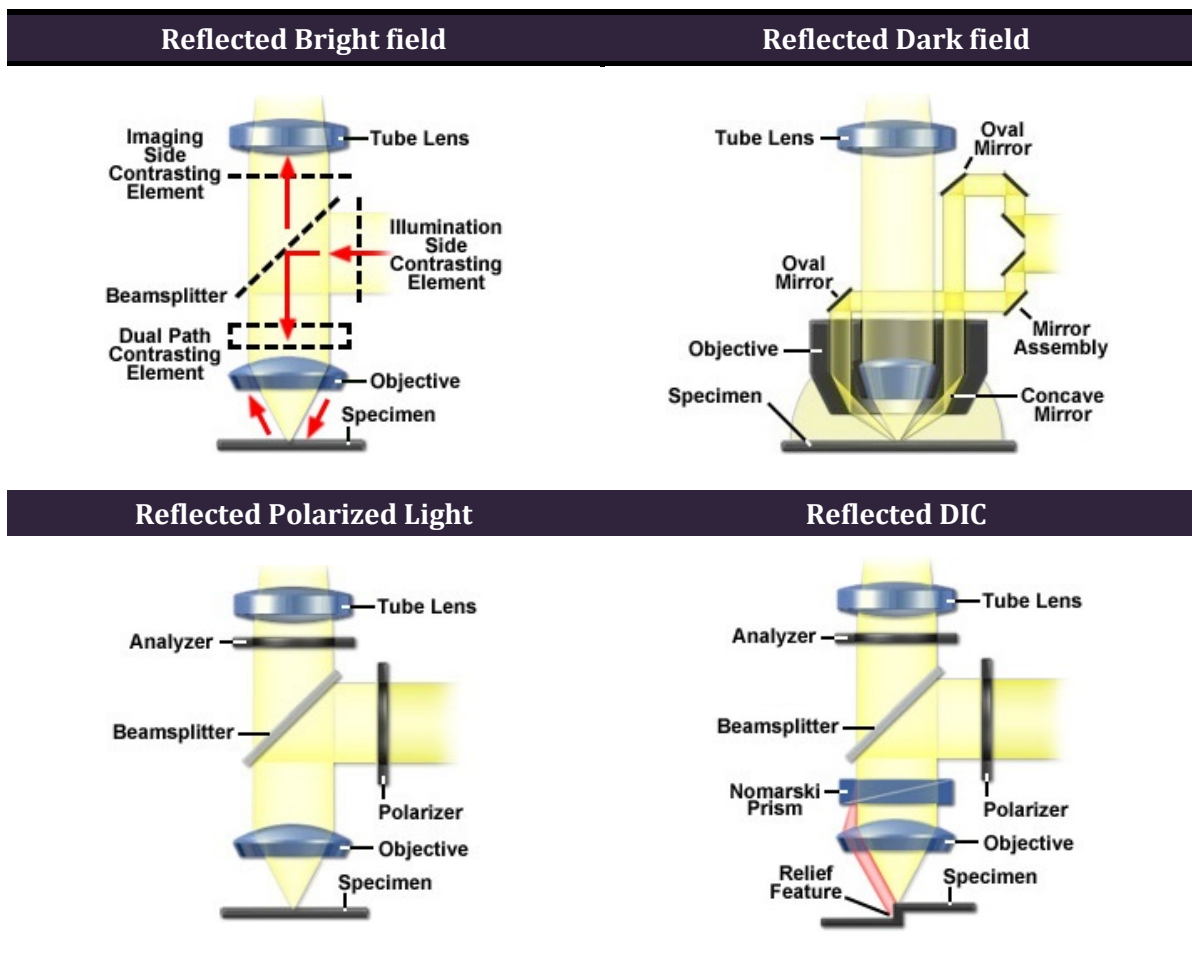


Figure 3-1 : Comparison of contrast mechanisms in reflected light microscopy, Zeiss Systems.

I.1.2. Detail about C-DIC microscopy prism

Prisms are planar. This introduces a dependency of the contrast gradient and the orientation of the prism in the optical train. As seen on figure 3-2, this parameter is critical for diamond surface investigation because in the case of oriented defects such as polishing lines, these lines are visible only if the prism is well oriented. In addition, depending on the prism orientation, light appears diffracted on sample edges and makes topography microscopy by this technique impossible.

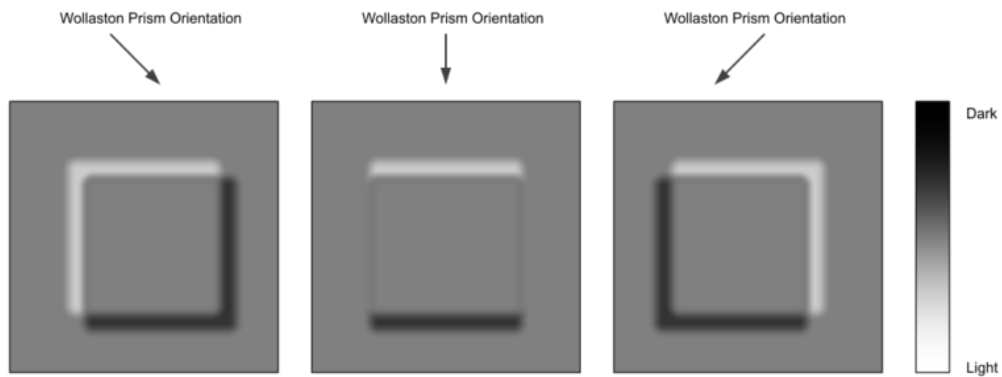


Figure 3-2 : Influence of the prism orientation

I.1.3. Contrast modes comparison in reflected light microscopy

The sample presented in figure 3-3 represent 25 hours of lateral overgrowth made in collaboration at NIMS* (2571Kp) containing a low boron doping level. Pictures are taken on the corner cut area with the same objective $\times 10$ on the same ZEISS microscope.

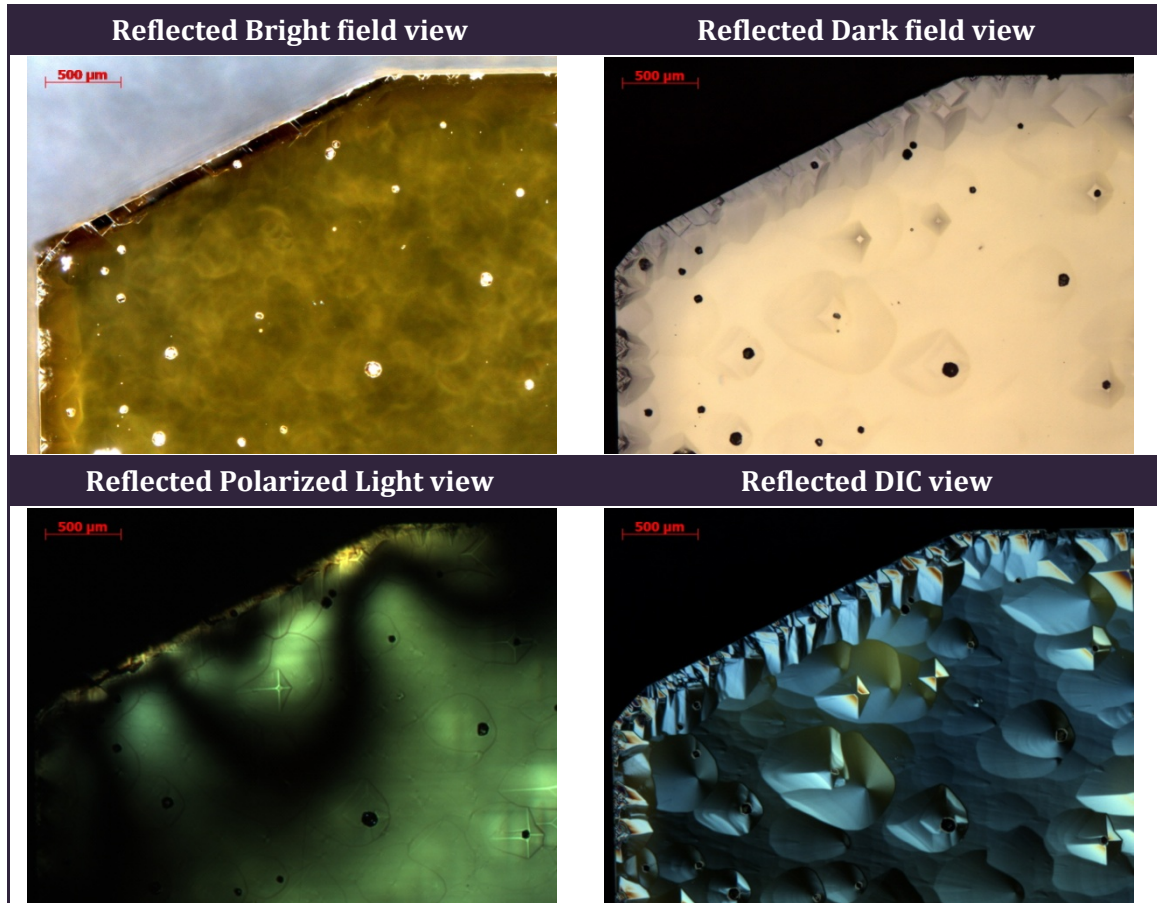


Figure 3-3 : Same diamond sample observed $\times 10$ in reflected light microscopy under several configurations.

The bright field (BF) view is the first step of the observation. Under this mode, the focus can be set on the top surface by following edges of the sample and dusts. On this picture, it is possible to see very bright dots which are attributed to unepitaxial crystallites (UCs). These 3D defects are visible as dark point on DF view. In this configuration, the base of large pyramidal and rounded hillocks appears like a shadow on the surface. The POL view underlines bright lines attributed to edges of pyramidal hillocks, black area and green area informs on the strain field near the corner cut. The best mode to evaluate surface morphology is the DIC view. In this view the prism is oriented at 45° and the difference in the optical path way is very small, the contrast is very sensitive to small height variations, this explain the reason why the difference between pyramidal (2 faces in the light, 2 faces in the shadow) and rounded hillocks (with a continuous light gradient) is so clear. The small

* Drs. S. Koizumi and T. Teraji

surface roughness can be appreciated too, but only qualitatively. The accurate surface height is given by profiling techniques (stylus, laser or light fringes...).

1.2. Optical profile

Optical profilers are specialized microscopes using the interference of two light beams for mapping and modeling surface topographies. The optical profiler used here is Contour GT from Veeco Instruments Inc.

1.2.1. System modes

The optical profiler traditionally use two complementary modes of operation, phase shifting interferometry (PSI) and vertical scanning interferometry (VSI). PSI is very precise and is used to measure smooth and continuous surfaces. VSI can measure a wider range of surfaces, but with a lower level degree of precision as compared to PSI. The mode selection depends on the sample surface. However, the advancement of new technologies and the presence of a wider range of applications for optical profilers have challenged the capabilities of both PSI and VSI. For example, for a smooth surface and height discontinuities less than 150 nm, PSI mode could be used. A similar surface with step heights larger than 150 nm would require VSI mode; however, although VSI could measure the step height, noise inherent in VSI limits the vertical resolution to around 3 nm, which is much worse than the PSI mode vertical resolution of 0.1 nm! For these kinds of surfaces Veeco Instruments has developed a measurement mode that combines the accuracy of PSI with the versatility of VSI, and this third mode is called HDVSI.

A. Phase Shifting Interferometry (PSI)

PSI is used to map optically smooth surface topographies and can achieve sub-nanometer vertical resolution better than any other optical method. PSI mode uses a nearly monochromatic light source to generate interference fringes, and the surface topography is calculated by measuring the shape (position) of the fringes on the sample. Only a few frames are collected by a solid-state camera during the approximately 1 micron vertical scan, and the full-field measurement is completed in less than 200 ms. The fringes generated represent a topography map of the sample's surface from which the shape is then derived. Vertical resolution refers to the point where measurement data drops into the noise of the system.

B. Vertical Scanning Interferometry (VSI)

VSI typically uses a white light source and looks at the fringe contrast rather than the shape of the fringes as in PSI. During the VSI measurement the objective moves vertically down the full height range of the sample while collecting frames at the camera frame rate. Although

the scanner generally moves at speeds of *ca.* 5 $\mu\text{m.s}^{-1}$, 100 $\mu\text{m.s}^{-1}$ scans are possible with reduced vertical resolution. During a VSI scan each pixel on the camera sees fringes only when the given point on the sample comes into focus. The position of maximum fringe contrast is then found for each pixel. Because the white light source has a short coherence length, fringes only appear around the best focus position. For this reason VSI can be considered an array of best-focus sensors. VSI is an extremely versatile mode, for it can measure the full range of most surfaces.

C. High Definition Vertical Scanning Interferometry (HDVSI)

The HDVSI mode combines the high vertical resolution of PSI with VSI's ability to measure discontinuous and rough surfaces. From a single set of data acquired during a VSI scan, both the position of maximum fringe contrast (VSI) and the position of the fringes on the sample (PSI) are calculated concurrently and independently of each other. The VSI data provides an approximate surface profile, while the PSI information imparts sub-nanometer precision to the measurement. HDVSI mode applies a unique PSI quadrature demodulation algorithm to the fringe data already contained in the VSI measurement. This procedure allows the position of the fringes (phase) to be calculated independently of the position of maximum fringe contrast. The VSI data is then combined with the PSI data to avoid the ambiguities inherent to pure PSI measurements on rough or discontinuous surfaces. The resulting topography map merges the sub-nanometer vertical resolution of PSI with the large vertical scanning range of VSI.

I.2.2. Optical profile on diamond

Optical profiles were performed whether the diamond was doped or not. In the case of low/high doping level bilayer or superlattice, no particular artifacts were observed. The use of a particular operation mode is determined by the characteristics of the surface under study. As presented below, this choice depends mainly of the defects heights (discontinuity).

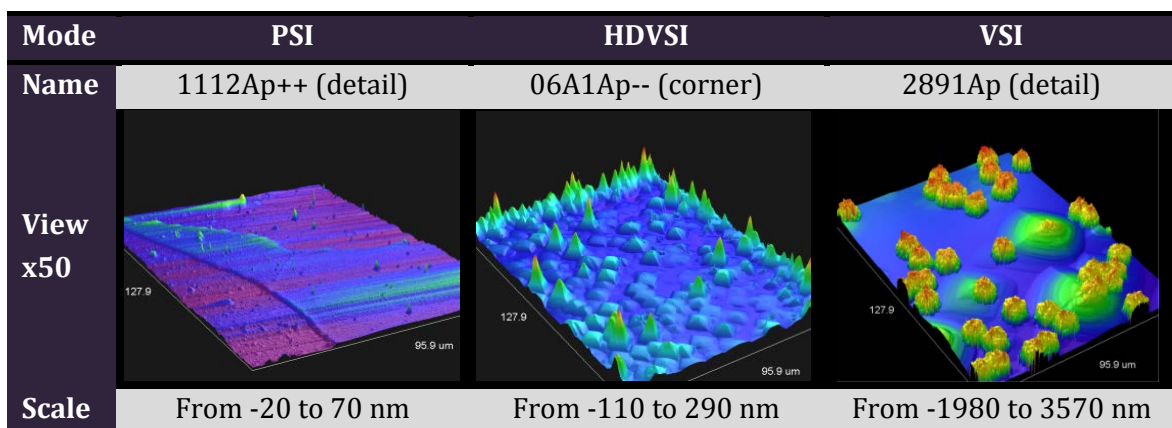


Figure 3-4 : Diamond samples observed by optical profile under different configuration.

PSI is used to check the roughness, polishing line and holes at the substrate surface and at flat overgrown surfaces too. In the PSI mode, 1 nm-high steps between growth sectors are clearly seen, as shown on figure 3-4. HDVSI mode is used on diamond samples when their surface has both pyramidal hillocks and flat regions. If such a surface is measured by PSI mode, then the measurement of the flat surface roughness is not accurate due to errors induced by edges discontinuities. The HDVSI mode is applied on etched samples too, like in the case of MESA-structures. However, if large irregular defects (like unepitaxial crystallite) are present at the epilayer surface, it cannot be analyzed by HDVSI mode. In that case the VSI is used to localize the least defective areas on the sample in order to perform a HDVSI analysis. However, if the vertical resolution is perfect to analyze the surface roughness, the poor lateral resolution ($1\mu\text{m}$) is not enough to measure with the same accuracy the base of objects (hillocks, MESA structures...).

1.3. In-lens Secondary Electron Detector

SEM-FEG Carl Zeiss Gemini column design includes an integrated In-lens SE detector (figure 3-5). The weak magnetic field at the specimen surface intercepts the low energy secondary electrons (SE) at the point of impact. They are then accelerated in the booster column and focused on the In-lens above the objective lens. The recently introduced 3rd generation of In-lens detectors boost increases signal to noise ratio (factor 2–3 improvement).

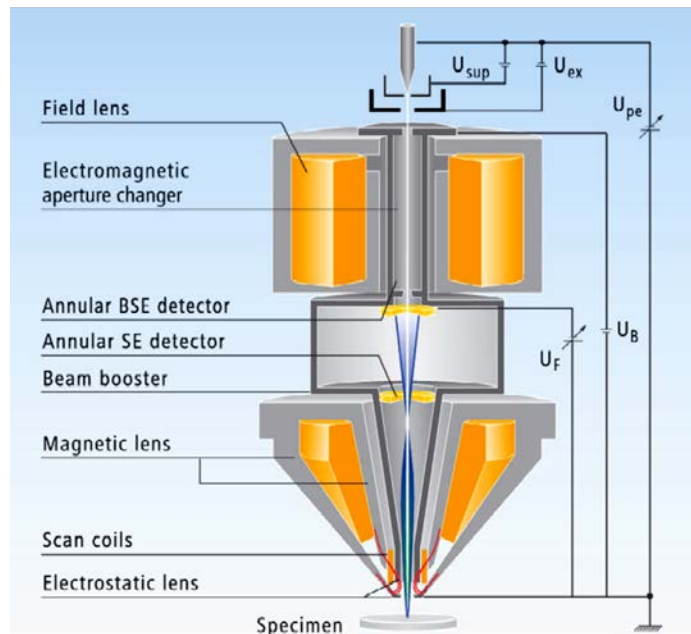


Figure 3-5 : Cross section of the Gemini electron optical column used. U_{ex} – extractor voltage of first anode. U_{pe} – primary beam voltage. U_B – booster voltage. U_F – EsB filtering grid voltage

The in-lens image is mainly composed of low energy electrons whose energy are less than 40 eV and are easily attracted by the electrostatic field generated by the booster voltage. This can be the reason why SE images of in-lens detector have high surface sensitivity

(Kumagai & Sekiguchi, 2009). In addition, the coaxial geometry with the electron beam source (produced by a field emission gun (FEG)) reduce artefacts like distortion effects and the measurement of distance is more accurate (as example for MESA structure parameters determination) than SE detector localized somewhere out-lens. The image of the sample is made at a low electron acceleration voltage in order to reduce surface charging effect.

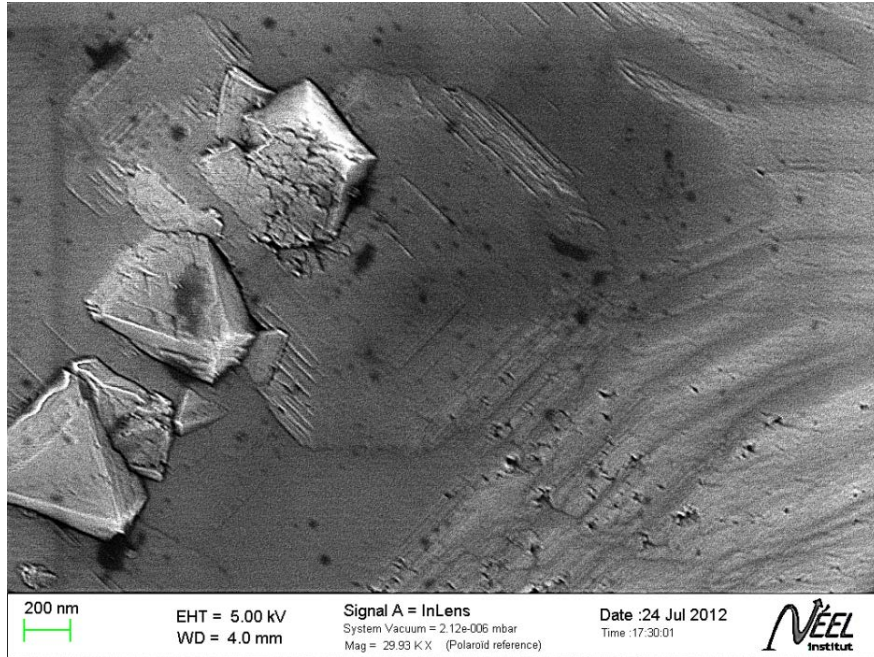


Figure 3-6 : Details on twinning at the surface of the sample 2162A used for the determination of α growth parameter.

II. CATHODOLUMINESCENCE SPECTROSCOPY

II.1. Theory

Cathodoluminescence (CL) is light emission produced by a substance under electron excitation. CL mechanism can be described in three steps: excitation: electron beam induce a lot of electron-hole pairs (at the bottom of the conduction band and at the top of the valence band respectively); drift: carriers generated drift by diffusions (this migration is characterized by a diffusion length); recombination: it can be radiative when a photon is emitted or non-radiative when phonons are generated which heat up the sample.

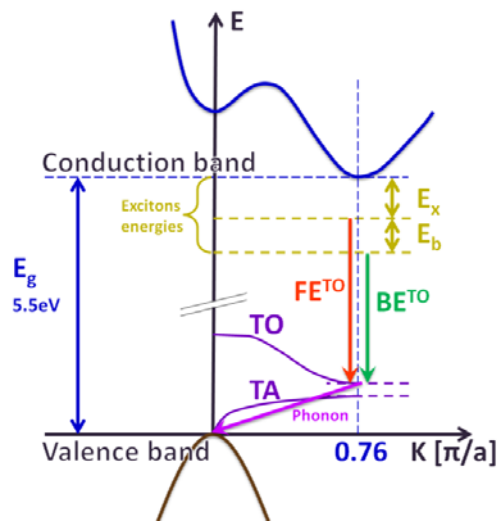


Figure 3-7: Band diagram of diamond with main intrinsic and extrinsic transitions.

In diamond the minimum of the conduction band is shifted by $0.76 \pi/a$ in the (100) direction of the first Brillouin zone. In this case excitonic radiative transitions are assisted by a phonon (Figure 3-7). Two kinds of phonons are present in the mechanism: transverse mode (TA for acoustic, TO for optic) and optic mode (LO for optic, LA for acoustic). Free excitonic recombination assisted by TO phonon corresponding transition called FE^{TO} are dominant, FE^{TA} and FE^{LO} are much weaker, about 5% (1% resp.)(Dean, et al., 1965). When the semiconductor is doped, excitons may bind to neutral impurities or-trapped carriers, leading to new possible transitions (generally assisted by transverse optic phonons and called BE^{TO}) as reported in table 3-1.

Transition	FE^{TA}	FE^{TO}	FE^{LO}	FE^{TO+O}	BE^{TO}	BE^{LO}	BE^{TO+O}
Energy (eV at 5K)	5.322	5.268	5.246	5.1	5.215	5.193	5.048
Wavelength (nm)	232.97	235.35	236.34	243.11	237.74	238.75	245.61

Table 3-1 : Position of intrinsic and extrinsic recombination peaks in boron-doped diamond.

Other transitions independent of excitonic recombination or from two energy levels in the gap can take place. These transitions are associated to extended or point defects, like dislocations (Blue A band 2.8 – 3 eV and Green A band 2.3 – 2.5 eV) or to “impurity-structural defect” complexes like Si-V center (1.681 eV) and N-V center (H3, 2.547 eV). All these CL emission lines have been collected in handbooks (Zaitsev, 2001).

II.2. Experimental setup

The cathodoluminescence (CL) near UV – visible – near IR system at low temperature used (figure 3-8) is composed of a high resolution electron excitation and scanning system (SEM) (1), an efficient system which collects the light (parabolic mirror) (2), a high spectral resolution detector (monochromator with detectors) (3) and a cold stage (temperature regulation from 5 to 300K) (4) under a secondary vacuum (10^{-6} – 10^{-7} Torr).

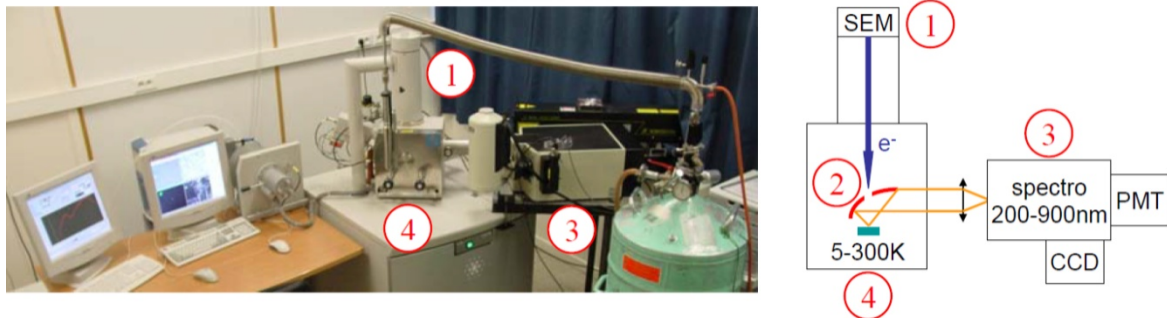


Figure 3-8 : CL system. (1) SEM, (2) parabolic mirror, (3) monochromator, (4) cold stage.

- 1) The SEM is a FEI Quanta 200 with a tungsten filament source. The ultimate resolution is 3 nm. The electron acceleration voltage can be tuned from 200 V and 3 kV and the electron current from 5 pA to 50 nA.
- 2) A parabolic mirror catches the light present in a wide solid angle and reflects it in parallel rays. A planar-convex lens ensures the light focalization on the entrance slit of the monochromator.
- 3) The monochromator used is a HR460 Jobin Yvon with 2 grating: near UV 600gr/mm and 1800gr/mm. Associated detectors are a photomultiplier (PM) and CCD (256×1024 matrix) pixels cooled at 140K by liquid nitrogen. PM detector is used to get panchromatic or monochromatic CL images and also to records spectra by grating rotation. CCD is used for fast spectra measurement or composed spectrums by grating rotation. For cartography and spectra profiling (one spectrum per pixel) the CCD is very useful.
- 4) The cold stage GATAN under liquid helium flux ensures a thermal regulation of the sample from 5 to 300K by changing the helium flow and warming the sample holder. The stage has three degree of freedom along X, Y and Z axis on 20 mm in length.

II.3. Cathodoluminescence of diamond

The CL signal comes from a limited volume in the matter which depends of the electron beam acceleration voltage. Some relations between the depth and the energy, type $Z(\mu\text{m}) = \alpha \times E(\text{keV})^\beta$ have been proposed by the past. Most popular parameters have been proposed long ago by Davies and by Kanaya & Okayana with $\alpha = 0.018$, $\beta = 1.67$ (Davies, 1977) and $\alpha = 0.02$, $\beta = 1.67$ (Kanaya & Okayama, 1972).

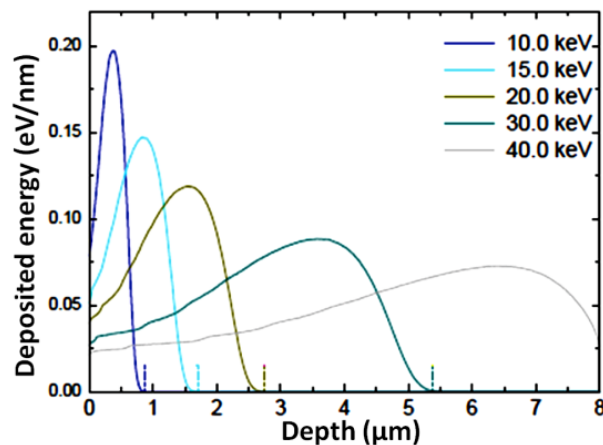


Figure 3-9 : Deposited energy in diamond calculated by Monte-Carlo calculations*.

As shown on figure 3-9, superficial diamond layers are exclusively probed for acceleration voltage from 3 kV to 10 kV. At high voltage, the bulk signal is dominant. Usually 30 kV is applied to substrate crystallinity quality / defects mapping.

However, it is difficult to predict the suitable acceleration voltage required to analyse diamond at fixed volume; the deposited energy does not decrease quickly with the depth; the variations become smoother at higher voltages (figure 3-9).

Analysis of epilayers properties mean to work at low acceleration voltage in order to avoid any substrate contribution. Imaging at low voltage imply to increase the current of electron in order to get enough signal. On the other hand, due to the diamond insulating nature, electrons accumulate on the surface. This accumulation induces a deflection of the beam. As CL mirror is set to collect the light from a dot, its deflection makes the signal not stable in time, with a tendency to decrease.

In addition, dislocations are non radiative recombination centers. This phenomenon is manifested by black dots, whose gray to black contrast is varying with the electron excitation beam sweeping frequency. When the trapped electron density and the dislocation density are important, under a fast sweeping image of the sample appear like exposed to rain droplets (figure 3-10).

* Graph extracted from (Volpe, 2009 PhD thesis, p. 57)

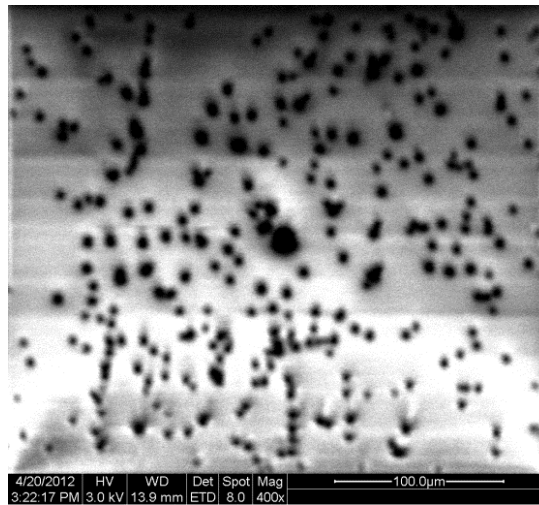


Figure 3-10 : Secondary electrons picture: Everhart-Thornley Detector. Sample 2932Ap-- under 3 kV and spot size 8. Black dots are non radiative recombination centers.

The spot size is related to the acceleration voltage and the current. Typically for the maximum spot size 8, at 10 kV the current is around 10 nA[†], while at 3 kV it is around 40 nA.

[†] Measured by a Faraday electron cage device.

III. TRANSMISSION ELECTRON MICROSCOPY

In transmission electron microscopy (TEM) an electron beam is transmitted through an ultra thin (electro-transparent) specimen, interacting with matter on the way. An image is formed from the interaction of the electrons transmitted through the specimen; the image is magnified and focused onto an imaging device, such as a fluorescent screen, or detected by a sensor, such as a CCD camera.

A TEM is composed of several components, which include a system generating the vacuum where the electrons travel, an electron emission source, a series of electromagnetic lenses, as well as electrostatic plates to guide and manipulate the beam as required. The last device allows the specimen insertion, motion and removal from the beam path. Different imaging devices are subsequently used to create an image.

III.1. Imaging methods

Imaging methods in TEM utilize the information contained in the electron waves exiting from the sample to form an image. The projector lenses allow the position correction of electron wave distribution onto the viewing system. The observed image intensity can be approximated by the time-average of the exit electron beam wavefunctions amplitude.

Different imaging methods therefore consist in the modification and collection of electron waves exiting the sample in order to obtain complementary information. The observed image depends not only on the electron beam amplitude, but also on the phase of the electrons. Higher resolution imaging requires thinner samples and higher energies of incident electrons, as well as brighter sources.

III.1.1. Contrast formation

Contrast formation in the TEM depends deeply on the operation mode. Complex imaging techniques, which utilize the unique ability to change lens strength or to deactivate a lens, result in many operating modes. These modes may be used to select the specific information interesting the investigator. In this paragraph, a few of these modes will be shortly reviewed: bright field, diffraction contrast, conventional dark field, weak beam, electron energy loss and phase contrast.

A. Bright field

The most common operation mode for a TEM is the bright field imaging mode. In this mode the contrast formation is formed directly by occlusion and absorption of electrons in the sample. Thicker regions of the sample, or regions with a higher atomic number will appear darker, while regions with no sample matter in the beam path will appear bright – hence the

term "bright field". The image is a two dimensional projection of the sample onto the optic axis.

B. Diffraction contrast

Samples can exhibit diffraction contrast, whereby the electron beam undergoes Bragg scattering, which in the case of a crystalline sample, disperses electrons into discrete locations in the back focal plane. Placing apertures in the back focal plane, *i.e.* the objective aperture, the desired Bragg reflections can be selected (or excluded), thus only the parts of the sample that are causing the electrons to scatter to the selected reflections will be projected onto the imaging sensor. TEMs are often equipped with specimen holders that allow the user to tilt the specimen in order to obtain specific diffraction conditions. Apertures placed above the specimen allow the user to select electrons that would otherwise be diffracted in a particular direction from the specimen entrance.

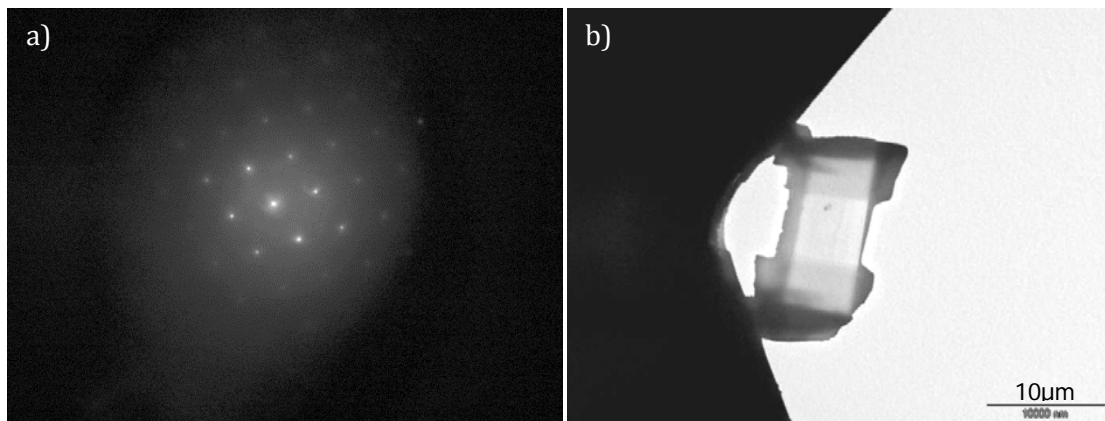


Figure 3-11 : (a) BF [110] pole on 1012AML diamond sample. (b) Cross-section BF picture of diamond sample FIB lamella preparation fixed on the Cu grid by carbon soldering.

The image will appear dark wherever no sample scattering from the selected peak is present. This is known as a dark-field image. Applications for this method include the identification of lattice defects in crystals. By carefully selecting the orientation of the sample, it is possible to determine the position and the type of present defects. However, defects producing displacement of atoms only that do not tilt the crystal to the Bragg angle (*i.e.* displacements parallel to the crystal plane) will not produce strong contrast.

C. Conventional dark field imaging

In single crystal specimens, single-reflection dark field images of a specimen tilted just off the Bragg condition allow one to "light up" only those lattice defects, like dislocations or precipitates, which bend a single set of lattice planes in their neighborhood. Analysis of intensities in such images may then be used to estimate the amount of bending. In polycrystalline specimens, on the other hand, dark field images serve to light up only that subset of crystals which is Bragg reflecting at a given orientation.

D. Weak beam imaging

Weak beam imaging involves similar optics to conventional dark field, but use of a harmonic diffracted beam rather than the diffracted beam itself. Much higher resolution of strained regions around defects can be obtained in this way.

E. Electron energy loss

Electrons can be rejected or collected depending on their energy using magnetic sector devices known as EELS spectrometers. These devices allow to select particular energy values, which can be associated with the electron interaction with the sample. For example, different elements in a sample result in different electron energies in the beam after passing through the sample. This effect can be used to generate an image which provides information on elemental composition. EELS spectrometers can often be operated in both spectroscopic and imaging modes, allowing for isolation or rejection of elastically scattered beams. That kind of imaging can be used to enhance contrast in observed images, including both bright field and diffraction, by rejecting unwanted components.

III.1.2. Scanning transmission electron microscopy

A scanning transmission electron microscope (STEM) is distinguished from conventional transmission electron microscopes (CTEM) by focusing the electron beam into a narrow spot which is scanned over the sample in a raster. The raster scan of the beam across the sample makes these microscopes suitable for analysis techniques such as mapping by energy dispersive X-ray (EDX) spectroscopy, electron energy loss spectroscopy (EELS) and annular dark-field imaging (ADF). These signals can be obtained simultaneously, allowing direct correlation of image and quantitative data. Usually STEM is a conventional transmission electron microscope equipped with additional scanning coils, detectors and needed circuitry; however dedicated STEMs are manufactured also.

Different STEM operation modes are detailed below. Geometry and position of detectors are different and allow the analysis of complementary information. ADF and HAADF mode will be shortly reviewed.

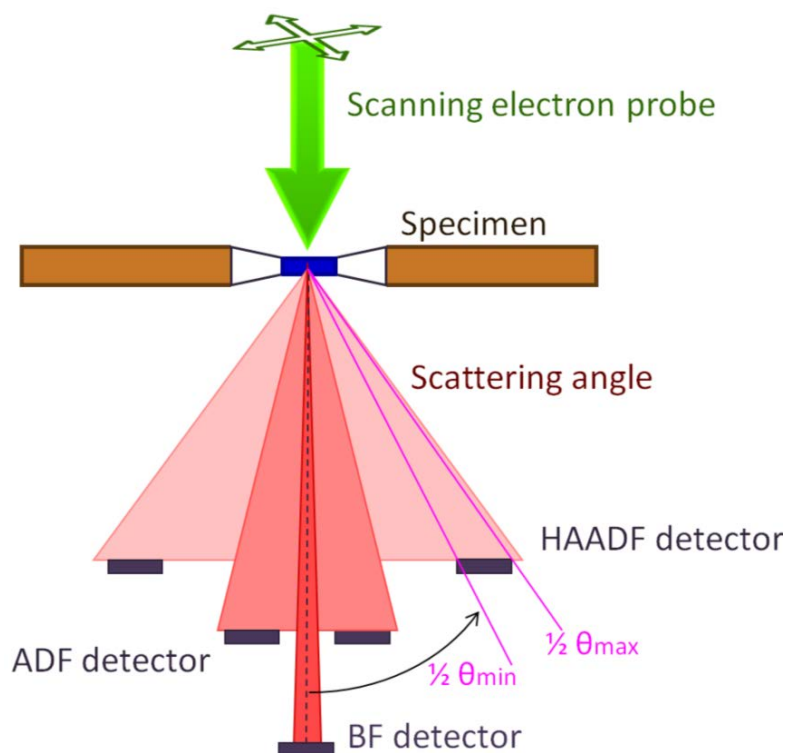


FIGURE 3-12 : Detector positions in angle and working distance in STEM.

A. Annular dark-field imaging (ADF)

Such images are formed by collecting scattered electrons with an annular dark-field detector in a scanning transmission electron microscope (STEM). In traditional dark-field imaging, an objective aperture is placed in the diffraction plane to only collect electrons scattering through that aperture, avoiding the main beam. An annular dark field detector collects electrons from an annulus around the main beam (figure 3-12), sampling far more scattered electrons than can pass through an objective aperture. This gives an advantage in terms of signal collection efficiency and allows the main beam to pass through an EELS detector, allowing both types of measurement to be performed simultaneously. ADF images are formed of both incoherently scattered electrons and Bragg scattered electrons. Atomic number variations of atoms in the sample (Z-contrast images) and dislocations are visible. By going to high-angle annular dark-field imaging (HAADF), it is possible to exclude dislocation contrast.

B. High-angle annular dark-field imaging (HAADF)

In this technique, the signal collected at high angles results from incoherent scattering with thermally excited atoms of the analyzed sample. These high angle scattered electrons do not contribute to the Bragg diffraction (BS), *i.e.* elastic electrons intensity is reduced by the effect of the temperature as electrons are diffused at higher angles, and are labelled

“thermally diffuse scattering (TDS)”. HAADF is also named Z-contrast, as the amplitude is linear with thickness and intensity depends on Z^2 . One of the main advantages of HAADF measurements versus DC ones is that tilting effects are completely eliminated.

HAADF experiments presented on Chapter 6. were performed under scanning transmission electron microscopy (STEM) mode of a TEM (JEOL 2010F) by focusing the electron beam probe on a point of the specimen and scanning it afterwards. The signal was collected on an annular detector, with a collecting angle typically from 0.06 rad to 0.2 rad (8 mm camera length), located at the focal plane of the objective length. The collecting angle can be optimized by changing the camera length in order to avoid Bragg diffraction spots to illuminate the detector.

III.1.3. Z-contrast images & numerical simulations

While the thermally diffuse scattering (TDS) intensity was integrated over the detector, collecting angle for each atom crossed by the electron beam to obtain the HAADF signal, the Bragg scattering (BS) intensity is integrated at the same time. Expressions of these intensities with the spatial frequency (s) are given by: $I^{BS}(s) = |f_{atom}(s)|^2 \exp(-2DW \cdot s^2)$ and $I^{TDS}(s) = |f_{atom}(s)|^2 [1 - \exp(-2DW \cdot s^2)]$ where DW is the Debye-Waller factor (attenuation caused by thermal motion) and $f(s)$ the atomic scattering factor. The atomic scattering factor depends of the atomic number (Rutherford scattering) as followed: $f_{atom}(s) = Z/8\pi^2 a_0 s^2$. In this equation: $s = \frac{\sin(\theta)}{\lambda}$, $a_0 = \frac{\epsilon_0 h^2}{\pi m_0 e^2}$ the Bohr's radius, and Z the atomic number. Finally $I^{HAADF}(s) = \int_{s_{min}}^{s_{max}} [I^{BS}(s) + I^{TDS}(s)] ds$, thus $|f_{atom}(s)|^2 \propto Z^2$ and $I^{HAADF}(s) \propto Z^2$. I^{TDS} and I^{BS} intensities of all elements likely to be present in the sample (according to secondary ion mass spectrometry investigations) are calculated in the interval of spatial frequencies (s) corresponding to the two angles of detection of the annular detector $2\theta_{min}$ and $2\theta_{max}$. The detection angles are chosen in the manner that I^{BS} is negligible in comparison to I^{TDS} (see figure 3-13) and the detector is moved in consequence.

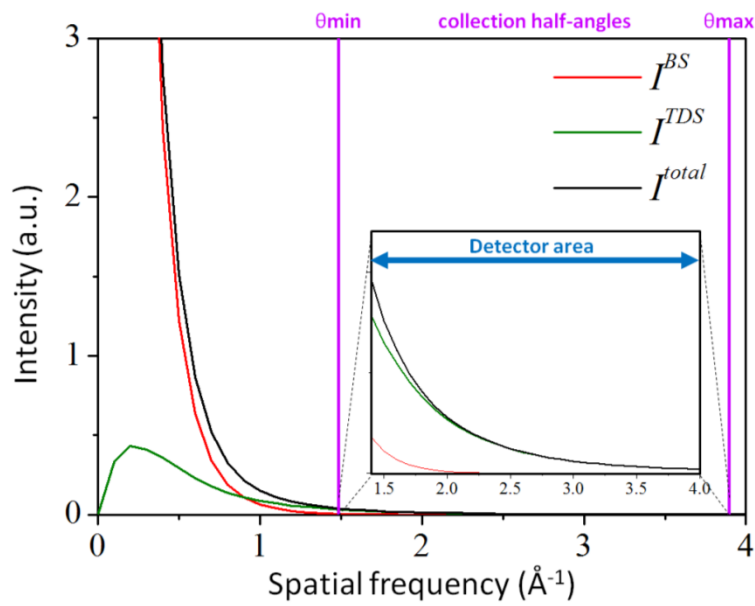


Figure 3-13 : Calculation of IBS and ITDS components of the scattered electron intensity.

Then the HAADF image is formed by scanning the sample surface with the probe position. N.B. the size of electron beam crossing the sample is spreading. The probe's diameter becomes broader and the number of illuminated pixels becomes larger, increasing the computing time considerably.

III.2. Sample preparation

Sample preparation for TEM observations required a complex procedure made in UCA (Universidad de Cádiz), Spain (Araújo, et al., 2010). Because diamond is the hardest known material, specimen preparation for cross-section TEM observation was made using a Focused Ion Beam in a Dual Beam Scanning electron microscope (FIB Dual Beam). High quality samples should have a thickness that is comparable to the mean free path of the electrons that travel through the samples, which may be only a few tens of nanometers. Constraints on the thickness of the material may be limited by the scattering cross-section of the atoms from which the material is made.

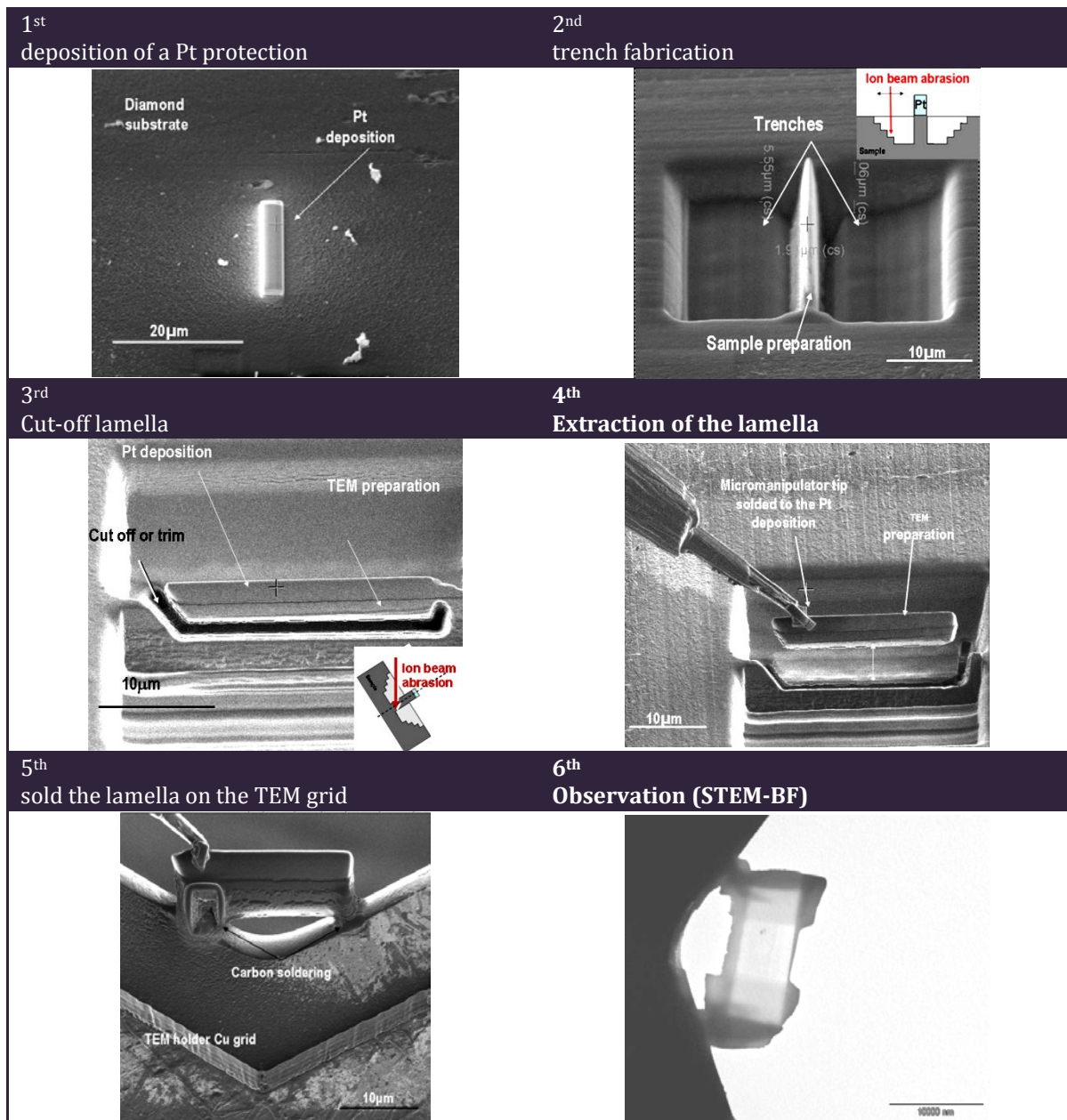


Figure 3-14 : Steps for the preparation of electron-transparent samples using FIB (Focus Ion Beam) from (Araújo, et al., 2012)

IV. SECONDARY ION MASS SPECTROSCOPY

Secondary ion mass spectroscopy (SIMS) is a powerful technique for the analysis of impurities in solids. The technique extracts material by sputtering and analyses the sputtered ionized matter. A primary ion beam entrenches on the sample and (ionized) atoms from the sample are ejected from the sample when they receive enough energy from the incident primary ions. These secondary ions are further analyzed with a mass spectrometer.

It allows simultaneous detection of different elements with sensitivity limits (depending on the element and the background signal) as low as 10^{14} to 10^{15} cm⁻³. The secondary ion signal of a given element is monitored as a function of time giving access to the dopant density profile on a scale of several microns, with a depth resolution of 1 to 5 nm depending of the sputtering rate. The impurity density is obtained by comparison with the secondary ion signal of a reference sample with a well-known reference dopant profile.

N.B.: the secondary ion mass spectroscopy determines the total, and not the electrically active impurity density. No information about the actual configuration of the impurity atoms in the host lattice is obtained. SIMS is a destructive characterization method since removing material by sputtering leaves a crater in the sample. Depth profile measurements of the crater (sputter matter) were used for the sputtering etch determination.

In the case of single crystal diamond, all measurements presented on Chapter 5. and Chapter 6. have been performed by François Jomard at the GEMaC (Groupe d'Etude de la Matière Condensée) at the CNRS and Université de Versailles Saint Quentin (UVSQ). A commercially available CAMECA IMS 4f instrument was used and a diamond reference implanted with 2×10^{15} cm⁻² was measured in the same runs for calibration. An incident beam of Cs⁺ ions with an acceleration energy of 14.5 keV (incident angle 27°) was used.

Complementary SIMS low ion energy measurements were performed by MST Co. in Japan. The primary beam consists of O₂⁺ ions with a nominal impact energy of about 3 keV (incident angle 45.7°).

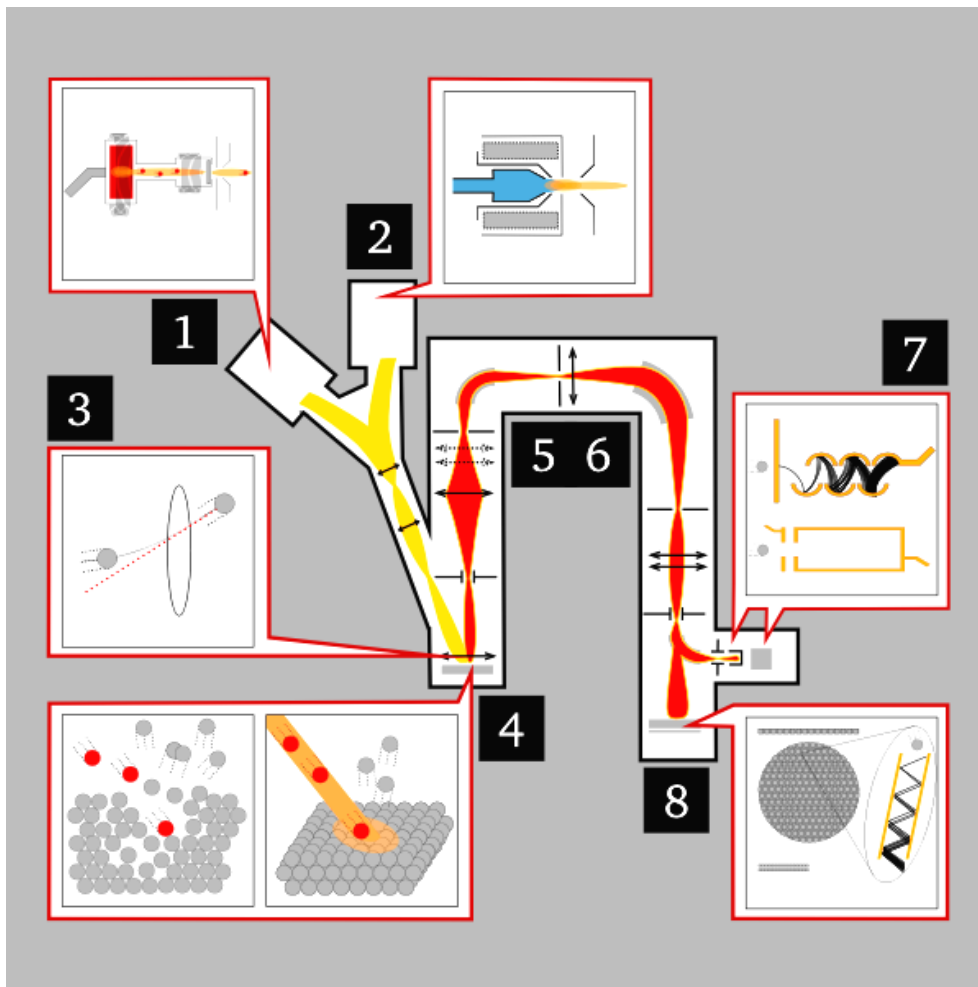


Figure 3-15 : Schematics of a dynamical SIMS instrument. High energy ions are supplied by an ion gun (1 or 2) and focused on to the target sample (3), which ionizes and sputters some atoms off the surface (4). These secondary ions are then collected by ion lens (5) and filtered according to atomic mass (6), then projected onto an electron multiplier (7, top), Faraday cup (7, bottom), or CCD screen (8).

IV.1. De-convolution and profile reconstruction

Usually, quantitative evaluation of measured profiles is done in the following three steps:

- (1) Conversion of the elemental signal intensity into elemental concentration
- (2) Conversion of the sputtering time into sputtered depth
- (3) Assessment of the depth resolution and of the depth resolution function

Tasks (1) and (2) are most important and generate the framework of any quantification. Quantification of the depth scale not only requires one point for the sputtering time in the measured profile to be attributed to a certain depth (for example by a stylus measurement of depth the sputtered crater after profiling), but generally has to consider nonlinear time/depth dependencies in case of a composition dependent sputtering rate. If carried out properly, tasks (1) and (2) establish the linear conditions necessary for step (3). In favourable cases, the time/depth and intensity/concentration relations are already

practically linear and can easily be obtained by appropriate sputtering rates and elemental sensitivity factors, respectively.

In high resolution depth profiling, a known resolution function applied to a sharp interface can be used to establish the correct relations time/depth and intensity/concentration by fitting of the measured profile with the result of a convolution. The sputter depth profiling is the transformation of a real world compositional distribution into an image of it, namely the measured depth profile. This transformation is described by the convolution integral which is governed by the depth resolution function (DRF) $g(z-z')$ (Hofmann, 1998):

$$I(z)/I(0) = \int_{-\infty}^{+\infty} X(z') \cdot g(z-z') dz', \quad (\text{Equation 3-A})$$

where $I(z)/I(0)$ is the measured and normalized intensity at the sputtered depth z and $X(z')$ the mole fraction of the respective element at depth z . Deconvolution means solving equation (1) for $X(z')$ which is possible *e.g.* by inverse Fourier transformation schemes if $g(z-z')$ and $I(z)/I(0)$ are known. However, such a "reverse" problem often faces practical difficulties because of insufficient data precision or too high signal-to noise level (Benninghoven, et al., 1997).

Therefore it has become customary to solve the problem by "forward calculation" of the convolution eqn. (3-A), *i.e.* assuming a suitable $X(z')$ and comparing the calculated profile with the measured profile $I(z)/I(0)$. By changing the input $X(z')$ until an optimum fit is obtained, the "original" in-depth distribution of composition is finally reconstructed (Hofmann, 1998), (Hofmann, 1994).

IV.2. Ion implantation and recoiling

Monte-Carlo simulation model: Stopping and range of ions into matter (SRIM) calculation was used to evaluate atoms forward diffusion induced by Cs^+ primary ions during SIMS measurement. As schematised in figure 3-16(a) when primary ions impact the sample, matter is sputtered and at the same time primary ion are implanted, generated cascade collisions with sample atoms. Impurities are diffused forward depending of primary ions mass, energy and incidence angle.

SRIM is a group of programs which calculate the stopping and range of ions into matter using a quantum mechanical treatment of ion-atom collisions (assuming a moving atom as an "ion", and all target atoms as "atoms"). This calculation is made very efficient by the use of statistical algorithms which allow the ion to make jumps between calculated collisions and then averaging the collision results over the intervening gap. During the collisions, the ion and atom have a screened Coulomb collision, including exchange and correlation interactions between the overlapping electron shells. The ion has long range interactions creating electron excitations and plasmons within the target. These are described by

including a description of the target's collective electronic structure and inter-atomic bond structure when the calculation is setup (tables of nominal values are supplied). The charge state of the ion within the target is described using the concept of effective charge, which includes a velocity dependent charge state and long range screening due to the collective electron sea of the target.

A full description of the calculation is given in a tutorial book (Ziegler, et al., 2010).

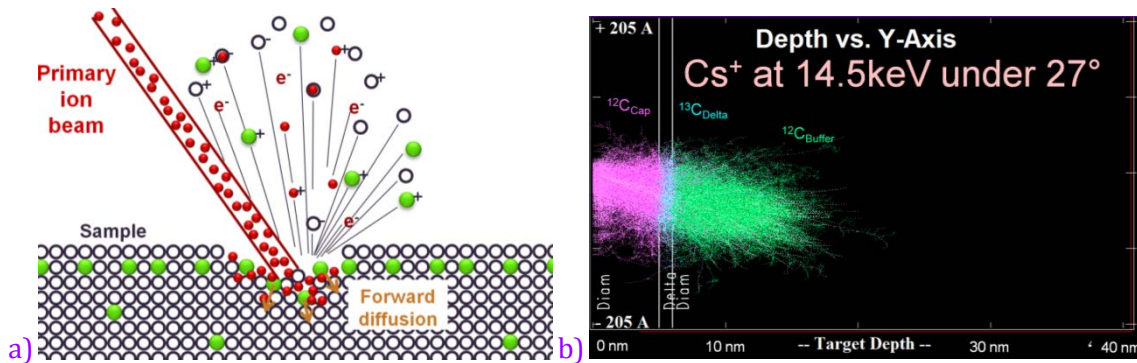


Figure 3-16 : SIMS primary ions effects. (a) Scheme of possible interaction with the matter. (b) SRIM simulation of cascade recoiling in diamond.

The figure 3-16(b) represent the Cs+ recoiling on diamond carbon atoms in a delta-structure made of an isotopic ^{13}C , 1 nm thin delta-layer located at 5 nm below the surface. The recoil is efficient over 18 nm below the surface, this implies a quite wide cascade ion-mixing when compared with the studied layer. On Figure 3-17, we can see clearly the forward and the backward scattering of atoms initially present in a 1 nm thin box. At a distance of 5 nm below the SIMS criteria, 20% of atoms have been forward scattered under these primary ion conditions according to SRIM calculations.

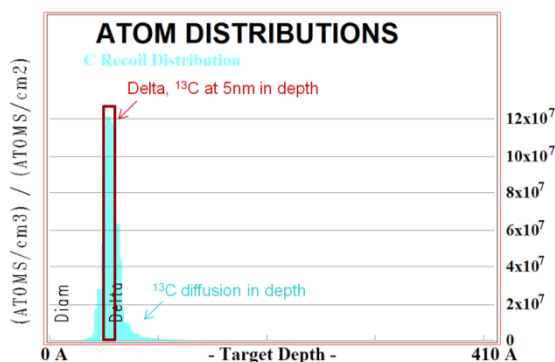


Figure 3-17 : 1nm thin delta-layer ^{13}C atoms redistributions induced by Cs^+ ions at 14.5 keV (27°) from SRIM calculations.

The concentration of impurity diffused increase with the sputtering depth. Mixing-roughness-information model has been built in order to take this phenomenon into account, in order to correct the SIMS depth profile.

IV.3. Mixing-Roughness-Information model (MRI)

Generally any experimental spectrum or profile is a convolution of a real (genuine) spectrum with an apparatus function. For SIMS, the experimental depth profile result from the convolution of the original distribution with the SIMS depth resolution function (DRF). The DRF contains the physical parameters determining the "response" of the system under study in terms of the measured profile. These parameters can be divided in the following three categories: change of surface composition (atomic mixing, preferential sputtering etc.), change of surface topography (roughness) and information depth of the analysis method. Although more detailed and complicated atomistic models exist (Hofmann, 1998), (Badheka, et al., 1990), the so called MRI model based on these three parameters (Mixing-Roughness-Information depth) was recently shown to be able to consistently describe AES depth profiles in GaAs/AlAs multilayers (Hofmann, 1994) as well as SIMS (Hofmann & Schubert, 1998) profiles. The MRI-model is capable of giving a mathematical description of the depth resolution function $g(z-z')$, based on the three fundamental contributions atomic mixing, surface roughness and information depth. Atomic mixing is described by an exponential function with a characteristic mixing zone length, w , the information depth by another exponential function with a characteristic length λ , and the roughness by a Gaussian term with standard deviation σ (corresponding to RMS roughness). These functions are employed sequentially to the (assumed) depth distribution of an element, given by thin layers each with (different) concentrations. For example, each mono-atomic layer at a location z_0 gives a normalized contribution at a sputtered depth z which is described by:

- atomic mixing: $g_w = \frac{1}{w} \cdot \exp \left[\frac{-(z-z_0+w)}{w} \right]$ (Equation 3-B)

- information depth: $g_\lambda = \frac{1}{\lambda} \cdot \exp \left[\frac{-(z-z_0)}{\lambda} \right]$ (Equation 3-C)

- surface roughness: $g_\sigma = \frac{1}{\sqrt{2\pi}\sigma} \cdot \exp \left[\frac{-(z-z_0)^2}{2\sigma^2} \right]$ (Equation 3-D)

Eqns. (3-B, C, D) can be applied by summing up all the contributions for each depth z after eqn. (3-A), thus representing the calculated depth profile which can be compared to the measured one. A more detailed derivation of the MRI model is given in (Hofmann, 1994). The MRI parameters have a well defined physical meaning. Therefore they can be theoretically predicted and/or experimentally measured by independent methods. For example, the information depth parameter λ , is given by the secondary ion escape depth in SIMS. The mixing length is at least approximately predicted by the SRIM code as explained before. Roughness is hard to predict, but surface roughness after profiling can be measured by AFM or optical profile. However, as pointed out by Hofmann, the "straggling" of the mixing length causes an additional roughness term which is difficult to determine (Hofmann, 1994).

V. HIGH RESOLUTION X-RAY DIFFRACTION

The X-ray diffraction (XRD) data were collected around symmetrical Bragg reflections, $\langle 004 \rangle$ -direction according to the orientation of the substrate. In order to get further information on the mosaicity and the strain distribution in the epilayer, reciprocal space mapping (RSM) around symmetrical ($\langle 004 \rangle$ -direction) and also on asymmetrical Bragg reflections ($\langle \bar{1}\bar{1}3 \rangle$ -direction) have been performed.

V.1. Diffractometer system

The triple axis diffractometer, present at the Institute for Nanoscience and Cryogenics (INAC), Grenoble, is using as a source the Cu $K\alpha_1$ line with a wavelength $\lambda = 0.15406$ nm, selected through a (220) Ge four-reflection channel cut monochromator. The angular resolution was better than 3×10^{-3} degrees. The rocking curves consist in fact of a (2θ - ω)-scan, by measuring the diffracted intensity as a function of the rotation θ , of the sample, with a continuous change of 2θ for the detector. This resembles the normally used rocking curves where only the sample is rotated due to the fact that our detector opening is not wide enough in order to detect the total signal. In the case of reciprocal space mapping, another analyzer was located in front of the detector to increase selectivity. A series of (2θ - ω)-scans is performed for a range of ω values about the specific X-ray reflection (table 3-2).

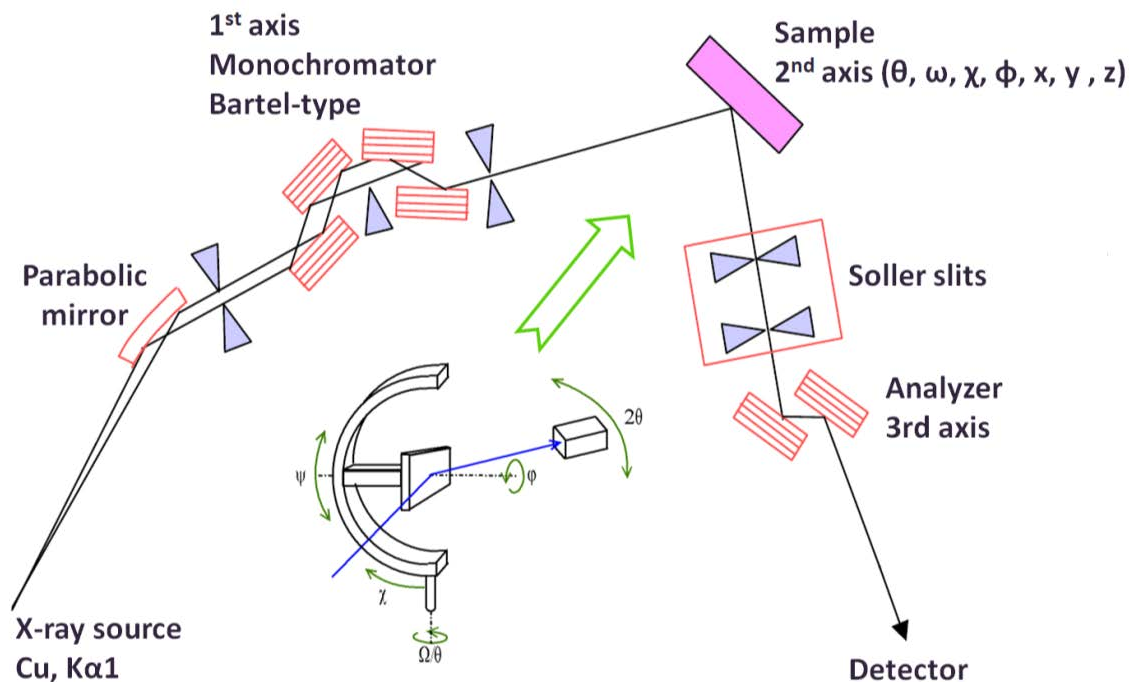


Figure 3-18 : Schematic description of the setup used for the HRXRD measurement localized at the Institute for Nanoscience and Cryogenics (INAC), Grenoble.

V.2. Diffraction peaks in diamond

In the case of highly boron-doped diamond, the in-plane lattice match leads to either an expansion or contraction of the lattice parameter a in the growth direction. Therefore, a XRD signal is detected under different angles for the substrate and the epilayer, corresponding to the different lattice spacings due to the difference in size of the constituent atoms (table 3-2). In the case of boron-doped diamond, the higher Bohr radius of boron with respect to carbon leads to a lattice expansion in the growth direction and hence a peak in XRD is seen at smaller diffraction angles than the substrate.

(hkl)	(111)	(220)	(311)	(400)	(331)
2 Theta (deg)	43.9154	75.3018	91.4952	119.5215	140.5870
d (Å)	2.0600	1.2610	1.0754	0.8916	0.8182
Relative intensity	100	25	16	8	16

Table 3-2 : Angular position, spacing and relative intensity of Bragg diffraction peaks of diamond (Diamond PDF card 00-006-0675).

The symmetrical peak is located around 120° . This wide angle required a HRXRD goniometer which allowed sufficient motions of the detector.

V.3. Relaxation/strain, composition and tilt

If the film is mismatched to the substrate, then the film might be strained so that the lattice parameters in the lateral direction (*i.e.* within the plane of the film) are forced to match the lattice parameters of the substrate. This distorts the unit cell of the film (from cubic unit cell to tetragonal on figure 3-19).

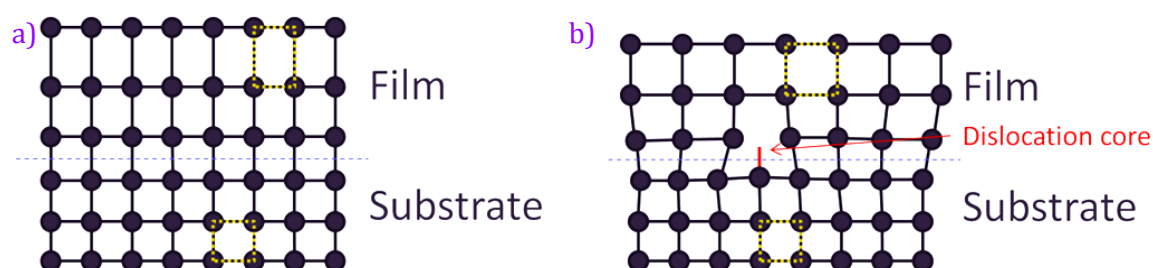


Figure 3-19 : Coherent growth of the epilayer on the substrate results either in (a) strained growth (with in-plane lattice matching) or (b) to relaxed growth (in-plane strain relaxed due to misfit dislocation).

If no relaxation (fully strained) occurs, then the lateral lattice parameters of the film in the plane are strained to be identical to the substrate. The Bragg angle for (004) shifts from its theoretical position, seen in rocking curve and coupled scans. Asymmetric coupled scan shows a film peak or substrate peak, but not both because they are not parallel.

If the film is fully relaxed, then the lateral lattice parameters of the film are equal to the bulk values and they have not been distorted at all. Difference in Bragg angles b/w film and substrate is by splitting of peaks in the Rocking Curve and multiple peaks in Coupled Scan. Asymmetric coupled scans show Bragg diffraction from both film and substrate.

When layers are under perpendicular strain ($\delta a^\perp/a$) (no in-plane lattice expansion), from the peak position of the diamond substrate θ_{sub} and the boron-doped epilayer θ_{epi} , it is possible to determinate the strain by $\frac{\delta a^\perp}{a} = \frac{\theta_{\text{sub}} - \theta_{\text{epi}}}{\tan(\theta_{\text{sub}})}$.

Changes in the composition will change the lattice parameters, which will change d_{hkl} and therefore the Bragg peak positions $n \cdot \lambda = 2d_{hkl} \cdot \sin(\theta_{hkl})$, where $d_{hkl} = \frac{a}{\sqrt{h^2+k^2+l^2}}$, a - lattice parameter, $\{h, k, l\}$ - Miller indices. Unlike relaxation, changes in composition will not change lattice tilts. In the symmetric scan, strain and compositional changes produce similar peak shifts. So, in order to quantify both strain and composition, we must combine a symmetric scan with an asymmetric scan. The typical way to collect reciprocal space maps is to vary relative omega and collect multiple $(2\theta-\omega)$ -scans.

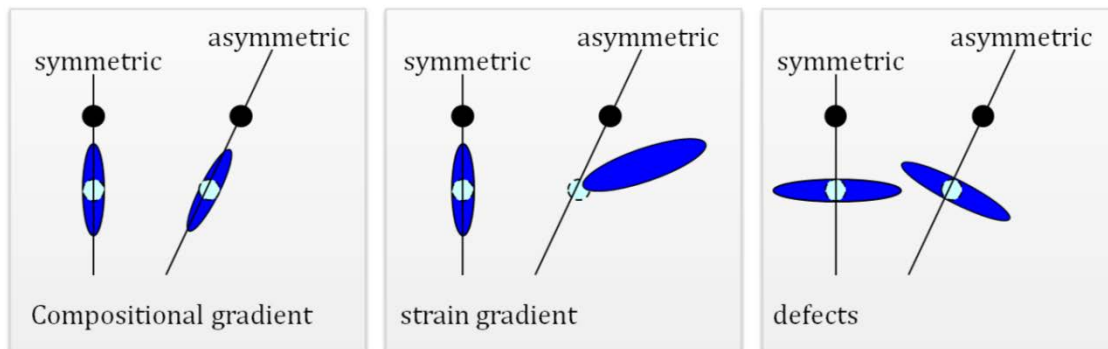


Figure 3-20 : Spreading of the reciprocal space point induced by defects, compositional and strain gradient around symmetric and asymmetric diffraction peaks.

VI. CONCLUSION

The surface analysis of diamond substrate and epilayers was systematically performed in order to discriminate good and bad quality substrates and to quantify the surface roughness evolution. The optical profile is an extremely powerful tool which can measure the surface roughness over the full sample i.e. $3 \times 3 \text{mm}^2$. Preliminary optical microscope observations are necessary to check the top face position and the presence of wild defect by applying the interferential differential contrast mode.

The analysis of surface wild defects and microstructures were possible with the intense light from a Field Emission Gun Scanning Electron Microscope (FEG SEM) and the good distance accuracy from an In-lens detector, which is located in the electron gun axis.

The diamond crystallinity was analyzed by cathodoluminescence and by high resolution X-ray diffraction. The boron doping was given, at first from the ratio of two cathodoluminescence peaks (BETO and FETO) in the case of light to moderate doping, and secondly by secondary ion mass spectrometry (SIMS).

The SIMS technique has a strong dependence with primary ions condition. The depth resolution function (DRF) became a problem when layers are too thin, especially in the case of delta-structure. A SIMS deconvolution code (MRI) was used to get the original layer thickness. However, the high-angle annular dark-field (HAADF) mode of scanning transmission electron microscope (STEM) drawn the chemical mapping of a sample cross-section, and at high resolution allows the direct observation the ultra thin layers.

VII. RÉSUMÉ DU CHAPITRE 3

La qualité de surface des substrats de diamant est essentielle pour épitaxier des couches sans défaut. Une attention toute particulière a été accordée au suivi de l'état de surface après croissance des films pour comprendre les mécanismes de croissance et l'origine des défauts de surface. Dans le cas du delta-dopage, la surface doit être la plus plate possible et la planéité doit être conservée au fil des croissances de couche tampon, delta et de couverture. Lorsque le projet implique des prises de contacts électriques (ohmique, Schottky ou MOS), les défauts 3D ont une forte incidence sur la détérioration des performances du composant.

Substrats et films de diamant ont été analysés par des techniques de microscopie (microscope optique, microscope électronique à balayage) et par profilomètre (optique) afin de quantifier la morphologie de la surface (RMS, hauteur et taille défaut). Pour ce faire, une approche systématique d'analyse de surface a été mise au point. Les techniques de caractérisation sont examinées dans ce chapitre.

En microscopie optique, l'observation dite en champ clair (noté BF) constitue la première étape de l'analyse. Ce mode permet de repérer la face supérieure en suivant les bords de l'échantillon et des poussières éventuelles (le diamant est transparent en général). Sur la photo 3.3, il est possible de voir des points très brillants qui sont attribués aux cristallites non-épitaxiaux (UC). Ces défauts apparaissent comme des points sombres sur la vue dite en champ sombre (DF). Dans ce mode, la base de grands défauts pyramidaux et arrondis trace une ombre sur la surface. L'observation en lumière polarisée (POL) fait ressortir des arêtes brillantes attribuées aux bords des monticules pyramidaux, les zones noires et les zones vertes nous renseignent sur le champ de déformation près du coin coupé. Le meilleur mode pour évaluer la morphologie de surface en microscopie optique est le contraste interférentiel différentiel noté DIC. Dans ce mode, un prisme décompose la lumière en deux composantes orthogonales qui vont interférer sur la surface rugueuse à observer. La différence de phase que l'on perçoit en contraste d'intensité traduit les variations de hauteur présentes sur la surface de l'échantillon. Le contraste est très sensible aux petites variations de hauteur. Cela explique la raison pour laquelle la différence entre pyramides (2 faces à la lumière, 2 faces à l'ombre) et monticules arrondis (avec un gradient de lumière continu) est si nette. La rugosité de surface peut être appréciée, mais seulement de façon qualitative. La mesure précise de la rugosité de surface s'effectue par des techniques de profilométrie (stylet, laser ou franges de lumière ...).

Les profils de rugosité de surface sont effectués sur du diamant dopé ou non. Dans le cas de bicouches de dopage ou de super-réseaux de dopage, aucun artefact particulier n'a été observé. L'utilisation d'un mode de fonctionnement particulier est déterminée par les caractéristiques de la surface à étudier. Ce choix dépend principalement de la hauteur des défauts (discontinuité de surface).

Le mode PSI est utilisé pour étudier la rugosité des lignes de polissage et des trous à la surface des substrats et des films. Le Mode HDVSI est utilisé sur des échantillons de diamant lorsque leur surface comporte des défauts pyramidaux et des régions planes. Si une telle surface est mesurée en mode PSI, la mesure de la rugosité de la surface plane est erronée en raison d'erreurs induites par les discontinuités des bords des défauts. Le mode HDVSI est également appliqué sur des échantillons gravés, comme dans le cas de MESA-structures. Cependant, si de larges défauts irréguliers (comme cristallites non-épitaxiaux) sont présents à la surface de couches épitaxiales, il ne peut pas être analysé par le mode HDVSI. Dans ce cas, le mode VSI est utilisé pour localiser les zones les moins défectueuses sur l'échantillon pour y effectuer une analyse HDVSI par la suite. Toutefois, si la résolution verticale est parfaite pour analyser la rugosité de surface (0.1nm), la faible résolution latérale (1 μm) ne permet pas de mesurer avec précision la base d'objets (monticules, structures MESA ...).

La cathodoluminescence (CL) est l'émission de lumière produite par une substance sous excitation électronique. Le mécanisme peut être décrit en trois étapes: excitation, quand le faisceau d'électrons induit un grand nombre de paires électron-trou (au bas de la bande de conduction et dans la partie supérieure de la bande de valence, respectivement); dérive des porteurs générés par diffusion (cette migration est caractérisée par une longueur de diffusion); recombinaison, qui peut être radiative lorsqu'un photon est émis ou non-radiative où les phonons qui sont générés servent à chauffer l'échantillon.

Dans le diamant, les transitions radiatives sont assistées par un phonon (Figure 3.7). Deux types de phonons sont présents dans le mécanisme: transversal (TA acoustique, TO optique) et longitudinal (LA acoustique, LO optique). Les recombinaisons excitoniques libres assistées par des phonons correspondant à la transition appelé FE^{TO} sont dominants ; FE^{TA} et FE^{LO} sont beaucoup plus faibles, environ 5% (et 1% resp.) (Dean et al., 1965). Lorsque le diamant est dopé, les excitons peuvent se lier à des impuretés neutres ou à des pièges, conduisant à de nouvelles transitions possibles (généralement assisté par des phonons optiques transverses, BE^{TO}) comme indiqué dans le tableau 3.1. D'autres transitions associées à des défauts étendus ou ponctuels, comme les dislocations se produisent également.

En microscopie électronique à transmission (TEM), un faisceau d'électrons est transmis à travers un échantillon ultra mince (électro-transparent) et interagit avec la matière sur son chemin. Une image est formée à partir de l'interaction des électrons transmis à travers l'échantillon, agrandie puis focalisée sur un dispositif d'imagerie, par exemple un écran fluorescent, ou détectée par un capteur, par exemple une caméra CCD.

Un TEM est constitué de plusieurs composants, qui comprennent un système de pompage, une source d'émission d'électrons, une série de lentilles électromagnétiques, ainsi que des plaques électrostatiques pour guider et manipuler le faisceau selon les besoins. Le dernier dispositif permet l'insertion, le mouvement et le retrait d'échantillons dans la trajectoire du faisceau. Différents appareils d'imagerie sont ensuite utilisés pour créer une image.

Un microscope à balayage électronique à transmission (STEM) se distingue des microscopes électroniques à transmission (CTEM) en focalisant le faisceau d'électrons dans un faisceau étroit qui balaye l'échantillon dans une trame. Le balayage de trame du faisceau sur l'échantillon rend ces microscopes adaptés aux techniques d'analyse telles que la cartographie par la spectroscopie de dispersion d'énergie des rayons X (EDX), la spectroscopie de perte d'énergie d'électrons (EELS) et l'imagerie en champ sombre annulaire (ADF). Ces signaux peuvent être obtenus simultanément, ce qui permet une corrélation directe entre l'image et des données quantitatives.

Dans nos études d'imagerie HAADF, le signal est recueilli par un détecteur annulaire à des angles élevés de diffusion incohérente issus des atomes de l'échantillon analysé excités thermiquement. Ces électrons dispersés aux angles élevés ne contribuent très peu à la diffraction de Bragg (BS). Le HAADF est également appelée Z-contraste, il donne une information chimique de la composition de l'échantillon, car l'amplitude du signal est linéaire avec l'épaisseur et dépend de Z^2 .

Les expériences HAADF présentées au chapitre 6 ont été réalisées en microscopie à balayage électronique en transmission (STEM) (JEOL 2010F) en focalisant le faisceau d'électrons sonde sur un point de l'échantillon. Le signal a été recueilli sur un détecteur annulaire, avec un angle de collecte typique de 0,06 rad à 0,2 rad (8 mm de longueur caméra), situé dans le plan focal de l'objectif. L'angle de collecte peut être optimisé en modifiant la longueur de la caméra, afin d'éviter d'illuminer le détecteur avec des taches de diffraction de Bragg.

La spectroscopie de masse d'ions secondaires (SIMS) est une technique puissante pour l'analyse des impuretés dans les solides. Un faisceau d'ions primaires bombarde la surface de l'échantillon et les atomes ionisés de l'échantillon sont éjectés (pulvérisation) lorsqu'ils reçoivent suffisamment d'énergie à partir des ions incidents primaires. Ces ions secondaires pulvérisés sont en outre accélérés, triés et analysés avec un spectromètre de masse.

Elle permet la détection simultanée des différents éléments avec des limites de sensibilité (en fonction de l'élément et le signal de fond) aussi faibles que 10^{14} à 10^{15} cm⁻³. Le signal d'ions secondaires d'un élément donné est contrôlé en fonction du temps d'accès donnant au profil de densité de dopant à l'échelle de quelques microns, une résolution en profondeur allant de 1 à 5 nm en fonction de la vitesse de pulvérisation. La densité d'impuretés est obtenue par comparaison avec le signal d'ions secondaires issus d'un échantillon de référence ayant un profil de dopage bien connu.

NB: la spectroscopie de masse d'ions secondaires détermine le total, et non la densité d'impuretés électriquement actives. Aucune information sur la configuration réelle des atomes dans le réseau hôte n'est obtenue. Le SIMS est une méthode de caractérisation destructive qui laisse un cratère dans l'échantillon. La profondeur du cratère (pulvérisation question) est utilisée pour la déterminer la vitesse de gravure.

Dans le cas du diamant monocristallin, toutes les mesures présentées au chapitre 5. et au chapitre 6. ont été réalisées par François Jomard au GEMaC (Groupe d'Etude de la Matière Condensée), unité mixte au CNRS et à l'Université de Versailles Saint-Quentin (UVSQ). Un

instrument CAMECA 4f IMS, disponible dans le commerce, a été utilisé et une référence implantée avec $2 \times 10^{15} \text{ cm}^{-2}$ a été mesurée dans les mêmes conditions pour l'étalonnage. Un faisceau incident d'ion Cs^+ avec une énergie d'accélération de 14,5 keV (27° d'angle d'incidence) a été utilisé.

Des mesures complémentaires à faibles énergies d'ions ont été réalisées par le MST Co. au Japon. Le faisceau primaire se compose d'ion O_2^+ avec une énergie d'impact nominale d'environ 3 keV ($45,7^\circ$ angle d'incidence).

La diffraction de rayons X (XRD) sur le diamant s'effectue autour d'un pic de réflexion de Bragg symétrique intense, dans notre cas en direction (004), situé à environ $2 \times \theta = 120^\circ$. Il faut un goniomètre HRXRD qui puisse accueillir les exigences angulaires suffisantes du détecteur, ce qui n'est possible que dans certains appareils.

Pour obtenir de plus amples informations cristallographiques, comme la mosaïcité et la distribution des déformations des couches épitaxiées, on réalise des cartographies en espace réciproque (RSM) autour du pic symétrique le plus intense (en direction 004) et autour d'un pic asymétrique, le $(\bar{1}\bar{1}3)$.

Dans le cas d'un dopage, l'accord de maille dans le plan de croissance conduit soit à une expansion ou à une contraction du paramètre de maille dans la direction de croissance. Cela se manifeste par un signal de diffraction des rayons X détecté selon différents angles pour le substrat et la couche épitaxiale (tableau 3-2).

Dans le cas du diamant fortement dopé au bore, le réseau cristallin a tendance à s'étirer dans la direction de la croissance tout en gardant un paramètre de maille identique au substrat dans le plan de base, on parle alors de déformation tétragonale (figure 3-19). Dans ce cas, on observe un pic de diffraction des rayons X vu à des angles plus petits que celui du substrat.

Chapter 4.
DIAMOND SUBSTRATES
P R O P E R T I E S

I. INTRODUCTION

The quality of diamond substrates is critical for devices fabrication and tests.

The aim of this chapter is to review defects in bulk diamond which are used as substrates for homoepitaxial overgrowth of functional layers. We shall see how to characterize them and to understand their origin from the diamond growth to the surface polishing.

II. GENERALITY ABOUT SYNTHETIC DIAMOND GROWTH

II.1. Ἀδάμας – Adámas – Unbreakable

In mineralogy, diamond (from the ancient Greek Ἀδάμας – adámas "unbreakable") is an allotrope of carbon, where the carbon atoms are arranged in a variation of the face-centered cubic crystal structure called a diamond lattice ($a = 3.56683 \text{ \AA}$). Diamond is less stable than graphite, but the conversion rate from diamond to graphite is negligible under ambient conditions. Diamond is renowned as a material with superlative physical qualities, most of which originate in the strong covalent bonding between carbon atoms. In particular, diamond has the highest hardness and thermal conductivity. These properties determine the major industrial application of diamond in cutting and polishing tools.

Most natural diamonds are formed at high temperature and pressure at depths of 140 to 190 kilometers in the Earth mantle (Erlich & Dan Hausel, 2002). Carbon-containing minerals provide the carbon source, and the growth occurs over periods from 1 billion to 3.3 billion years (25% to 75% of the age of the Earth). Diamonds are brought close to the Earth surface through deep volcanic eruptions by a magma, which cools into igneous rocks known as kimberlites* and lamproites†.

II.2. Diamond synthesis

Synthetic diamonds are diamonds produced through a technological process; as opposed to natural diamonds, which are created by geological processes.

There are several methods to produce synthetic diamond. The original method combines high pressure and high temperature (HPHT) and is still widely used because of its relatively low cost. The process involves large presses that can weigh hundreds of tons to produce a pressure of 5 GPa at 1500 °C. The second method, using chemical vapor deposition (CVD), creates a plasma of carbon species over a substrate onto which the carbon atoms deposit to

* A type of potassic volcanic rock.

† An ultra-potassic mantle-derived volcanic and sub-volcanic rocks.

form diamond. Other methods include explosive formation (forming detonation nanodiamonds) and sonication of graphite solutions (Werner & Locher, 1998), (Ōsawa, 2007), (Galimov, et al., 2003).

II.2.1. High pressure, high temperature processes

There are three kinds of press designs used to supply the pressure and temperature necessary to produce synthetic diamond by HPHT processes: the belt press, the cubic press and the split-sphere (BARS) press.

The original General Electric invention by Tracy Hall uses the belt press wherein the upper and lower anvils supply the pressure load to a cylindrical inner cell. This internal pressure is confined radially by a belt of pre-stressed steel bands. The anvils also serve as electrodes providing electrical current to the compressed cell. Belt presses are still used today, but they are built on a much larger scale than those of the original design (Barnard, 2000).

The second type of press design is the cubic press. A cubic press has six anvils which provide pressure simultaneously onto all faces of a cube-shaped volume (Ito, 2007). The first multi-anvil press design was a tetrahedral press, using four anvils to converge upon a tetrahedron-shaped volume (Hall, 1958). The cubic press was created shortly thereafter in order to increase the volume to which pressure could be applied. A cubic press is typically smaller than a belt press and can more rapidly achieve the pressure and temperature necessary to create synthetic diamond. However, cubic presses cannot be easily scaled up to larger volumes.

The BAPC[‡] apparatus (BARS) is the most compact, efficient, and economical of all the diamond-producing presses. In the center of a BARS device, there is a ceramic cylindrical "synthesis capsule" of about 2 cm³ in size. The cell is placed into a cube of pressure-transmitting material, such as pyrophyllite ceramics[§], which is pressed by inner anvils made from cemented carbide (*e.g.*, tungsten carbide or VK10 hard alloy) (Loshak & Alexandrova, 2001). The outer octahedral cavity is pressed by 8 steel outer anvils. After mounting, the whole assembly is locked in a disc-type barrel with a diameter about 1 meter. The barrel is filled with oil, which pressurizes upon heating, and the oil pressure is transferred to the central cell. The synthesis capsule is heated up by a coaxial graphite heater (Pal'yanov, et al., 2002). The growth rate for type Ib (yellow, nitrogen-rich) crystals using Fe-Ni catalyst reaches as high as ~20 mg.h⁻¹ towards the end of 100 hours growth cycle (Abbaschian, et al., 2005), *i.e.* crystals of 5 carats (1.0 g) to 6 carats (1.2 g) can be grown in less than 100 hours.

[‡] Беспрессовая Аппаратура высокого давления "Разрезная Сфера" from press-free high-pressure setup "split sphere"

[§] A phyllosilicate mineral composed of aluminum silicate hydroxide: Al₂Si₄O₁₀(OH)₂.



Figure 4-1 : Small presses - split-sphere apparatus (BARS) developed IGGM, Novosibirsk (since mid 1970s, improved in early 1990s)

II.2.2. CVD growth techniques

Deposition of diamond by CVD has been largely studied by different research groups worldwide since the early 1980s (Koizumi, et al., 2008). The substrate can be either bulk diamond (either natural or synthetic) or a non-diamond substrate. In the first case, if the growing conditions are appropriate to epitaxial overgrowth, the resulting films are said to be homo-epitaxial or single crystalline, in opposition to hetero-epitaxial or polycrystalline films in the latter case. Chemical vapor deposition diamond growth typically occurs under low pressure and involves feeding varying amounts of gases into a chamber, energizing them and providing conditions for diamond growth on the substrate. The gases always include a carbon source, and typically include hydrogen as well, though the amounts used vary greatly depending on the type of diamond being grown. Energy sources include hot filament, microwave power, and arc discharges, among others. The energy source is intended to generate a plasma in which the gases species are broken and where a complex chemistry occurs. The most important attribute of CVD diamond growth is the ability to control the properties of the diamond produced. By regulating the processing parameters — especially the gases introduced, the pressure, the temperature of the diamond, and the method of generating plasma — single crystal diamonds can be made containing various dopants (Isberg, et al., 2004).

II.3. Development in CVD growth

The first documented report of diamond growth at a low pressure was published in 1954 by Bundy and co-workers (Bundy, et al., 1955). These authors conducted a wide range of sophisticated experiments based on the following reactions: (1) $2 \text{ CO} = \text{C}_{(\text{diamond})} + \text{CO}_2$, and (2) $2 \text{ CO} = \text{C}_{(\text{graphite})} + \text{CO}_2$, which are thermodynamically possible due to the negative Gibbs

free energy. In these experiments, either diamond or graphite was used as seeds. The experiments were conducted at temperatures from 820 to 1000°C and pressures from 5×10^6 to 31×10^6 Pa. It was found that the measured equilibrium ratio CO/CO_2 over diamond (reaction (1)) was different from that over graphite (reaction (2)), which was expected from thermodynamic data, as the equilibrium is different for C_{diamond} and C_{graphite} . Furthermore, they found that the equilibrium and precipitation of diamond on the diamond seed was metastable. No graphite was detected, although under these process conditions (pressure and temperature) graphite was the thermodynamically stable modification.

In 1956, Spitsyn and Deryagin proposed in the former USSR the growth of diamond at low pressures through the thermal decomposition of carbon tetra-iodide (Spitsyn & Deryagin, 1980) at temperatures ranging from 800 to 1000°C and pressures of approximately 4×10^{-4} Pa. The Soviet group subsequently explored direct CVD from hydrocarbons and in 1969 it was stated that diamond was synthesized from pure methane at pressures from 13 to 40 Pa and temperatures from 950 to 1050 °C with a higher growth rate.

A major breakthrough on the CVD diamond process was achieved in the early 1970s. It was the use of atomic hydrogen during growth to remove graphite co-deposits, based on the fact that atomic hydrogen etches graphite much faster than it does diamond. This gave a much higher growth rate and, of equal importance, it permitted the nucleation of new diamond crystallites on non-diamond substrates. The use of atomic hydrogen was independently studied by J. Angus in the USA and by V. Varnin in the USSR (Prelas, et al., 1997).

The modern era of CVD diamond started in the early 1980s. A Japanese group, working at the National Institute for Research in Inorganic Materials (NIRIM), first published a remarkable series of papers in which different techniques, hot-filament CVD process, RF-plasma CVD and Microwave Plasma enhanced CVD, were described (Matsumoto, et al., 1982), (Matsumoto, et al., 1982), (Kamo, et al., 1983), (Matsui, et al., 1983). They reported that diamond particles and films could be deposited on various substrates heated around 850 °C, using a mixed gas of methane diluted by hydrogen, and preferred partial pressures in the range 10–100 Torr. A growth rate higher than several micrometers per hour was achieved. These results were soon confirmed by several research groups in the USA and Europe (Angus, 1994), (Spitsyn & Deryagin, 1980), (Prelas, et al., 1997). The success of the NIRIM group almost immediately spread and spawned numerous research programs around the world. These programs included process techniques, understanding the mechanism of CVD diamond nucleation and growth, diamond doping, investigation of optical, electronic, thermal, mechanical properties of CVD diamond, diamond coating on various substrates for specific applications, and characterization of CVD diamond.

II.4. Plasma-enhanced CVD methods

Alternative methods of diamond growth involve various forms of plasma-assisted CVD using carbon-containing species mixed in low concentration with hydrogen. The role of the plasma is to generate atomic hydrogen and to produce proper carbon precursors for the growth of diamond. Atomic hydrogen is produced by electron impact dissociation of molecular hydrogen. Thus, atomic hydrogen produced in plasmas generally has a high kinetic energy due to the difference between the hydrogen dissociation energy and the electron kinetic energy. This is to be contrasted with the thermal-assisted CVD process, where the produced atomic hydrogen has a low kinetic energy.

Similarly, electron impact and thermal dissociation processes are responsible for the formation of carbon-containing neutral and ionic radicals. In general, 1% of the molecules in plasma are converted into neutral radicals and about 0.01% into ions. Neutral molecules, for example, CH₄, usually do not participate in the growth of diamond due to a relatively high Gibbs free energy in the process of their decomposition. Thus, the growth rate of the diamond film is determined mainly by the concentration of neutral radicals. The effect of the ionized radicals is not clear. Although their contribution to the growth rate is minimal, one cannot rule out ion-assisted processes.

Among the plasma-enhanced methods, microwave plasma assisted CVD is the most popular for the growth of diamond films. It offers a number of distinct advantages over the other methods. Microwave deposition, being an electrode-less process, avoids contamination of the films due to electrode erosion. Furthermore, the microwave discharge at 2.45 GHz, being a higher frequency process than the RF discharges at 13.5 MHz, produces higher plasma density with higher energy electrons. This should result in higher concentrations of atomic hydrogen and hydrocarbon radicals. An additional advantage is that the plasma is confined in the centre of the deposition chamber in the form of a ball and this prevents carbon deposition on the walls of the chamber.

II.5. Mechanisms of CVD diamond growth

In diamond CVD, free radicals – particularly atomic hydrogen – play crucial roles. Gas-phase chemistry is an integral part of diamond CVD. A mixture of radicals, molecules and ions impinges on the substrate and contributes to the growth of diamond, even though the gas composition is a simple methane/hydrogen mixture. There have been many studies of the gas-phase chemistry during diamond CVD over the last 25 years. These investigations revealed that atomic hydrogen and hydrocarbon are perhaps the most critical determinants of CVD diamond synthesis, controlling its quality and growth rate as well.

II.5.1. Atomic hydrogen

The production mechanisms, loss mechanisms and concentration profiles of atomic hydrogen are basic subjects. In plasma-enhanced systems excited in the microwave range, H is produced homogeneously in the plasma. The energetic electrons and the high gas temperature may directly produce H through: $\text{H}_2 + \text{e}^- \rightarrow \text{H} + \text{H} + \text{e}^-$. Recombination of H is a slow process, and H atoms are able to diffuse to the walls or to the substrate before recombining in the gas. Measurements of the H concentration profile near a diamond substrate clearly show that diamond is a sink for H at typical substrate temperatures (Liou, et al., 1990).

Diamond surface consists of 'dangling bonds', which need to be terminated in order to prevent carbon cross-linkage, leading to graphite. When the surface termination is performed by hydrogen, the sp^3 diamond lattice is stable. During diamond growth, these H atoms have to be removed and replaced by carbon species. A large number of reactive H atoms close to the surface quickly bond to any excess dangling bonds that may have been created by thermal desorption or abstraction of surface H atoms, and prevent surface graphitization. As discussed, atomic H etches graphitic sp^2 carbon faster than sp^3 carbon; H atoms etch back to the gas phase any superficial graphitic. Diamond growth could thus be considered as a 'three steps forward, but two steps back' process.

II.5.2. Hydrocarbon chemistry

The first hydrocarbon concentration measurements during diamond growth were made by Celii *et al.*, who used infrared diode laser absorption spectroscopy to detect acetylene (C_2H_2), the methyl radical ($\bullet\text{CH}_3$) and ethylene (C_2H_4) in hot filament reactor (Celii, et al., 1988). A similar measurement was made by McMaster *et al.* for a 2.7 kPa microwave system (McMaster, et al., 1995). The measured acetylene concentration represented conversion of 10–20% of the initial methane. Since the gas-phase conversion of methane to acetylene requires several sequential reactions with atomic hydrogen, this observation clearly showed that significant gas phase chemistry occurred. A notable feature of these results is that methane and acetylene account for the majority of the gas-phase carbon. Ethylene is present at much lower levels and ethane (C_2H_6) is not detected. The only two radical species which are detectable are atomic hydrogen and the methyl radical $\bullet\text{CH}_3$. Chemical equilibrium analysis indicates that the distribution of the C_1 species depends only on the H/ H_2 ratio and the local temperature. Normally the H/ H_2 ratio in a diamond CVD system is in the range 10^{-3} – 10^0 , which leads to a result that the most abundant C_1 radicals are $\bullet\text{CH}_3$ and atomic carbon. For that reason, $\bullet\text{CH}_3$ and $\text{C}\bullet$ are most often postulated to be important for diamond growth.

The distribution of species with the C_2 system results from the fact that the species C_2H_2 , C_2H_4 and C_2H_6 are all stable molecules, and thus reactions, such as: $\text{C}_2\text{H}_2 + \text{H}_2 \rightarrow \text{C}_2\text{H}_3 + \text{H}$, have high activation energies and are consequently very slow. The concentrations of all C_2H_n

species with $n > 2$ are generally low, since these species are thermodynamically less stable at a high temperature and in the presence of atomic hydrogen than acetylene. Thus, C_2H_n ($n > 2$) species are rapidly converted to acetylene. C_2H_2 is still suggested to have a negative role in diamond growth (McMaster, et al., 1995).

II.5.3. Growth mechanisms

From measured concentrations of stable species, it was found that only CH_4 , $\bullet CH_3$ and C_2H_2 are present in sufficient quantities to play a role in the diamond growth mechanism. When the low reactivity of methane is taken into account, only $\bullet CH_3$ and C_2H_2 are candidate as the possible growth species under typical diamond CVD conditions. Several mechanisms for diamond CVD have been proposed, including $\bullet CH_3$ -based mechanisms, acetylene-addition mechanisms, and combined $\bullet CH_3$ - C_2H_2 mechanism (Goodwin & Butler, 1998).

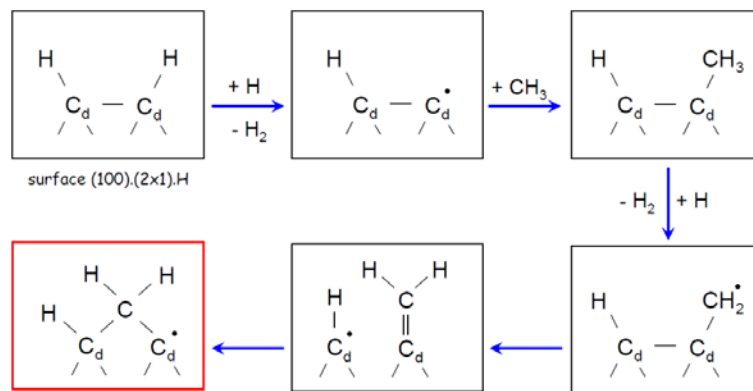


Figure 4-2 : Dimer opening & Carbon insertion. From (Goodwin & Butler, 1998).

II.5.4. Effect of oxygen addition

Because of the rapid gas-phase chemistry, the equilibrium composition provides, once again, a first estimate of the effect of oxygen addition on the gas composition. Since acetylene is typically one of the most abundant hydrocarbons, the oxidation reaction must be $C_2H_2 + O_2 \leftrightarrow 2 CO + H_2$. This reaction is highly exothermic so that both or one left-hand reactant is washed-out. Harris and Weiner have reported mass spectral measurements during diamond CVD growth with various mixtures of CH_4 , O_2 and H_2 (Harris & Weiner, 1989). In all cases, they found that adding O_2 reduced the hydrocarbon mole fractions. No O_2 was detected experimentally at the substrate, indicating that all injected O_2 was rapidly consumed. These results are also consistent with the empirical observations of Bachmann et al. (Bachmann, et al., 1991) and suggest that the oxygen rapidly oxidizes any available hydrocarbon.

Other effects may be significant for the film growth. For example, it has been shown that oxygen addition can increase $\bullet OH$ radical level. Since $\bullet OH$ can oxidize pyrolytic, non-

diamond carbon, it may play a role similar to H and thus oxygen addition may help diamond growth through creation of $\bullet\text{OH}$ radicals. These radicals are supposed to oxidize the BH_x gaseous species originating from the B_2H_6 plasma decomposition process, thus strongly reducing the chemically active $\bullet\text{BH}_x$ radicals reactive concentrations within the plasma ball ($x = 1, 2, 3$). Recent investigations on single crystalline diamond driven by Omnès and co-workers show a reduction by 2 decades of boron incorporation rate at a given value of the B/C ratio when oxygen was introduced at a 0.25% $[\text{O}_2]/[\text{H}_2]$ ratio in the growth chamber (Omnès, et al., 2011).

III. DIAMOND TYPE CLASSIFICATION

Pure diamond is made of only one element: carbon. The atoms are arranged in a regular repeating pattern (the diamond lattice) that is unique among gems. However, atoms of elements such as nitrogen (N) and boron can replace some of the carbon atoms in the lattice. While other impurities can also be incorporated, the diamond type classification system divides diamonds into categories based solely on the presence or absence of certain nitrogen and boron impurities and the ways in which they are arranged in the lattice (figure 4-3). The foundation of the type classification system is the presence or absence of nitrogen, the most common impurity in diamond.

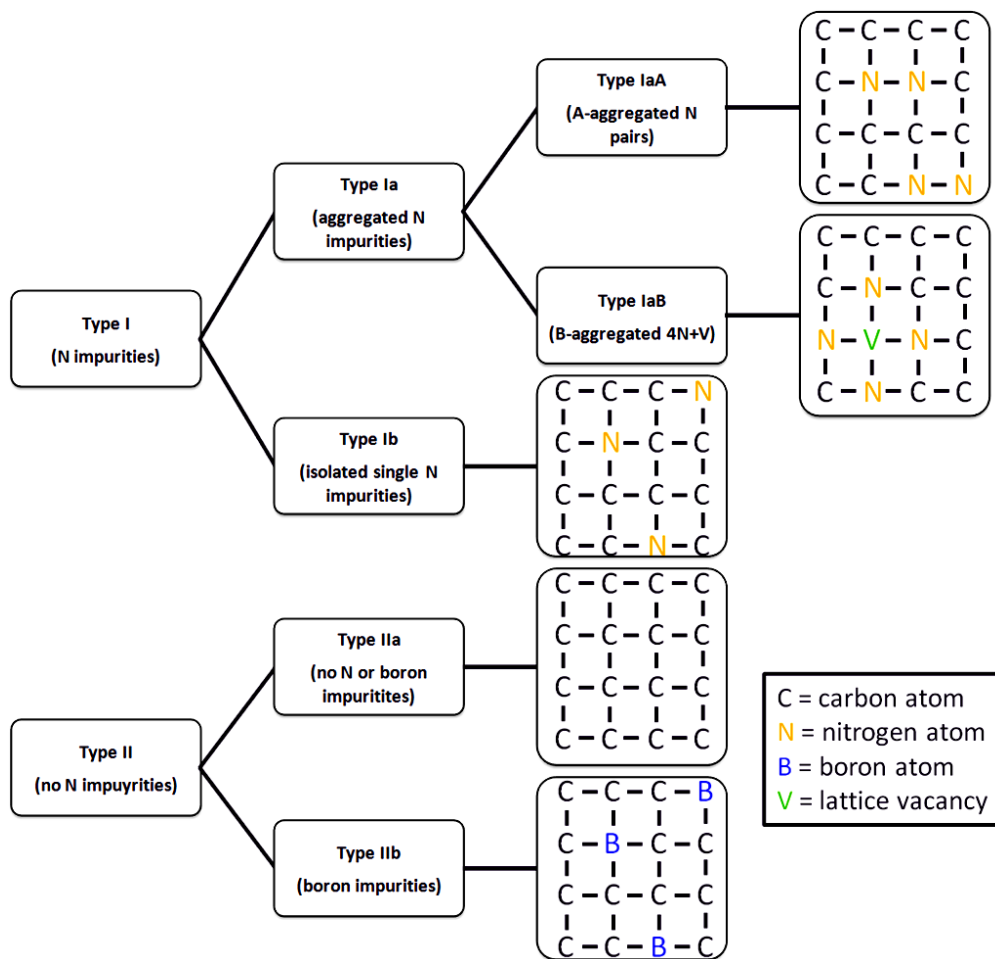


Figure 4-3 : Diamond type classification based on impurities. From (Breeding & Shigley, 2009)

Type I diamonds are defined as containing sufficient N to be measurable by IR absorption spectroscopy (typ. N > 5 ppm), whereas type II diamonds do not contain enough N to be detected by the IR spectrometer (typ. N < 5 ppm). These general categories are then subdivided based on the nature of the impurities that are present.

As noted above, type I diamonds are divided into type Ia and type Ib. Both subgroups contain nitrogen, but the nitrogen atoms in each are arranged differently (figure 4-3). In type Ib diamonds, single nitrogen atoms that have replaced carbon atoms in the lattice are isolated from one another; that is, they generally do not occur in adjacent lattice positions. These N impurities are called by several names in the scientific literature, including isolated N, single substitution N, and C centers. Ib-type diamonds are *n*-type, even if the ionization energy of nitrogen is around 1.7 eV. This induces therefore a thin interfacial depletion layer when p-type diamond is overgrown. In the case of delta-structure the buffer layer simply needs to be thicker than this depletion layer.

In contrast, type Ia diamonds contain N atoms that are in close proximity to one another in one of two spectroscopically detectable configurations. The most common configuration for type Ia diamonds involves two N atoms adjacent to each other in the lattice. Although these two atoms occupy neighboring sites, each pair is isolated from other N atoms in the lattice. These N impurities are commonly referred to as A aggregates (or A centers), and the diamonds that contain them are termed type IaA. The other configuration involves four N atoms that symmetrically surround a vacancy. (A vacancy is a lattice site normally occupied by a carbon atom that is not occupied by any atom.) This complex grouping is formed when two A centers combine. These N impurity groupings are called B aggregates (or B centers), and the associated diamonds are type IaB. Other arrangements of N atoms do occur, but they are not included in the diamond type classification system (Collins, 1982), (Collins, 2001).

Type IIa diamonds do not contain any easily measurable N or boron impurities (typ. N < 5ppm). Natural type IIb diamonds likewise are free of IR-measurable N impurities. Instead, type IIb diamonds contains boron impurities that are thought to be isolated single atoms that substitute for carbon in the diamond lattice. Characteristic properties of type IIb diamonds, such as p-type electrical conductivity, are a direct result of the presence of boron impurities.

IV. GROWTH SECTORS IN HPHT

IV.1. Definition

The single crystalline growth starts from a seed. This growth occurs in the three space dimensions at the same time from surfaces with different crystalline orientations. The growth rate depend of the crystalline direction, some faces ($\{100\}$, $\{110\}$, $\{111\}$ and $\{113\}$) are more stable than others. Once the growth stopped, the crystal “boule” is cut in slices. On the figure 4-4, diamond slices are oriented along $[001]$, and they are composed of different growth areas from the center, called “growth sectors”. The label assigned to growth sectors is composed of a double Miller index* type $[HKL]_{(hkl)}$, where $[HKL]$ is the crystal plane considered (orientation of the cut) and (hkl) indicates the planes of the reciprocal space corresponding to the growth direction of that particular sector. For a given orientation of the slices, this label is often simplified to the (hkl) -only notation. Such shortcuts should be handled with care...

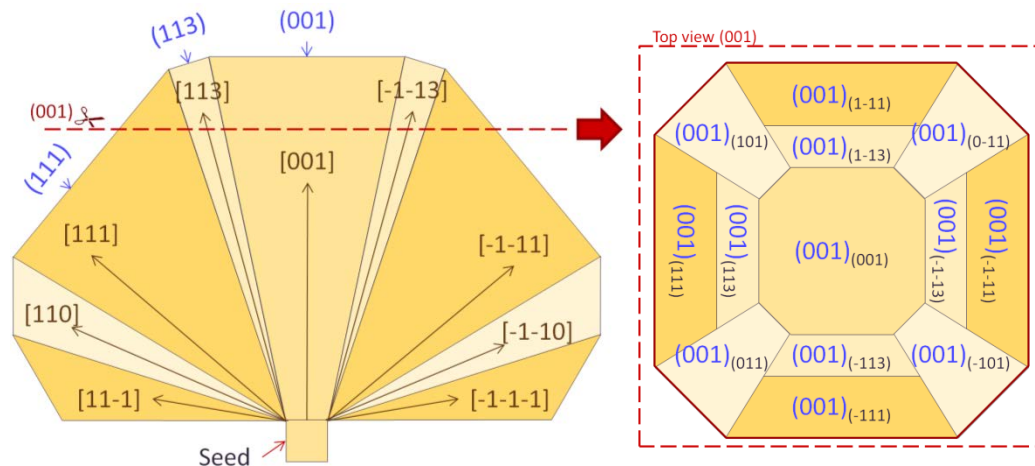


Figure 4-4 : (Left) Crystalline growth from a seed in labeled directions. The vertical axis correspond to $[001]$ direction. The crystal is cut in the horizontal plane (001) . (Right) Top view (001) of the diamond slice. Double Miller index are use to label the origin of the growth sector.

During growth, impurities do not have the same ability to incorporate into diamond according to the growth direction. This is usually visible by eye: growth sectors show a color variation as reproduced on figure 4-4. It has been establish by Burns and co-workers, that the sector dependence on nitrogen concentration $[N]$ is in the followed order: $[N]_{\{111\}} > [N]_{\{100\}} > [N]_{\{110\}} \approx [N]_{\{113\}}$ (Burns, et al., 1990).

* The notation $\{hkl\}$ denotes the set of all planes that are equivalent to (hkl) by the symmetry of the lattice. $[hkl]$ denotes a direction in the basis of the direct lattice vectors instead of the reciprocal lattice; and similarly, the notation $\{hkl\}$ denotes the set of all directions that are equivalent to $[hkl]$ by symmetry.

IV.2. Polishing steps induced by growth sectors

The difference in impurity concentration modifies diamond properties from a growth sector to another. For example the surface reveals the presence of nanometric steps at growth sector boundaries (figure 4-5). A relationship between impurity concentration and hardness exists, as well as a relationship with thermal dilatation, and could explain these steps.

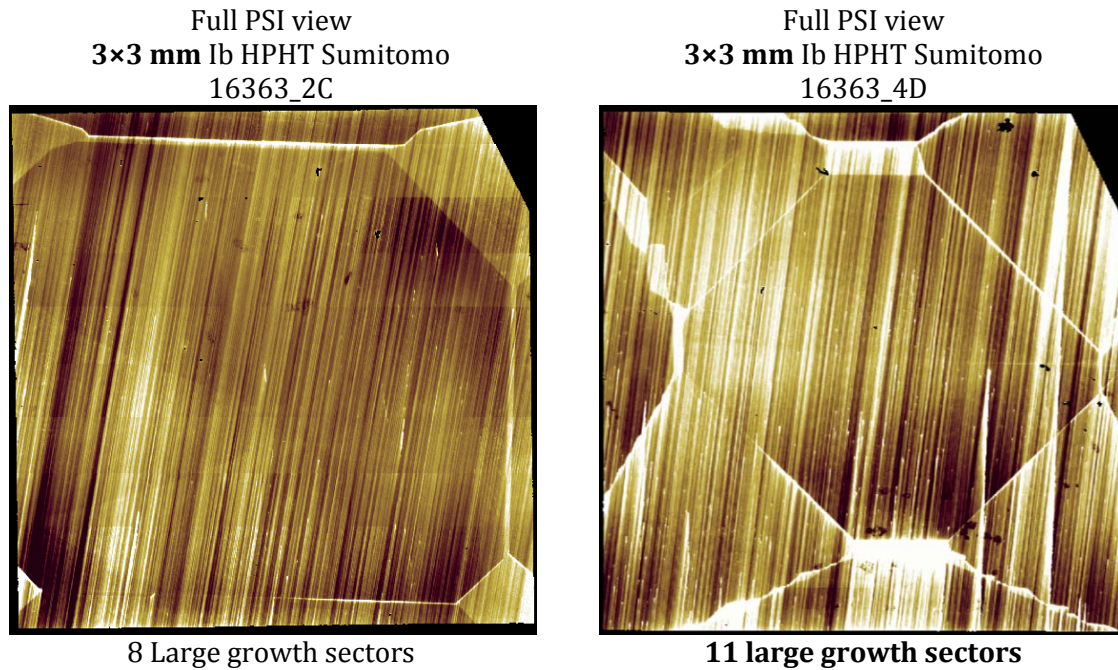


Figure 4-5 : Height difference on HPHT substrates highlighted by PSI optical profile view.

These steps were used to compare the growth rate dependence on growth sectors in the case of lateral growth, as studied in Chapter 5. IV.4.

IV.3. Impurity distribution in growth sectors

A wide variety of color centers and luminescence lines have been reported for diamond, caused by defects such as impurities, and related to its growth mechanisms. The color and luminescence are not uniform inside a crystal; they vary with growth sectors and along growth directions (Kanda, 2007). Luminescence patterns related to strain are also observed in diamond. On type I HPHT diamond, the (100) growth sector provide the highest green fluorescence by short UV light exposure (245 nm). It has been long known that type II natural diamond exhibit a mosaic patterning in CL images that is produced by strain (Sumida & Lang, 1981). A few monochromatic CL mapping examples are shown on figure 4-6. Images are taken from FE, BE, Band A and TH5 center in the present case. Depending on the wavelength, the signal intensity varies with growth sectors. By comparison to height topography revealed by optical profile, conclusions on the growth sectors names and distribution are drawn. Other maps could be established from H3 or N-V centers emission...

GROWTH SECTORS IN HPHT

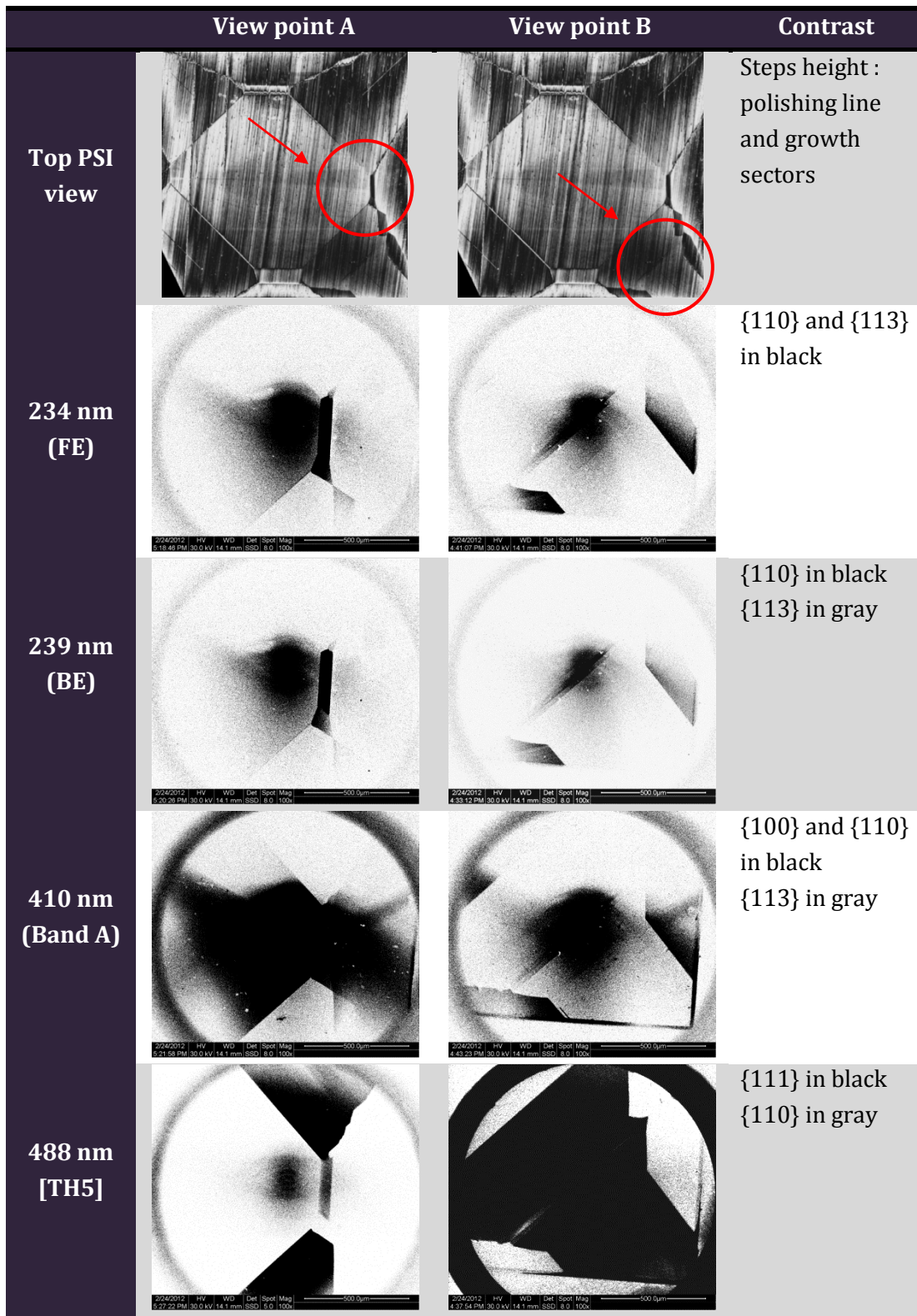


Figure 4-6 : Monochromatic CL mapping on the substrate 16363_4D. Contrast is reversed, and the central part of the field of observation is more luminous.

V. VOLUME IMPERFECTIONS IN TYPE I AND II DIAMOND

Crystal bulk and surface should be of high quality – defect free (in principle) when used as a substrate for epitaxial overgrowth. Dislocations in the bulk, threading to the surface continue to grow in an epitaxial layer (figure 4-8). Dislocations only start at an interface if a lattice mismatch, strain centers or defects are present. Imperfections in Bragg diffracting X-ray optical elements make diffracted beam inhomogeneous and reduce coherence.

Basic classes of crystal defects:

- Point defects – 0D, lattice vacancies, self-interstitial atoms, substitution impurity atoms, interstitial impurity atoms, antisites (in binary alloys);
- Linear defects – 1D, dislocations; bundles of linear defects may also occur;
- Planar defects – 2D, grain boundaries, stacking faults, external surfaces;
- Volume defects - 3D, precipitates, inclusions.

White beam X-ray topography (X-topo) reveals the presence of defects. Because it is based on diffraction processes, the information about defects depends of the crystal orientation. This is the same with the polarized light. Clearly visible in the case of IIa diamond, the position of contrasted lines appearing on POL views correspond with some black lines on X-topo, related to dislocation. However staking fault has no visible effects on the POL view in the image. I-type diamond is full of defects, X-topo is dark, but the POL view not.

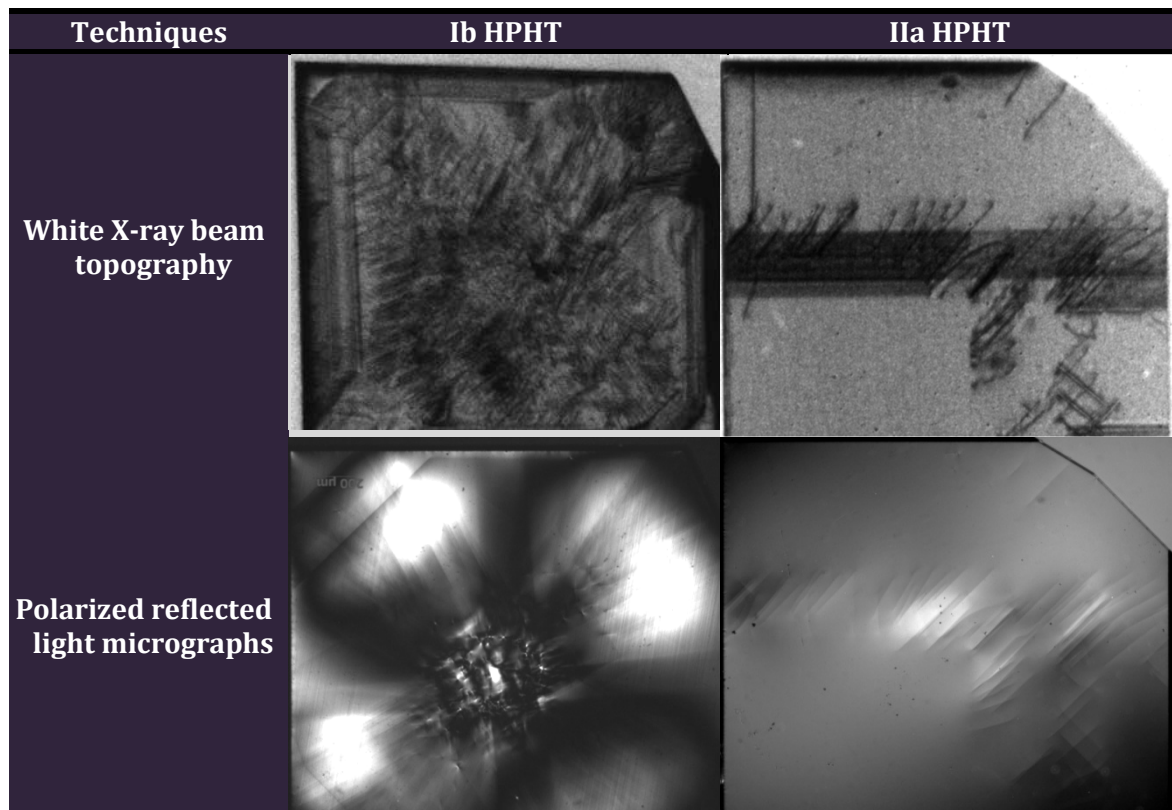
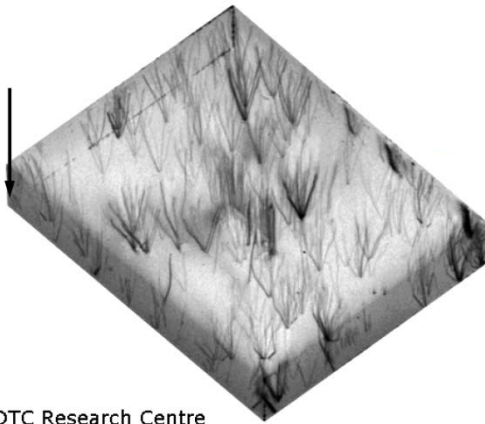


Figure 4-7 : Comparison of volume imperfection on HPHT Ib and IIa diamond sample by X-ray Topo. and by Pol. techniques.

On POL view, CVD substrate are most of the time covered of small bright dots. No wide homogenous areas in contrasts are visible. This could be coming from the nature of 1D defects (dislocation) with is opposite to the strain pattern (2D defects) observed in HPHT. The figure 4-8 shows a beautiful 3D picture of a CVD layer with dislocations starting points and bundles. Extended 2D defects are not seen.



DTC Research Centre

Figure 4-8 : (001)-oriented IIa CVD layers (with substrates removed), data from Mike Gaukroger and Philip Martineau (DTC Research Centre, Maidenhead, UK) (Härtwig, 2009).

VI. SURFACE IMPERFECTION ON TYPE I AND II DIAMOND

VI.1. Surface polishing

Ideas about polishing mechanisms have their historic origin in lens manufacture. The generally accepted classical mechanism of polishing was thought to be predominantly an abrasive process, and hence that it should be a function of the size of the polishing particle. Beilby (1921), however, showed that the polished layer had a different structure from the underlying bulk material, having lower crystallinity and showing signs of surface flow (polishing lines). In ‘hard’ directions, there is conclusive evidence from both EELS and SPM studies that wear proceeds predominantly via micro-fracture. For ‘soft’ direction polishing, it appears that a structural transformation is responsible for material removal. Van Bouwelen has proposed a model to structural transformation at the scaife–diamond interface. He argues that it becomes energetically more favourable for the diamond bonding to re-hybridise into an sp^2 configuration, if the crystal structure is deformed sufficiently through shear. The softer material is then removed by the next grit particle and the process repeats itself. The model is very effective at explaining the anisotropy of wear, since the elastic moduli and Poisson ratios of diamond are highly anisotropic (Field, 1992). The wear mechanisms governing traditional diamond polishing are complex. Despite more than 80 years of scientific study, this process is still not fully understood (Hird & Field, 2004). As received diamond substrates show polishing lines remaining from scaife polishing. However, some companies in the world proposed to re-polish the diamond (ultimate polishing) and they can provide perfection flatness (see table 4-2).

Scaife polishing induces subsurface hardening. This subsurface is known to be responsible of the defects inside the epilayer. Smooth removal techniques of this subsurface hardening were developed as ion-milling, ion-implantation / annealing / hydrogen treatment (Mer-Calfati, et al., 2009), (Tran Thi, et al., 2011), and oxygen plasma (Volpe, et al., 2008).

VI.2. ISO 25178-2: Geometric Product Specifications (GPS) – Surface texture parameters

The Roughness Average is defined as: $Sa = \frac{1}{MN} \sum_{k=0}^{M-1} \sum_{l=0}^{N-1} |z(x_k, y_k)|$.

The Root Mean Square (RMS) is defined as: $Sq = \sqrt{\frac{1}{MN} \sum_{k=0}^{M-1} \sum_{l=0}^{N-1} |z(x_k, y_k)|^2}$.

The Surface Skewness describes the asymmetry of the height distribution histogram, and is defined as: $Ssk = \frac{1}{MN Sq^3} \sum_{k=0}^{M-1} \sum_{l=0}^{N-1} |z(x_k, y_k)|^3$. A symmetric height distribution is indicated by $Ssk = 0$. $Ssk < 0$ indicates a bearing surface with holes and $Ssk > 0$ a flat surface with peaks. Ssk values greater than 1.0 may indicate extreme holes or peaks on the surface.

The Surface Kurtosis, Sku , describes the “peakedness” of the surface topography, and is defined as: $Sku = \frac{1}{MN Sq^4} \sum_{k=0}^{M-1} \sum_{l=0}^{N-1} |z(x_k, y_k)|^4$. For Gaussian height distributions Sku approaches 3. Smaller values indicate broader height distributions and vice-versa for values greater than 3.

The Peak-Peak Height, Sz , is defined as the height difference between the highest and lowest pixel in the image.

VI.3. Comparison CVD / HPHT substrates

“As received CVD” substrates have a nice average roughness but always show a large density of holes, confirmed by negative Ssk and high Sku values. “As received” HPHT substrates yield a small Ssk value and a Sku approaching 3, characterizing the waviness and the regularity of polishing lines. The roughness has to be evaluated along straight lines perpendicular to polishing lines.

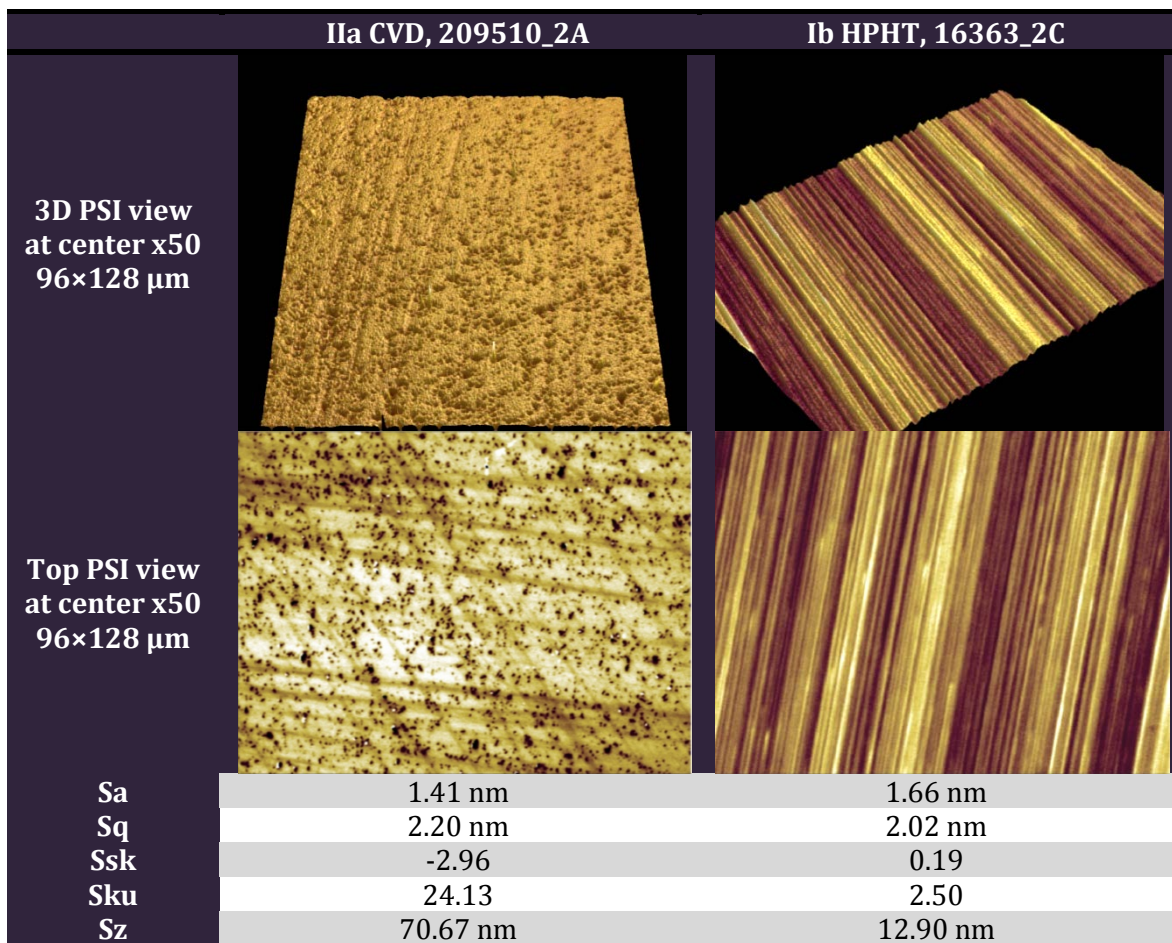


Table 4-1 : Comparison of surface morphology on CVD and HPHT "as received" substrates

VI.4. Ultimate polishing

The surface of a single crystal diamond has millions of polishing flaws (scaife polishing) which can have a huge impact on epitaxy. Some companies, like Syntek Co., Ltd.* in Japan, have excellent technology and skills to reduce surface defects by polishing method, on (100) and on (111)-orientations. As reported in table 4-2, they provide a superfine surface quality five times better than diamond providers. Re-polishing can be made on top, on bottom surfaces and on lateral sides too.

	Ila CVD, Element 6	Ib HPHT, Sumitomo	Ib superfine, Syntek
Sa	1.4 nm	1.5 nm	0.33 nm
Sq	2.2 nm	2 nm	0.44 nm
Ssk	-2.96	0.19	0.15
Sku	24.13	2.50	2.98

Table 4-2 : Statistics on diamond substrate surface roughness.

* <http://www.syntek.co.jp>

VII. DEFINITION OF SURFACE DEFECTS

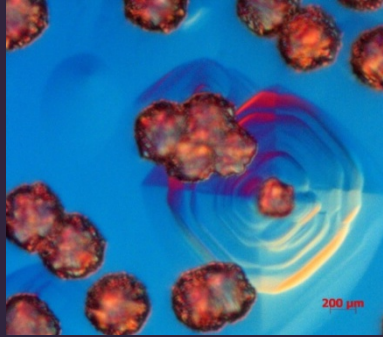



	<p>Unepitaxial crystallite (UC)</p> <p>These defects are sometimes found isolated at the top of pyramidal hillocks and most of the time randomly oriented at the diamond surface, usually embedded in the CVD layer as reported by (Tallaire, et al., 2008).</p>
	<p>Pyramidal Hillocks (PH)</p> <p>The PH consists of four-fold symmetry defects with (111) lateral facets, quadrilateral basis and sometimes can be topped with a diamond crystallite or UC.</p>
	<p>Flat-topped Hillocks (FH)</p> <p>The FH consist of a flat (100) quadrilateral facet (square facet under low miscut, as see on the picture) surrounded by four (111) truncated lateral facets.</p>
	<p>Round hillocks (RH)</p> <p>They are usually difficult to observe by optical microscope because of their size ten times smaller than PH or FH. They can be mistaken for etch-pits. Contrary to FH and PH, the base is elliptical (circular when the miscut is small). Oblique circular cones were found on misoriented substrates</p>

Table 4-3 : Definition of main defects found at the surface observed by C-DIC microscopy.

As listed in table 4-3, under our experimental conditions, four types of growth defects were clearly identified: unepitaxial crystals (UCs), pyramidal hillocks (PHs), flat hillocks (FHs) and round hillocks (RHs). The predominant defects in the growth conditions are PHs.

Round hillocks are difficult to observe because of their small size. On figure 4-9, the statistics about CHs don't show any relationship between their diameter and height, but they appear mostly on HPHT substrates; especially on starting points of polishing lines. RHs heights are around ten times smaller than PHs. To explain how these extended defects could generate both PHs and FHs at the CVD layer's surface, (Tallaire, et al., 2008) carried out some investigations. It was concluded that flat and pyramidal hillocks had a similar origin in an extended crystallographic defect: a bunch of dislocations formed at the interface between the substrate and the layer. These dislocations, created at dark inclusions containing impurities, were found to be of the 60° glide type. It is proposed here that such a dislocation acts as a growth centre from which the deposition rate is locally enhanced. As a consequence, (111) micro-facets will be formed and, in particular growth conditions (as lateral growth with low methane concentration and oxygen), will develop into a flat hillock. If twinning occurs either directly or indirectly at this outcropping defect, which can obviously happen more easily than on a perfect diamond surface, then a typical twinned crystal will be formed in the centre of the hillock. The steps generated from that twin will rapidly flow to the sides of the hillock thus turning it into a pyramidal hillock.

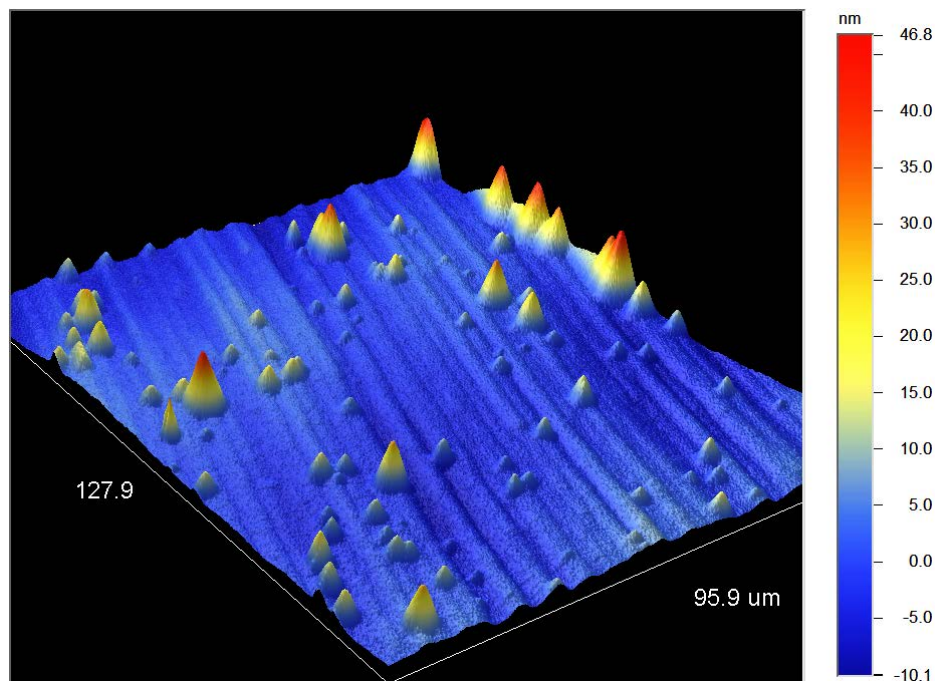


Figure 4-9 : Round hillocks at p-- surface epitaxy on p++ layer observed by optical profile in PSI mode.

It has been widely reported that the control and inhibition of the growth defects in CVD epitaxial growth requires efficient suppression of the dislocations in the material (Ri, et al., 2002), (Teraji & Ito, 2004), (Tallaire, et al., 2008). These dislocations are created in the first instants of growth, and impurities at the surface seem to play an important role in their formation.

VIII. CONCLUSION

Three types of diamond substrates were used in the study (CVD, HPHT, re-polished). The surface roughness, which depends of the polishing and the elaboration technique of these substrates, was main difference.

The origin of roughness was briefly study and techniques (optical profile, polarized light optical microscopy, X-ray topography) were used in parallel, in order to classified substrates in term of surface, sub-surface and bulk quality (dislocations, growth sectors, polishing lines...).

Defects free areas inside flat surface substrates were systematically searched in order to perfumed some devices (hall bars and transistors).

IX. RÉSUMÉ DU CHAPITRE 4

En minéralogie, le diamant (du grec Ἀδάμας, «incassable») est une forme allotropique du carbone, où les atomes de carbone sont disposés dans une variante de la structure cristalline, dite cubique à faces centrées, appelée un réseau de diamant (avec un seul paramètre de maille 3,56683 Å). A pression et à température standard, le diamant est moins stable que le graphite, mais la conversion du diamant en graphite est un mécanisme très long à l'échelle humaine. Le diamant est reconnu comme un matériau plein de superlatifs en ce qui concerne ses qualités physiques, dont l'origine provient de la forte liaison covalente entre les atomes de carbone. En particulier, il possède la dureté et la conductivité thermique la plus élevée des matériaux. Ces propriétés expliquent son application industrielle majeure dans la coupe et dans le polissage.

Les diamants synthétiques sont des diamants produits par un procédé technique; par opposition aux diamants naturels, qui sont créés par des processus géologiques. Il existe plusieurs méthodes pour produire des diamants synthétiques. La méthode traditionnelle allie la haute pression et la haute température (HPHT) pour reproduire les phénomènes géologiques et est encore largement utilisée en raison de son coût de production relativement faible. On utilise de grosses presses qui peuvent peser plusieurs centaines de tonnes pour produire une pression de 5 GPa et le tout chauffé à 1500 ° C.

La croissance monocristalline du diamant commence à partir d'un germe de diamant. Cette croissance survient dans les trois dimensions de l'espace à la fois, sur des surfaces d'orientations cristallines différentes. Or, la vitesse de croissance dépend de la direction cristalline. Les faces ($\{100\}$, $\{110\}$, $\{111\}$ et $\{113\}$) sont plus stables que d'autres. Une fois que la croissance s'arrête, le cristal forme une "boule" qui est coupée en tranches. Cependant, lors de la croissance, les impuretés n'ont pas la même capacité à intégrer de diamant en fonction de la direction de croissance. Cela est généralement visible à l'œil: on observe des secteurs de croissance qui montrent une variation de couleur visible sur la figure 4-4. Il a été d'établi par Burns et ses collègues, que la dépendance du secteur sur la concentration d'azote [N] est dans l'ordre suivant : $[N]_{\{111\}} > [N]_{\{100\}} > [N]_{\{110\}} \approx [N]_{\{113\}}$ (Burns et al., 1990).

La différence de concentration en impuretés modifie les propriétés du diamant d'un secteur de croissance à un autre. Par exemple, la surface polie révèle la présence de marches de tailles nanométrique aux limites des secteurs de croissance (figure 4-5). Une relation entre la concentration en impuretés et la dureté existe, ainsi que d'une relation avec la dilatation thermique, et peut expliquer ces marches après polissage. Ces mesures ont été utilisées pour comparer la dépendance en vitesse de croissance des secteurs dans le cas d'une croissance latérale, comme étudié dans le chapitre 5. IV.4.

Une autre méthode, utilisant les réactions chimiques en phase vapeur (CVD), nécessite un plasma d'espèces carbonées et un substrat sur lequel le dépôt des atomes de carbone forme couche après couche du diamant. D'autres méthodes plus exotiques existent, comme la détonation (formant des nanodiamants) et la sonication de solutions de graphite (Werner & Locher, 1998), (Osawa, 2007), (Galimov, et al., 2003).

Le premier rapport documenté de croissance du diamant à basse pression a été publié en 1954 par Bundy et ses collaborateurs (Bundy et al., 1955). Ils ont mené une vaste gamme d'expériences sophistiquées basées sur les réactions suivantes: (1) $2 \times \text{CO} = \text{C}_{\text{diamant}} + \text{CO}_2$, et (2) $2 \times \text{CO} = \text{C}_{\text{graphite}} + \text{CO}_2$, qui sont thermodynamiquement possibles grâce à la forme négative d'énergie libre de Gibbs. Dans ces expériences, le diamant et le graphite furent utilisés comme germes. Les expériences ont été réalisées à des températures allant de 820 à 1000°C et des pressions de 5×10^6 à 31×10^6 Pa. On a constaté que le rapport CO/CO₂ mesuré sur diamant (réaction (1)) était différent de celle du graphite (réaction (2)), ce qui était attendu par la thermodynamique, comme l'équilibre est différent pour C_{diamant} et C_{graphite}. En outre, ils ont constaté que l'équilibre et la précipitation de diamant sur un germe de diamant était métastable. Le graphite n'a pas été détecté, bien que dans ces conditions de travail (température et pression) le graphite soit la forme thermodynamiquement stable.

En 1956, Spitsyn et Deryagin proposèrent en ex-URSS la croissance du diamant à basse pression au travers de la décomposition thermique du tétrachlorure/trétraiodure de carbone (Spitsyn & Deryagin, 1980) à des températures allant de 800 à 1000°C et pour des pressions de l'ordre de 4×10^{-4} Pa. Le groupe soviétique a exploré par la suite la CVD à partir d'hydrocarbures, et en 1969, on rapporte que le diamant a été synthétisé, avec un taux de croissance plus élevé à partir du méthane, à des pressions allant de 13 à 40 Pa et sous une température de 950 à 1050 °C.

Une percée majeure sur le processus de diamant CVD a été atteinte dans les années 1970. C'est l'utilisation de l'hydrogène atomique pendant la croissance qui permet de supprimer les co-dépôts graphite, sur la base du fait que l'hydrogène atomique grave le graphite beaucoup plus vite qu'il ne le fait avec le diamant. Cela a donné un taux de croissance beaucoup plus élevé. D'égale importance, cela a permis la nucléation des cristallites de diamant sur de nouveaux substrats autres que le diamant. L'utilisation de l'hydrogène atomique a été étudié indépendamment par J. Angus aux Etats-Unis et par V. Varnin en URSS (Prelas, et al., 1997).

L'ère moderne du diamant CVD a commencé dans les années 1980. Un groupe japonais, travaillant à l'Institut National de Recherche en Matériaux Inorganiques (NIRIM), a d'abord publié une remarquable série d'articles dans lesquels différentes techniques, procédé CVD à filament chaud, CVD assisté par plasma RF et par micro-ondes, furent ainsi décrits (Matsumoto et al., 1982), (Kamo et al., 1983), (Matsui et al., 1983). Ils ont indiqué que des particules de diamant et des films peuvent être déposés sur divers types de substrat chauffés autour de 850°C, en utilisant un mélange gazeux de méthane dilué dans l'hydrogène, et de préférence à des pressions partielles dans la gamme de 10 à 100 Torr. Un taux de croissance supérieur à quelques micromètres par heure a été atteint. Ces résultats

ont été rapidement confirmés par plusieurs groupes de recherche aux Etats-Unis et en Europe (Angus, 1994), (Spitsyn & Deryagin, 1980), (Prelas, et al., 1997). Le succès du groupe NIRIM a immédiatement engendré la création de nombreux programmes de recherche dans le monde entier. Ces programmes comprennent des recherches sur les techniques de traitement, la compréhension du mécanisme de croissance et la nucléation par CDV, le dopage, les propriétés optiques, électroniques, thermiques, mécaniques, et le revêtement de diamant sur différents substrats pour des applications spécifiques.

Les diamants sont classés en différentes catégories. Les diamants de type I sont définis comme contenant suffisamment d'atomes d'azote pour pouvoir les mesurer par spectroscopie d'absorption IR (typ. $N > 5$ ppm), tandis que les diamants de type II ne contiennent pas assez d'azote pour les détecter par le spectromètre infrarouge (typ. $N < 5$ ppm). Ces catégories sont ensuite subdivisées sur la base de la nature des impuretés qui sont présentes. Ainsi, les diamants de type I sont divisés en type Ia et Ib. Les deux sous-groupes contiennent de l'azote, mais les atomes d'azote y sont agencés différemment (figure 4-3). Dans le type Ib diamants, des atomes d'azote qui ont remplacé les atomes de carbone dans le réseau sont isolés les uns des autres. Ces impuretés N sont appelées par plusieurs noms dans la littérature scientifique. Les diamants de type Ib sont dopés du type n, même si l'énergie d'ionisation de l'azote est d'environ 1,7 eV. Ceci induit donc une couche mince de déplétion lorsque diamant de type p est épitaxié. Dans le cas de structure delta, la couche tampon a simplement besoin d'être plus épaisse que cette couche de déplétion. En revanche, les diamants de type Ia contiennent des atomes d'azote qui sont à proximité immédiate les uns des autres suivant deux configurations spectroscopiquement détectable. La configuration la plus courante pour les diamants de type Ia comporte deux atomes d'azote adjacents dans le réseau. Bien que ces deux atomes occupent des sites voisins, chaque paire est isolée des autres atomes d'azote dans le réseau. Ces impuretés sont communément appelées agrégats A (ou centres A), et les diamants qui contiennent eux sont nommés type IaA. L'autre configuration comporte quatre atomes d'azote qui entourent symétriquement une lacune de carbone. Ce regroupement complexe est formé lorsque deux centres A se combinent. Ces groupements sont appelés agrégats B (ou centres B), et les diamants sont associés type IaB. D'autres arrangements d'atomes d'azote se produisent, mais ils ne sont pas inclus dans le système de classification de type diamant (Collins, 1982), (Collins, 2001). Les diamants de type IIa ne contiennent pas d'azote facilement mesurables ou impuretés de bore (typ. $N < 5$ ppm). En revanche, les diamants naturels de type IIb contiennent des impuretés de bore qui sont isolés en substitution du carbone dans le réseau du diamant. Les propriétés caractéristiques des diamants de type IIb, tels que la conductivité électrique de type p, sont une conséquence directe de la présence d'impuretés de bore.

Pour faire croître du diamant, le substrat et sa surface doivent être de haute qualité - exempts de défauts. En principe, les dislocations dans le substrat, se propagent à la surface et continuent à se développer dans une couche épitaxiale (figure 4-8). Les dislocations

peuvent s'amorcer à une interface si un désaccord de maille, des centres de contrainte ou des défauts sont présents.

Parmi les défauts cristallins, on trouve dans le diamant:

- Les défauts ponctuels - 0D lacunes du réseau, les atomes auto-interstitiels, l'impureté de substitution, les impuretés interstitielles;
- Les défauts linéaires - 1D, luxations; liasses de défauts linéaires peuvent également se produire;
- Les défauts plans - 2D, joints de grains, fautes d'empilement, les surfaces externes;
- Les défauts de volume - 3D, les précipités, les inclusions.

Un faisceau blanc de rayons X permet par topographie (topo-X) de révéler la présence des défauts. Comme cette analyse est fondée sur des processus de diffraction, les informations sur les défauts dépendent de l'orientation du cristal. Il en est de même avec la lumière polarisée. Dans le cas de diamant de type II, la position des lignes contrastées qui apparaissent sur les vues en mode POL correspondent à des lignes noires sur les topo-X, liées aux dislocations. Cependant les fautes d'empilement n'ont pas d'effets visibles sur la vue POL. Les diamants de type I sont pleins de défauts, les images de topo-X sont sombres, mais pas la vue en mode POL.

Les idées sur les mécanismes de polissage ont leur origine historique dans la fabrication de lentilles. Le mécanisme de polissage classique généralement accepté a été pensé pour être principalement un processus abrasif, et donc que l'état de surface devrait être fonction de la taille des particules de polissage. Cependant, Beilby (1921) a montré que la couche polie avait une structure différente de la matière sous-jacente, ayant un taux plus faible de cristallinité et montrant des signes d'écoulement en surface (les lignes de polissage). Dans les axes dit «durs», il obtient une preuve concluante par EELS et par SPM sur l'abrasion produite principalement par le biais de micro-fracture. Pour le polissage dans les axes «mous», il semble que la transformation structurelle soit responsable de l'enlèvement de matière. Van Bouwelen a proposé un modèle pour la transformation structurelle à l'interface du plateau de polissage et du diamant. Il démontre qu'il devient énergétiquement plus favorable pour le diamant de se ré-hybridiser dans une configuration sp^2 , lorsque la structure cristalline est suffisamment déformée par cisaillement. Le matériau plus souple est ensuite éliminé par le grain de particule suivant et le processus se répète. Le modèle est très efficace pour expliquer l'anisotropie de l'abrasion, puisque les modules d'élasticité et les coefficients de Poisson du diamant sont fortement anisotropes (Field, 1992). Les mécanismes d'écrouissages issus du polissage traditionnel du diamant sont bien complexes. Malgré plus de 80 années d'études scientifiques, ce processus n'est pas encore été pleinement compris (Hird & Field, 2004). Les substrats de diamant «brut d'usine» montrent des lignes résiduelles de polissage du plateau de polissage utilisé. Toutefois, certaines sociétés dans le monde proposent de re-polir le diamant (polissage final) et ils peuvent fournir la planéité parfaite (voir le tableau 4 2). Le polissage induit un écrouissage de la sous-surface. Cette région est connue pour être responsable des défauts à l'intérieur de

la couche épitaxiale. Plusieurs techniques d'élimination de cette sous-surface ont été développées comme les plasmas de gravures, l'implantation ionique / recuit / plasma d'hydrogène (Mer-Calfati, et al., 2009), (Tran Thi, et al., 2011), et plasma d'oxygène (Volpe , et al., 2008).

Les substrats CVD « brut d'usine » ont une rugosité moyenne assez faible mais possèdent toujours une grande densité de trous, confirmé par des valeurs de Ssk négatifs et des Sku élevées. Les substrats HPHT « brut d'usine » ont une petite valeur de Ssk et un Sku approchant 3, caractéristique de l'ondulation et de la régularité des lignes de polissage. Sur ces substrats, la rugosité doit être évaluée selon des droites perpendiculaires aux lignes de polissage. La surface d'un diamant monocristallin a des millions de défauts de polissage qui peuvent avoir un impact énorme sur l'épitaxie. Certaines entreprises, comme Syntek Co., Ltd au Japon, ont une excellente technologie et les compétences nécessaires pour réduire les défauts de surface par un procédé de polissage. Comme il est indiqué dans le tableau 4-2, ils offrent une qualité de surface superfine, cinq fois meilleure que les fournisseurs de diamants.

Comme indiqué dans le tableau 4-3, dans nos conditions expérimentales, quatre types de défauts de croissance ont été clairement identifiés: les cristaux non-épitaxiés (UC), des défauts pyramidaux (PH), des pyramides tronquées (FH) et des défauts arrondis (RH). Les défauts prédominants dans les conditions de croissance sont les PHs. Les défauts arrondis sont difficiles à observer en raison de leur petite taille. Sur la figure 4-9, les statistiques sur les CHs ne montrent aucune relation entre leur diamètre et leur hauteur, mais ils apparaissent surtout sur des substrats HPHT en particulier sur des points de départ des lignes de polissage. La hauteur des RHs est environ dix fois plus petite que celle des PHs. Tallaire a réalisé quelques enquêtes pour expliquer comment les défauts étendus pourrait générer des PHs et FHs à la surface des reprises d'épitaxies (Tallaire, et al., 2008). Il a conclu qu'ils ont une origine semblable à un défaut cristallographique élargie: un bouquet de dislocations formées à l'interface entre le substrat et la couche. Ces dislocations se propagent avec un angle de 60° . Il est proposé ici qu'une telle dislocation agit comme un centre de croissance à partir duquel la vitesse de dépôt est localement augmentée. En conséquence, des micro-facettes (111) se forment, et, dans des conditions de croissance particulières (comme la croissance latérale avec une faible concentration de méthane et de l'oxygène), une pyramide tronquée se développe.

Chapter 5.
HEAVY AND LIGHT BORON
DOPING – LATERAL GROWTH

I. INTRODUCTION

This chapter is focused on the monocrystalline (100)-oriented boron-doped diamond layers homoepitaxy. The aim of this chapter is to present doping and thickness solutions for the realization of delta-doping. Targets lie in the homogeneity and constancy of heavily boron-doping (same doping level and same thickness on $3 \times 3 \text{mm}^2$ area), the very light boron doping overgrowth ($[\text{B}] < 1 \times 10^{15} \text{ at.cm}^{-3}$) and the low surface roughness.

First of all, the interaction between the sample and the plasma was investigated and understood in order to optimize the homogeneity of the growth for doping and thickness. After the determination of the most suitable contact position in the plasma, the next effort will bear on the doping efficiency at low methane concentration, in order to achieve heavily boron-doped slow growth. The last point will be the study of the lateral growth and the light boron-doping which are the key in the growth of a cap layer (i.e. the overgrowth of a delta-layer).

Names given to diamond layers depending of the doping level and the oxygen addition in the gas mixture are defined in table 5-1.

Type	Boron (diborane)	Oxygen	Doping level (at.cm ⁻³)
Intrinsic (i)	No flow and no residual	No	$[\text{B}] < 10^{14}$
O₂-intrinsic (o)	No flow and no residual	Yes	$[\text{B}] < 10^{14}$
p--	No flow and residual	Yes	$[\text{B}] < 10^{15}$
p-	Yes	Yes	$10^{15} < [\text{B}] < 10^{16}$
p	Yes	No	$10^{16} < [\text{B}] < 10^{18}$
p+	Yes	No	$10^{18} < [\text{B}] < 4.5 \times 10^{20}$
p++	Yes	No	$[\text{B}] > 4.5 \times 10^{20}$

Table 5-1 : Definition of layer's names. The name given to layers depends of the dopant concentration and the gas mixture used.

II. INFLUENCE OF THE SAMPLE POSITION IN THE PLASMA ON THE GROWTH

In our NIRIM-type cylindrical quartz tube reaction chamber, it is possible to adjust the position of the sample inside or at the border of the plasma ball region (see figure 5-1), providing a rare additional degree of freedom with respect to other MPCVD reactors. This mainly allows to finely tune the plasma/diamond sample surface physicochemical interactions. We will briefly discuss how the interaction between the plasma and the sample determines in particular both the homogeneity and level of doping.

II.1. Definition of plasma/sample contact modes

In order to rationalize our discussion of the geometry of diamond growth, three positions (figure 5-1) have been selected which correspond to dedicated process flows depending of the doping, the growth rate and area of the sample.

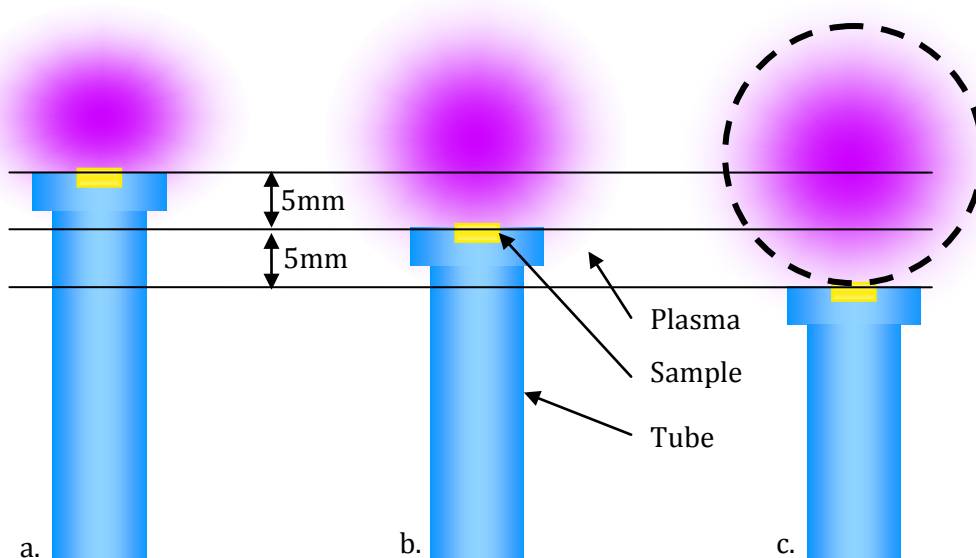


Figure 5-1 : Different positions of the sample in the plasma: (a) center contact, (b) surface contact, (c) point contact, i.e. the sample is located at the periphery of the plasma ball.

- At the position called “center contact” within the typical 20 mm diameter microwave-generated plasma ball, the top side of the sample is localized just below the central horizontal plane of the wave guide. This position is very close to the hottest part of the plasma, and it is located near the center of the plasma ball. In this configuration, the plasma simultaneously sticks on the sample, on the sample holder and on the top side of the electrically and thermally insulating quartz stage (top of the internal tube).
- The position called “surface contact” is located 5 mm below the previous “center contact” position. The top side of the sample is similarly in a complete interaction with the plasma ball, but the plasma ball is no longer in contact with the sample holder and the internal quartz tube.
- The “point contact” restricts the interaction with the plasma ball to a central area of the sample top side. This position is located 5 mm below the “surface contact” position, therefore at the very edge of the plasma region. A careful alignment of the surface sample center and the plasma ball center is required on the horizontal plan (X, Y) in order to ensure the best growth uniformity of the epitaxial layer.

II.2. Growth uniformity

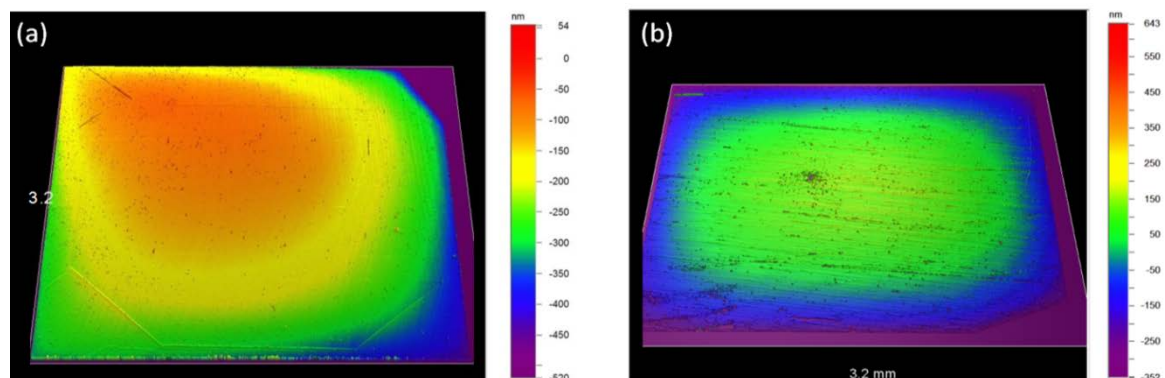


Figure 5-2 : PSI optical profile picture of 3x3mm Sumitomo sample after growth (a) in point- and (b) in surface contact modes ($\approx 1 \mu\text{m}$ thick).

The growth made in the “point contact” mode shows a tilted top surface when the “surface contact” mode leads to a thickness gradient of 50 nm surrounding the $3 \times 3 \text{ mm}^2$ diamond sample, figure 5-2(b). The alignment operation is more difficult in “point contact” mode, especially when the plasma ball is large. Most of the times, the growth made in “point contact” didn’t show any homogeneity of the thickness, as shown on figure 5-2(a). Note that, for the example chosen to illustrate “surface contact”, the alignment of the plasma above the sample surface was correct; the round surface is symmetric.

On the contrary, on the figure 5-3, it is possible to see the sample on its sample holder after a superlattice growth on the “surface contact” with an accidental misalignment of the

plasma ball; the center of the plasma was above one corner of the sample. The resulting top face showed a similar tilted surface as shown in figure 5-2(a). Nevertheless, this was the demonstration of the deposition homogeneity ($5 \times 5 \text{ mm}^2$) on “surface contact” mode; this contact mode was selected for the delta-layer growth.

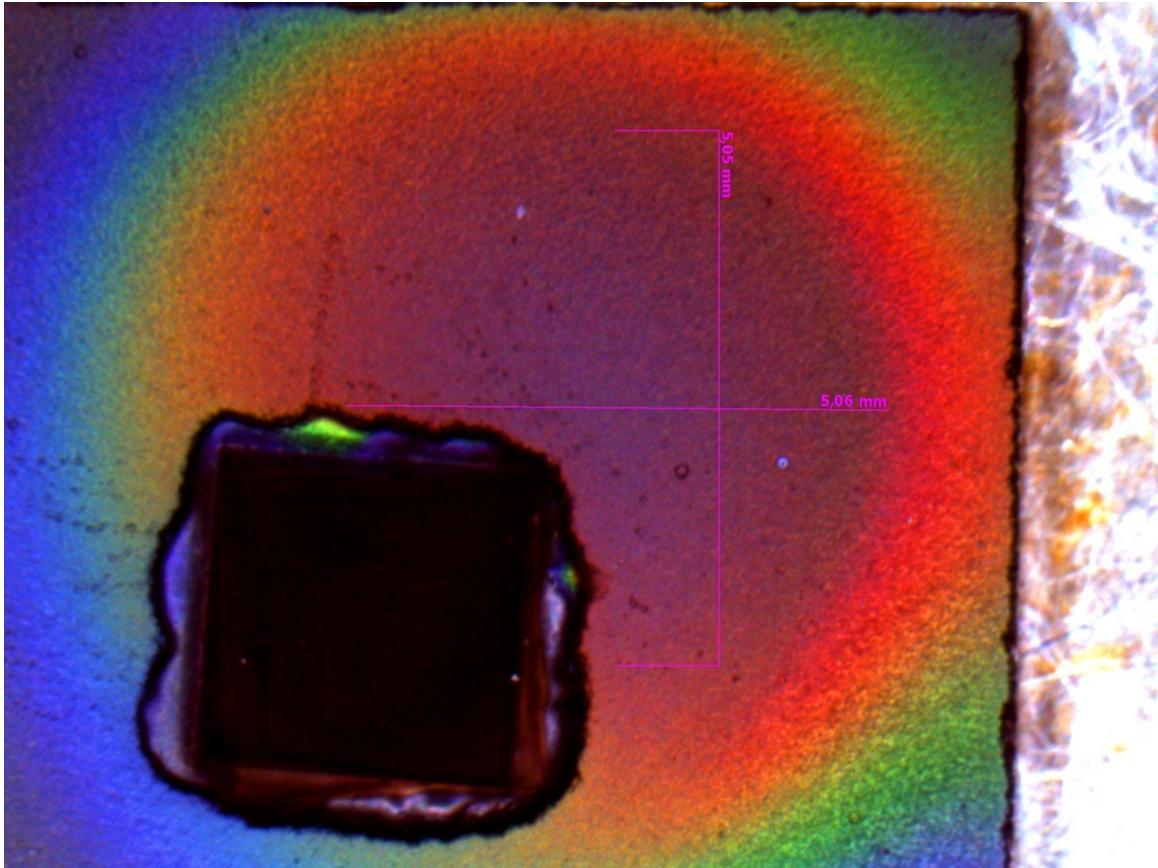


Figure 5-3 : Optical picture ex situ 0.79x under white light of both diamond sample and diamond-coated sample-holder after superlattice growth in the "surface contact" mode. The plasma was pinned at one corner.

II.3. Plasma density and doping efficiency

As reported by previous students (Baron, 2005 PhD thesis, p. 57) and (Volpe, 2009 PhD thesis, p. 85), the surface temperature and the boron doping were strongly dependent on the sample vertical position in the plasma (plasma/diamond sample surface contact modes). As reported in table 5-2 : influences of the plasma , the growth parameters must therefore be adjusted accordingly.

Sample position	Center contact	Surface contact	Point contact
Relative height in the waveguide (mm)	0	-5	-10
Pressure in the reaction chamber (Torr)	33	50	50
Microwave power <i>for 880°C in H₂ plasma</i> (Watt)	340	310	280
<i>Microwave power density (Watt.cm⁻³)</i>	<i>80 – 85</i>	<i>73 – 78</i>	<i>66 – 71</i>
Surface temperature (°C)	830	830	830
B/C ratio in the gas phase (ppm)	660	660	660
B/C ratio in the solid phase (ppm) <i>at 4% (CH₄/H₂)</i>	454	3180	8500
Doping efficiency <i>at 4% (CH₄/H₂)</i>	0.7	4.8	12.9

Table 5-2 : Influences of the plasma contact modes. Doping efficiency = (B/C)_{gas}/(B/C)_{solid}.

These growths were performed with diborane (B₂H₆) as the boron source, at a substrate temperature of 830°C in a 2.45 GHz microwave power quartz wall NIRIM type MPCVD reactor. The microwave power was real time-adjusted in order to keep the surface temperature constant at 830°C. The temperature was measured using a single color pyrometer working at the 0.98 μm wavelength. The boron-doped layers were grown with 4% of methane in the gas phase (CH₄/H₂) and 660 parts per million (ppm) of boron in the gas phase (B/C) on the same series of diamond substrates (CVD, element 6). This resulted in different doping levels as a function of the sample position with respect to the plasma with [B]_{Point contact} > [B]_{Surface contact} > [B]_{Center contact}. The calculated boron doping efficiency is the B/C ratio in the solid phase over the B/C ratio in the gas phase.

II.4. Boron incorporation mechanisms: a short tentative discussion

The thermal decomposition of B₂H₆ into BH₃ (Govender, et al., 2003) and the rapid conversion between BH_X (X=1–3) driven by many plasma-induced H-shifting reactions are expected to produce abundant BH_X radicals during growth. Similarly to the CH_X (X=1–3)

reaction with the diamond surface, the reactive BH_x radical binds on a vacant $C\bullet^*$ site of the diamond surface by a B–C covalent bond and is then further covered and buried in the bulk with the help of CH_x species behaving in a similar manner to form a boron doped diamond layer. The behavior of a plasma mixture composed of diborane, methane and hydrogen has been modeled (Liang, et al., 2008). It was concluded that the insertion of BH onto the diamond surface is much more favorable, arguing to conclude this that it is ten times more exothermic than the same insertion process for BH_2 . These authors also confirmed experimentally a correlation between the BH molecular fraction and the boron content incorporated in diamond layer.

The BH specie is very reactive with the diamond surface, because its significantly lower electronegativity with respect to carbon gives a much more polar and stronger covalent bond than the C–C bond which might result from the reaction of the methyl radical CH_3 on the diamond surface during growth. Therefore, there is a greater probability for a boron atom to be chemically adsorbed on the diamond surface than for carbon. This may explain why one generally obtains high boron bulk incorporation in diamond CVD growth with low values of the B/C ratios in the gas phase. The ratio between BH radical concentration ($[BH]$) and CH_3 concentration ($[CH_3]$) at the diamond surface is also critical to keep a good crystallinity during heavily boron-doped diamond growth. This ratio depends on the location and the inherent chemical reactions in the plasma. If $\alpha \geq [BH] \geq [CH_3]$ (α being the fraction of vacant $C\bullet^*$ sites on the diamond surface), then the exposed growing carbon surface becomes excessively enriched with boron, thus giving birth to boron pairs and clusters and inducing a local graphitization that finally macroscopically yields a poorer quality of the diamond epilayer bulk (Achatz, 2008 PhD Thesis). It seems to be important to maintain $\alpha \geq [CH_3] \gg [BH]$ for keeping a good crystallinity, with a majority of carbon species near the diamond surface. If $[BH]$ is low enough in comparison with $[CH_3]$, the possibility to form B–B bonds and boron clusters becomes very low.

Computer models of carbon and hydrogen species distribution in the MPCVD plasma have been reported by Silva et al. (Silva, et al., 2009). Boron species distribution have also been recently investigated by laser spectroscopy and modeling (Ma, et al., 2010). These calculations were made for a cylindrical metallic cavity MPCVD reactor. In such a configuration, there are two kinds of microwave electromagnetic resonance mode types, transverse electric (TE) and transverse magnetic (TM), depending on the electric or magnetic field linear polarization with respect to the wave propagation direction, therefore orthogonal to the cavity vertical axis. Boundary conditions of the cavity (equipotential metal walls) impose zero tangential components for the electric field on the metallic cavity walls as well as on the conductive stage surface, which therefore forces the magnetic field to be normal to the stage surface (in that case the sample holder is metallic and materialize indeed the back side of the cavity). Consequently, transverse electric modes cannot have high electric field regions in contact with metallic walls, which mean that ignited plasma will

not be in contact with the sample holder. The microwave power density is not uniform in the plasma; an enhanced power transfer is especially expected near the substrate surface.

Under 50 mbar, H-atoms are mainly produced by direct electron-impact induced H_2 dissociation. A relevant 1D model in a cylindrical symmetry describes the coupled phenomena of chemistry, energy transfer, species and energy transport in hydrogen/methane plasma. This model takes into account 28 species and 130 reactions (Lombardi, et al., 2005). It requires some input data related to the process control parameters, the collision frequencies in the gas phase and the species diffusion mass transport coefficients. It assumes that the microwave power density distribution is similar to the one obtained for pure H_2 plasma using a 2D self-consistent model. Silva's results showed that CH_3 production at low pressure takes place in the plasma bulk. Its kinetics is governed by H-atom concentration (Silva, et al., 2009). The peak production of H-atom species is located on a vertical Z axis at 10mm above the sample surface (figure 5-4). This point represents the center of the plasma. An optimal CH_3 production is obtained for gas temperature values in the 1200–2200 K range. Under 50 mbar, the CH_3 concentration increases from the center of the plasma on 10 mm along the Z-axis perpendicular to the stage surface.

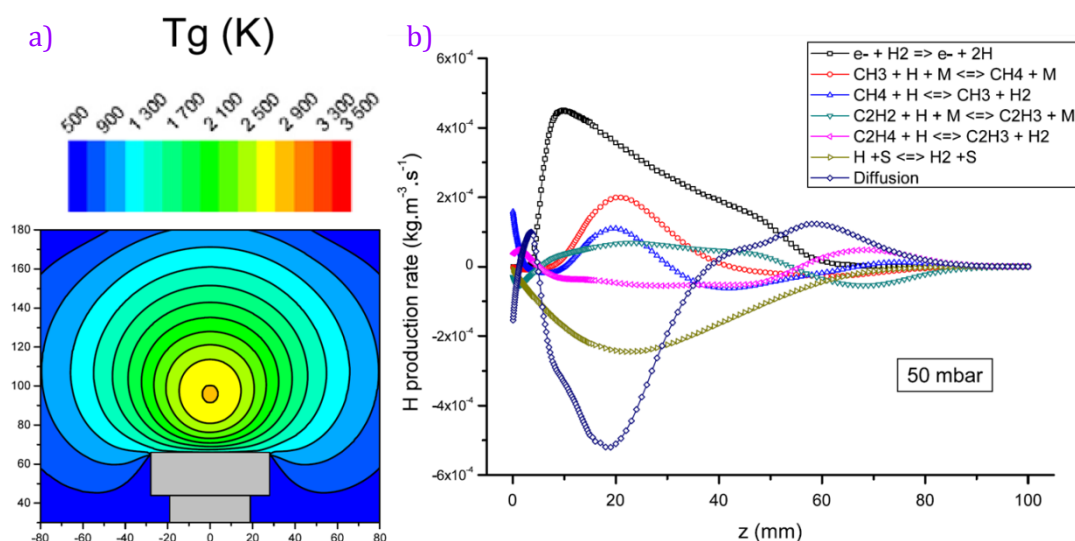


Figure 5-4 : (a) Gas temperature (T_g) for a pure hydrogen plasma. (b) Axial balance of atomic hydrogen derived from the 1D H_2/CH_4 model with 4% methane concentration in the feed gas (from (Silva, et al., 2009)).

In the case of the NIRIM type reactor, the plasma is generated at the intersection between the quartz tube and the waveguide. The local electric field is in the TE_{01} resonant mode. When the sample holder position is in the “point contact” mode under 50 Torr, the plasma naturally shapes into a perfect spheroid ball of 20 mm in diameter. The shape of the plasma is therefore similar to the case described by (Silva, et al., 2009). When the sample holder, made of quartz (highly electrically insulating), is introduced in the plasma, the stationary wave is perturbed and we observed that the plasma ball is moving up and shrinking. This is

the reason why in the “center contact mode” the pressure has to be lowered from 50 down to 33 Torr in order to expand the plasma ball and to keep the same level of microwave plasma power density. We can assume that the profile distribution of CH_3 species on our different plasma/diamond sample surface contact modes in the NIRIM-type geometry remains that described by (Silva, et al., 2009) corresponding to the “point contact” mode, because the plasma physico-chemical properties (active chemical species notably) are mainly governed by the gas temperature distribution, which depends on the microwave plasma power density. Modeling and layer spectrometry analysis by cavity ring-down spectroscopy (CRDS) investigated by (Ma, et al., 2010) reports a relatively constant distribution of BH inside the hot area of the plasma i.e. the plasma ball. Consequently, the $[\text{BH}]/[\text{CH}_3]$ ratio decreases from the border of the plasma ball to the center.

As a conclusion, this is the reasonable way we can tentatively explain that with a constant average $[\text{B}_2\text{H}_6]/[\text{CH}_4]$ ratio in the gas phase, we get $([\text{BH}]/[\text{CH}_3])_{\text{Point contact}} > ([\text{BH}]/[\text{CH}_3])_{\text{Surface contact}} > ([\text{BH}]/[\text{CH}_3])_{\text{Center contact}}$ close to the diamond sample surface in the NIRIM type growth reactor. The local enrichment in boron species at the sample surface exposed to the plasma when the sample is moving away from the plasma ball center is in good agreement with the observed results presented in table 5-2. Experimentally, using the same gas composition, the boron solid state incorporation depends of the contact mode: $[\text{B}]_{\text{Point contact}} > [\text{B}]_{\text{Surface contact}} > [\text{B}]_{\text{Center contact}}$.

III. HEAVILY BORON DOPING OF DIAMOND UNDER SLOW GROWTH CONDITIONS

The goals of the present study are:

- the heavily boron doping of $\langle 100 \rangle$ -oriented single crystalline diamond ($[\text{B}] > 4.5 \times 10^{20} \text{ at.cm}^{-3}$);
- the slow growth with a $\langle 100 \rangle$ growth rate lower than 0.1 nm per second;
- the low surface roughness (equivalent to the substrate roughness ($\Delta\text{RMS} \approx 0 \text{ nm}$)).

The effect of the growth rate on the heavy boron incorporation (incorporation efficiency is the main problem) was investigated. In order to do so, different CH_4/H_2 ratios were used, from 4% down to 0.25%. The boron-doped growths were performed with diborane (B_2H_6) as the boron source, at a substrate temperature of 830°C in a 2.45 GHz microwave power quartz wall NIRIM type MPCVD reactor. The microwave power was real time-adjusted in order to keep the surface temperature constant at 830°C. The temperature was measured using a single color pyrometer working at 0.98 μm .

III.1. On the reference growth conditions for heavily boron doped diamond layers growth

Samples grown with a 4% (CH_4/H_2) and 1200 ppm (B/C) in the gas phase at the position “center contact” (30 Torr, 100 sccm and 830°C (Baron, et al., 2006)) on “as received” prepared surface following the process show a surface roughness increasing by 1 nm (RMS), depending of the substrate polishing finish (typ. 1 nm for CVD e6 and 3 nm for HPTP Sumitomo). High conductivity and superconductivity have been reported in such samples (Achatz, 2008 PhD Thesis) and can reasonably be interpreted as a sign of a low defects density in the volume of the layer (dislocations ...). In our samples, the boron doping level lies in the typical $8.8 \times 10^{20} - 1 \times 10^{21} \text{ at.cm}^{-3}$ range. However, this set of growth parameters typically gives high growth rates in the 25 – 30 nm.min⁻¹ range, which are not compatible with the slow growth requirements ($V_{g(100)} < 0.1 \text{ nm/sec}$) of delta-doped epitaxy.

In 2012, Edgington et al. reported the homoepitaxial growth at Waseda University of boron-doped diamond layers on (111)-oriented substrates with a 0.3% (CH_4/H_2) and a 600 ppm TMB/ CH_4 ratios under optimized plasma process resulting in a growth rate of about 0.9 nm per minute and a doping level of $1 \times 10^{21} \text{ at.cm}^{-3}$ (Edgington, et al., 2012). It has been reported by (Bustarret, et al., 2008) (Wojewoda, et al., 2008) that the (100) plane of diamond is less efficient at incorporating boron at low methane percentages. The (111) plane does not share this reduced ability to incorporate boron at low methane percentages and as a result lower methane percentages can be used to achieve a slower and more controllable diamond growth, while maintaining high boron incorporation densities. However, in our case, the surface RMS roughness of the homoepitaxial (111)-oriented heavily boron doped diamond material is larger by a few nanometers than on the (100) surface orientation.

On (100) monocrystalline diamond substrates, (Kunze, et al., 1999) reported an optimized p++ growth at 0.5% with a solid boron rod technique resulting in a growth rate of ca. 1.6 nm/min and $1.9 \times 10^{21} \text{ at.cm}^{-3}$. This was achieved at a total pressure of 30 Torr, a substrate temperature of 650°C, a 700 Watt RF-Power at 2.45 GHz in a metallic wall ASTeX type MPCVD reactor

This is the reason why lower CH_4/H_2 ratios (1%, 0.5% and 0.25%) were investigated. In addition, the decrease of diamond growth is expected to be favorable to achieve p++ / p-- interface sharpness compatible with the criteria of delta doped structures.

III.2. Measurements of high boron concentration in the solid phase

Several ways to measure boron content in diamond are available. Here, we use secondary ion mass spectrometry (SIMS) and cathodoluminescence (CL). These techniques are complementary because the SIMS provide the boron profile in depth (including interstitial boron atoms and complex of boron) and the CL provides the information of the active doping level, in a small volume, over a given depth (depending on the acceleration voltage) while providing additional information about the crystalline quality.

III.2.1. Evaluation of boron doping in the bulk by SIMS

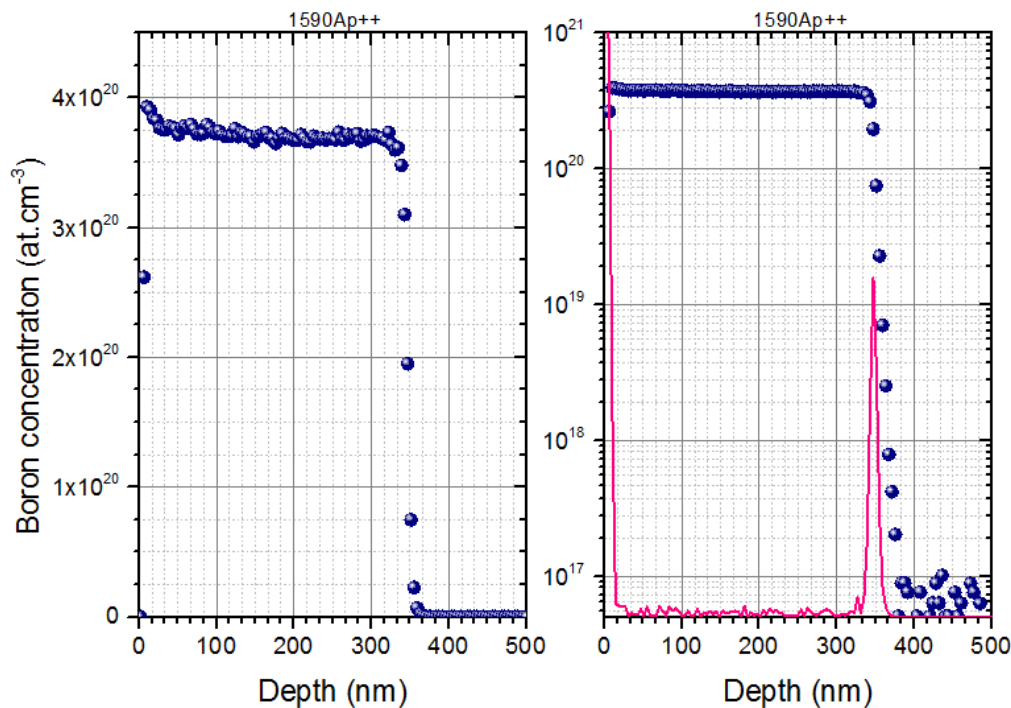


Figure 5-5 : SIMS profile of a 350 nm thick boron-doped layer grown with a low methane concentration ($\text{CH}_4/\text{H}_2 = 0.25\%$). Ion used: Cs^+ accelerated at 14.5 kV. On blue: Boron data, on pink: normalized 1st derivative curve.

Figure 5-5 displays the boron profile concentration in depth of a 350 nm-thick p⁺⁺ layer grown along the $\langle 001 \rangle$ -axis with 0.25% (CH_4/H_2) and 6000 ppm (B/C)_{gas} ratio at 50 Torr and 830°C. A continuous boron concentration (blue dots) is observed in the area corresponding to the p⁺ layer (located on the left side of the graph), giving a clear indication of a highly homogeneous boron doping in the bulk. This ordinary doping indicates a constant doping efficiency and this is very encouraging for satisfying the delta-doping criteria (top-flat box-shape boron profile). At a depth of 350 nm, the boron concentration rapidly drops down to values lower than the limit detection of the SIMS (a few 10^{16} B/cm³) with a 9 nm/decade transition width. The 1st derivative curve (in pink) is used to indicate the interface.

III.2.2. Evaluation of boron doping by cathodoluminescence

Boron-doped layers thicker than 300 nm were grown at the 0.25 % and 1% (CH_4/H_2) ratio, 50 Torr and 830°C in the “point contact” mode with different boron concentrations in the gas phase to study the incorporated boron content variations with the methane ratio. These boron-doped layers have been made on Ib HPHT (100)-oriented substrates coming from the same batch from Sumitomo. CL spectra were recorded at a temperature equals to 5(\pm 1) K, under an acceleration voltage of 10 kV with 40 nA electron beam excitation conditions. The zoom on 230 – 270 nm (figure 5-6) points out the shift in recombination energy of the boron bound exciton assisted by the transverse optic phonon (BE^{TO}) associated, in this precise case, to heavy boron doping (Baron, et al., 2006). All cathodoluminescence spectra were calibrated in energy by the same mercury line of reference located at 253.652 nm* in order to correct the monochromator (HR460 from Jobin Yvon, 600 grooves/mm or 1800 grooves/mm) read out error in position.

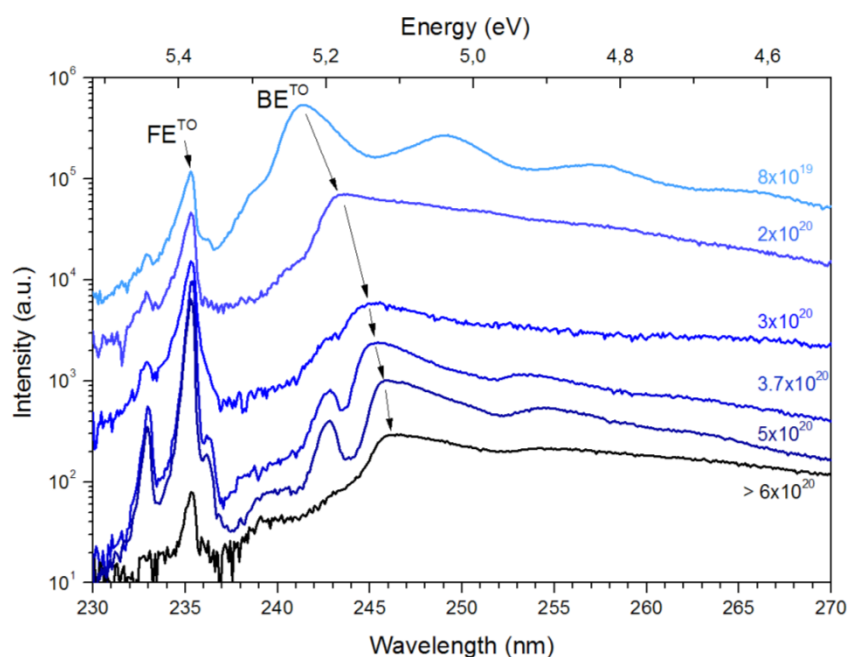


Figure 5-6 : Cathodoluminescence at 5K of boron-doped layers containing different boron doping levels. Arrows point out the shift in energy of the BE^{TO} for the estimation of the active doping which is given from a law detailed in the text below.

As reported by (Baron, et al., 2006) on (100)-oriented homoepitaxial samples, the BE^{TO} energy decreased from 5.211 eV to 5.036 eV when the boron concentration increased from 1.5×10^{19} to 6×10^{20} at.cm^{-3} . This shift in energy depends on the boron concentration and it follows a curve proposed by (Baron, et al., 2006) which is limited by two values: at 5.211 eV below 1.5×10^{19} at.cm^{-3} and at 5.036 eV above 6×10^{20} at.cm^{-3} . According to an empirical law deduced from an experimental data fit, the relationship between energy and doping can be written as follows: $E(\text{eV}) = 5.211 - 0.112 \log([B]/1.5 \times 10^{19})$.

* Handbook of Chemistry & Physics, 92nd Ed.

This equation was used in our case to estimate roughly the active boron content of boron-doped layers grown under different methane concentrations. The upper limit of the proposed model is above the metal-to-insulator transition (MIT) fixed at $4.5 \times 10^{20} \text{ at.cm}^{-3}$ (Klein, et al., 2007), but this model gives a wrong doping value when the boron concentration is higher than $6 \times 10^{20} \text{ at.cm}^{-3}$, because the BE^{T0} peak never drops an energy value inferior to 5.035 eV. Some samples under and above the MIT were analysed by SIMS to check the exact value of boron concentration and its in-depth profile.

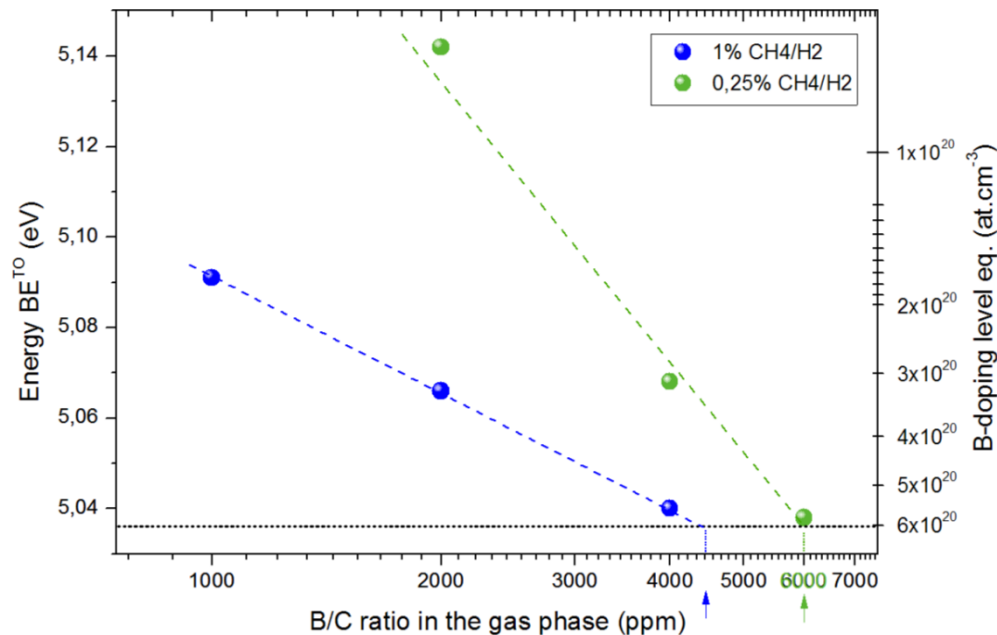


Figure 5-7 : Energy of the BE^{T0} peak detected by CL at 5 K of boron-doped layers grown at different boron concentrations with 1 and 0.25% CH_4/H_2 molar ratios. The limit of the model dependence between boron doping and BE^{T0} shift in energy proposed by Baron is 5.036 eV. Arrows in color point out the theoretical $(B/C)_{gas}$ ratio needed to reach a doping level of $6 \times 10^{20} \text{ at.cm}^{-3}$ at a given CH_4/H_2 ratio.

The plot of the BE^{T0} energy versus the boron concentration in the gas phase shows two different tendencies depending of the CH_4/H_2 ratio used, which underline directly the influence of the methane concentration in the plasma on the active boron doping efficiency.

The efficiency to incorporate boron into diamond is reduced with the methane concentration in the gas phase. Thus, at 1% (CH_4/H_2) the shift is smoother than at 0.25% (CH_4/H_2), resulting in a lower $(B/C)_{gas}$ needed to archived a doping above the metal-to-insulator transition (4400 ppm and 6000 ppm for respectively 1 and 0.25% (CH_4/H_2)).

III.3. Discussion on heavily boron doping efficiency

Results plotted on figure 5-8 come from both SIMS and CL. Three groups of icons colours represent different the methane ratios. For doping from 1×10^{20} to $6 \times 10^{20} \text{ at.cm}^{-3}$, we have an agreement between CL and SIMS data. Doping values above $6 \times 10^{20} \text{ at.cm}^{-3}$ are reliable by SIMS only. The tendency in the incorporation efficiency (ratio $(B/C)_{solid}$ versus $(B/C)_{gas}$)

estimated from the energy shift of the BE^{T0} peak shown on figure 5-7 is consistent with additional data obtained for different gas mixtures. Thus the boron incorporation increases with the methane concentration in the 0.25% - 4% (CH_4/H_2) range.

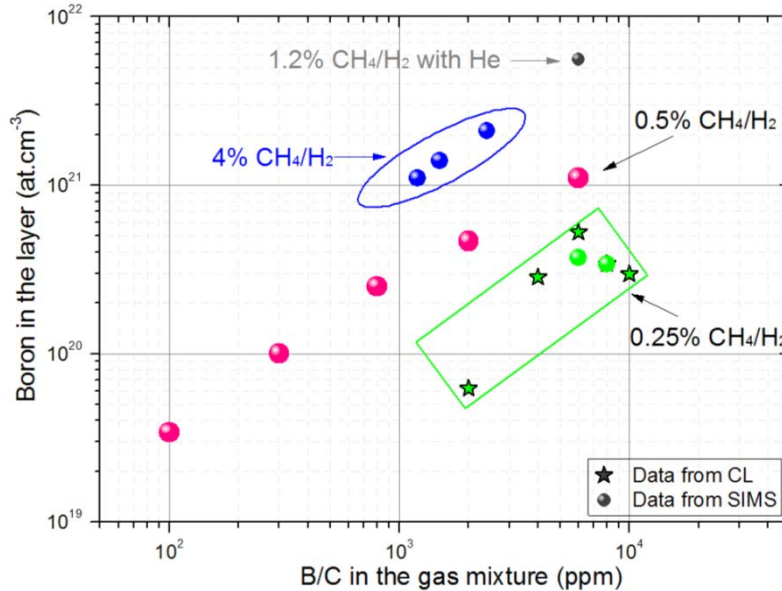


Figure 5-8 : Incorporated boron vs. (B/C) in the gas mixture at different C/H ratios. Dots are data from SIMS and stars are data estimated from CL energies.

With 0.25% (CH_4/H_2) in the gas mixture, the concentration of incorporated boron tends to saturate at high $(B/C)_{gas}$ ratios. This was first evidenced from CL 5K measurements and it was confirmed by SIMS measurements on the same samples. The 0.25% (CH_4/H_2) ratio provides a suitable slow growth ($1.4 - 1.5 \text{ nm}\cdot\text{min}^{-1}$) for delta-doping, comparable with the growth rate reported by Kunze et al. (Kunze, et al., 1999). The RMS surface roughness after 240 min of growth was $2.5 - 2.9 \text{ nm}$, which was the same surface roughness of substrates used for this study ($\Delta RMS \approx 0 \text{ nm}$). As reported by other authors (Ri, et al., 2002) (Mer-Calfati, et al., 2009), the polishing effect and the misorientation interfere with the surface morphology in homoepitaxial diamond film grown by CVD method, especially at extremely low methane concentration. In this study, the misorientation angle (θ_{off}) of our samples was less than 1 deg, indicating that the growth mode was able to limit the propagation of defects (see below section IV. Low boron doping). However, the incorporated boron concentration remains lower than the metal-insulating transition when the boron concentration in the gas phase is below 6000 ppm. An increase of the boron concentration was performed, but the result was not good. We suggest that the formation of boron “complex” or “interstitial” boron might be present above the boron concentration saturation threshold (Bustarret, et al., 2008). The situation at the sample surface might be close to $[BH] \approx [CH_3]$ which is not favorable for diamond growth.

With 0.5% (CH_4/H_2) and 6000 ppm (B/C), the boron doping level is in the $9 \times 10^{20} - 1 \times 10^{21} \text{ at}\cdot\text{cm}^{-3}$ range and the grow rate is in the $4.5 - 5 \text{ nm}\cdot\text{min}^{-1}$ range at the “point contact” mode. The growth rate is less than the double of the growth rate at 0.25% under the same plasma

conditions (working pressure at 50 Torr, surface temperature at 830°C) and contact mode. As shown on the figure 5-8 by pink points, the doping efficiency is constant; no saturation effect appears as in the case of 0.25% (CH₄/H₂). Compared with (Kunze, et al., 1999) and (Edgington, et al., 2012) this growth rate is fast, but we are using a low power plasma in a NIRIM type reactor, doping is made with diborane and we are working on (100)-oriented sample, the growth rate on (111)-oriented sample is usually smaller. This may explain a faster growth rate at high boron doping levels in our case. Nevertheless, this set of parameters is compatible with delta-doping growth; in one second less than 0.1 nm is deposited on the (100) face. The growth can be computer-assisted to manage precisely the p++ growth duration in order to growth a few nanometer in thinness.

Helium addition to the previous mixture composed of 0.5% (CH₄/H₂) with 6000 ppm (B/C) reduce the growth rate (around 2.5 nm.min⁻¹), but at the same time it increases the boron incorporation, leading to heavily boron doping above 5.6×10²¹ at.cm⁻³ with a worse crystalline quality.

III.4. Effects of the boron concentration in the gas phase on the diamond growth rate

The growth rate is modified by the boron concentration in the gas phase, as reported in the Figure 5-9 below.

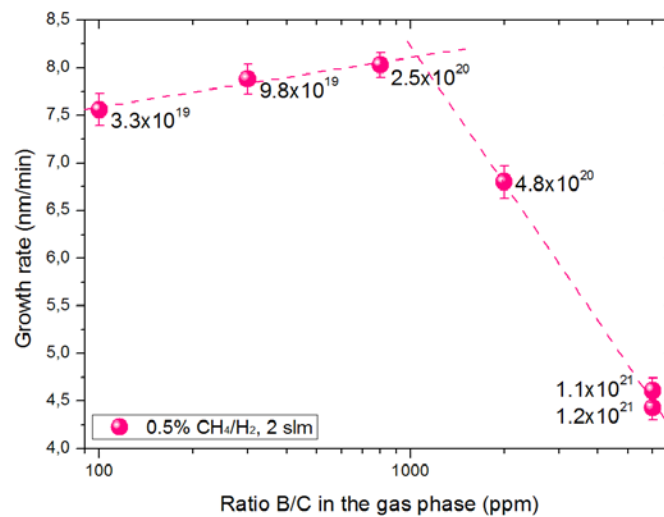


Figure 5-9 : Growth rate (100) vs. (B/C) in the gas mixture with 0.5% (CH₄/H₂) and under a total flow of 2 slm. Doping level is given in at.cm⁻³.

For (B/C)_{gas} ratios below 1000 ppm, the growth rate is increasing slowly with the boron concentration. This trend is similar to the observation of Issaoui et al. in the case of thick diamond boron-doped layer growth (Issaoui, et al., 2011). In their study, the B/C in the gas phase was varied from 60 to 5000 ppm (0.5% (CH₄/H₂)) and the growth rate along the <100>-direction was continuously increasing with the boron concentration, but they were working in a high power density bell-jar reactor (140 mbar and 2400 W) and consequently

the boron incorporation efficiency is different; in our growth conditions (figure 5-9) the doping efficiency (DE, $(B/C)_{\text{solid}} \text{ over } (B/C)_{\text{gas}}$) is 1.1 – 1.9 and for the LSPM team it is 0.06 – 0.11 (Issaoui, et al., 2012). In this case, we can assume the doping from 60 to 5000 ppm for Issaoui et al. yield in a lower active boron species density in the plasma and is comparable with a doping from 6 to 500 ppm under our growth conditions.

However, figure 5-9 illustrates the reduction of the growth rate on $\langle 100 \rangle$ -oriented substrates when the ratio B/C in the gas phase is above 1000 ppm and in the particular case of 0.5% (CH_4/H_2) under a total flow of 2 slm. This phenomenon was also reported on polycrystalline diamond (Gonon, et al., 1995) and on monocrystalline diamond (Gheeraert, et al., 1999), (Tokuda, et al., 2007); in the case of 0.6% (CH_4/H_2) the growth rate is decreasing drastically around 1000 – 2000 ppm $(B/C)_{\text{gas}}$ (Tokuda, et al., 2007). The doping efficiency was in the same range that means the reduction of growth rates yields into a low concentration of active species (B and C) at the surface. A possible explanation for this behavior is the competition in adsorption between boron and carbon at the surface. Boron is more reactive than carbon. The diamond surface tends to be fully covered by boron, but as the growth is ensured by carbon species the growth rate is reduced. Finally, as it takes a longer time to finalize an atomic layer, more boron has the time to desorb and it could explain the same boron incorporation efficiency in the solid phase. The growth mode could be anisotropic with high boron concentration. An alternate explanation yields in the change in plasma chemistry, governed by the gas temperature which is modified by boron addition; more precursor species could be consumed in the bulk of the plasma leading in a slowest growth and at the same time. This must be investigated by spectroscopy and plasma modeling.

III.5. Effects of the total gas flow on the growth rate and on the boron incorporation

On the path to grow delta-structures, the total flow was increased from initial heavy doping conditions (Baron, et al., 2006) using 100 sccm up to 2 slm. The idea was to reduce the diffusion time of carbon and boron-related species. A shorter diffusion time is expected to provide a sharper boron concentration profile at the onset of the p++ layer growth.

At high gas flows (liters per minutes), turbulences near the sample holder are not negligible (see “fluid dynamics calculations” in annexes I.). The ionized matter is visibly affected and finally the plasma ball appears flattened. When the flow changes from 100 sccm up to 6000 sccm, under a constant pressure (50 Torr), the plasma ball is squeezing along the main flow direction. If the microwave power is kept constant (310[†] Watt), the surface temperature of the sample naturally increases from typ. 880°C to 900°C for pure hydrogen plasma. In

[†] In the “surface contact” mode.

practice, when the flow is high, the increase of the sample surface temperature was manually compensated by a reduction of the incident microwave power.

It has been reported that increasing the input microwave power, was reducing the measured BH concentration (Ma, 2008 PhD thesis). According to this study, the variation of BH might come from the following fact: when more power is introduced, more H-atoms are produced, which may push the equilibrium between the BH_x species (reaction of H-shifting) from BH to B. So the B-atoms density could be seen to increase as the power increases and BH density drop. In parallel, methyl density rises as the power is increased. In our case, the modification of the power is very light, so this shouldn't be a major effect.

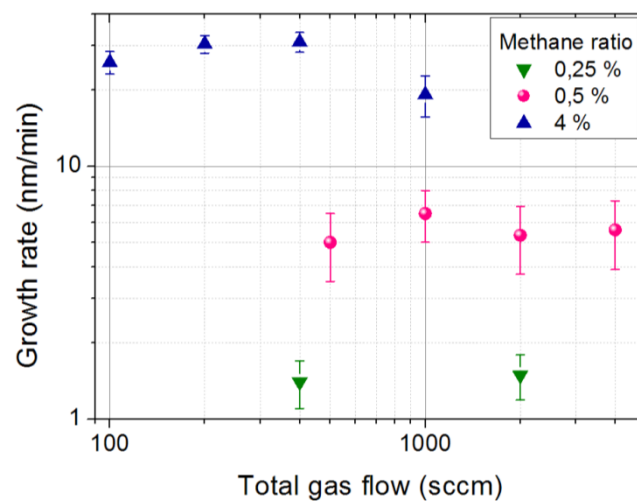


Figure 5-10 : Effect of gas flow on the growth rate at constant (B/C) ratio (1200 ppm at 4% (CH_4/H_2) in “center contact” mode and 6000 ppm at 0.25 – 0.5% (CH_4/H_2) “surface contact” mode).

Figure 5-10 illustrates the effect of the total gas flow on the growth rate, in the case of samples exposed to the same boron/methane ratio in the gas phase. We observe that the increase of the total gas flow does not affect the growth rate when the methane ratio is below 4% (CH_4/H_2). At 4% (CH_4/H_2), the growth rate seems to decrease for gas flows higher than 400 sccm.

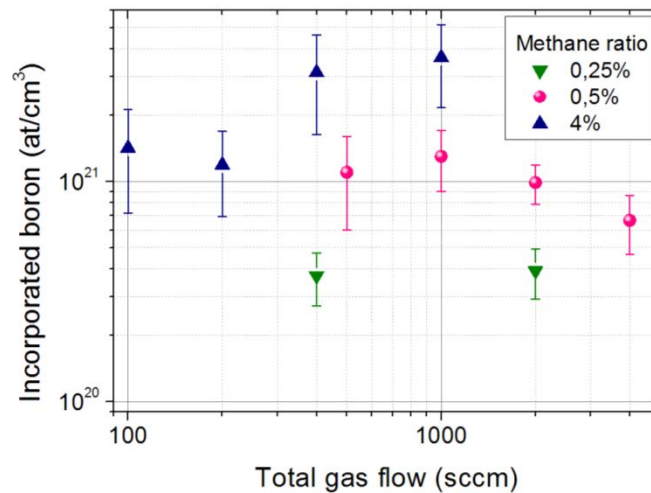


Figure 5-11 : Effect of gas flow on boron incorporation at constant B/C ratio (1200 ppm at 4% (CH₄/H₂) and 6000 ppm at 0.25 – 0.5% (CH₄/H₂)).

The relationship between the incorporated boron concentration and the total gas flow is not clear. However, with a gas flow above 400 sccm, in the case of 4% (CH₄/H₂), the incorporated boron concentration increased and at the same time soot deposition was observed in our reactor. The sample is located very close to center of the plasma (“center contact” mode). According to its dependence on the gas temperature, we suppose the bulk chemistry is modified and the methyl concentration near the surface was reduced. In parallel, the surface concentration [BH] decreases, but with a narrower range as compared to [CH₃]. It results in a local increase of the ratio [BH]/[CH₃] providing a higher doping incorporation and slower growth rate, as reported previously.

This tendency is not visible at lower methane concentration; the variation reported is in same order of the error on the plasma/sample contact. Low methane concentration growths are made at the “surface contact” mode. In this position, when the flow is high, the temperature is less enhanced than in the previous case (4% (CH₄/H₂)). The thermal compensation by microwave power is lower. In consequence, methyl density decreases a little bit, and because of fast diffusion of carbon species and low methane concentration, the concentration of methyl and the ratio [BH]/[CH₃] may slightly decrease. As a consequence, the growth rate remains constant and this could explain lower boron incorporation at 4 slm.

These studies on the influence on growth rate and boron incorporation allows us to make possible some comparisons between layers growths made at different boron and low methane concentrations, but under the hypothesis of a common sample/plasma contact mode, pressure and surface temperature.

IV. LOW BORON DOPING AND LATERAL GROWTH*

p-- growth conditions set up by Volpe required the addition of oxygen to the plasma gas mixture (Volpe, 2009 PhD thesis, p. 144). This technique was optimized in term of methane and oxygen concentration (1.00% (CH₄/H₂) and 0.25% (O₂/H₂) on (100)-oriented diamond), keeping the same pressure (50 Torr) and surface temperature (910°C), in order to reduce drastically the incorporated boron concentration in the grown layer and at the same time to keep a suitable crystalline quality by measuring of the width of FE^{T0} peaks and the ratio between FE^{T0} and BE^{T0} peaks. These excellent low boron doping and good crystal quality where confirmed in the fabrication of Schottky diodes withstanding breakdown voltages up to 10 kV (Volpe, et al., 2010). However, this optimization in growth conditions yielded wide defects at the sample surface and a large RMS roughness. This process cannot be suitable to overgrowth homogeneous and flat p++ layers; the target is a surface RMS roughness below 1 nm.

In order to simplify the study, all growths were made under the same plasma condition (50 Torr, 910°C, 200 sccm total flow) and in the same sample position (surface contact mode) used for the delta-layer. The idea to use the same position comes from the p++ process optimization. Keeping the same position between p++ and p-- is an advantage for growing multilayers samples such as delta-layers or superlattice, because it suppresses an uncertainty in position, which introduced a series of errors in the doping and in the growth rate.

The lateral growth is an anisotropy growth where the vertical growth rate is lower than the longitudinal (lateral) growth rate. Methane-to-hydrogen and oxygen-to-hydrogen ratios have an important influence on the diamond growth mode (2D nucleation, step-flow...). The purpose is to reach a slow vertical growth (equivalent to 0.1 nm per second in order to get precision on the deposited thickness) on (100)-oriented diamond and to reduce the surface roughness by a fast lateral growth (flat surface). The first task was to fill up holes induced by polishing on CVD diamond substrates and to smooth polishing line on HPTH diamond substrates.

* This study was performed under the supervision of Drs. T.Teraji and S.Koizumi at NIMS, Tsukuba, Japan during a 6 months internship. This work was also supported by the Strategic International Collaborative Research Project from the Japan Science and Technology Agency, Japan and Grant-in-Aid for Scientific Research from the Japan Society for the Promotion of Science, Japan (No. 18760241).

IV.1. Origin of the roughness

The first point was the investigation of the effect of methane and oxygen mixture on the lateral growth efficiency to reduce surface defects height. It is understood that the density of defects depends strongly of the substrate surface (polishing lines, holes) and sub-surface (hardening). However by controlling the lateral growth conditions ($\%CH_4/H_2$ and $\%O_2/H_2$), it must be possible in theory to flatten as many defects as possible such as pyramidal Hillocks (PHs), Flat-topped pyramidal Hillocks (FHs) and Rounded Hillocks (RHs)[†].

IV.1.1. Angle misorientation

Sample miscut angle value seems to drive the PHs and UCs occurrence. Takeuchi was reported the dependency of the misorientation angle on the surface morphology (Takeuchi, et al., 2000). When the misorientation is below 1° , then atomically flat surface were observed only for growth conditions using CH_4/H_2 ratios below 0.15%. At higher methane content and at lower miss-oriented substrates, UCs and PHs were found on samples surface. In our case, the misorientation of sample is below 1° and the CH_4/H_2 ratios will be above 0.2% in order to avoid any hydrogen etching, but the gas mixture will be not composed of methane and hydrogen only, oxygen will be added. So we guess the small misorientation of our samples will induce PHs and UCs, but we expect that the addition of oxygen will compensate for that phenomenon.

IV.1.2. Subsurface defects

Diamond mechanical polishing generates a defective volume area just below the surface over several microns characterized by a large dislocation density, more or less random oriented. Depending of the polishing techniques, the defective volume is removed or present over few nanometers in depth. Smooth removal techniques of this subsurface hardening were developed as detailed in Chapter 4. VI.1.

The increase of the emerging dislocation or fracture induces a direct change on the surface morphology after the growth. If the subsurface is not hardened, then the overgrown surface is totally flat with a limited numbers of PHs, as shown on table 5-3.

[†] See “defects definition” in Chapter 4. VII.

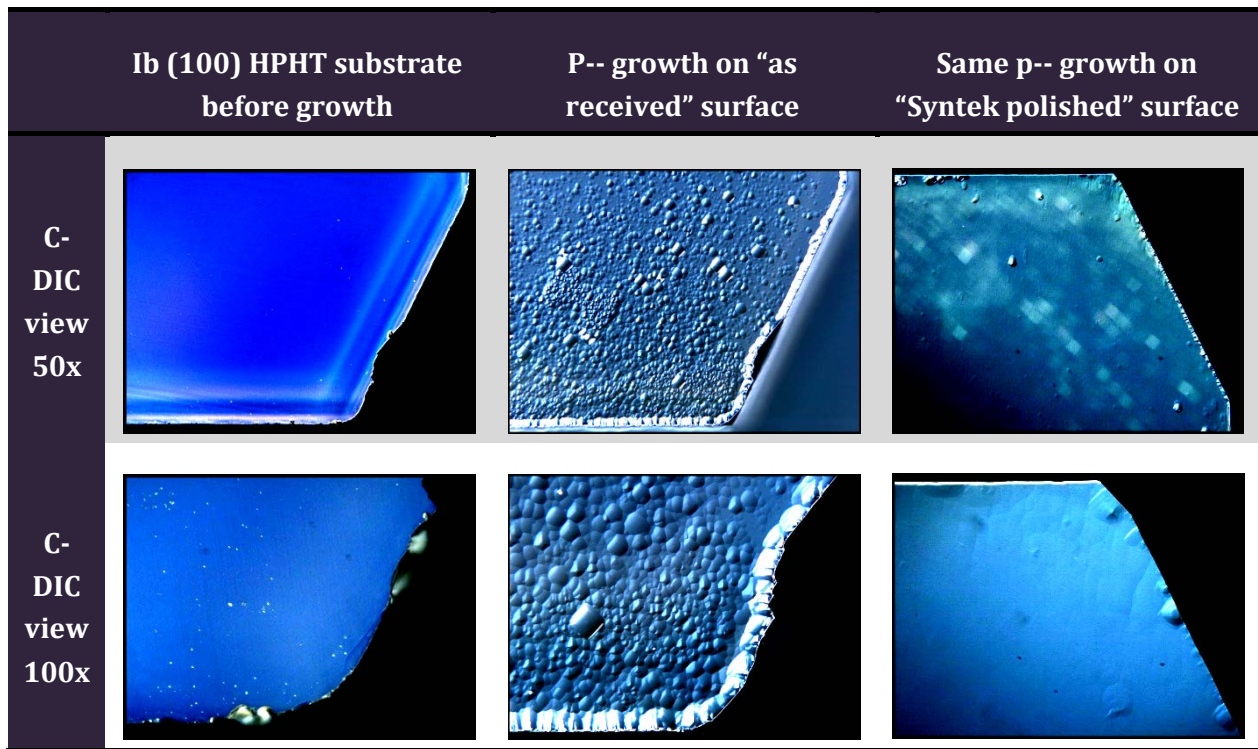


Table 5-3: Overgrown surface morphology vs. polishing on the same substrate with one face polished "as received" and the other face re-polished.

The FE^{T0} peak signal measured on the epilayers made on p-- growth on "as received" and on re-polished sample shows a difference in full width at half maximum (FWHM) value.

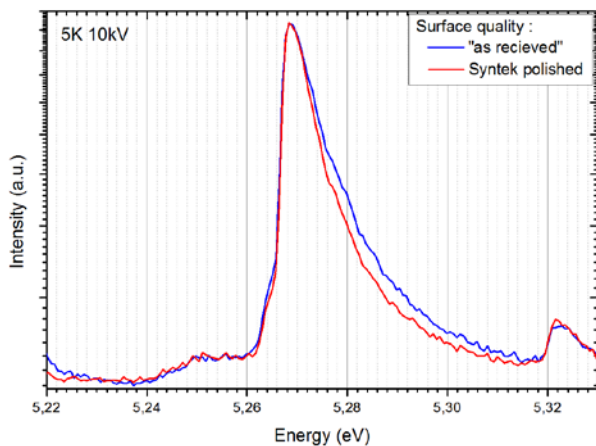


Figure 5-12 : CL spectra of p-- growth made on "as received" and re-polished substrate.

On figure 5-12, FWHM are 9.997 meV and 8.45 meV for epilayers made on "as received" and on re-polished respectively. The higher value of FWHM is related to a poorest crystalline quality of the epilayer, with the inherent presence of a larger density of structural defects. In

this case, it must be coming from a higher density of dislocations present at the beginning in the “as received” substrate.

IV.1.3. Substrate surface roughness dependence

The initial surface roughness coming from the substrate has a strong influence on the final surface morphology. Indeed, the response to the same p-- growth applied on both CVD and HPHT substrate shows, as described below, a complete difference in the surface roughness RMS value.

As detailed in Chapter 4. VI.3. , CVD and HPHT diamond substrates providers companies give different RMS roughness and defective surface. To summarize, CVD substrates are covered by micrometric holes and HPHT are covered with parallel polishing lines.

It is important to notice that RHs were found only on layers grown on HPHT substrates. In figure 5-13, the surface of p--/p++ was observed by optical profile in PSI mode. It is possible to see clearly the location of RHs at the starting point of polishing lines. As shown on table 5-4, polishing lines are still visible on direct growth on substrate, while flat surface are observed on overgrown p++ layers. In the p--/p++, RHs are located at the same point as the original polishing tips; their density cannot be reduced but their height becomes smaller by tuning the oxygen ratio. We proposed that the geometry of RHs comes from the random orientation of the defect, *i.e.* tip after polishing. As the orientation is random, the overgrown defect has a circular base and this explains the large distribution in base diameter and in height.

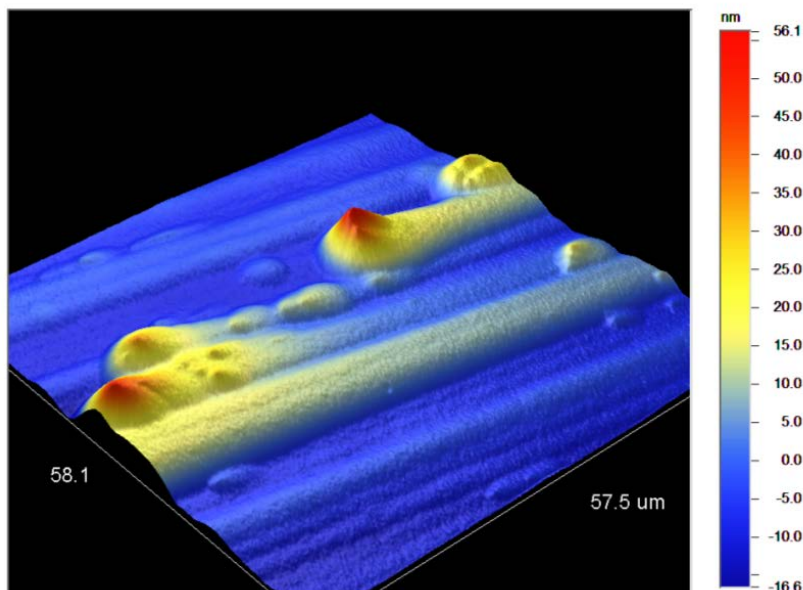


Figure 5-13 : Detail on RHs at the p-- /p++ surface by PSI mode optical profile.

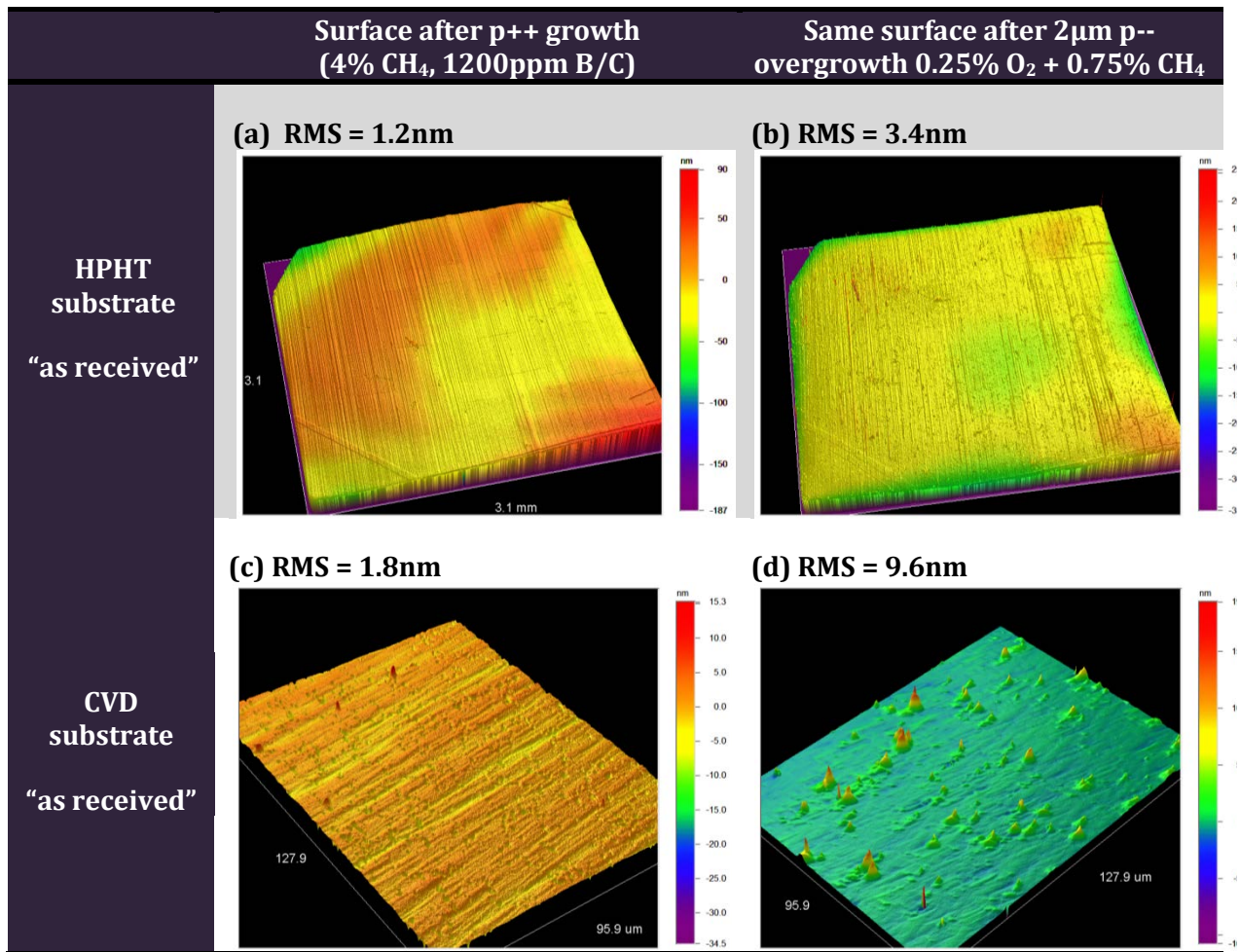


Table 5-4 : PSI mode optical profile pictures of p-- growth on p++ (c, d) and on “as received” HPHT substrates (a, b). 2 μm thick p-- were performed with 0.75% (CH₄/H₂) + 0.25% (O₂/H₂) on 300 nm p++ doped at 10²¹ cm⁻³ (4% CH₄/H₂, 1200 ppm (B/C)_{gas}).

No polishing lines are observed on “as received” CVD substrates and that could explain the RHs apparition on “as received” HPHT. To confirm this trend, p-- growth on both super-polished CVD and HPHT substrates were made and they show neither PHs nor RHs after few μm. So the origin of the substrate (CVD or HPHT) has no major effect on the final surface roughness.

IV.2. Effect of lateral growth on surface defects height reduction

Figure 5-14 illustrates the effect of methane concentration in the gas phase during growth on surface roughness and on the nature of 3D surface defects observed.

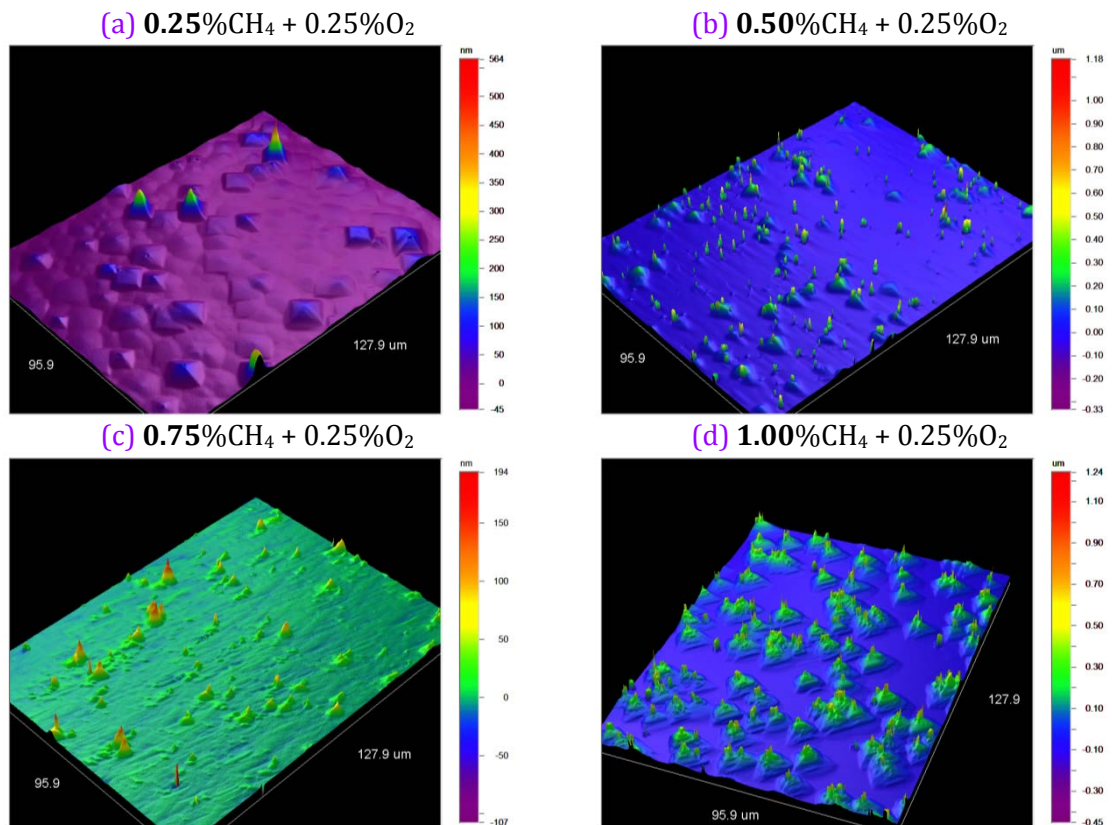


Figure 5-14 : Surface roughness after growth on “as received” CVD diamond substrate as observed by optical profilometry.

A gas mixture composed of 0.25% (CH_4/H_2) and 0.25% (O_2/H_2) places the reaction system near the growth/etching equilibrium. This situation is marked by a predominance of FHs over the entire surface with a sparse PHs density. It could be attributed to a strong difference between the lateral growth and the vertical growth; defects initially present pinned terraces which are growing in the (100)-plane. Finally, the surface is covered by independent terraces which might evolve into FHs when terraces are growing in plan per plan, while the growth of PHs is made in spiral above a screw dislocation.

By keeping the same oxygen content (0.25% (O_2/H_2)) and increasing the methane ratio from 0.5 to 1% (CH_4/H_2), FHs are not observed anymore. The surface is composed of tilted PHs following the substrate misorientation and with a surface density comparable to the density of micrometric holes present at the “as received” substrate surface. This illustrates the effect of the 3D (island) growth mode modulated by the methane concentration and the oxygen concentration in the gas phase. The height of PHs is decreasing with the improvement of lateral growth mode. If the surface RMS roughness on flat surface is compared, then the recipe with 0.75% of methane provides the lowest roughness value with very flat tiny PHs on “as received” CVD substrates. One step beyond this investigation was made in order to reduce 3D defects height by tuning methane and oxygen concentration in the gas phase. Some tendencies are reported (figure 5-15).

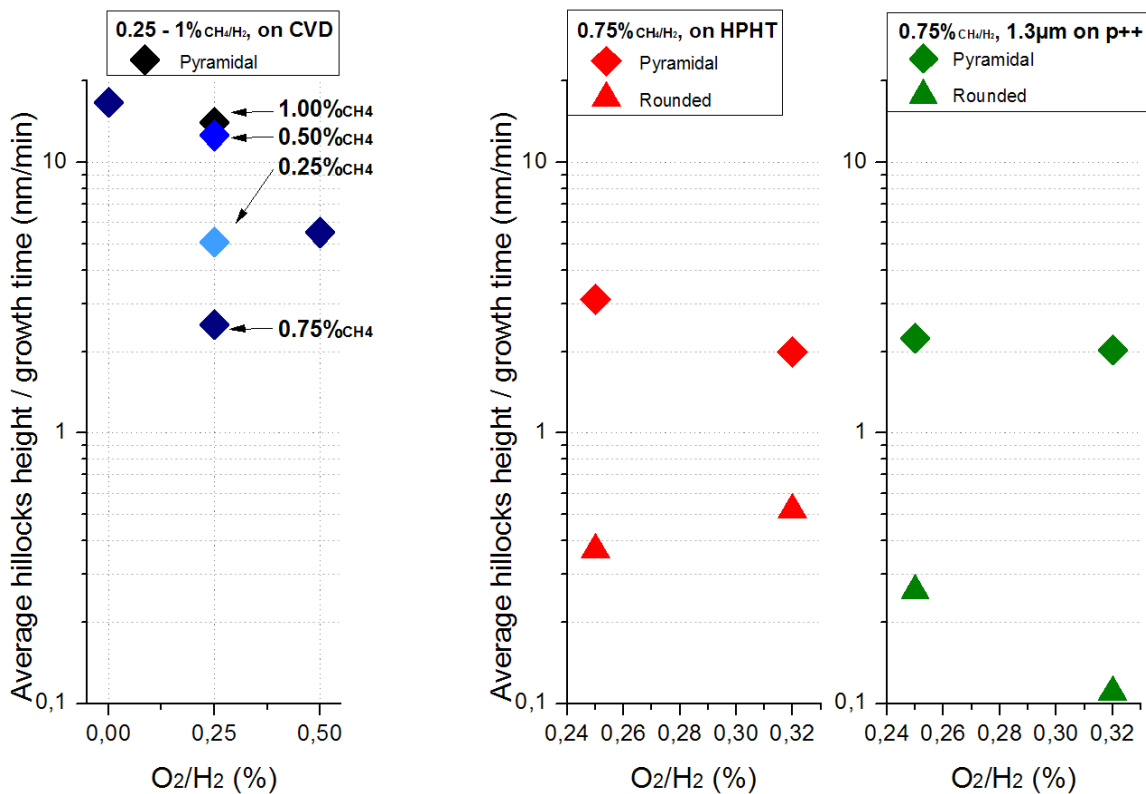


Figure 5-15: Effects of methane and oxygen in the plasma (using different kinds of substrates) on Hillocks height (PHs & RHs) normalized to the growth time.

The figure 5-15 points out differences in the evolution of the height in the case of PHs and RHs. To do so, the reported value consists in the ratio of hillocks height (average) to growth time. This value is independent of the thickness of the layer growth; the variation of methane and oxygen concentrations induce a modification of the vertical growth rate (the growth is anisotropic). It is important to perceive the clear difference in the evolution in height between RHs and PHs. Independently of the substrate used or the gas mixture, RHs are ten times lower than PHs; the distribution in height of RHs is very broad when compared to the case of PHs. This stems from their origin and from the growth mechanism which makes them bigger. The main origin of surface roughness comes from PHs. Studying PHs height evolution on CVD, the best methane ratio found was 0.75% of methane with 0.25% of oxygen in hydrogen. This growth condition was applied to as received HPHT substrates and to p++ overgrown pseudosubstrates. A slightly increased ratio of oxygen (0.32%) was applied too.

IV.3. Determination of growth anisotropy parameters

The equilibrium shape of crystal CVD diamond (i.e. at equilibrium state, after a time of infinite growth) is determined by the slowest growth rates faces (figure 5-16). In most cases, these are the faces {100} and {111} that define the shape of the crystal (F faces). The morphology is then governed by the parameter defined as follows: $\alpha = \sqrt{3} \frac{V_{\{100\}}}{V_{\{111\}}}$. In some cases, the faces {110} and {113} are also present and the morphology is then governed by the parameters α , β and γ with: $\beta = \sqrt{3} \frac{V_{\{100\}}}{V_{\{110\}}}$ and $\gamma = \sqrt{3} \frac{V_{\{100\}}}{V_{\{113\}}}$.

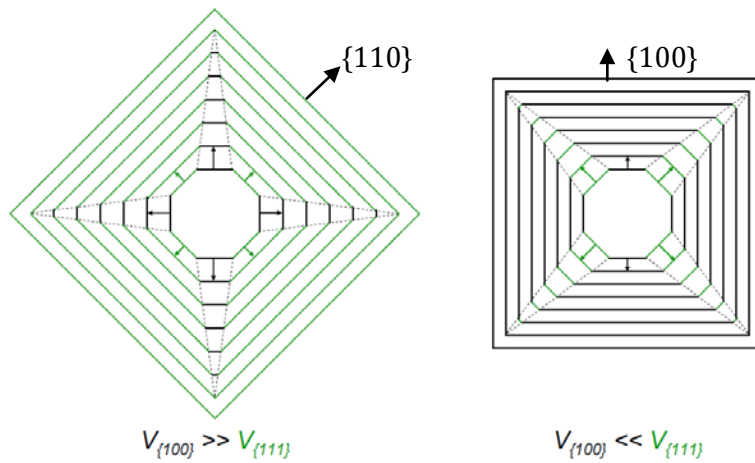


Figure 5-16 : Illustration of growth speed and facets morphology.

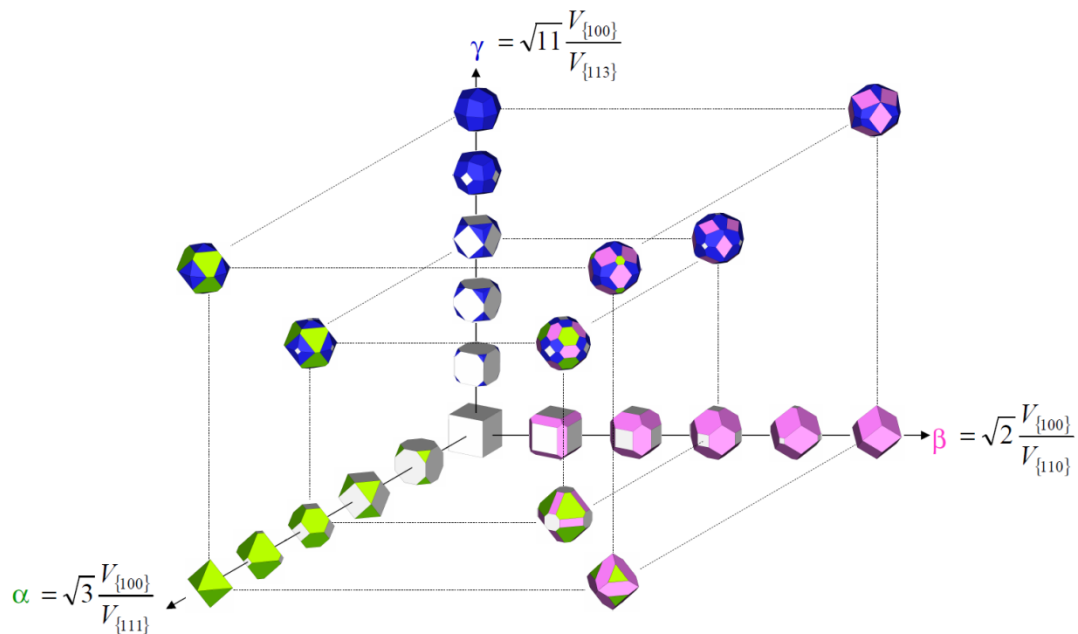


Figure 5-17: Phase diagram of crystal morphologies at equilibrium.

IV.3.1. Test sample

The test sample (SEM view on figure 5-18) is composed of two layers etched out at one corner by Oxygen RIE plasma. The main layer is thicker than 500 nm and is boron-doped at few 10^{18} at.cm⁻³. The final layer is 270 nm thick and heavily boron doped at 1×10^{21} at.cm⁻³ checked by SIMS measurement. This sample was MESA-processed in order to calibrate an etching setup. Several arrays of circular-shaped MESA-structure with different diameters are localized at one corner of the sample. In this case, the diamond was etched 720 nm in depth. The 8/9 of the surface was not etched out.

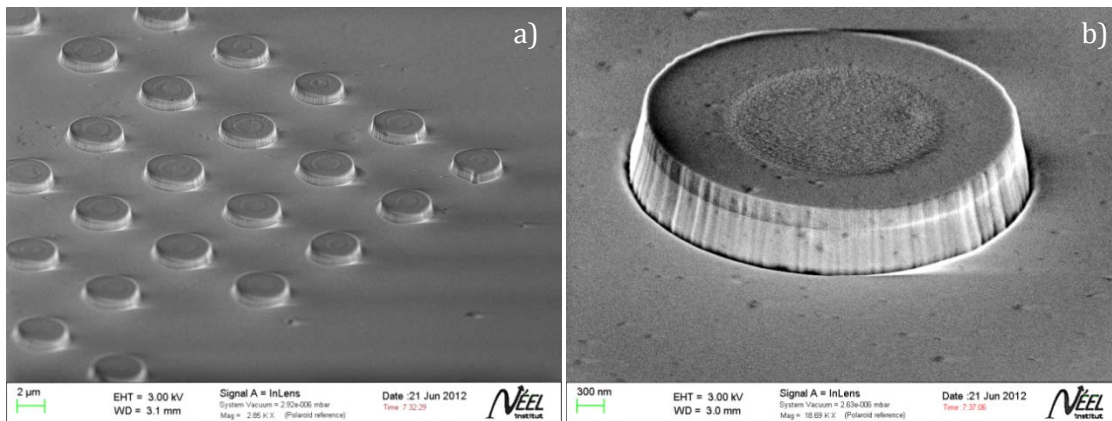


Figure 5-18 : Tilted SEM pictures at 60° of MESA-structures $\varnothing 4 \mu\text{m}$ dots array (on sample 1911Ap++).

IV.3.2. p-- overgrowth on mesa-structured cylinders

The test sample presented before was overgrown by a plasma mixture composed of 0.75% of methane with 0.32% of oxygen in the hydrogen. Surface temperatures read out oscillations were recorded in order to measure in situ the deposited thickness as described in Chapter 2. III.2.2. The sample was observed by SEM and by optical profile. SEM pictures were taken with an InLens ZEISS detector located at the vertical of the sampled surface on the same axis of the electron gun (figure 5-19). Pictures are not distorted and it is possible to measure precisely orthogonal distances. The optical profiler doesn't have a similar lateral resolution (1.3 μm sampling), but it provides a high resolution on the vertical axis, giving the information of the height.

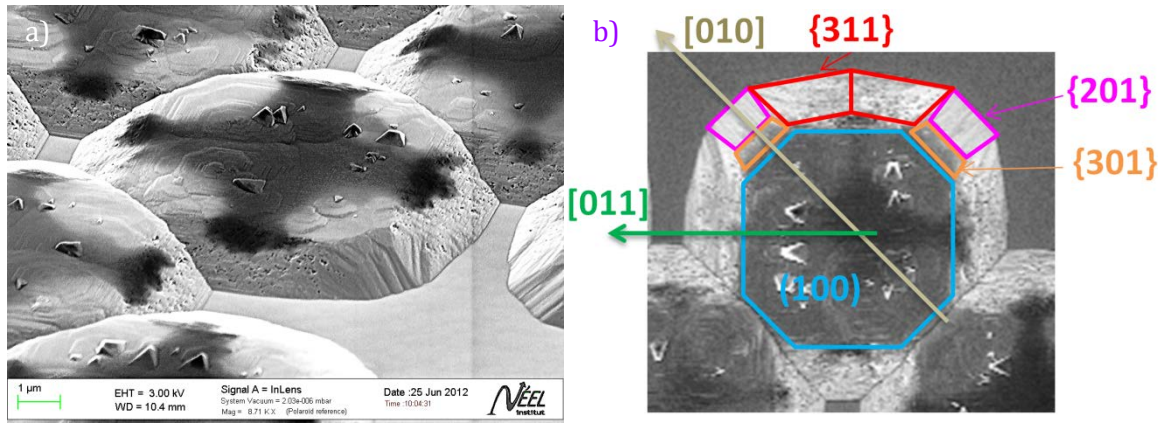


Figure 5-19 : SEM pictures of MESA-structures \varnothing 4 μ m array after overgrowth (0.75% (CH₄/H₂) and 0.32% (O₂/H₂) (name 2162A)). (a) tilted view at 60° and (b) top view.

There was no difference in height between the top and MESA bottom before and after overgrowth, but the diameter and the shape was totally different; regular facets appear and the base of the MESA is finally octagonal. The lateral growth was so fast that MESA structures were coalescing after only 70 min of growth. Under these conditions, growth parameters were extracted from MESA structures located at the border of the array. Figure 5-20 shows the graphical determination of the facets orientation and their growth rate. The vertical growth rate was measured by IR interferences coming from the 8/9 of the p++ layer which yields, a usual, a vertical growth rate of 7.3 nm (already measured in cross section in the case of thick growths under these conditions). The tangent angle from facets and the (100) plane was evaluated from the orthogonal (top view) SEM measurement and the height data from the optical profile. Facets found were oriented along (311) (angle between the planes: $\approx 25.2^\circ$), (201) (angle between the planes: $\approx 26.6^\circ$) and (301) (angle between the planes: $\approx 18.4^\circ$). The estimate of the facets growth rate was made by the projection of the plan in cross-section view ((010) or (011)) and the intersection with the (100) plan before overgrowth. Then, this distance was multiplied by the sinus of the angle from facet plan and the (100) plan. For example, the growth rate of the (311) results from $4240 \times \sin(\approx 25^\circ) / 70$.

Growth rates are summarized in table 5-5. The anisotropy factor $R = \frac{V_{g(010)}}{V_{g(100)}} = \frac{V_{g(001)}}{V_{g(100)}}$ was estimated around 6.65.

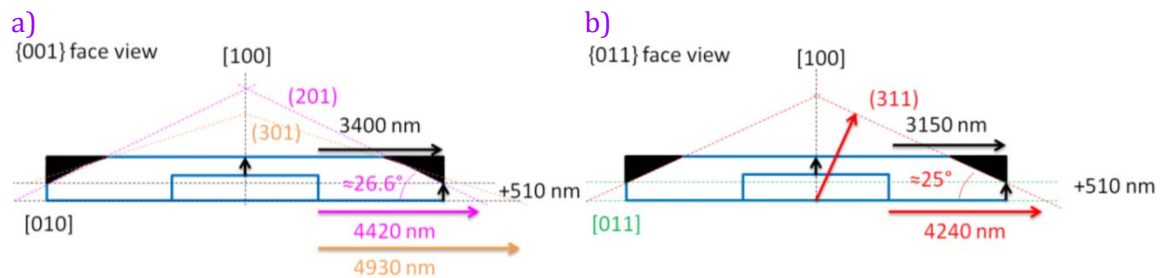


Figure 5-20 : Determination of growth rates for different faces.

Face considered	Type	Growth rate measured (nm/min)
(100)	normal	7.30
(011)	lateral	> 45.0
(010)	lateral	> 48.6
(201)	composed	22.3
(301)	composed	28.2
(311)	composed	25.8

Table 5-5 : Estimation of growth rates on the p-- overgrowth (0.75% (CH₄/H₂) and 0.32% (O₂/H₂)).

The slowest growing face was the (201) (growth rates along [201], [301] and [311] axis are in the same order), so composed faces look like more stable. However, because of defects present at the bottom of the MESA structures (trenching), it is not possible to conclude on the reliability of the stability of such composed faces. Twinning may also arise on an edge of a face, or on the faces of a re-entrant etch pits, and emerge at the surface. In our case, twinings are localized in circle at the position of the primary border of the MESA structure (visible on figure 5-19). The form of twinning was an accurate determination of the parameter α (Wild, et al., 1994). From SEM observation, $\alpha_{\text{vertical}} \approx 1.55$, leading to a {111} growth rate of 8.15 nm/min. $V_{g(100)} < V_{g(111)}$; $\beta_{\text{vertical}} \approx 1.55$ and $\gamma_{\text{vertical}} \approx 0.9$. In the lateral growth direction, $\alpha_{\text{lateral}} \approx 10.3$, $\beta_{\text{lateral}} \approx 1.53$ and $\gamma_{\text{lateral}} \approx 6.25$. These values might indicate a disappearance of {111} faces on the top side ($\alpha = \beta$, $\alpha > 1$, $\gamma < 11\alpha/5$) and dominance of {113} over {111} faces (Silva, et al., 2008).

To conclude, the top face (100) is the slowest to grow, which might be the reason of a very flat surface and the reduction of defect height. Faces {111} are visible only at twinning emergence. Face {113} are supposed to constitute borders of the sample at the equilibrium and face type {x10} with $x = 1, 2, 3$ appears as transition phases.

IV.4. Influence of growth sectors

A difference in thickness on the same layer was observed from a growth sector to another on the same HPHT sample. The analysis is reported in table 5-6.

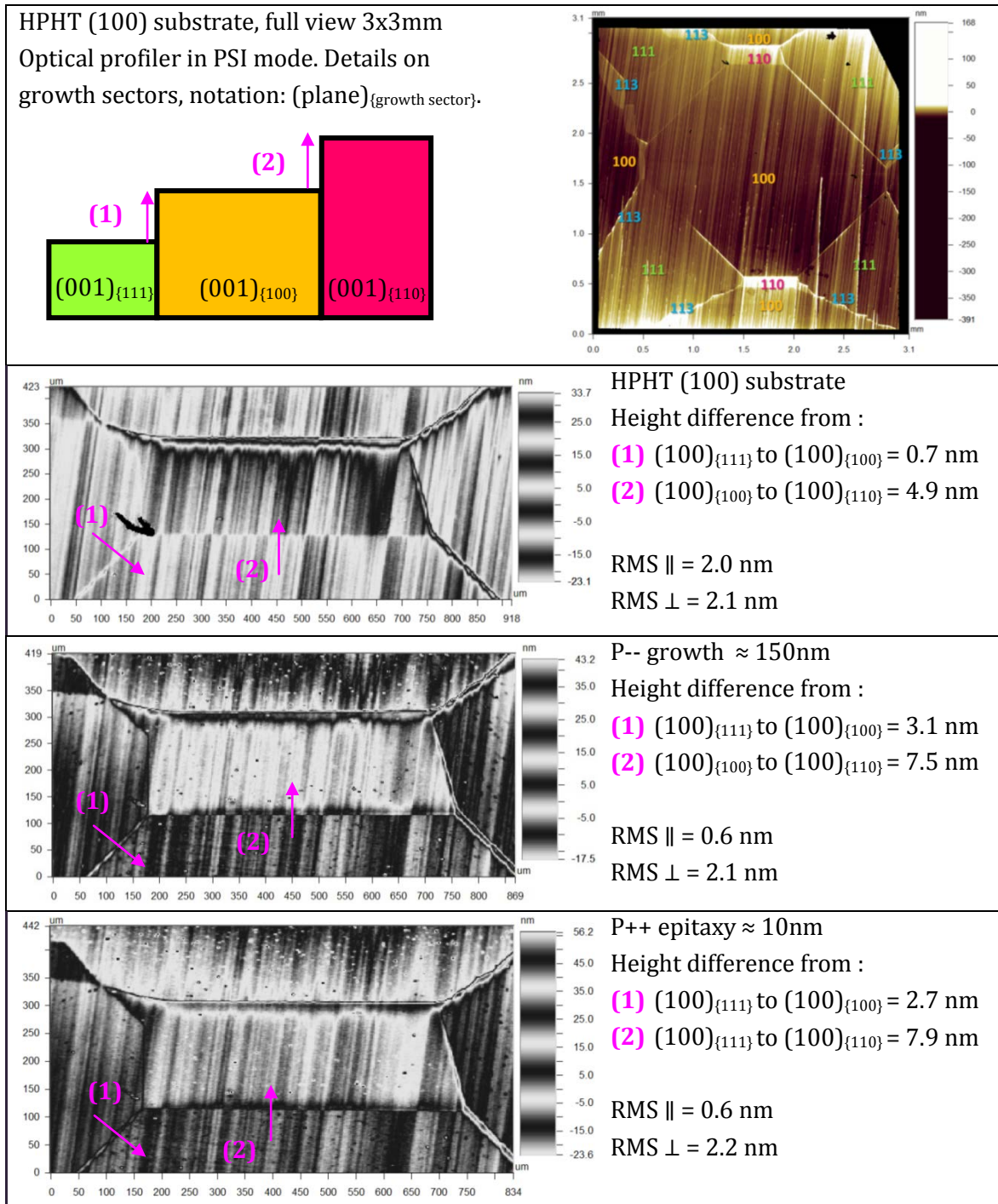


Table 5-6: Analysis of the height difference after growth by optical profile. The height difference was measured at the same starting and ending points on all pictures. The surface RMS roughness comes from an average of 5 lines, 90 μm long, taken parallel and perpendicular to polishing lines.

The substrate used was a 1b HPHT from Sumitomo with an “as received” polished surface with a typical 2 nm surface roughness. Growth sectors were labeled after determination of their impurity concentration from several CL monochromatic maps recorded at different wavelengths (FE^{T0} , Band A, H3, Ni...). The difference in altitude between $(100)_{\{100\}}$, $(100)_{\{110\}}$, $(100)_{\{113\}}$ and $(100)_{\{111\}}$ growth sectors was coherent with the sector’s nitrogen concentration which decreases in the order $\{111\} > \{100\} > \{110\} = \{113\}$ (Burns, et al., 1990). The p-- growth applied here is the same as used for the MESA overgrowth (0.75% (CH_4/H_2) and 0.32% (O_2/H_2)) leading to lateral overgrowth. The RMS surface roughness parallel to polishing line was reduced by a factor of 3 while it remained constant in the perpendicular direction. The p++ growth was made in the delta-layer growth condition, i.e. 0.5% (CH_4/H_2) and 6000 ppm (B/C). The RMS surface roughness parallel to polishing line was found to be of the same order as before, and in the perpendicular direction as well.

The height difference between $(100)_{\{110\}}$ or $(100)_{\{111\}}$ growth sectors with respect to the $(100)_{\{100\}}$ was increased by 2% on average (2.5 nm for 150 nm of growth) after p-- growth and by 4% after the p++ overgrowth (figure 5-21). We suppose that the initial height difference from the substrate was not enhancing this phenomenon, because in the case of the MESA structure overgrowth, the same step height was found before and after overgrowth. The most probable explanation in the difference of percentage could be coming from the change in the growth mode; the p-- growth is more anisotropic and could reduce this phenomenon. The layer grown on the $(100)_{\{110\}}$ growth sector was growing faster than on the $(100)_{\{100\}}$ growth sector, independently of the growth mode. On the contrary, on the $(100)_{\{111\}}$ growth sector the dependence is stronger; the step height is reduced after p++ overgrowth.

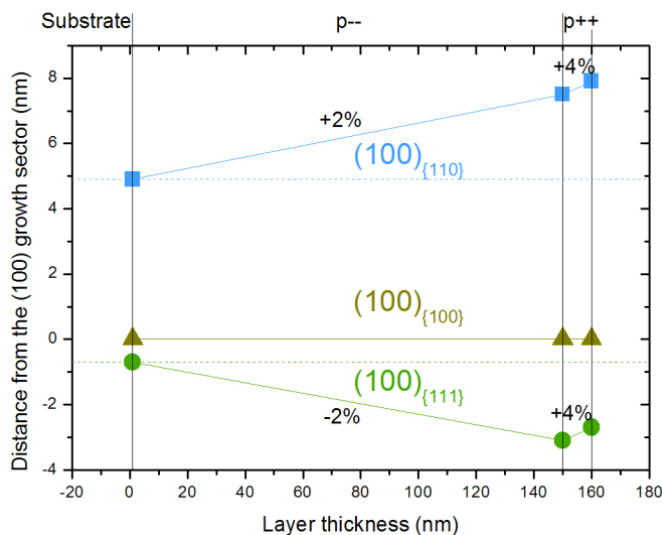


Figure 5-21 : Evolution of the distance separated two growth sectors with the growth.

The growth sector dependence is critical of delta-layer growth. It introduces local variations of the thickness. No evidence for doping efficiency alteration was identified.

V. CONCLUSION

New growth conditions were optimized to comply with delta-doping requirements.

The heavy boron doping of (100)-oriented single crystalline diamond ($[B] > 4.5 \times 10^{20} \text{ at.cm}^{-3}$) was grown with a (100) growth rate lower than 0.1nm per second (0.5% CH_4/H_2 and 6000 ppm in "surface contact" mode), providing homogenous layers in term of doping and thickness. Low surface roughness, equivalent to the substrate roughness ($\Delta\text{RMS} \approx 0 \text{ nm}$), have been reported.

The light boron doping of (100)-oriented single crystalline diamond (estimated $[B] < 1 \times 10^{15} \text{ at.cm}^{-3}$) was grown with a (100) growth rate equivalent to 0.1nm per second (0.75% CH_4/H_2 and 0.32% O_2/H_2 in "surface contact" mode) in lateral growth mode. Defects can be drastically flattened, minimizing alteration of the delta-layer properties.

The next step will be the optimization of the p⁻/p⁺⁺ and p⁺⁺/p⁻ interfaces sharpness.

VI. RÉSUMÉ DU CHAPITRE 5

Ce chapitre se concentre sur l'épitaxie de diamant monocristallin orientée 100 et sur le dopage au bore. L'objectif de ce chapitre est de présenter des solutions de dopage et d'épaisseur pour la réalisation du delta-dopage. Les points clés se trouvent dans l'homogénéité et dans la constance du dopage (p++) fort en bore (même quantité de dopage et d'épaisseur sur $3 \times 3 \text{ mm}^2$), ainsi que le dopage (p-) très léger ($[\text{B}] < 1 \times 10^{15} \text{ at.cm}^{-3}$) et la faible rugosité de surface.

Tout d'abord, l'interaction entre l'échantillon et le plasma a été étudiée afin d'optimiser l'homogénéité du dopage et de son épaisseur. Après la détermination de la position de contact la plus appropriée dans le plasma, l'effort suivant porte sur l'efficacité de dopage à concentration en méthane réduite, afin de réaliser des couches fortement dopées au bore en croissance lente. Le dernier point est l'étude de la croissance latérale et du faible dopage qui sont la clé dans la croissance d'une couche de recouvrement.

Dans notre chambre de réaction cylindrique en quartz (réacteur de type NIRIM), il est possible d'ajuster la position de l'échantillon à l'intérieur ou à la frontière de la boule de plasma (voir figure 5-1). Cela fournit un rare degré de liberté supplémentaire par rapport aux autres réacteurs MPCVD, qui permet notamment de régler finement les interactions physico-chimiques à la surface de l'échantillon. Nous allons examiner brièvement comment l'interaction entre le plasma et l'échantillon détermine l'homogénéité et le niveau de dopage.

- En position dite « contact au centre » la face supérieure de l'échantillon est localisée juste au-dessous du plan horizontal médian du guide d'onde. Cette position est très proche de la partie la plus chaude du plasma, près du centre de la boule de plasma. Dans cette configuration, le plasma colle simultanément sur l'échantillon, sur le porte-échantillon et sur le côté supérieur du quartz (sommets du tube interne).
- La position appelée « contact en surface » est située 5 mm en dessous de la précédente. La face supérieure de l'échantillon est en interaction avec la boule de plasma, mais la boule de plasma n'est plus en contact avec le porte-échantillon et le tube interne en quartz.
- Le « contact ponctuel » limite l'interaction avec la boule de plasma à une zone centrale sur la face supérieure de l'échantillon. Cette position est située à 5 mm en dessous de la précédente, et se trouve donc à la bordure du plasma. Un alignement précis de la surface de l'échantillon avec le centre de la boule de plasma est nécessaire dans le plan horizontal (X,Y) en vue d'assurer l'uniformité de la croissance de la couche épitaxiale.

De façon raisonnable, nous pouvons montrer que, avec un rapport constant de $[\text{B}_2\text{H}_6]/[\text{CH}_4]$ de la phase gazeuse, on obtient, en fonction du type de contact, des concentrations d'espèces réactives différentes à proximité de la surface : $([\text{BH}]/[\text{CH}_3])_{\text{point}} > ([\text{BH}]/[\text{CH}_3])_{\text{surface}} > ([\text{BH}]/[\text{CH}_3])_{\text{centre}}$. L'enrichissement local en espèces borées à la surface de l'échantillon exposé au plasma lorsque l'échantillon se déplace du centre de la boule de plasma vers la

bordure est en bon accord avec les résultats observés et présentés dans le tableau 5-2. Expérimentalement, en utilisant la même composition du gaz, on relève une incorporation de bore dans le diamant qui dépend du mode de contact: $[B]_{\text{point}} > [B]_{\text{surface}} > [B]_{\text{centre}}$.

L'effet de la vitesse de croissance sur l'incorporation du bore a été étudié (l'efficacité de l'incorporation est le problème principal). Pour ce faire, différents ratios CH_4/H_2 ont été utilisés, de 4% à 0,25%. Les croissances dopées au bore ont été réalisées avec du diborane (B_2H_6) comme source de bore, à une température de substrat de 830°C dans un réacteur MPCVD de type NIRIM avec une fréquence micro-onde standard de 2,45 GHz dans un tube en quartz. La puissance micro-onde est ajustée pour maintenir la température de surface à 830°C. La température est mesurée à l'aide d'un pyromètre monochromatique de longueur d'onde 0,98 μm .

Plusieurs façons de mesurer la teneur en bore dans le diamant sont disponibles. Ici, nous utilisons la spectrométrie de masse des ions secondaires (SIMS) et la cathodoluminescence (CL). Ces techniques sont complémentaires car le SIMS fournit le profil de bore en profondeur (y compris des atomes de bore interstitiels et complexes de bore) et la CL fournit les informations sur le niveau de dopage actif, dans un faible volume, sur une profondeur donnée (en fonction de la tension d'accélération) tout en fournissant des informations sur la qualité cristalline.

L'efficacité d'incorporer du bore diminue lorsque la concentration de méthane dans la phase gazeuse se réduit. Ainsi, à 1% (CH_4/H_2) le dopage est plus important qu'à 0,25% (CH_4/H_2), et il faut augmenter le rapport $(\text{B}/\text{C})_{\text{gaz}}$ pour atteindre un dopage au-dessus de la transition métal-isolant (4400 ppm et 6000 ppm pour respectivement 1 et 0,25% (CH_4/H_2)).

Avec des ratios $(\text{B}/\text{C})_{\text{gaz}}$ inférieurs à 1000 ppm, la vitesse de croissance augmente lentement avec la concentration en bore. Cette tendance est similaire à l'observation d'Issaoui et al. dans le cas d'une croissance épaisse de diamant dopé au bore (Issaoui, et al., 2011). Dans leur étude, le rapport (B/C) dans la phase gazeuse varie de 60 à 5000 ppm (0,5% (CH_4/H_2)) et la vitesse de croissance le long de l'axe $\langle 100 \rangle$ est en constante augmentation avec la concentration en bore. Mais cependant ils travaillent avec une densité de puissance élevée (140 mbar et 2400 W) et par conséquent l'efficacité de l'incorporation de bore est différente. Dans nos conditions de croissance (figure 5-9) l'efficacité de dopage (rapport de $(\text{B}/\text{C})_{\text{solide}}$ sur $(\text{B}/\text{C})_{\text{gaz}}$) est de 1,1 à 1,9, alors qu'il est de 0,06 à 0,11 pour l'équipe du LSPM (Issaoui, et al, 2012). Dans ce cas, on peut supposer que le dopage de 60 à 5000 ppm pour Issaoui vient d'une plus faible densité d'espèces borées actives dans le plasma et se compare à un dopage de 6 à 500 ppm dans nos conditions de croissance.

Toutefois, la figure 5-9 illustre une chute de la vitesse de croissance lorsque le rapport $(\text{B}/\text{C})_{\text{gaz}}$ dépasse les 1000 ppm (dans le cas particulier de 0,5% (CH_4/H_2) sous un débit total de 2 slm). Ce phénomène a également été signalé sur le diamant polycristallin (Gonon, et al, 1995.) et sur le diamant monocristallin (Gheeraert, et al, 1999.), (Tokuda, et al, 2007.). Dans

le cas de 0,6% (CH_4/H_2) la vitesse de croissance diminue de façon drastique vers 1000-2000 ppm (B/C)_{gaz} (Tokuda, et al, 2007). Ce comportement peut être issu du changement dans la chimie du plasma, régie par la température du gaz qui est modifiée par l'ajout de bore, et ainsi, les précurseurs pourraient être d'avantages consommés dans la majeure partie du plasma, conduisant à une croissance plus lente. En même temps, il faut tenir compte de la plus grande réactivité des espèces borées par rapport au carbone et ce ralentissement de croissance laisse plus de temps à la désorption du bore sur la surface en croissance. Il est possible que cette croissance soit anisotrope. Cela doit être étudié par la spectroscopie et la modélisation des plasmas.

La relation entre la concentration en bore incorporé et le débit total de gaz n'est pas claire. Cependant, avec un débit de gaz supérieur à 400 sccm, dans le cas de 4% (CH_4/H_2), la concentration de bore incorporé a augmenté et un dépôt de suie dans le réacteur a été observé en même temps. Selon la dépendance des réactions de décomposition chimique avec la température des gaz, nous supposons que la concentration en méthyle a été réduite près de la surface. En parallèle, la concentration en [BH] diminue, mais dans une moindre mesure. Il en résulte une augmentation locale du rapport [BH]/[CH₃], qui engendre une incorporation de bore plus élevée et une vitesse de croissance plus lente.

Cette tendance n'est pas visible aux faibles concentrations de méthane, car dans ce cas, la variation de dopage est du même ordre de l'erreur sur le contact plasma/échantillon. De plus, les croissances à faible concentration de méthane sont faites en position «contact en surface». Dans cette position, lorsque le débit est important, la température augmente moins que dans le cas précédent (4% (CH_4/H_2)). Par conséquent, la densité de méthyle diminue un très légèrement, et en raison de la diffusion rapide des espèces de carbone et le méthane en faible concentration, le rapport [BH]/[CH₃] ne diminue que légèrement. Alors, le taux de croissance reste constant, ce qui pourrait expliquer une plus faible incorporation de bore à 4 slm.

Ces études de l'influence du débit de gaz sur la vitesse de croissance et sur l'incorporation de bore permet de comparer des croissances de couches faites à différentes concentrations de bore et à faibles concentrations de méthane, mais gardant l'hypothèse d'un contact échantillon / plasma commun, et une pression et une température de surface identique. Dans la suite du procédé, les conditions retenues sont : 0,5% (CH_4/H_2) avec 6000ppm (B/C)_{gaz}, ce qui offre une vitesse de croissance de 5 nm.min⁻¹.

Les conditions de croissance du faible dopage (p--) mis en place par Volpe a nécessité l'ajout d'oxygène dans le mélange de gaz (Volpe, 2009 Thèse de doctorat, p 144.). Cette technique a été optimisée en terme de concentration du méthane et de l'oxygène (1,00% (CH_4/H_2) et 0,25% (O_2/H_2) sur diamant orienté (100)), en maintenant la même pression (50 Torr) et la même température de surface (910°C), dans le but de réduire considérablement la concentration en bore incorporé dans la couche épitaxiée, et en même temps, pour maintenir une qualité cristalline appropriée (en mesurant par CL la largeur des pics FE^{T0} et le rapport entre les pics et FE^{T0} et BE^{T0}). Ce type de dopage au bore est excellent et de bonne

qualité cristalline, confirmé par la fabrication de diodes Schottky qui résistent à des tensions de claquage de près de 10 kV (Volpe et al., 2010). Toutefois, cette optimisation des conditions de croissance provoque l'apparition de larges défauts à la surface de l'échantillon et une rugosité RMS importante. Ce processus peut ne pas convenir à la reprise d'épitaxie de couche p++ homogènes et planes; la cible est une rugosité de surface RMS inférieure à 1 nm.

Afin de simplifier l'étude, toutes les croissances ont été faites dans les mêmes conditions de plasma (50 Torr, 910°C, débit total de gaz : 200 sccm) avec la même position (contact de surface) utilisés lors de la couche p++. L'idée d'utiliser la même position provient de l'optimisation du processus p++ et garder la même position entre p++ et p-- est un avantage pour la réalisation d'échantillons multicouches tels que les structures delta et les super-réseaux. Cela supprime une incertitude dans la position qui peut introduit une série d'erreurs dans le dopage et la vitesse de croissance.

La croissance latérale est une croissance anisotrope où la vitesse de croissance verticale est plus faible que dans le plan longitudinal (en latéral). Les rapports méthane-hydrogène et de oxygène-hydrogène ont une influence importante sur le mode de croissance du diamant (nucléation 2D, écoulement de marches...). L'objectif est d'atteindre une croissance lente selon l'axe de croissance (équivalent à 0,1 nm par seconde pour obtenir une bonne précision sur l'épaisseur déposée) et de réduire la rugosité de surface par une croissance latérale rapide (surface plane). La première tâche à consister par combler les trous induits par le polissage de substrats diamant CVD et de lisser les lignes de polissage substrats diamant HPTH.

Un mélange gazeux constitué de 0,25% (CH_4/H_2) et 0,25% (O_2/H_2) place le système de réaction proche de l'équilibre croissance/gravure (la croissance du diamant est un mécanisme hors équilibre). Dans cette situation, la surface est marquée par une prédominance de FHs avec une densité clairsemée PHs. Ils peuvent être la conséquence d'une croissance sous la forme d'îlots. En maintenant la même teneur en oxygène (0,25% (O_2/H_2)) et en augmentant le rapport de méthane de 0,5 à 1% (CH_4/H_2), les FHs ne sont plus observées. La surface est alors composée de PHs inclinées suivant la désorientation du substrat et avec une densité comparable à la densité de trous micrométriques présents à la surface du substrat « brut d'usine ». Ceci illustre l'effet de la croissance 3D (îlots) modulé par la concentration de méthane et la concentration d'oxygène dans la phase gazeuse. La hauteur des PHs diminue avec l'anisotropie de la croissance latérale. Si l'on compare la rugosité de surface RMS sur une surface plane, alors la recette avec 0,75% de méthane fournit la rugosité la plus faible avec de minuscules PHs très plats sur les substrats CVD « brut d'usine ». En allant plus loin dans cette enquête, la hauteur des défauts 3D peut être modulée et certaines tendances apparaissent (figure 5-15).

Les figures 5 15 soulignent les différences dans l'évolution de la hauteur dans le cas des PHs et des RHs. Pour ce faire, on trace le rapport de hauteur (en moyenne) des défauts sur le temps de croissance. Cette valeur est indépendante de l'épaisseur de la couche de

croissance; la variation de concentrations d'oxygène et de méthane induit une modification de la vitesse de croissance verticale (la croissance est anisotrope). Il est important de percevoir clairement la différence dans l'évolution de la hauteur entre RHs et PHs. Les RHs sont dix fois plus petits que les PHs, indépendamment du substrat utilisé ou du mélange de gaz; la distribution en hauteur des RHs est très large par rapport aux PHs. Cette situation découle de leur origine et du mécanisme de croissance qui les rend plus gros. L'origine principale de la rugosité de surface provient des PHs. La hauteur des PHs est la plus faible, avec un taux de méthane de 0,75% avec 0,25% d'oxygène dans l'hydrogène. Cette condition de croissance a été appliquée à des substrats HPHT « brut d'usine » et pseudosubstrats p++. Un rapport d'oxygène légèrement plus élevé (0,32%) a montré une légère amélioration de la rugosité.

Une reprise d'épitaxie dans ces conditions p-- a été effectuée sur des plots de diamant cylindriques gravé MESA, afin d'observer l'effet de l'anisotropie. On ne constate aucune différence de hauteur entre le haut et le bas des plots MESA avant et après re-croissance, mais le diamètre et la forme sont totalement différents; des facettes régulières apparaissent et la base de la MESA est enfin octogonale. La croissance latérale a été si rapide que les structures MESA se sont rejointes après seulement 70 min de croissance. Dans ces conditions, les paramètres de croissance ont été extraits des structures MESA situées à la frontière du motif de plots par MEB et par profilométrie optique. La face supérieure (100) est 6,7 fois le plus lente à croître qu'en latéral, ce qui explique la surface très plate et la réduction de la taille des défauts. Des facettes {111} sont visibles seulement en bordure des plots initiaux. Des facettes {113} sont supposées constituer les bords des plots MESA à l'équilibre (octogone) et un type de facette {x10} avec $x = 1, 2, 3$ apparaît comme des phases de transition.

Chapter 6.

OPTIMIZATION OF P-- /P++/P-- INTERFACES, APPLIED TO DELTA- S T R U C T U R E S

I. INTRODUCTION

This chapter is focused on the optimization and the characterization of the interface between p++ and p-- homoepitaxial (100)-oriented diamond layers. The aim of this chapter is to present how the plasma conditions and process flows were optimized in order to achieve the delta-doping of diamond. The target value for the steepness of the boron concentration gradient from heavily boron-doping p++ layer to lightly boron-doped p-- layer (and the symmetric p++/p--) was in the Debye length range, which is about 0.1 nm/decade for an acceptor density of 9×10^{20} at.cm⁻³.

First of all, multilayers samples were made under growth conditions determined in Chapter 5. . Within each of these samples, one process parameter was varied in order to analyze the optimization of the process flow toward sharper interface. The effect of the growth and etching rates will be discussed. New processes for the rinsing plasma mixture will be investigated. The second part deals with characterization techniques. The most common one is the Secondary Ion Mass Spectrometry (SIMS). The extremely low thickness of delta-doped layers pushes the analysis to its limits. These limitations will be discussed in detail. Because of them, other kinds of characterization were performed, such as X-ray diffraction (XRD) and transmitted electron microscopy (TEM). The combination of these techniques brought a new point of view and helped to conclude about the sharpness criteria satisfaction for the diamond delta-structure manufacture.

II. SIMS ION MIXING EFFECT ON ULTRA-THIN LAYER

SIMS techniques use a bombardment by energetic ions (in our case Cs⁺ or O₂⁺) to interact with the sample by etching it and simultaneously analyzing recoiled secondary ions, as explained in Chapter 3. IV. . The depth resolution of the concentration profile depends on these primary ion masses, energy, incidence angle and on the roughness of the sample. Below 100 nm in thickness, the SIMS induced ion mixing effect is no longer negligible. This affects strongly the boron doping profile measurements by broadening. Ion mixing is particularly visible when two adjacent layers in the same sample have a large difference in doping level (from 1×10^{15} at.cm⁻³ to 1×10^{21} at.cm⁻³) or in chemical composition. Takano *et al.* applied on co-doped (B, N) delta-doped silicon a method to extract the depth resolution parameters (Takano, et al., 2003) using a theoretical model proposed by Hofmann, also called the mixing-roughness-information (MRI) depth model (Hofmann, 1977) (see Chapter 3. IV.3.). From this model, it is possible to localize the position of the delta-layer. To do so, some parameters (mixing length, information depth and roughness) have to be determined.

II.1. Effects on the thickness determinations in thin layers

To estimate clearly the SIMS ion mixing phenomenon on the p++ diamond layer thickness resolution, isotopic-enriched methane (^{12}C : 99.998% + ^{13}C : 200 ppm) was used to grow the buffer and capping diamond layers, while standard methane (^{12}C : 98.9 % + ^{13}C : 1.1%) was used to grow the p++ layer*. To avoid any effects from surface roughness, a particularly flat sample was selected. The surface was polished by Syntek Co., Ltd.; the resulting surface RMS roughness checked by optical profile was below 0.3 nm before overgrowth. In this study, 500 nm of p-- buffer layer were grown at NIMS in a high plasma density NIMS-type reactor with the ^{12}C -enriched methane, at 10% (CH_4/H_2) in order to keep a good crystalline quality and a flat surface (Teraji, 2006). A p++ layer was then grown at Institut Néel in the modified NIRIM-type reactor from normal $^{13}\text{CH}_4$ methane abundance (^{12}C : 98.9 %) with 0.5% (CH_4/H_2) and 6000 ppm $(\text{B}/\text{C})_{\text{gas}}$ during 3 minutes. The final layer, *i.e.* cap layer was grown at NIMS with isotopic-enriched methane, 1% (CH_4/H_2) to overgrow 50 nm of intrinsic diamond. The surface RMS roughness as checked by optical profilometry was below 1 nm after growth. No particular etching-back process including either oxygen or hydrogen was applied. Boron concentration evolution with depth followed a typical (thick) delta-doping profile, as shown on figure 6-1, and boron (green dots) and ^{13}C (blue dots) signals were matching. However, performing SIMS measurement with cesium primary ions under an acceleration energy of 14.5 keV or with oxygen primary ions at 3 keV led to totally different profiles.

* This study was performed under the supervision of Drs. T.Teraji and S.Koizumi at NIMS, Tsukuba, Japan during a 6 months internship. This work was also supported by the Strategic International Collaborative Research Project from the Japan Science and Technology Agency, Japan and Grant-in-Aid for Scientific Research from the Japan Society for the Promotion of Science, Japan (No. 18760241).

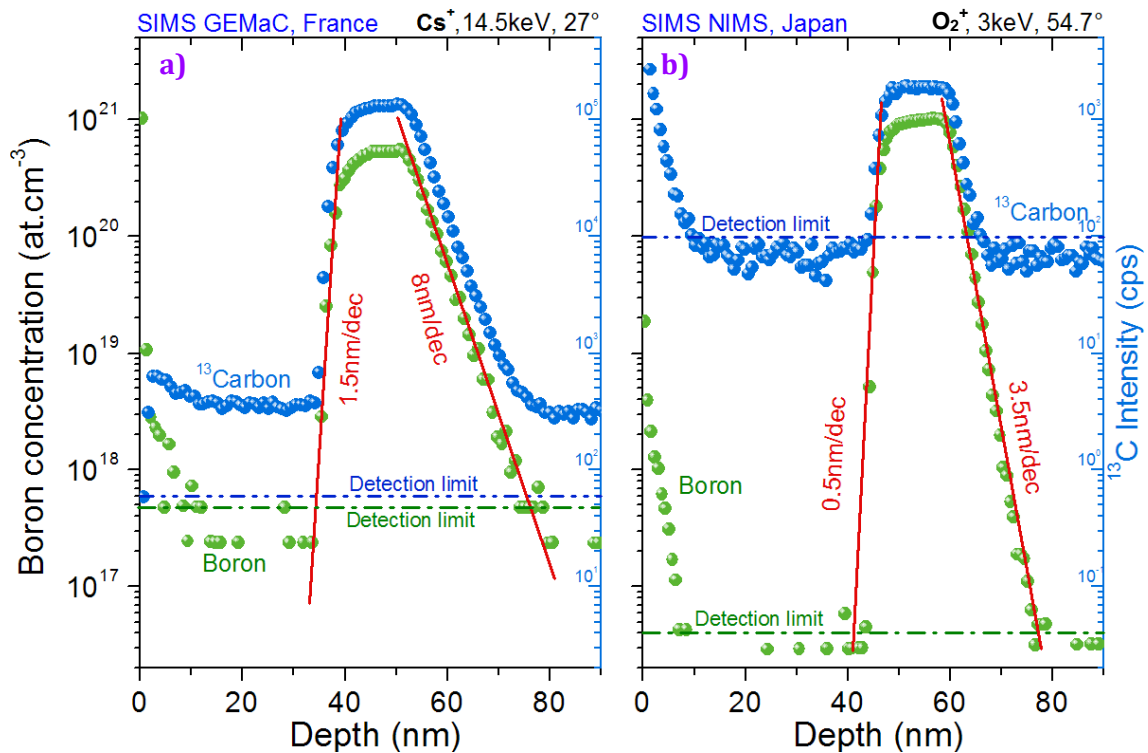


Figure 6-1 : Comparison of SIMS boron (green) and ¹³C (red) concentration profiles for two different analysis conditions ((a) Cs⁺ at 14.5keV and (b) O₂⁺ at 3 keV) on the same sample (2871Aδ) composed of an isotopically ally natural p++ layer embedded between two isotopically enriched ¹²C undoped layers.

On such profiles, the substrate is always localized on the right side; the surface is on the left at the depth position quoted "0". SIMS analysis was performed from the surface to the substrate. Memory effect and ion mixing (atoms forward scattering) are effective from the left to the right of the figures. In consequence, if we consider a box-shaped doping profile (the profile of ¹³C), then the falling interface (localized at the p++ top side) will be always shows a sharper leading signal compared to the broad trailing tail at the rising interface (localized at the p++ bottom side). We can observe this phenomenon on the SIMS profiles both with Cs⁺ and O₂⁺. The same slopes in ¹³C and ¹⁰B concentrations were observed. Indeed, the boron incorporation in the diamond follows the incorporation of ¹³C from the methane. This observation points out the similarity in fast incorporation mechanism kinetic of carbon and boron during the growth. The use of low energy oxygen ion is benefic in mass spectrometry analysis because the ion-mixing effect is reduce; the leading signal decrease from 1.5 to 0.5 nm/dec and the trailing signal from 8 to 3.5 nm/dec. However, at low energy primary, on both interfaces, the SIMS signal analyzed shows an exponential behavior which indicate a true interface sharp enough to not been detected and no conclusions on the interface asymmetry can be made. Nevertheless, with the profile of the first derivative of the boron concentration variation with depth, it is possible to estimate the thickness of the p++ layer (15 nm) under both SIMS conditions.

This estimation of the p++ thickness is confirmed by mixing-roughness-information (MRI) simulation (figure 6-2) presented in Chapter 3. IV.3.

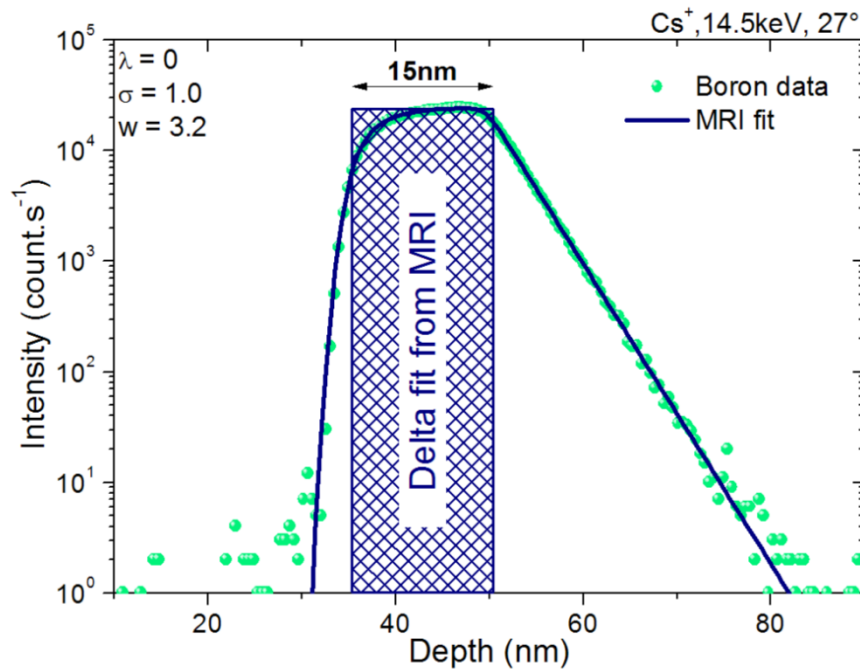


Figure 6-2 : Best fit of SIMS boron profile by MRI model.

At first the information length parameter, which defined the relation of forward diffusion with the depth was supposed to equal to zero. This hypothesis is coherent with the studied structure, because the p++ layer is localized very close to the surface (*ca.* 40 nm). Then, the boron profile was input into the calculation as a box-shaped boron profile with a doping level of 1×10^{21} at.cm⁻³. Finally the position of the delta-layer in the virtual structure (blue box in figure 6-2) is adjusted with mixing and roughness parameters in order to make the MRI fit (blue line) corresponding with SIMS data (green dots). A roughness contribution value taken at 1.0 nm and a value of 3.2 nm for the ion-mixing length provide the best fit for SIMS data with Cs+ primary ions. 3.2nm in ion-mixing is in the same ion-recoiling Monte-Carlo range (detailed in Chapter 3. IV.2.).

The slope of ¹³C and B profile shows a similar trailing signal, the SIMS limit, even at low energy. With the enrichment in ¹²C of buffer and cap layer it has been possible to identify a very fast incorporation of both C and B atoms, but the SIMS resolution is not good enough to conclude on the fastest incorporated atom. If the boron doping layer thickness can be measured and confirmed by simulation, no value on the top-side interface sharpness below 0.5 nm/decade may be drawn from SIMS measurements and MRI simulation. The corresponding sharpness value got with Cs+ ion has been found on delta-samples after in-situ and ex-situ etching,.

II.2. Thickness effects on peak concentration values

Another effect of the ion-mixing associated to the SIMS technique is an under-estimate of the peak concentration when a layer becomes too thin (visible from 15 nm in the present situation). This is typically the case on figure 6-3; five p++ layers have been growth under the same condition but with different durations (1, 2, 3, 4 and 5 minutes).

In this sample, the growth started with the buffer layer made with p-- growth condition (1% (CH₄/H₂) and 0.25% (O₂/H₂), 50 Torr at 910°C) with a total flow of 200 sccm. Before starting the growth of p++ layer, the plasma gas mixture was switched to pure hydrogen at 2 slm under 50 Torr. According to gas monitoring (see annexes II.), 3 min of pure hydrogen at 2 slm were enough to reduce by 3 orders of magnitude the methane and oxygen ratios, keeping the pressure stable and the surface temperature high enough to avoid any boron passivation effects. During this time, the temperature was decreased around 830°C, a temperature well-suited to p++ growth. The total flow was kept at 2 slm when the plasma composition was switched from the pure hydrogen into boron doping growth. P++ growth was made with 0.5% (CH₄/H₂) and 6000 ppm (B/C), 50 Torr at 830°C to reach 1×10²¹ at.cm⁻³. As described in detail in Chapter 2. II.2.2. , pure hydrogen and the doping gas mixture are flowing in parallel. When the switch is made, the p++ growth starts at nominal conditions very quickly (monitored by mass spectrometry). The end of the p++ growth corresponds to a switch to pure hydrogen plasma at 2 slm, and the same pure hydrogen plasma rinsing at 2 slm was applied. During a second rinsing step (3 minutes), the temperature was increased to around 880°C (plasma composed of H₂ only), suitable for the p-- growth. The p- growth started after switching from pure hydrogen plasma to NID plasma; the surface temperature increased to 910°C with the addition of methane and oxygen. These steps were reproduced several times depending the numbers of p++ required.

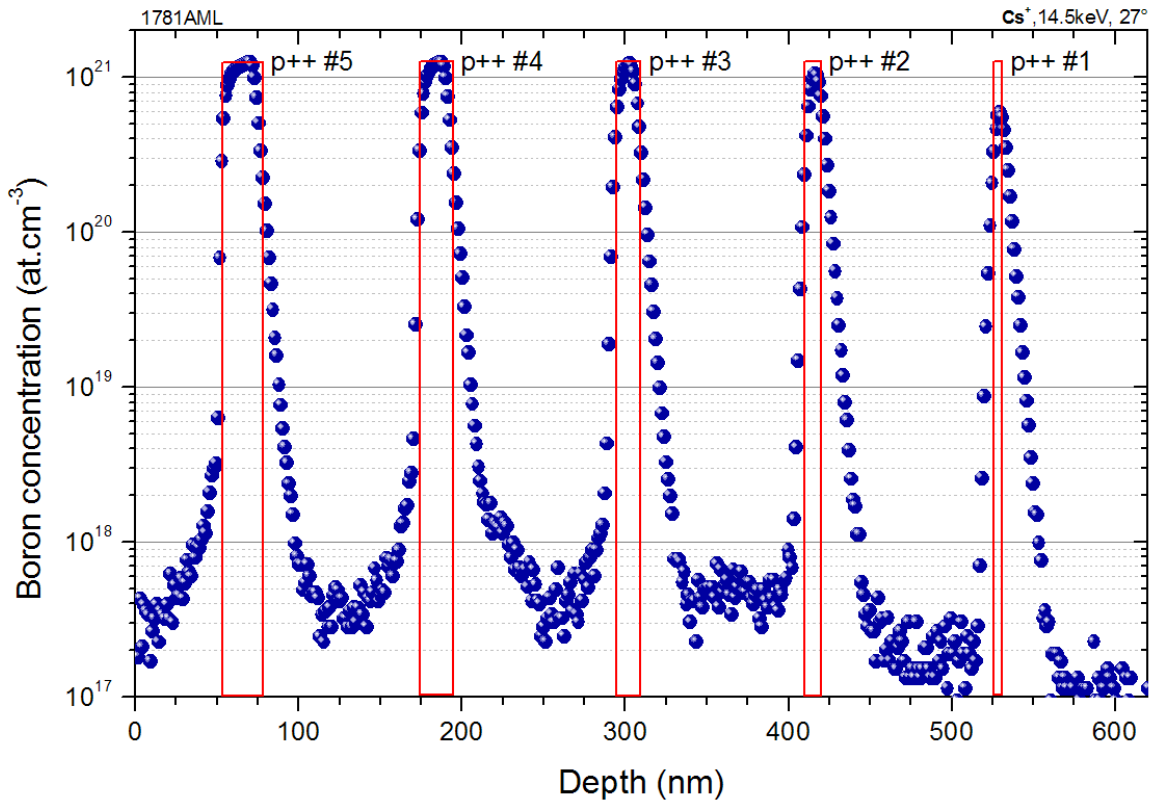


Figure 6-3 : (blue): boron profile of a multilayer sample composed of p++ with different thicknesses. p++ growth were made with 0.5% (CH₄/H₂) and 6000 ppm (B/C)_{gas}, 50 Torr, at 830°C under 2 slm, to reach 1×10²¹ cm⁻³ in boron doping. p-- growth conditions are 1% (CH₄/H₂) and 0.25% (O₂/H₂), 50 Torr at 910°C with a total flow of 200 sccm. In between p++ and p-- growth steps, 3 min of pure hydrogen plasma was applied. P++ growths durations were 1, 2, 3, 4 and 5 min; p- growth time was fixed at 10 min. (red): expected positions of box-shaped p++ layers.

Thicknesses of p++ layers are extracted from the first derivative curve of the boron depth profile. Leading and trailing slopes of the boron doping profile show a pure exponential behaviour. This is a confirmation of a very sharp interface (limitation by the measurement technique). Local extrema of the first derivative curve give the position of virtual interfaces the p++, if we consider the doping as box-shaped. The layer on the left side (5 min of p++ growth) shows a peak concentration similar to that of a thick p++ sample. On the contrary, the thinnest layer grown in this sample (on the p++ #1 right side) was very thin (1 min of p++ growth). If we assume that growth started immediately at the nominal boron doping (*i.e.* 1×10²¹ at.cm⁻³), then the boron concentration peak appearing markedly lower in concentration is an effect of the SIMS conditions used here. A fit of the apparent peak boron concentration as a function of the layer thickness by a cumulative distribution function $y = A \cdot (1 - e^{-\lambda x}) + y_0$ gives a mean value $1/\lambda$ around 4 nm. Thus, under these measurement conditions, more than 50% of the nominal concentration are not detected when the layer is thinner than $\ln(2)/\lambda = 2.8$ nm. This value is similar to the RMS surface roughness of the sample studied here.

In conclusion, SIMS does not provide any reliable peak boron concentration value on boron-doped layers when their thickness becomes lower than 15 nm. In the case presented above,

this appears to result from ion-mixing and roughness combined effects. An alternate possibility to study very thin layers on rough substrates would be to use cross-section high resolution transmission electron microscopy (HTEM).

II.3. SIMS memory effects

On figure 6-4, we can examine a periodic multi-layers sample composed of an alternate of p- and p++ layers. These thin p++ layers are located between 550 nm and 1150 nm below the surface. The RMS surface roughness of the substrate was around 3 nm and it was 7 nm after growth. This growth was 1.5 μm thick, which is too thick to ensure a good surface quality; this results mainly from PHs[†] height and density.

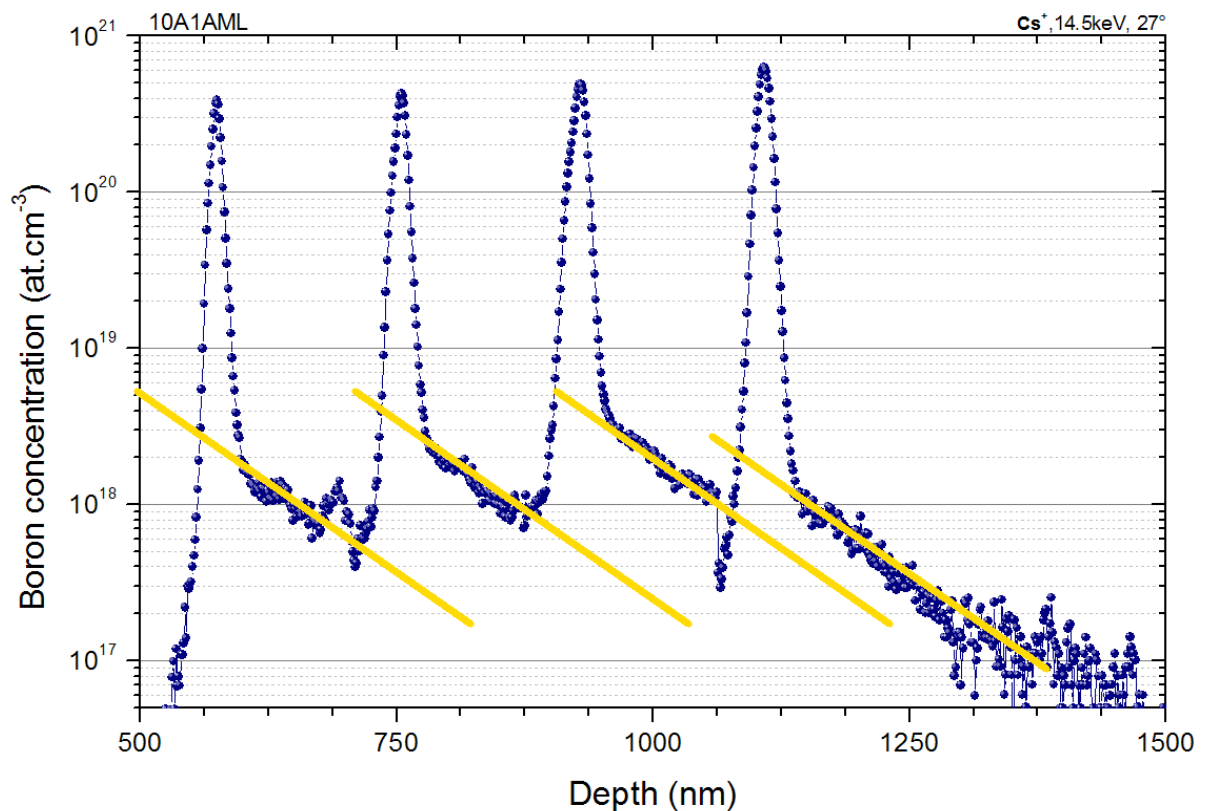


Figure 6-4 : Boron profile of a periodic four p++ layers (5 nm) in a buried superlattice sample plotted on indigo balls; parallel yellow lines illustrate the boron memory effect (-220 nm/decade).

For this sample, the growth started with the buffer layer made with p-- growth condition (1% (CH₄/H₂) and 0.32% (O₂/H₂), 50 Torr at 910°C) with a total flow of 200 sccm. Before starting the growth of p++ layer, the plasma was switched into pure hydrogen plasma at 2 slm under 50 Torr, as presented before. P++ growth was made with 0.5% (CH₄/H₂) and 6000 ppm (B/C), 50 Torr at 830°C to reach 1×10²¹ at.cm⁻³.

[†] See "defects definition" in Chapter 4. VII.

On figure 6-4, the cap layer (last p-- layer just below the surface) has a boron concentration lower than 1×10^{16} at.cm⁻³ (not visible on the graph). In between each p++ layer, we repeated the same p-- growth conditions. However, as we can see on the figure, the apparent boron profile shows a regular decreasing slope on p-- areas (yellow lines). The same slope remains inside the buffer layer (below 1150 nm), which is historically the purest p-- layer, *i.e.* grown before boron-enriched plasmas. This could be a clear memory effect: boron atoms contaminate the SIMS chamber during the analysis, and its concentration decrease with the sputtering time, leading in a tilted background. A fit of the boron profile in the buffer layer (1140 – 1500 nm from the surface) by an exponential distribution $y = A \cdot e^{-\lambda x} + y_0$ gives a mean value $1/\lambda$ around 85 nm. The sputtering rate in these conditions was 0.175 nm.sec⁻¹. In consequence, the residual boron concentration decreases with a time constant of 8 minutes.

This cannot explain the exponential increase of the p++ peak concentration with depth. Another artifact can occurs, as for example, a tilt of the sputtering crater. Usually, over long p++ growth, the doping level is stable. In this case if the sampling crater is tilted, it introduces an additional boron memory effect, which might justify the high value of the time constant previously calculated.

However, no gas monitoring was performed during this multilayer growth, and this point warrants further investigation.

Whatever the depth of the p++ layer in the multi layer, when the sample is not too rough at the surface, it is possible to compare p++ layers together independently of their location within the sample. The sample on figure 6-4 was the worst case for SIMS analysis; usually p++ layers were much shallower (*ca.* 50 nm).

III. OPTIMIZATION OF INTERFACES SHARPNESS

In the case of alternate p-- and p++ growth, the rinsing plasma is extremely important if the plasma is kept on. Helium was added to the gas mixture in order to increase the gas flow and to reduce the boron memory effect in the reactor. Helium atoms are not reactive and do not participate chemically to the growth mechanism. However, helium metastable species are generated in the plasma and increased the density of reactive species, like oxygen radicals. In addition, helium and hydrogen are purified at the same time in our catalytic gas purifier (trapping nitrogen, water, argon...). This continuous plasma process is an original development at Institut Néel. In contrast to this option, other groups (Edgington, et al., 2012) or (El-Hajj, et al., 2008(b)) used a dedicated MPCVD growth reactor for each kind of growth. We have also performed some multi-reactor growth sequences, for example for the isotopically purified samples described above.

III.1. Diamond growth conditions properties on p++ layer interfaces

We are now aware of various artifacts introduced by SIMS: the underestimate of the peak boron concentration when the layer becomes very thin, the exponential broadening of the composition interfaces and the difficulty to precisely localize these interfaces. We have proposed to determine this position assuming a box-shape doping and using the first spatial derivative of the doping profile.

In figure 6-5, we can see two different types of growth conditions applied to thin p++ growth. In blue, p++ was made with 0.5% (CH_4/H_2) and 6000 ppm (B/C), 50 Torr, 830°C, at 2 slm in the “surface contact” mode as described before. In green, p++ are made with 4% (CH_4/H_2) and 1200 ppm (B/C), 30 Torr, 830°C at 100 sccm in the “center contact” mode; these growth conditions have long been used at Institut Néel as reported in previous works (Baron, 2005 PhD thesis), (Achatz, 2008 PhD Thesis) and (Volpe, 2009 PhD thesis).

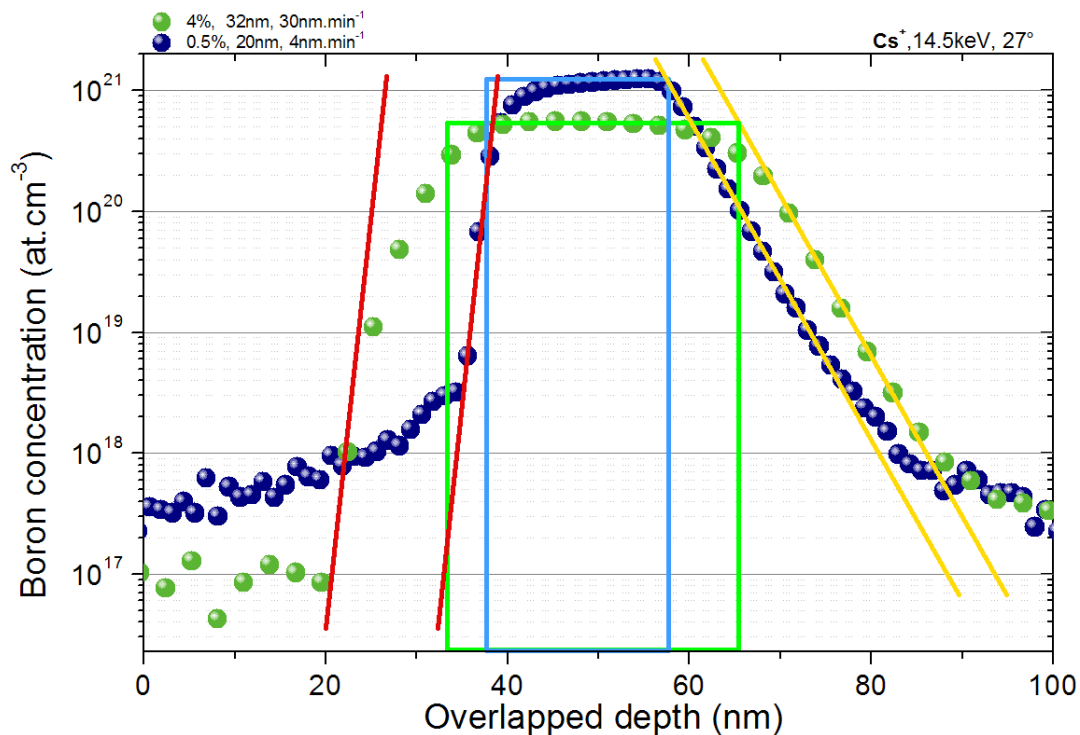


Figure 6-5 : Boron profiles of two p++ layers grown with a different growth conditions : 4% (CH_4/H_2), 1200 ppm (B/C)_{gas} (on green dots, sample 10B1AML) and 0.5% (CH_4/H_2), 6000 ppm (B/C)_{gas} (on blue dots, sample 1781AML). Green and blue boxes represent the location of the box-shaped p++ layer. Parallel yellow and red lines indicate the exponential component induced by ion mixing.

Thicknesses of p++ layers are extracted from the first derivative curve of the boron profile. Local extrema of the first derivative curve yield the boundaries of the p++ region if we consider the doping spatial distribution as box-shaped. These layers have not been subjected to any particular plasma treatment (*i.e.* etch-back) but for the usual 3 min of hydrogen plasma before and after the p++ growth step. They showed a similar thickness.

P⁺⁺ growth at 4% (CH₄/H₂) (in green) showed a smoothly rising interface with an inflection point (cusp) at 65 nm (on the right side of figure 6-5). Ion-mixing during the SIMS analysis follow an exponential law, resulting in a straight line on the semi-logarithm graph. This growth was quite fast (30 nm.min⁻¹), and it resulted in a growth transition between the p⁻ with a low boron concentration and the p⁺⁺ peak concentration. In other words, because of the short growing time (*ca.* 1 min) the p⁺⁺ layer had a very small boron concentration plateau since the boron concentration above the surface of the diamond took just a little bit less than 1 minute to stabilize. This was observed by gas monitoring and it is especially true because the growth at 4% (CH₄/H₂) was performed at 100 sccm. At 2 slm, in the case of the growth at 0.5% (CH₄/H₂), this plateau was larger. The rising interface was straight, and the falling interface was very sharp (below 1 nm/decade), so the process at low methane concentration and at high flow is the best to build a delta-structure.

III.2. Optimization of the rising interface

At the beginning of a p⁺⁺ growth, we do not use a methane pulsed into a stable plasma mixture composed of hydrogen and diborane (Tranchant, et al., 2012). We do not use background plasma of hydrogen and methane with a short injection of a diborane, either (Kunze, et al., 1999). In our case, p⁺⁺ growth starts after rinsing plasma. From measurement of the time diffusion of methane, oxygen, diborane and hydrogen by mass spectrometry (see annexes I.), it was possible to determine the minimum duration of the rinsing plasma necessary to eliminate efficiently carbon and boron species in the gas phase before starting a new growth. The reduction of the trailing length was investigated. To do so, the p⁺⁺ total gas flow was modified, preparation plasma composed of diborane and hydrogen was introduced in the process, the plasma was interrupted and the contact mode was changed during growth. In spite of various attempts, the trailing length could not be reduced below 8 nm/decade. At the opposite, the introduction of preparation plasma composed of diborane and hydrogen before the p⁺⁺ growth increased the boron contamination: the boron background was higher in the sample after the growth of the p⁺⁺ epilayer. The interruption of the plasma and its ignition under the p⁺⁺ gas mixture did not induce any modification in the trailing length. The change of contact mode during the H₂/p⁺⁺ plasma switch introduced a stepped trailing: the interface was broadened. However, the SIMS at low primary ions has revealed a low trailing of 3.5 nm. In addition, the isotopic methane tracer has confirmed the broadening of the trailing signal by the ion-mixing effect. In conclusion, the p⁺⁺ growth at 2 slm provided a rising interface sharper than 3.5 nm/decade. Scanning transmission electron microcopies at high angle annular dark field view (STEM-HAADF) should allow the sharpness evaluation of these interfaces below the SIMS limit resolution. 3 minutes of rinsing plasma at 2 slm was selected as an efficient and short hydrogen plasma step. On multilayers grown under these conditions, the rising interface shows a straight slope. This is the indication of a pure ion-mixing effect, and leads us to expect the sharpness of the interface to be below 0.5 nm/decade (see figure 6-1). On the other hand, when the rinsing

plasma was not applied, the rising interface showed an ion mixing with different slopes. Cusps indicated a non-uniformity of the boron doping evolution at the interface; this was especially true when the p-- growth needed higher methane content than the p++.

III.3. Optimization of the falling interface

Oxygen is a key point to grow multi-layers as shown on figure 6-6. Oxygen was added in the p-- growth recipe. As reported by Omnès and co-workers, generation of hydroxyl species in the plasma is critical for an efficient elimination of residual boron (Omnès, et al., 2011). By adding some plasma treatments (pure hydrogen rinsing and oxygen exposure) the residual boron could be reduced as much as possible, yielding sharper interfaces.

III.3.1. Interface sharpness improved by an H₂ plasma rinse

The multilayer sample presented in figure 6-6 was grown with helium/hydrogen mixture and three different rinsing times were applied between the p++ and the p-- growth. As explained in Chapter 5. III. , helium is effective for increasing the boron incorporation and reducing the hydrogen density. In this particular case, the hydrogen density is reduced and then the concentration of hydroxyl species (OH) is reduced consequently. Therefore, at the beginning of the p-- growth, a large amount of boron species react with hydroxyl species and the incorporated boron concentration drops drastically. Nevertheless, the kinetics of this reaction are limited by the total concentration of boron initially present and by the time to produce hydroxyl species.

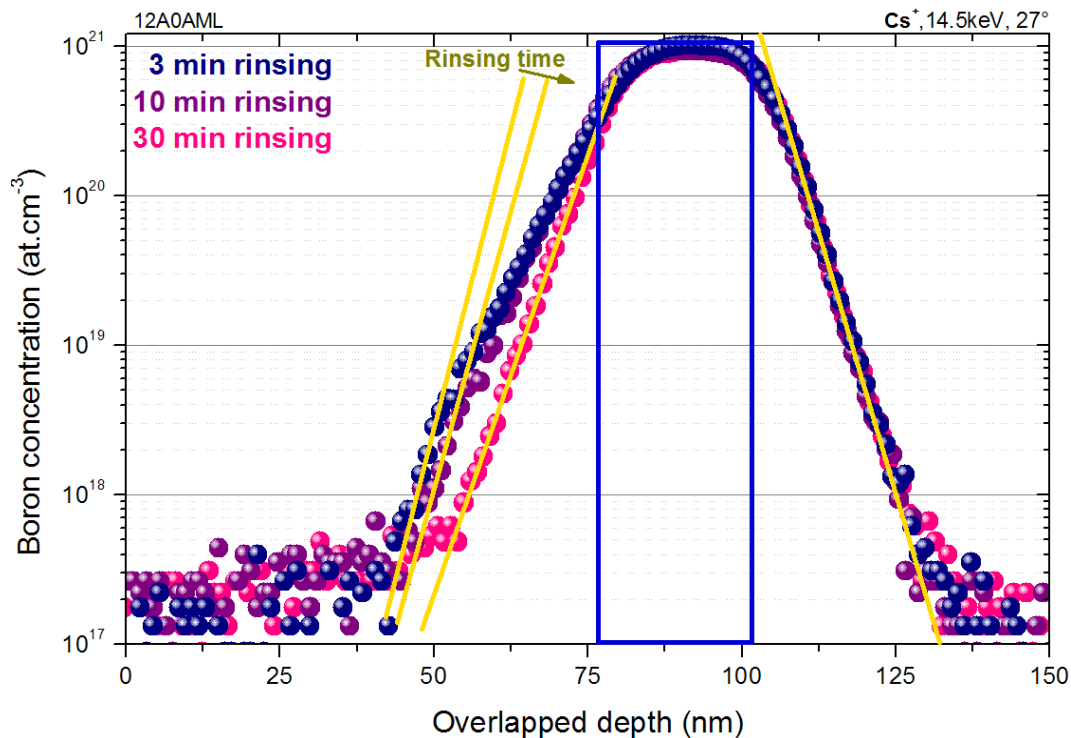


Figure 6-6 : Effect of hydrogen plasma rinse on p++ multilayers.

The interface treated with 30 min of hydrogen plasma exhibit a single and continuous slope, the SIMS limitation by ion-mixing, whereas the others show irregularities. These modifications in the slope indicate an remaining boron concentration before the p-- overgrowth, but lower enough to be eliminated by hydroxyl species generated at the beginning of the p-- growth, leading into a smooth decrease in the incorporate boron concentration during the p-- overgrowth an into an irregular leading SIMS signal at the analysis. After a long rinsing time i.e. 30 minute, this phenomenon is too low to be visible because of the SIMS limit. A slow etch ($\leq 0.3 \text{ nm}\cdot\text{min}^{-1}$) induced by the (He + H₂) plasma at 2 slm has been reported (Fiori, et al., 2012). When no helium is added to the gas mixture, then the leading signal exhibit no such irregularities after applying 3 min of pure hydrogen rinsing plasma (see Figure 6-4 as example).

III.3.2. In-situ etch-back

An intermediate and particularly efficient etching step was provided by adding O₂ to the gas vector (composed of helium 60% and hydrogen 40%) with a molar fraction of 0.25% (same as for NiD growth at 910°C). The resulting profiles are shown in figure 6-7 where five p++ epilayers grown sequentially at (CH₄/H₂) and B/C molar ratios in the gas phase of respectively 0.5% and 6000 ppm were etched for up to 15 minutes. The thicknesses of the p++ layers vary linearly with the time of exposure to this plasma, yielding an etching rate 4.7 nm.min⁻¹. Also, the non-intentional doping level in the spacer layer was found to be slightly lower for longer exposures, illustrating the efficiency of this diluted oxygen plasma to reduce “memory effects” in our reactor as described just before with rinsing plasma.

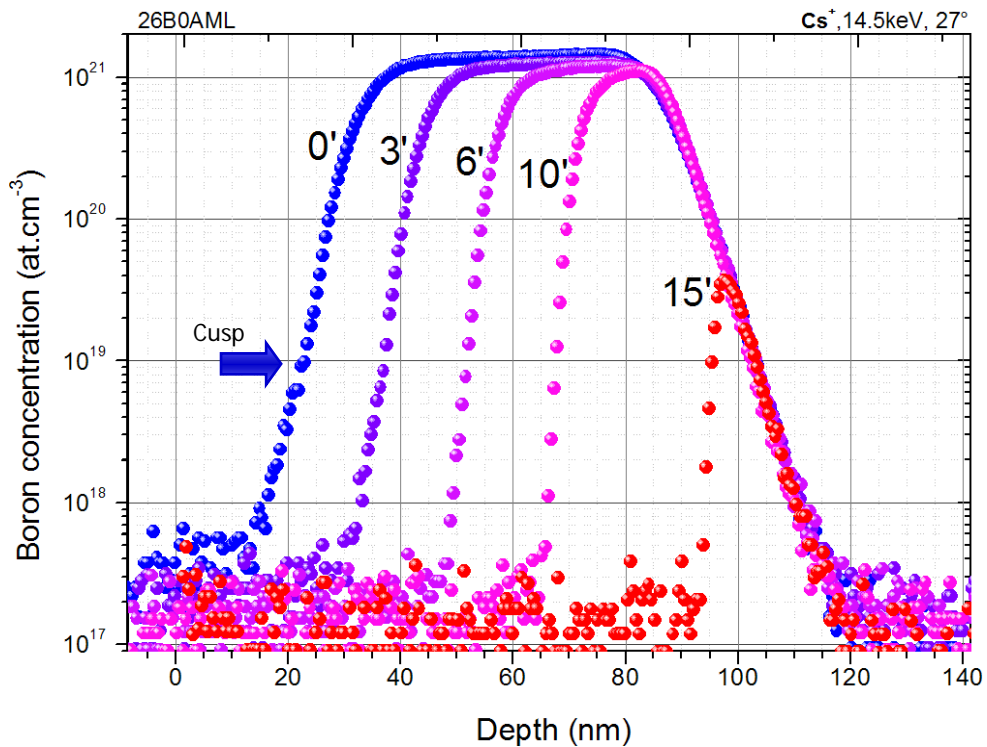


Figure 6-7 : Etch-back in situ effect on a multilayer sample grown with helium and hydrogen gas vector. (Fiori, et al., 2012)

In figure 6-7, five p++ layers are superimposed in such a way as to illustrate the effect of the in situ etch-back process. As you can see, on the first “falling” interface, a cusp is clearly visible at the position 23 nm. This cusp has been explained before by oxygen effects on the boron contamination. When the etching back time increases, the cusp is shifted down; it is not visible anymore after 10 minutes. Boron profiles of etched-back p++ at 10 and 15 minutes showed a pure exponential behaviour at the leading part (top side of p++ layer); this is a sign of a sharp falling interface, below 1 nm per order of magnitude (in respect with low ion energy SIMS on figure 6-1).

Full width at half maximum (FWHM) of the signal obtained after 10 minutes was below 2 nm, close to the expected depth resolution of the SIMS equipment, or to the lowest value reported in the literature (Balmer, et al., 2008). The determination of the #5 p++ layer from the thickness-peak relation established before gives a thickness of 2.6 nm in the case of a box-shaped profile. This thickness value is not compatible with the fit of the previous MRI model ($\lambda = 0, \sigma = 1.0, w = 3.2$) which indicates a true thickness below 1 nm. However, this difference might yield into the surface roughness quality which was deteriorate by the cumulative etching time (34 minutes totally).

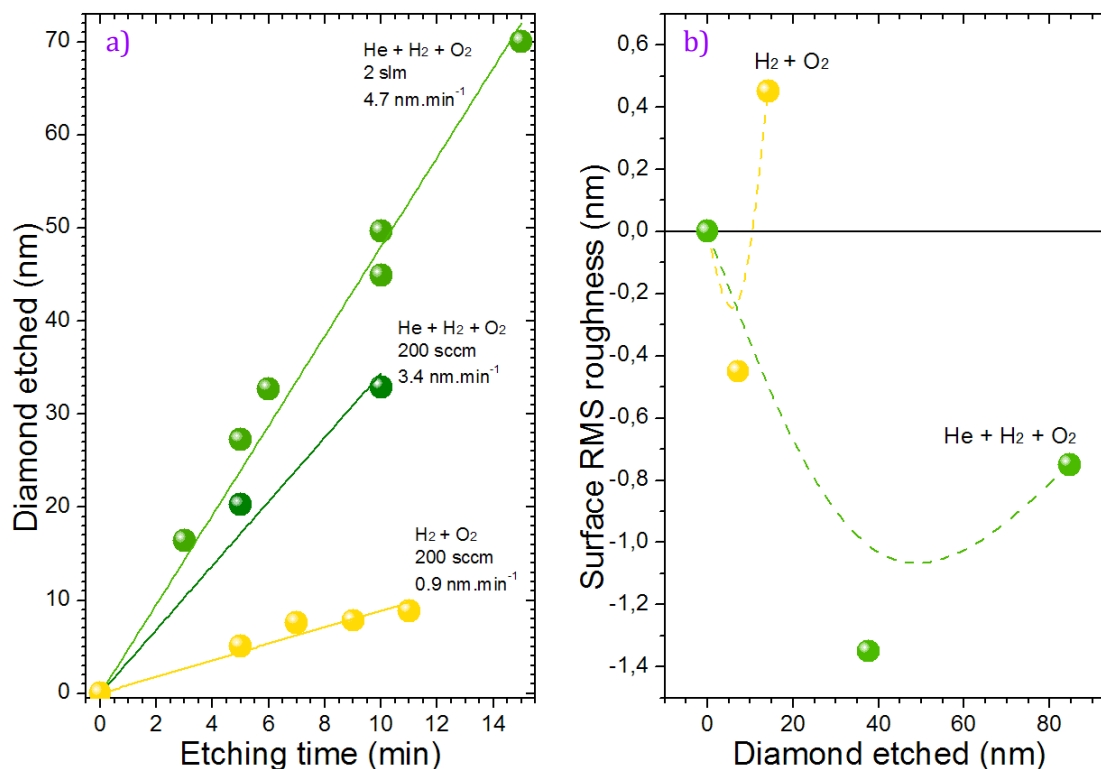


Figure 6-8: (a) etching rate, (b) evolution of the surface RMS roughness under different etchant gas mixture and flows with the same O₂ molar ratio (0.25%) at 910°C and 3 min of 2 slm H₂ rinsing at 880°C.

As shown on figure 6-8b, complementary tests demonstrate a slight roughness smoothing (negative gain on the figure) of the p++ layer when the etching time is short, measured in the case of *ex situ* etching. This is true independently the flow and the helium presence. When the etching was applied for a longer time, the surface roughness became significantly worse (especially when no helium is added). The rule play by helium is benefic in the roughness smoothing. The figure 6-8a reports the p++ diamond thickness etched versus time, by applying 3 minutes of rinsing plasma followed by the oxygen mixture containing the same molar fraction (0.25%), this at different gas flows, with and without helium.

Despite of the enhancement in surface smoothness by adding helium to the gas mixture, the consequently etching rate is too fast for a “high precision” etch on a p++ layer, even while the total gas flow was reduced by ten, for a second series. At 200 sccm with helium, the etching rate was reduced but remained still too high to be applied in a delta-growth process. In the third attempt, the helium was removed. In comparison with argon/oxygen gas mixture for rapid ion etching (RIE process) where Ar improves the O₂ dissociation, its introduction in the plasma enhances the etching rate of diamond by an increase of the oxygen radical concentration. This phenomenon was confirmed here; by removing helium, the etching rate was divided by 3.8, providing a slow etching-rate around 0.9 nm.min⁻¹; corresponding to about 6 seconds to etch each atomic layer. Using the mass-spectrometry system (detailed in Chapter 2. III.4.), it was possible to follow the gas composition in the

reaction chamber, particularly when the etching-back occurs. This is discussed in annexes for an *in situ* etching monitoring.

III.3.3. Conclusion on the sharpness of the falling interface

By applying a hydrogen rinsing step and an *in situ* etching-back process, the sharpness of the falling interface was drastically modified. The lowest width value of 1.3 nm per order of magnitude was limited by SIMS profiling conditions. However, the effect of oxygen on the p-growth process was twofold: on one hand, it reduced efficiently (100 times) the residual boron concentration, and it provided a sharper interface on the other. The best sharpness was obtained by applying 3 minutes of high flow H₂ rinsing (2 slm) followed by 5 minutes etch-back (200 sccm without He in the 0.25% (O₂/H₂) gas mixture) at 910°C and again 3 minutes of high flow H₂ rinsing at 880°C. In order to keep a good surface roughness, the etching time is limited to 7 minutes using this recipe. However, we demonstrate a possibility to *in situ* etch thicker p++ layer by the addition of helium which induce a smoothing of the etched surface.

IV. INTERFACE CHARACTERIZATION BY STEM*

Some multilayers were subjected to Transmission Electron Microscopy in order to complement the SIMS results. The idea was to use the HAADF-STEM mode in order to check the thickness and sharpness of p⁺⁺ layers (Araújo, et al., 2010). HAADF images are formed by collecting high-angle scattered electrons with an annular dark-field detector in dedicated scanning transmission electron microscopy (STEM) instruments. The contrast observed in HAADF is a signature of the doping (fraction between the carbon and the boron) as detailed in Chapter 3. III.1.3.

IV.1. HAADF contrast

The figure 6-9 presents a FIB lamella HAADF picture of the multilayers sample used to determine the etching rate of the oxygen-hydrogen-helium plasma mixture. The variation of lamella thinness (bezel) introduces a tilt in the line contrast analysis. Modulation of the contrast between p⁺⁺ and p⁻ layers is visible even if the signal-to-noise ratio is low due to the small difference in atomic diffusion factors; in this preparation 4 p⁺⁺ are identified: the non-etched one (#1), and 3, 6, 10 minutes etched-back (respectively #2, #3 and #4).

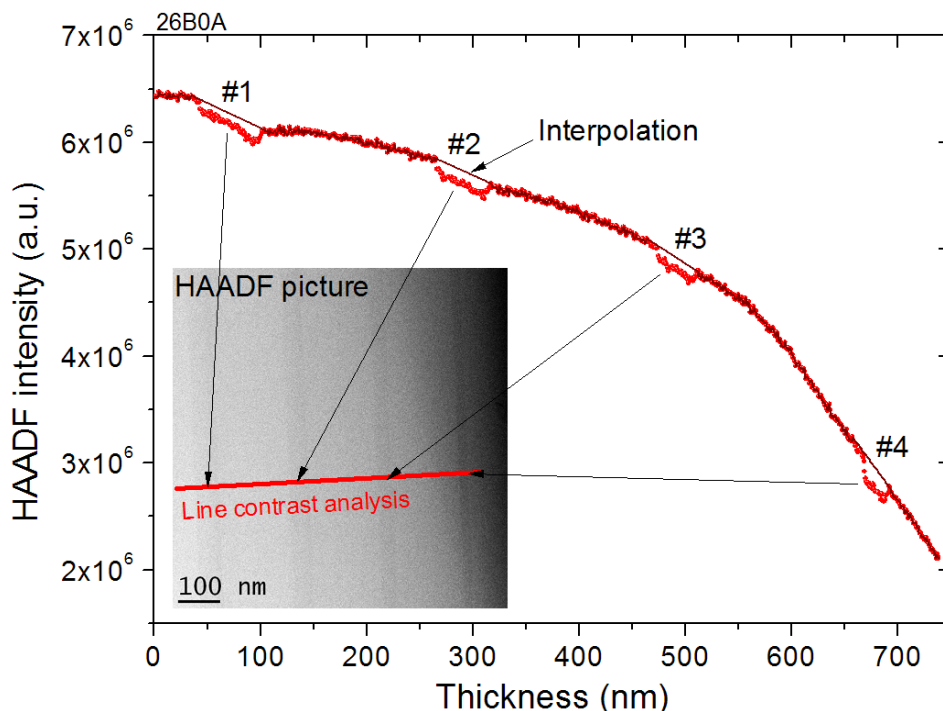


Figure 6-9 : Variation of the contrast along a line taken in the HAADF picture of a multilayer sample. This sample is the same as presented in figure 6-7 for the calibration of *in situ* etching-back. The interpolation shows the loss in contrast attributed to variations of the lamella preparation thickness (70 nm). The thinnest layer, *i.e.* 15 min of etching was not observed in the lamella.

* Study made in collaboration with Daniel Araujo, José Carlos Piñero Charlo and Maria de la Paz Alegre Salguero, at Universidad de Cádiz, Spain

After extraction of the background, the relative HAADF intensity makes doping shapes observable (figure 6-10). The #4 p++ layer appears with a stronger contrast which, after conversion leads to higher doping level, which is not compatible the process flow and the SIMS analysis, where all p++ show a similar doping level.

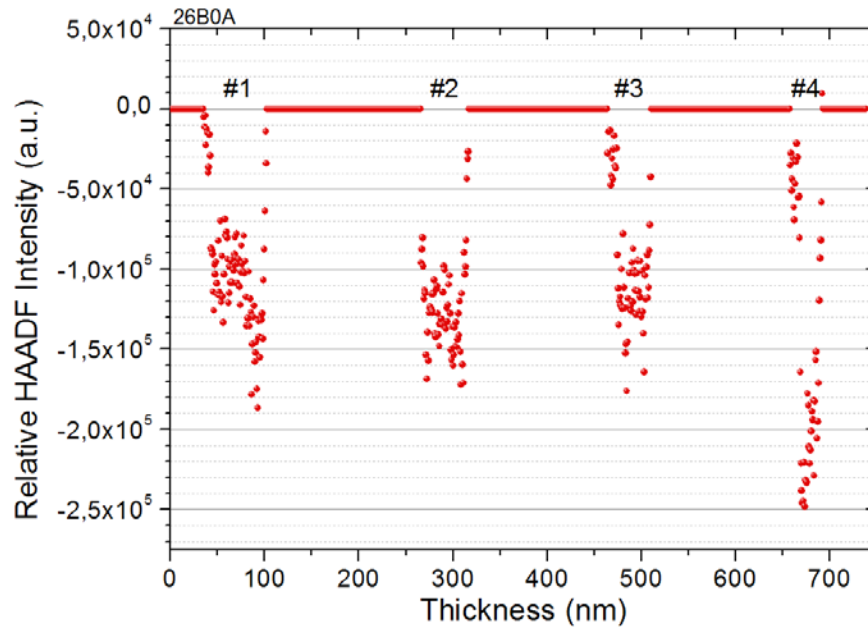


Figure 6-10 : Relative HAADF intensity after background subtraction.

Another image processing consists in the subtraction of a 2D background from the original HAADF image (figure 6-11). Then, by this technique, the sample lamella is found non homogeneous in thickness, especially in the area of the #4 p++ layer, where some matter seems to be peeled out during the FIB.

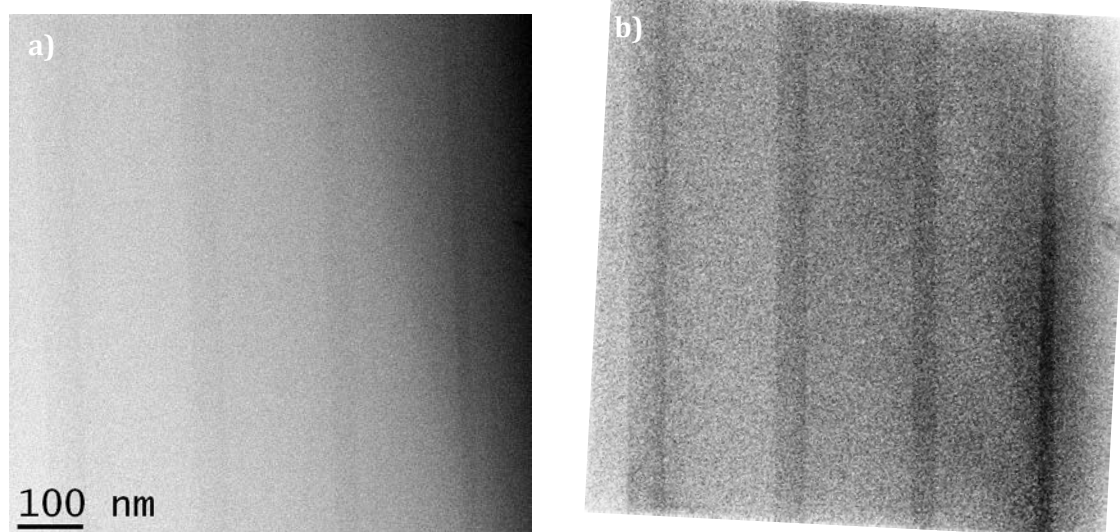


Figure 6-11 : (a) original HAADF image of the multilayer sample. (b) data after 2D background subtraction and tilt.

The pixel average on 253 lines (figure 6-12) taken at the top side of the figure 6-11b (when no thickness irregularities are revealed), confirmed the #4 p++ layer has the same doping level as other p++; same relative HAADF intensity. However, the signal-to-noise ratio is too low to carry out accurate estimation of interfaces sharpness.

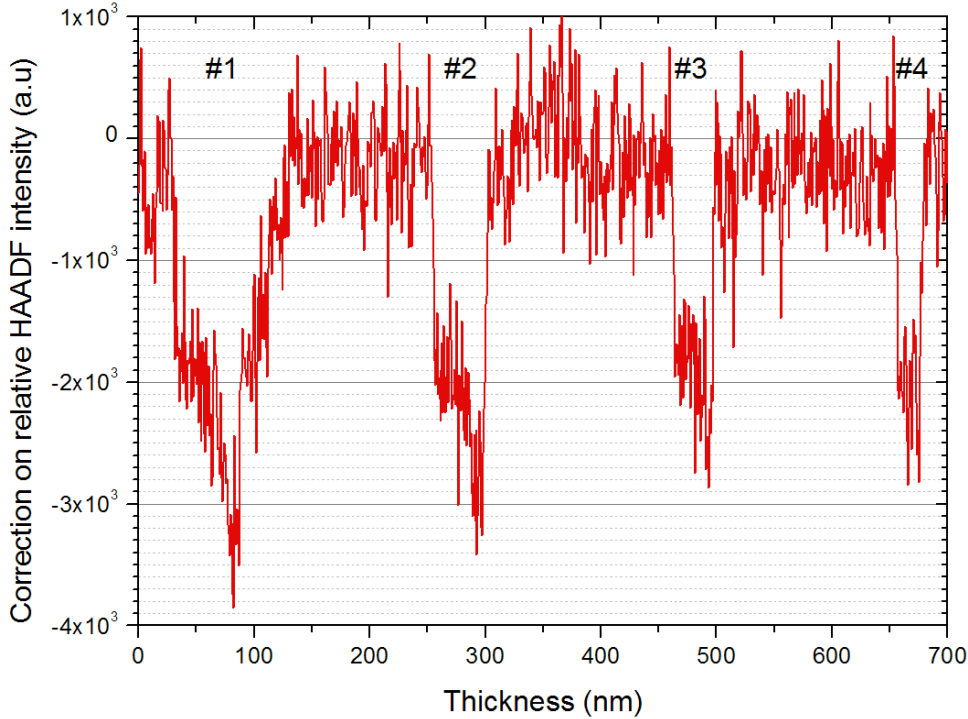


Figure 6-12 : Mean average value of 253 pixel lines of the HAADF after background subtraction and tilt.

The figure 6-12 reveals an asymmetry in the layer #1 interface sharpness. This layer was not exposed to etching back process and from #2; interface might show more symmetric interfaces slopes.

IV.2. From contrast to boron doping

The HAADF intensity depends on the fraction of boron x as follows:

$I(x) = I_0 \cdot N \cdot [(1-x)f_C^2 + xf_B^2]$, where N is the number of irradiated atoms, I_0 the incident electron beam intensity, f_i the atomic diffusion factor integrated over the detector collection angle ($f_C^2 = 0.0016667$ and $f_B^2 = 0.0011944$).

The relative HAADF intensity is the ratio between the intensity of boron-doped diamond and the intrinsic diamond: $R(x) = \frac{I(x)}{I(0)} = (1-x) + x \frac{f_B^2}{f_C^2}$.

The last step involves the detector calibration using a 10^{21} at.cm⁻³ boron-doped diamond of reference. Finally, the boron concentration is extrapolated as followed:

$$[B]_{\text{Solid}} = \frac{1-R_{t/h}(x)}{1-\frac{f_B}{f_C}} \cdot [C]_{\text{Solid}} \approx \frac{1-1.0106 R_{exp}(x)}{0.7166257} \cdot 1.76 \times 10^{23} \text{ at.cm}^{-3}.$$

This data extrapolation (figure 6-10) is plotted on figure 6-13 together with the SIMS boron concentration. Both boron profiles are corresponding in width and in concentration (except for the #4 as explained before). The visible difference on the p++ peak concentration can be explained by the memory effect and the ion-mixing in case of the SIMS and by the background removal (lamella thickness) for the HAADF (*N.B.* the effect is inverted). The dynamical range of the HAADF measurement is greatly reduced by the background level. However, Boron concentrations as low as 1×10^{20} at.cm⁻³ (*i.e.* 0.05 at.%) were detected in a consistent manner.

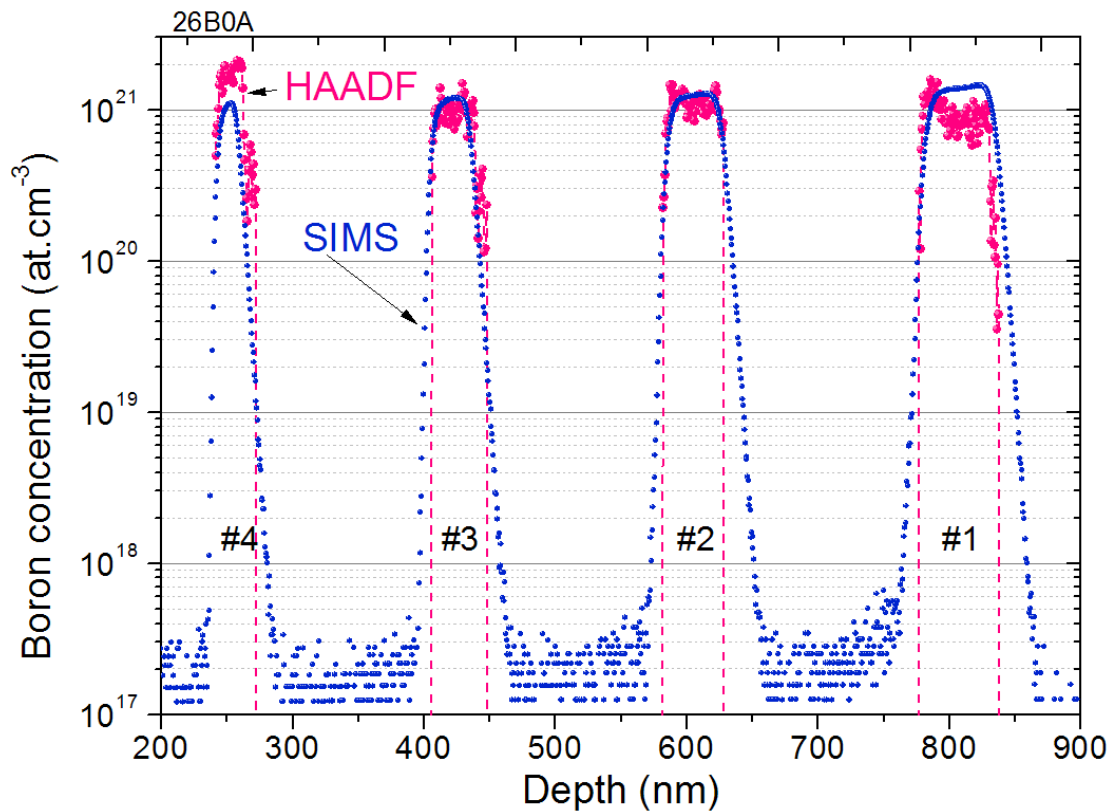


Figure 6-13 : Superimposition of SIMS boron profile (blue) and HAADF extrapolated boron profile (pink) of the same multilayers sample. The thinnest layer, *i.e.* 15 min of etching-back is not represented.

The 1D background extrapolation (figure 6-9) introduces, after removal, an asymmetry in the signal and boron concentration evolutions at interfaces are not reliable. In order to check at the interface sharpness, localized intensity HAADF measurements have to be performed.

This work was made for the #3 and #4 p++ and extrapolated boron profiles were plotted on figure 6-14.

IV.3. Extrapolation on interface sharpness

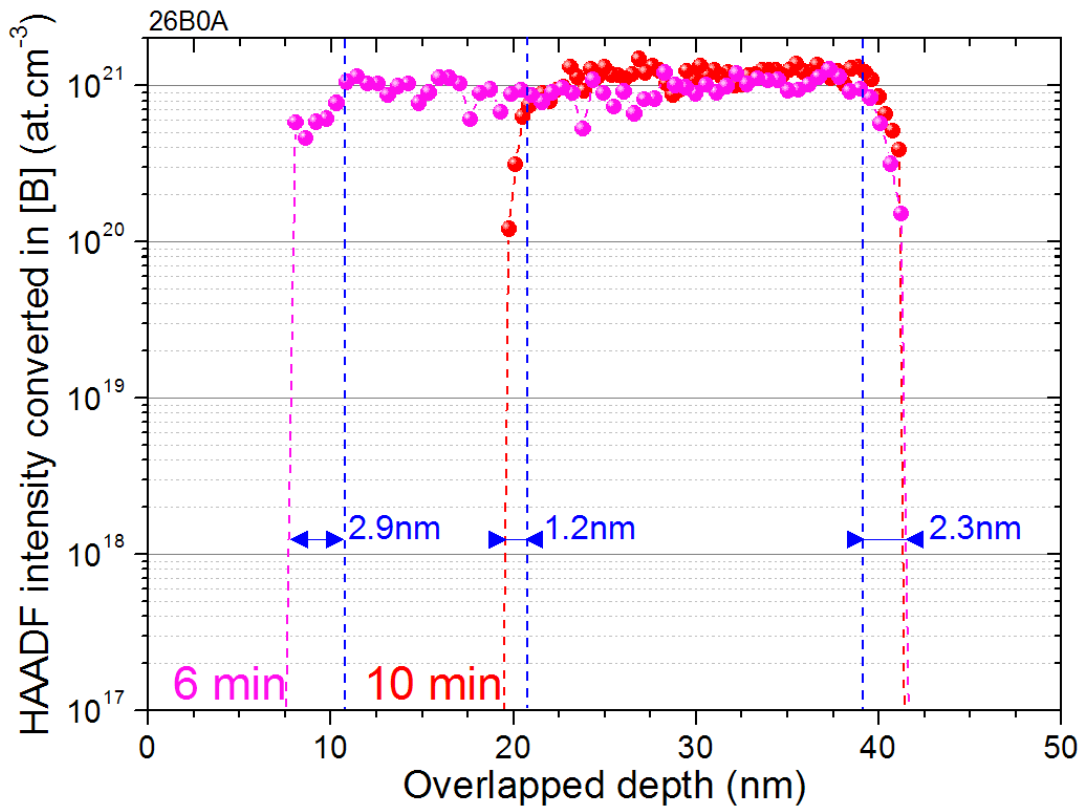


Figure 6-14 : p⁺⁺ layers interfaces from HAADF extrapolated boron profile for 6 and 10 min of etching-back.

As shown on figure 6-14, and assuming that the reduced dynamical range of HAADF measurements (1 to 2 orders of magnitude at best) allows such an extrapolation, a trailing value around 0.5 nm/decade was found for both p⁺⁺ boron concentration peaks associated to layers #3 and #4 of fig. 6-13. This value is quite similar with the leading value measured by the SIMS at low O₂⁺ acceleration energy, in Japan (figure 6-1). By HAADF, leading values were more difficult to determine due to the poorest dynamic range, but it appears lower than SIMS values; it was respectively 2.7 and 1.8 (figure 6-7).

IV.4. H-TEM on delta-layers

The sample studied was composed of four identical p++ layers already shown before by SIMS (figure 6-4).

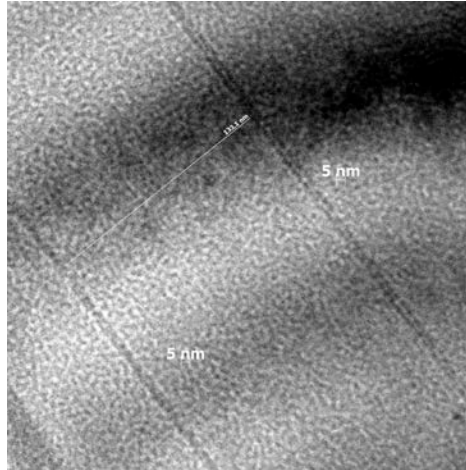


Figure 6-15 : Bright field picture showing two 5nm thick p++ layers.

On the figure 6-15, two p++ are visible (dark gray lines) with a background noises induced by the graphite at the sample TEM preparation surface. The p++ thickness is in the 5 nm range and corresponds to the 1 minute deposition. The p-- thickness, in this picture, is 133 nm and is in good agreement with its deposition time too. The p++ shown are labeled #4 and #3 on the corresponding SIMS profile. The same image processing as applied on the HAADF analysis of the sample 26B0AML, was reproduce here on figure 6-16.

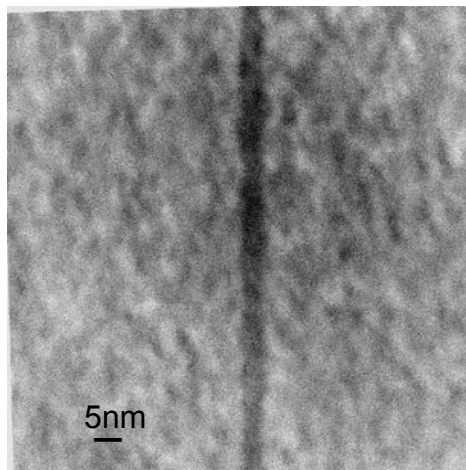


Figure 6-16 : HAADF image of a p++ layer after 2D background subtraction and tilt correction.

After 2D background subtraction, p++ layer appears boarded by light and dark dots. We made the hypothesis; this is an additional contrast, independent of the change in the atomic composition, but coming from a surface graphitization of the sample lamella in the cross

section. This introduces a limitation in the determination of interface sharpness. However, by the average of enough lines, we can reduce this “white” noise and extract from the HAADF picture the corresponding boron profile.

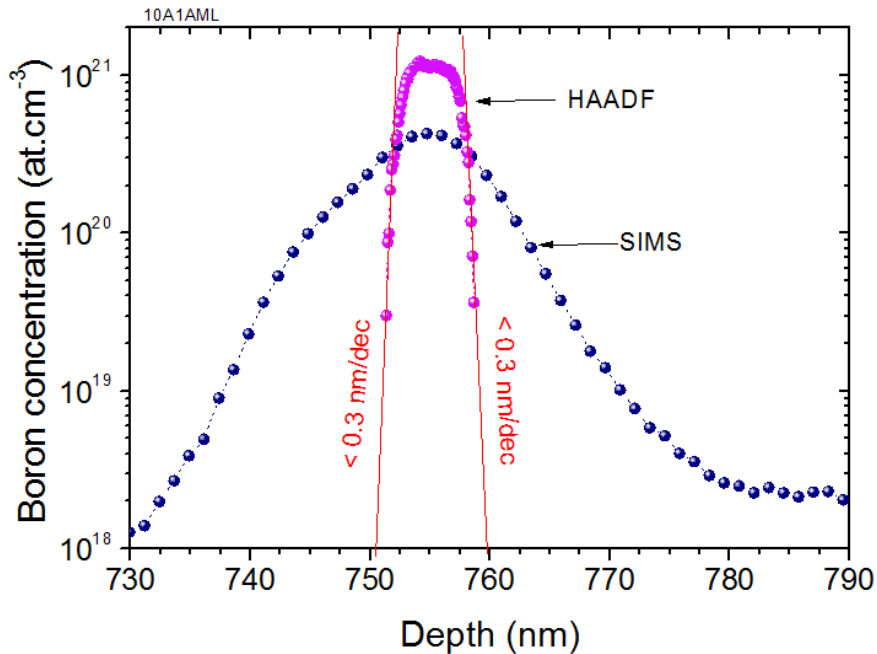


Figure 6-17 : Overlapping of SIMS and HAADF boron profile of the same p++ layer.

The figure 6-17 illustrates the difference between the SIMS and the HAADF analysis. In the case of SIMS, the p++ layer is very deep in the material, the information depth is not negligible and the boron profile appears distorted. The HAADF is made on a cross-section, and despite the surface graphitization, we can observe a 5nm thick p++ layer with ultra sharp interfaces. Once again, the dynamic on interfaces information by HAADF remain limited, but we can supposed a sharpness below 0.3 nm/dec.

V. X-RAY DIFFRACTION OF BORON-DOPED P++ STRUCTURES AND SUPERLATTICE

V.1. HRXRD on P++ layers

The sample analyzed here* is composed of a p++ on a buffer layer. The p++ has been grown with 0.5% (CH₄/H₂) and 6000 ppm (B/C)_{gas}, in the “surface contact” mode. This p++ layer is 270 nm thick and heavily boron-doped (1×10^{21} at.cm³). The buffer layer measured 240 nm in thickness and its doping level was around 5×10^{18} at.cm³ (SIMS).

Diamond material is very dense, (004) peak is located at high diffraction angle (119.46° with Cu K α 1) and is composed of low Z-number atoms, in consequence X-ray penetrates very deep inside the sample on few microns in depth. When layers are thin, reflection information comes mainly from the bulk. As explained in Chapter 3. V. , 2theta-omega scans provide information about distortion and lattice parameter gradient. On figure 6-18, two peaks are visible. The peak #1 (119.54 deg.) is linked to both buffer and diamond substrate; the corresponding lattice parameter is 3.5667Å. The peak #2 (119.36 deg.) is associated to the p++ diamond layer with a change of the lattice parameter along the growth direction $\frac{\delta a}{a} = 9 \times 10^{-5}$ which is coherent with a p++ doping level at 1×10^{21} at.cm³, if all boron atoms are localized in substitution site (Achatz, 2008 PhD Thesis, p. 33), (Wojewoda, et al., 2008).

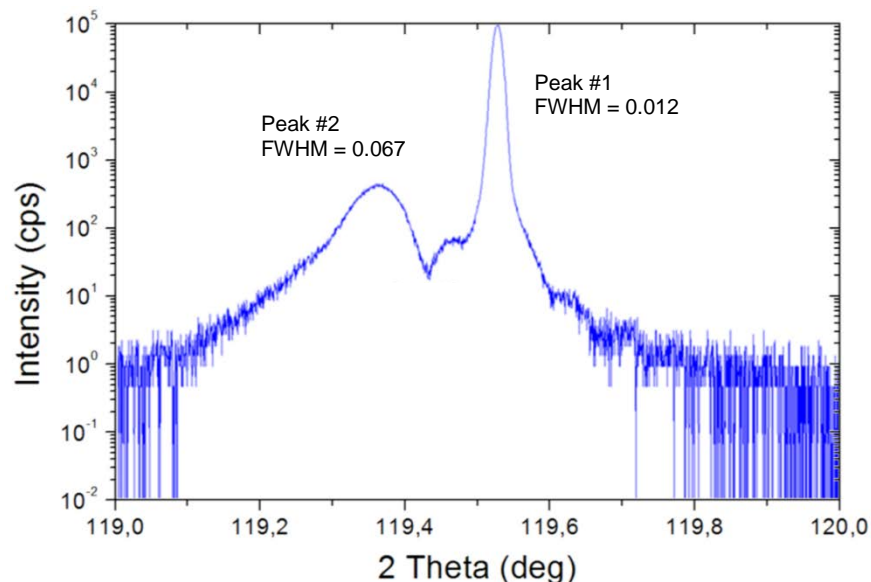


Figure 6-18 : High resolution X-ray diffraction specter for highly-boron-doped monocrystalline diamond along the (004) Bragg reflection.

* Study made in collaboration with Edith Bellet-Amalric at INAC, Grenoble, France

No additional peaks appear at larger 2θ angle. Oscillation neighboring the peak at 119.35 degrees seems to be compatible with a layer thickness of 300 nm.

Omega scans shows no FWHM difference (0.0026 deg.) between peaks associated to the p++ layer and the substrate. Peaks have the same asymmetry (0.05 deg.) and the same shape tendency, ($\eta = 0.06$); Gaussian peaks dominated by a mosaicity effects. The mosaicity value is inferior to 10 arcsec, it is attributed to growth sectors (sample made on HPHT diamond substrate) and it is a sign of good single-crystallinity quality.

A typical reciprocal space map of an (100)-oriented homoepitaxial epilayer is presented in figure 6-19. Reciprocal space mapping compares the shape and position of the film and substrate reciprocal lattice points and gives information such as layer tilt, strain, relaxation, lattice parameter, and mosaicity. The intensity contours show the symmetrical diffraction peak originating from the epilayer and from the diamond substrate. The boron-doped diamond layer shows no tilt with respect to the diamond substrate, confirming the coherent growth. The width of the rocking curve along the vertical axis (scan) confirms a maintain of the mosaicity from the HPHT-type Ib substrate in the p++ epilayer. The line-shape along the horizontal axis (in the detailed zoom) underlines the strain distribution; it becomes somewhat larger in the p++ layer.

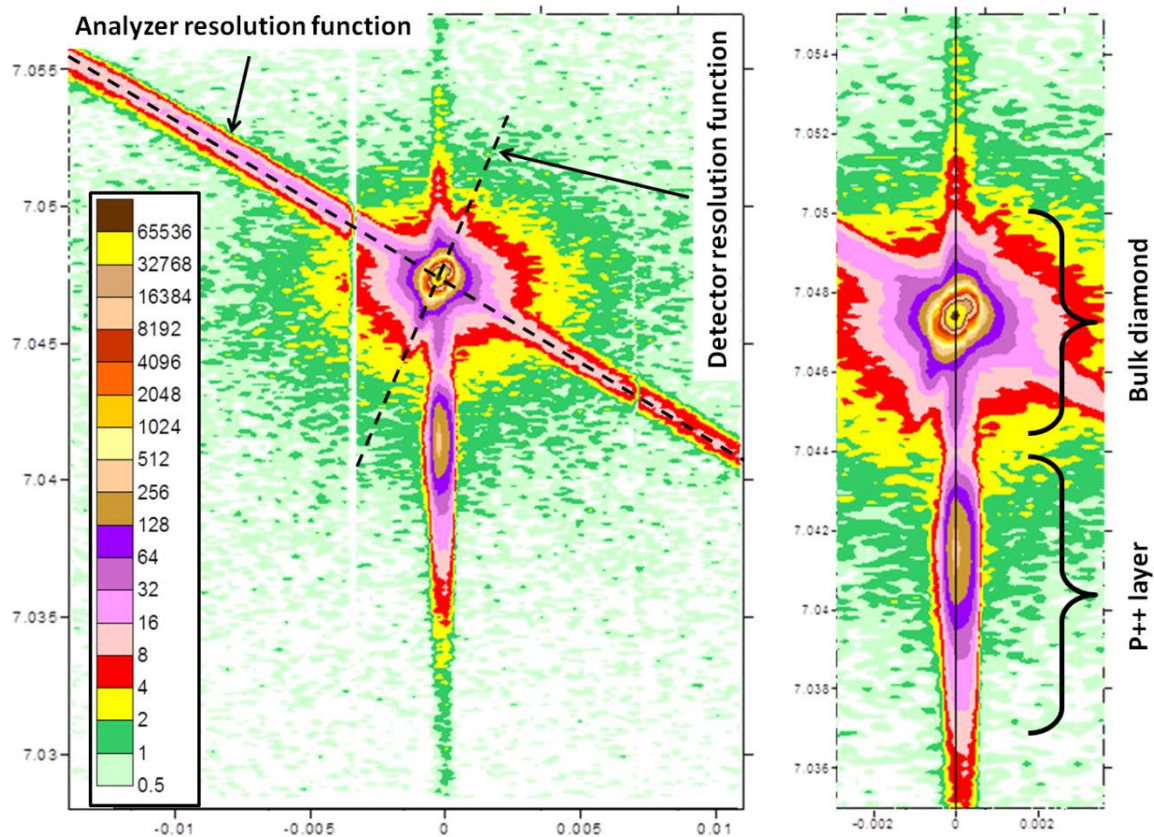


Figure 6-19 : Reciprocal space map around the symmetric reflection (004).

In order to get information not only along the symmetrical growth axis $\{100\}$, but also on plans inclined to the sample surface, reciprocal space maps around so-called asymmetric reflections $(\bar{1}\bar{1}3)$ have been performed. This data is critical for the strain determination; to know if the p++ epilayer has been grown under relaxed or constrained conditions, as one can probe the in-plane lattice parameter change. This analysis along the $(\bar{1}\bar{1}3)$ plane has convinced us that the p++ layer was fully strained on the substrate.

The same strained growth (also called “pseudomorphous”, since there is no detectable in-plane lattice expansion) has been studied previously at Institut Néel (Achatz, 2008 PhD Thesis), (Wojewoda, et al., 2008). Achatz reports in particular a p++ layer grown with 4% (CH_4/H_2) and 1200 ppm (B/C). This growth has the same boron doping level as the sample studied in this section. For the growth at 4%, he measures a FWHM value of 0.088 degrees. The small FWHM of 0.067 degrees measured on the sample is coherent with an improvement of the p++ quality growth at low methane concentration (0.5% CH_4/H_2).

V.2. HRXRD on p++/p-- superlattice

After the peak diffraction determination and the fully strained mode of the p++ identification, periodic multilayers (so-called superlattices) were simulated by computer in order to select a suitable set of p-- and p++ thickness which would yield strong satellites peaks.

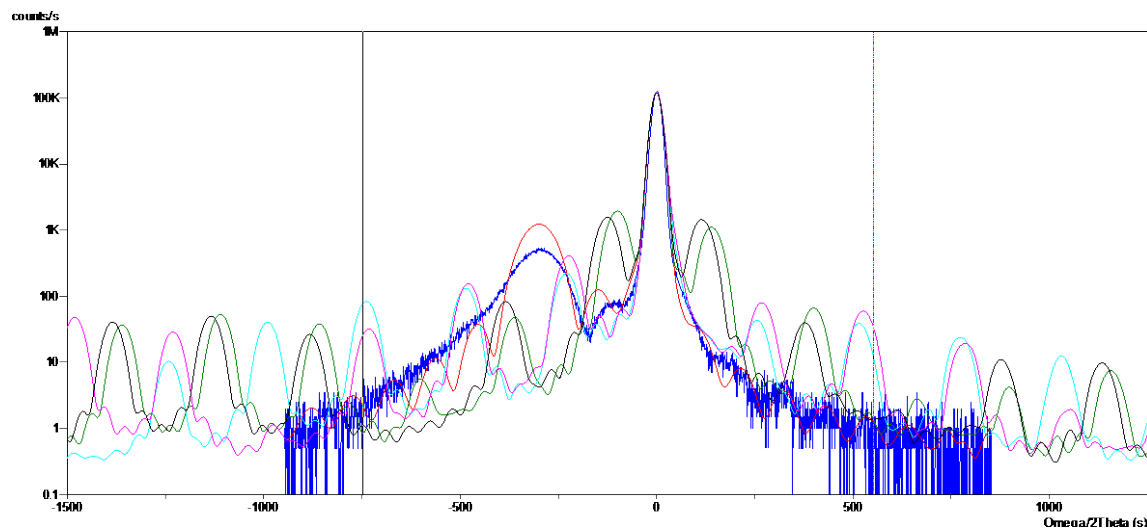


Figure 6-20 : (004) Bragg diffraction simulated. On red: 1 thick layer C:B 0.5%, On green, light blue, pink and black : 5 periods of 125 nm composed of the p--/p++ (100/25, 105/20, 95/30, 99/26 resp. with colors). The green curved shows a nice peaks satellite intensity irregularity.

A superlattice composed of 5 p++/p-- alternate similar to simulations shown in figure 6-20 was grown on CVD diamond substrates. Spectra around the (004) Bragg diffraction, show the diamond substrate peak diffraction with more than six satellites peaks. The distance between satellites peak yield into 120 nm of alternate.

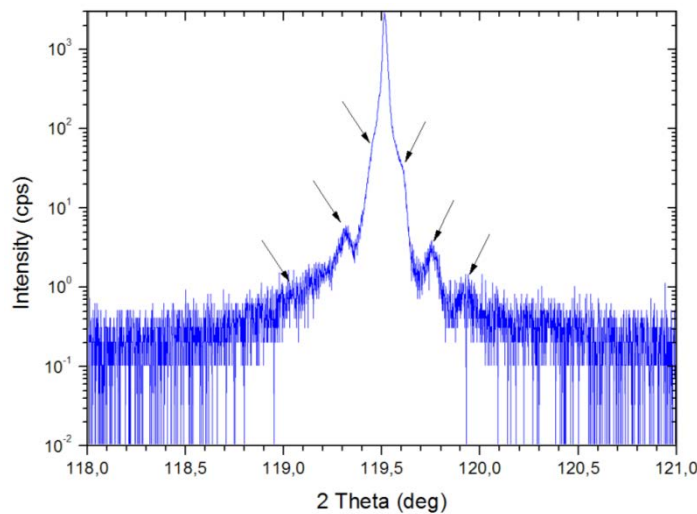


Figure 6-21 : (004) $\theta/2\theta$ diffraction on the superlattice sample (1872A). Six satellite peaks are identified and corresponds to a super-periodicity of 120 nm (HRXRD).

The determination of layers thickness and interfaces sharpness are still under analysis and cannot be presented in this actual manuscript version. It will be added as soon as possible.

VI. COMPARISON WITH OTHER MPCVD TECHNIQUES FOR DELTA-DOPING IN (100) DIAMOND

Kunze *et al.* (University of Ulm, Germany) used a constant total flow at 200 sccm and the doping was provided by a boron rod inserted inside the plasma ball (Kunze, et al., 1999). The technique used was called “pulsed-doping”. The growth was performed in using 1.5% (CH_4/H_2) at a total pressure of 30 Torr and 650°C, leading into a growth rate around 5 $\text{nm}\cdot\text{min}^{-1}$ to grow the undoped buffer layer. Then the boron rod was inserted into the plasma for a short time (≥ 3 s) and finally the temperature is increased at 750°C to overgrow the cap-layer at 11 $\text{nm}\cdot\text{min}^{-1}$. The process was optimised by pure hydrogen plasma treatments for etching the delta and for reducing the boron contamination. Following this procedure a delta structured showing a FWHM less than 6 nm was reported from elastic recoil detection; however the sheet carrier concentration in the cap-layer was above $1.6 \times 10^{13} \text{ cm}^{-2}$ which implies difficulties in the channel modulation.

In 2008, El-Hajj and co-workers (University of Ulm, Germany) had pursued the optimization process. Now, at first the boron rod was inserted into hydrogen plasma for 2 seconds with no methane content. Then, a methane pulse diluted into hydrogen occurred and induced a p++ growth step of 3 seconds, after which the plasma was switched off and the vessel pumped. The cap layer was grown in a further step. Multilayers were grown by this plasma interrupted technique. By ERD, the thinnest delta-layer had a FWHM of 1.1 nm, with rising interface sharpness around 0.9 nm/decade and falling interface sharpness around 1.2 nm/decade. N.B. no oxygen addition in the cap layer was claimed.

A conductance and time residence study made by Volpe *et al.* point out a total flow of 10 slm is necessary to reduce the diffusion time at 0.2 seconds using an ASTeX type reactor (Volpe, et al., 2012). By adding a new gas injector (quartz pipeline approaching the plasma inside the reactor) to inject the boron doping source (TMB) Tranchant et al. reported a thin delta-layer with a FWHM of 7 nm measured by SIMS from the front-side and back-side, rising interface sharpness was around 5 nm/decade and falling interface sharpness around 2.5 nm/decade (oxygen is added to growth p-- layers; $[B]_{p+} = 2 \times 10^{20} \text{ at.cm}^{-3}$, $[B]_{p-} \leq 5 \times 10^{16} \text{ at.cm}^{-3}$) (Tranchant, et al., 2012). The p-- growth rate was around 9 nm.min⁻¹, which is similar to growth rate of University of Ulm and on our case. Both leading and trailing SIMS signals from delta-interfaces are in the same range of our samples. In consequence, it is reasonable to estimate their rising interface sharpness is below 1 nm/decade and their falling interface sharpness too.

VII. CONCLUSION

In this study, we succeed in the fabrication of thin (few nanometers) and heavily boron doped films ($>5 \times 10^{20} \text{ at.cm}^{-3}$) embedded into a lightly doped diamond crystal with abrupt interfaces (below 1 nm/decade). Following this technique, single and multi-delta structures were grown in the modified MOCVD-like MPCVD reactor. The precise plasma switching timing provides homogeneous boron concentration in p++ layer together with more abrupt interfaces with the intrinsic diamond regions, leading into exceptional superlattice. Optimized contact mode with in plasma provides a good uniformity in the boron doping (same doping on $3 \times 3 \text{ mm}^2$) and the doping was constant with the time.

The thickness of the delta layer was reducing down to SIMS characterization limits. TEM information are not easy to analyze; the contrast induce by boron atoms is weak and good sample preparations are difficult to obtain. The cap layer (its thickness is critical in the channel conductivity modulation) can be deposited with good accuracy from *in-situ* thickness measurement by thermal infra-red oscillations. Growth rates have been drastically reduced in order to control the deposited matter, and processes provide low surface roughness and fewer defects as possible.

The last challenge, and maybe to most difficult one, concern delta-layer interface. The 3D concentration of dopant located in these transition areas induces a decrease in the conductivity and reduce the ability to modulate/close the channel of delta-FET.

VIII. RÉSUMÉ DU CHAPITRE 6

Ce chapitre traite de l'optimisation et de la caractérisation des interfaces entre les couches p++ et p-- de diamant orienté (100). L'objectif est de présenter la façon dont les conditions de plasma et les procédés ont été optimisés afin d'atteindre le delta-dopage du diamant. La cible concernant le gradient de concentration de bore à partir du fort dopage en couche p++ vers le faible dopage au bore en couche p-- (et le symétrique p++/p--) est dans l'ordre de grandeur de la longueur de Debye, qui est d'environ 0,1 nm par décade pour une densité d'accepteur de 9×10^{20} at.cm⁻³.

Tout d'abord, des échantillons multicouches ont été réalisés dans des conditions de croissance déterminées au chapitre 5. Dans chacun de ces échantillons, un paramètre du procédé a été modifié afin d'analyser les effets sur les interfaces. En particulier, les effets des vitesses de croissance et de gravure y sont discutés. De nouveaux procédés pour le mélange de rinçage ont été étudiés. La deuxième partie traite des techniques de caractérisation. La plus courante est la spectrométrie de masse d'ions secondaires (SIMS). L'épaisseur extrêmement faible des couches delta dopées au bore pousse l'analyse jusqu'à ses limites. Ces limites sont discutées en détail, et d'autres types de caractérisation ont été réalisés, tels que diffraction des rayons X (XRD) et la microscopie électronique en transmission (TEM). La combinaison de ces techniques a apporté un nouveau point de vue et a aidé pour conclure sur la réussite de la fabrication de structures delta en diamant.

Pour estimer clairement les phénomènes de mélange ionique issus du SIMS sur la résolution en épaisseur des couches diamant, du méthane isotopique (¹²C: 99,998% + ¹³C: 200 ppm) a été utilisé lors des croissances des couches tampon et de recouvrement, alors que le méthane standard (¹²C: 98,9% + ¹³C: 1,1%) a été utilisé pour la couche p++. Pour éviter tout effet lié à la rugosité de surface, un échantillon particulièrement plat a été sélectionné. La surface a été polie par Syntek Co. Ltd, et montre une rugosité RMS vérifiée par profilométrie optique comme inférieure à 0,3 nm avant reprise d'épitaxie. Dans cette étude, la couche tampon 500 nm a été au NIMS dans type réacteur à haute densité de plasma avec le méthane enrichi en ¹²C, avec CH₄/H₂ = 10% afin de maintenir une bonne qualité cristalline et une surface plane (Teraji, 2006). Une couche p++ a ensuite été réalisée à l'Institut Néel dans le réacteur NIRIM modifié avec du méthane d'abondance ¹³CH₄ normale (¹²C: 98,9%) avec CH₄/H₂ = 0,5% et B/C = 6000 ppm pendant 3 minutes. La couche finale, à savoir couche de recouvrement a été réalisée au NIMS avec le méthane isotopique, CH₄/H₂ = 1% pour déposer 50 nm de diamant intrinsèque. La rugosité RMS de la surface par profilométrie optique était inférieure à 1 nm après la croissance. Aucun procédé de gravure particulier, y compris avec de l'oxygène ou de l'hydrogène n'a été appliqué. L'évolution de la concentration de bore avec la profondeur suit un profil typique delta-dopage, comme le montre la figure 6-1. Le bore (points verts) et ¹³C (points bleus) ont des allures correspondantes. Cependant, les mesures SIMS avec des ions primaires césium sous une

énergie d'accélération de 14,5 keV ou avec des ions primaires d'oxygène à 3 keV conduit à des profils totalement différents.

Les mêmes pentes en concentrations de ^{13}C et ^{10}B ont été observées côté couche tampon. En effet, l'incorporation de bore dans le diamant suit l'incorporation du ^{13}C à partir du méthane. Cette observation souligne la cinétique rapide du mécanisme d'incorporation du carbone et du bore lors de la croissance. L'utilisation d'ions d'oxygène à faible énergie est bénéfique dans l'analyse par spectrométrie de masse à cause de l'effet réduit du mélange d'ions. Ainsi, le front montant passe de 1,5 à 0,5 nm/déc., et le front descendant, de 8 à 3,5 nm/déc. Cependant, même à faible énergie le signal SIMS analysé montre un comportement exponentiel qui indique une véritable interface assez abrupte pour ne pas être détectée, sur les deux fronts, et aucune conclusion sur l'asymétrie ne peut être maintenue. Néanmoins, avec le profil de la dérivée première sur la variation de la concentration en bore en profondeur, il est possible d'estimer l'épaisseur de la couche p++ (15 nm) dans des deux conditions SIMS.

Un autre effet du mélange ionique associé à la technique SIMS est une sous-estimation de la concentration lorsqu'une couche devient trop mince (visible à partir de 15 nm dans la situation des ions Cs). C'est typiquement le cas sur la figure 6-3, où les cinq couches p++ résultent d'une croissance faite dans les mêmes conditions mais avec des durées différentes (1, 2, 3, 4 et 5 minutes).

Cependant, lorsque l'échantillon n'est pas trop rugueux à la surface, il est possible de comparer des couches p++, indépendamment de leur emplacement à l'intérieur de l'échantillon. L'échantillon sur la figure 6-4 représente le pire des cas pour l'analyse SIMS, généralement p++ couches sont beaucoup moins profondes (environ 50 nm sous la surface).

Au début d'une croissance p++, nous n'utilisons pas de méthane pulsé dans un mélange plasma stable composé d'hydrogène et de diborane (Tranchant, et al., 2012). Nous n'utilisons pas non plus de plasma d'hydrogène et de méthane avec une brève injection de diborane (Kunze et al., 1999). Dans notre cas, la croissance p++ commence après le plasma de rinçage. Grâce à la spectrométrie de masse, il a été possible de mesurer la diffusion de méthane, d'oxygène, d'hydrogène et de diborane (voir annexes), pour déterminer la durée minimale nécessaire du plasma de rinçage pour éliminer efficacement les espèces de carbone et de bore dans la phase gazeuse avant de commencer une nouvelle croissance. De multiples tentatives ont été employées pour réduire le front de montée en concentration de bore. Pour ce faire, le débit de gaz a été augmenté, un plasma de préparation composé de diborane et de l'hydrogène a été introduit dans le processus. Le plasma a été interrompu et le mode de contact a été changé au cours de la croissance. En dépit de toutes ces tentatives, la raideur du front de montée en concentration n'a pas été réduite à moins de 8 nm/déc. A l'inverse, l'introduction d'un plasma de préparation composé de diborane et d'hydrogène augmente la contamination en bore. L'interruption du plasma et son allumage sous mélange de gaz p++ n'a pas été concluant. Le changement du mode de contact au cours du basculement du plasma élargie l'interface au lieu de la réduire. Toutefois, l'analyse SIMS à

faible énergie a révélé une pente de 3,5 nm/dec et le traceur isotopique a confirmé l'effet de mélange d'ions dans la limite précédente de 8 nm/dec. En conclusion, la croissance p⁺⁺ à 2 slm précédée d'un rinçage de 3 minutes fournit une interface abrupte inférieure à 3,5 nm/décade. L'imagerie au microscope à balayage électronique à transmission en champ sombre annulaire aux grands angles (STEM-HAADF) devrait permettre l'évaluation nette de ces interfaces limitées par la résolution du SIMS.

En ce qui concerne l'interface de concentration descendante, côté surface, l'application d'une étape de rinçage et de gravure *in situ*, en a considérablement modifié la raideur. La valeur la plus faible observée par SIMS au Cs⁺ de 1,3 nm/dec est clairement limitée par les conditions du SIMS. L'effet de l'oxygène dans la croissance p⁻ est double: d'une part, il réduit efficacement la concentration en bore résiduel (100 fois), et il fournit une interface plus abrupte. La meilleure raideur a été obtenue en appliquant 3 minutes de rinçage à fort débit d'H₂ (2 slm) suivi de 5 minutes de gravure *in situ* (200 sccm et O₂/H₂ = 0,25% mélange de gaz) à 910°C et à nouveau 3 minutes de rinçage à fort débit d'H₂ à 880°C. Afin de maintenir une bonne rugosité de surface, le temps de gravure est limité à 7 minutes en utilisant cette recette. Cependant, nous avons démontré la possibilité d'une gravure plus profonde de la couche p⁺⁺ par addition d'hélium qui induit un lissage de la surface plus prononcé, mais en contrepartie, une vitesse d'attaque 5 fois plus grande, et donc, non applicable au procédé delta.

Certains échantillons multicouches ont été découpés en fines lamelles puis soumis à la microscopie à balayage électronique à transmission afin de compléter les résultats SIMS. L'idée est d'utiliser le mode HAADF afin de vérifier l'épaisseur et la raideur des interfaces des couches p⁺⁺ (Araújo et al., 2010). Le contraste observé en mode HAADF est une signature du dopage (fraction entre le carbone et le bore) comme expliqué en chapitre 3. III.1.3.

Comme le montre les figures 6-14 et 6-17, malgré le manque de dynamique du HAADF (1 à 2 ordres de grandeur au mieux sur les concentrations en bore), on peut extrapoler une raideur d'interface autour de 0,5 nm par décade. Cette valeur est très proche de la valeur mesurée par SIMS à faible énergie d'accélération d'O₂⁺, réalisée au Japon (figure 6-1). Par HAADF, les mesures de raideur d'interfaces sont plus difficiles à déterminer en raison de la dynamique plus pauvre et du bruit issu de la graphitisation en surface des lamelles. Néanmoins, contrairement au SIMS, les interfaces paraissent plus symétriques et très abruptes.

Comme expliqué dans le chapitre 3. V., la position des pics de diffraction lors de mesures 2Theta-oméga fournissent des informations sur la distorsion et le gradient de paramètre de maille. Sur la figure 6-19, deux pics sont visibles. Le pic n°1 (119,54 deg) est lié à la fois à tampon et au substrat de diamant, le paramètre de maille correspondant est 3.5667Å. Le pic n°2 (119,36 deg) est associé à la couche de diamant p⁺⁺ avec un changement du paramètre

de maille dans la direction de croissance $\delta a/a = 9 \times 10^{-5}$, ce qui est cohérent avec un niveau de dopage à 1×10^{21} at.cm⁻³, si tous les atomes de bore sont localisés sur des sites de substitution (Achatz, 2008 Thèse, p. 33), (Wojewoda, et al., 2008).

L'analyse du pic de diffraction asymétrique ($1\bar{1}\bar{3}$) confirme que la couche p++ est entièrement contrainte sur le substrat. Le même type de croissance contrainte (également appelé «pseudomorphe») a été étudié précédemment à l'Institut Néel (Achatz, 2008 Thèse de doctorat), (Wojewoda, et al., 2008). Les recherches d'Achatz ont porté en particulier sur des couches p++ réalisées avec 4% (CH₄/H₂) et 1200 ppm (B/C). Ses couches ont la même teneur en bore que l'échantillon étudié dans ce chapitre. Pour la croissance à 4%, il mesure une largeur de pic à mi-hauteur de 0,088 degrés. Les 0,067 degrés mesurés sur l'échantillon sont ainsi en accord, et montrent une amélioration de la qualité cristalline avec l'emploi d'une concentration de méthane plus faible (CH₄/H₂=0,5%).

GENERAL CONCLUSION

GENERAL CONCLUSION

The results of this PhD project strongly rely first on the optimisation of the MPCVD diamond growth reactor itself. The new MOCVD-like gas flow management gave a fundamental change in the diamond growth process. Gas mixtures are stable in composition and in pressure before their introduction in the plasma. This is used to prepare in parallel: doping, hydrogen rinsing, non-intentionally doping and etching-back gas mixtures. The free volume has been drastically reduced and gas flows have been increased by 20, leading into shorter times of residence. Reactor walls are made of quartz; contaminations can be eliminated by low pressure oxygen plasma exposition.

In this study, we demonstrated the possibility to grow steps by steps (on (100)-oriented diamond $3 \times 3 \text{ mm}^2$) heavy boron-doped layers (typ. $[B] > 5 \times 10^{20} \text{ at.cm}^{-3}$) on lightly boron-doped layers (typ. $[B] < 1 \times 10^{15} \text{ at.cm}^{-3}$) in the same run, without stopping the plasma. More original, we demonstrated the reverse situation, where a light boron-doped layer is grown after heavy boron-doped layers deposition (a difference in boron doping of 5 orders of magnitude) in the same run, without stopping the plasma. In parallel, we report slow growth rates for both heavy boron doping (ca. 5 nm.min^{-1}) and light boron doping (ca. 7 nm.min^{-1}). This provides p--/p++/p-- structure where the p++ is thin enough to be called delta-structure. Over decades, researcher groups have optimized the p++ thickness reduction (down to 0.9 nm); in this study the priority was given to interface sharpness.

In order to reduce the doping transition width at delta-structure interfaces, we demonstrated the possibility to etch-back in situ the delta-layer by oxygen-hydrogen plasma. Etching rates and modification in the surface roughness were investigated as function of the gas composition (oxygen, hydrogen, helium) and gas flow (200 sccm and 2 slm). We report as slow etching rate and surface smoothing ideal to overgrowth light boron doping on a flat nanometric delta-layer. At the same time, we report the deposition rate monitoring of the light boron-doped layer by emitted infrared interference phenomenon brought by the pyrometer used to measure the sample surface temperature. These allow precision in thickness for both delta and light boron-doped layers.

In addition, the growth mode of the light boron-doped layer was tuned (by optimization of O_2/H_2 and CH_4/H_2 ratios) to get a lateral growth. An anisotropy factor around 6.7 was determined from the overgrowth of circular-shaped MESA structures. With this additional study, we report ultra-sharp delta-structure ($< 1 \text{ nm/decade}$). Such structures were grown on single or superlattice pattern.

The extreme sharpness of these interfaces was a new problem to SIMS analysis. The original idea of Drs T. Teraji and S. Koizumi to use isotopic carbon source brought the conclusion on the SIMS limitation to estimate the true sharpness of interfaces, even at low ion energy.

Complementary to SIMS analysis, STEM-HAADF was performed in order to localise the chemical presence of boron atoms in the diamond carbon structure. In despite of the low signal-to-noise ratio (carbon and boron are two light atoms), high resolution images have been analysed and confirmed delta-layer position estimated by SIMS.

Finally, boron doped p--/p++ diamond superlattices were grown under these optimised growth conditions. Such samples exhibit for the first time superlattice diffraction peaks by X-ray, indicating a periodic variation of strain related to the alternate heavy/light boron-doped diamond layers. No relaxations were reported, the material remain perfectly strained.

This thesis represents also the solid foundation for two other PhD thesis that are presently continuing in the SC2G team, one with the aim to measure carrier transport in diamond boron delta-doped structures in the direction of MOSFET applications, and the second, focused on superconductivity in ultra-thin heavy boron-doped diamond films.

CONCLUSION GENERALE

Les résultats de ce projet de thèse s'appuient fortement sur l'optimisation du réacteur de croissance du diamant par MPCVD. Le nouveau système de gestion des flux de gaz, basé sur la MOCVD, a apporté un changement fondamental dans le processus de croissance du diamant. Les mélanges de gaz sont stabilisés en composition et en pression avant leur introduction dans le plasma. Les mélanges de gaz utilisés pour le dopage, le rinçage sous hydrogène, le non-intentionnellement dopé et la gravure *in situ*, sont préparés en parallèle. Les volumes morts ont été considérablement réduits et les flux de gaz ont été augmentés par 20, ce qui conduit à des temps de résidence plus courts. Les parois du réacteur sont en quartz; la contamination peut être éliminée par un plasma d'oxygène basse pression.

Dans cette étude, nous avons démontré la possibilité de faire croître étape par étape (le diamant orienté (100) sur $3 \times 3 \text{ mm}^2$) en couches lourdement dopées au bore (typ. $[B] > 5 \times 10^{20} \text{ at.cm}^{-3}$) sur des couches faiblement dopées (typ. $[B] < 1 \times 10^{15} \text{ at.cm}^{-3}$) dans le même processus, sans arrêter le plasma. Plus original, nous avons démontré la situation inverse, où une couche faiblement dopée au bore est homoépitaxiée après dépôt d'une couche de fort dopage au bore (une différence de dopage sur 5 ordres de grandeur) dans le même processus, sans arrêter le plasma. En parallèle, nous présentons des faibles vitesses de croissance à la fois pour le dopage lourd (environ 5 nm.min^{-1}) et le pour le dopage léger (environ 7 nm.min^{-1}). Ceci permet d'obtenir des structure de type p-- /p++ / p--, où la couche p++ est suffisamment mince pour être appelé structure delta. Au fil des décennies, des équipes de recherche ont optimisé la réduction de l'épaisseur p++ (jusqu'à 0,9 nm). Dans cette étude, l'accent a été porté sur la raideur des interfaces.

Afin de réduire la largeur des transitions du dopage aux interfaces des structures delta, nous avons démontré la possibilité de graver la couche delta, *in situ*, par un plasma d'oxygène-hydrogène. Les vitesses d'attaque et de la modification de la rugosité de surface ont été étudiées en fonction de la composition du gaz (oxygène, hydrogène, hélium) et le débit total de gaz (200 sccm et 2 slm). Nous rapportons des vitesses de gravure suffisamment lentes et lissant la surface pour être idéales dans la reprise d'épitaxie des couches de faible dopage sur une couche de type delta d'épaisseur nanométrique. Dans le même temps, il est désormais possible de contrôler la vitesse de dépôt de la couche faiblement dopée au bore par phénomène d'interférence dans les émissions infrarouge de l'échantillon captées par le pyromètre (utilisé pour la mesure de la température de surface de l'échantillon). Ces nouveaux moyens permettent de faire croître la couche delta et la couche faiblement dopée avec une précision nanométrique.

En outre, le mode de croissance de la couche faiblement dopée au bore a été sélectionné (par l'optimisation des rapports O_2/H_2 et CH_4/H_2) pour obtenir une croissance latérale. Un facteur d'anisotropie autour 6,7 a été déterminé à partir de matrices de structures MESA cylindriques. Avec cette étude supplémentaire, nous présentons des structures delta aux interfaces très abruptes ($<1\text{nm}/\text{décades}$). De telles structures ont été réalisées sur un modèle unique ou en super-réseau.

La raideur extrême de ces interfaces pose un nouveau problème à l'analyse SIMS. L'idée originale des Drs T. Teraji et S. Koizumi d'utiliser une source isotopique du carbone, a permis de conclure sur la limite de la SIMS dans l'estimation des interfaces réelles (épaisseur et position), et ce, même à faible énergie d'ions. En complément de l'analyse SIMS, de la STEM-HAADF a été réalisée afin de localiser la présence chimique d'atomes de bore dans la structure en carbone diamant. En dépit du faible rapport signal-sur-bruit (carbone et bore sont deux atomes légers), des images à haute résolution ont été analysées et confirment les positions des couches dopées estimées par la SIMS.

Enfin, des super-réseaux de diamants dopés au bore p⁻/p⁺⁺ ont été réalisées dans ces conditions de croissance optimisée. Ces échantillons présentent des pics satellites de diffraction super-réseau par rayons X, indiquant une variation périodique de la contrainte liée à l'alternance du dopage lourd/léger du diamant. Aucune relaxation n'a été signalée ; le matériau reste parfaitement contraint.

Cette thèse constitue également une base solide pour deux thèses d'autres étudiants actuellement dans l'équipe SC2G ; l'une dans le but de mesurer le transport de porteurs de charges dans les structures delta en diamant dopé bore, en complément d'études de MOSFET, et la seconde, axée sur la supraconductivité en films ultra-minces de diamant lourdement dopé au bore.

GENERAL CONCLUSION

REFERENCES

REFERENCE

REFERENCE

- Abbaschian, R., Zhu, H. & Clarke, C., 2005. High pressure–high temperature growth of diamond crystals using split sphere apparatus. *Diamond & Related Materials*, 14(11-12), pp. 1916-1619.
- Achatz, P., 2008 PhD Thesis. *Metal-insulator transition and superconductivity in heavily boron-doped diamond and related materials*, Grenoble: Thèse à l'Université Joseph Fourier – Grenoble I / Technische Universität München.
- Aleksov, A. et al., 1999. Diamond junction FETs based on delta-doped channels. *Diamond & Related Materials*, Volume 8, pp. 941-945.
- Anda, Y., Ariki, T. & Kobayashi, T., 1995. Quantum Analysis of Hole Distribution in Multiple-Delta-Doped Diamond with a Deep Impurity Level. *Japanese Journal of Applied Physics*, Volume 34, pp. 3987-3990.
- Angus, J., 1994. *Synthetic Diamond: Emerging CVD Science*. New York: KE Spear and JP Dismukes, eds. John Wiley& Sons, Inc.
- Anthony, T. R. et al., 1989. Thermal conductivity of isotopically enriched ¹²C diamond. *Physical Review B*, 42(2), pp. 1104-1111.
- Araújo, D. et al., 2010. Local boron doping quantification in homoepitaxial diamond structures. *Diamond & Related Materials*, Volume 19, pp. 972-975.
- Araújo, D. et al., 2012. *STEM-HAADF quantification of doping level in diamond based HEMT homoepitaxial structure*, Island of Porquerolles (France): EXMATEC conference.
- Bachmann, P. K., Leers, D. & Lydtin, H., 1991. Towards a general concept of diamond chemical vapour deposition. *Diamond & Related Materials*, 1(1), pp. 1-12.
- Badheka, R. et al., 1990. Theoretical and experimental studies of the broadening of dilute delta-doped Si spikes in GaAs during SIMS depth profiling. *Surface and Interface Analysis*, 15(9), pp. 550-558.
- Baliga, B. J., 1982. Semiconductors for high-voltage, vertical channel field-effect transistors. *Journal of Applied Physics*, 53(3), pp. 1759-1764.
- Balmer, R. S. et al., 2008. Unlocking diamond's potential as an electronic material. *Phil. Trans. R. Soc. A*, 366(1863), pp. 251-265.
- Barnard, A. S., 2000. *The diamond formula: diamond synthesis - A gemological perspective*. 1 ed. Amsterdam: Elsevier.
- Baron, C., 2005 PhD thesis. *Dopage au bore et défauts associés dans des couches homoépitaxiées de diamant*. Grenoble: Thèse à l'Université Joseph Fourier.
- Baron, C. et al., 2006. Cathodoluminescence of highly and heavily boron doped (100) homoepitaxial diamond films. *Diamond & Related Materials*, 15(4-8), pp. 597-601.
- Benninghoven, A., Hagenhoff, B. & Werner, H. W., 1997. *Secondary Ion Mass Spectrometry, SIMS X*. Chichester: Wiley.
- Birner, S. et al., 2006. Modeling of Semiconductor Nanostructures with nextnano3. *Acta Physica Polonica A*, 110(2), pp. 111-124.
- Birner, S. et al., 2007. nextnano: General Purpose 3-D Simulations. *IEEE*

REFERENCE

- Transactions on Electron Devices*, 54(9), pp. 2137-2142 .
- Borst, T. H., Münzinger, P. C. & Weis, O., 1994. Characterization of undoped and doped homoepitaxial diamond layers produced by microwave plasma CVD. *Diamond & Related Materials*, 3(4-6), pp. 515-519.
- Borst, T. H. & Weis, O., 1995. Electrical characterization of homoepitaxial diamond films doped with B, P, Li and Na during crystal growth. *Diamond & Related Materials*, 4(7), pp. 948-953.
- Brambilla, A. et al., 2001. CVD diamond gamma dose rate monitor for harsh environment. *Nuclear Instruments and Methods in Physics Research Section A*, 458(1-2), pp. 220-226.
- Breeding, C. M. & Shigley, J. E., 2009. The "type" classification system of diamond and its importance in gemology. *Gems & Gemology*, 45(2), pp. 96-111.
- Bundy, F. P., Hall, H. T., Strong, H. M. & WENTORF JUN, R. H., 1955. Man-Made Diamonds. *Nature*, Volume 176, pp. 51-55.
- Burns, R. C. et al., 1990. Growth-sector dependence of optical features in large synthetic diamonds. *Journal of Crystal Growth*, 104(2), pp. 257-279.
- Bustarret, E. et al., 2008. Metal-to-insulator transition and superconductivity in boron-doped diamond. *Phil. Trans. R. Soc. A*, 366(1863), pp. 267-279.
- Casanova, N. et al., 2002. Epitaxial growth of phosphorus-doped diamond on {111} substrate. *Diamond & Related Materials*, 11(3-6), pp. 328-331.
- Celii, F. G., Pehrsson, P. E., Wang, H. & Butler, J. E., 1988. Infrared detection of gaseous species during the filament-assisted growth of diamond. *Applied Physics Letters*, 52(24), pp. 2043-2045.
- Chen, C.-F., Chen, S.-H., Hong, T.-M. & Wang, T.-C., 1994. Boron-doped diamond films using trimethylborate as a dopant source in methane-carbon dioxide gas mixtures. *Diamond & Related Materials*, 3(4-6), pp. 632-637.
- Chow, T. P. & Tyagi, R., 1994. Wide Bandgap Compound Semiconductors for Superior High-Voltage Unipolar Power Devices. *IEEE Transactions on Electron Devices*, Volume 41, pp. 1481-1483.
- Chrenko, R. M., 1973. Boron, the Dominant Acceptor in Semiconducting Diamond. *Physical Review B*, 7(10), pp. 4560-4567.
- Cifre, J., Puigdollers, J., Polo, M. C. & Esteve, J., 1994. Trimethylboron doping of CVD diamond thin films. *Diamond & Related Materials*, 3(4-6), pp. 658-631.
- Collins, A., 1982. Colour centres in diamond. *Journal of Gemmology*, 18(1), pp. 37-75.
- Collins, A., 2001. The colour of diamond and how it may be changed. *Journal of Gemmology*, 27(6), pp. 341-359.
- Collins, A. T. & Williams, A. W. S., 1971. The nature of the acceptor centre in semiconducting diamond. *Journal of Physics C: Solid State Physics*, 4(13), p. 1789.
- Davies, G., 1977. "Chemistry and Physics of Carbon", Vol 13. New York: Marcel Dekker.
- Dean, P. J., Lightowers, E. C. & Wight, D. R., 1965. Intrinsic and Extrinsic Recombination Radiation from Natural and Synthetic Aluminum-doped

REFERENCE

- Diamond. *Physical Review*, 140(1A), pp. A352-A368.
- Deguchi, M., Kitabatake, M. & Hirao, T., 1996. Electrical properties of boron-doped diamond films prepared by microwave plasma chemical vapour deposition. *Thin Solid Films*, Volume 281-282, pp. 267-270.
- Edgington, R. et al., 2012(a). Boron delta-doped (1 1 1) diamond solution gate field effect transistors. *Biosensors and Bioelectronics*, Volume 33, pp. 152-157.
- Edgington, R. et al., 2012. Growth and electrical characterisation of δ -doped boron layers on (111) diamond surfaces. *Journal of Applied Physics*, 111(3), p. 033710.
- El-Hajj, H. et al., 2008(a). Characteristics of boron δ -doped diamond for electronic applications. *Diamond & Related Materials*, Volume 17, pp. 409-414.
- El-Hajj, H. et al., 2008(b). Diamond MISFET based on boron delta-doped channel. *Diamond & Related Materials*, 17(7-10), pp. 1259-1263.
- Erlich, E. I. & Dan Hausel, W., 2002. Diamond Deposit. *Society for Mining, Metallurgy and Exploration*, pp. 74-94.
- Field, J. E., 1979. *Properties of diamond*. New York: Academic Press.
- Field, J. E., 1992. Appendix: tables of properties. In: J. E. Field, ed. *The properties of natural and synthetic*. 1 ed. s.l.:Academic, p. 667-698.
- Fiori, A., Pernot, J., Gheeraert, E. & Bustarret, E., 2010. Simulations of carrier confinement in boron delta-doped diamond devices. *Physica Status Solidi A*, 207(9), pp. 2084-2087.
- Fiori, A. et al., 2012. In situ etching-back processes for a sharper top interface in boron delta-doped diamond structures. *Diamond & Related Materials*, Volume 24, pp. 175-178.
- Fujimori, N., Imai, T. & Doi, A., 1986. Characterization of conducting diamond films. *Vacuum*, 36(1-3), pp. 99-102.
- Fujimori, N., Nakahata, H. & Imai, T., 1990. Properties of Boron-Doped Epitaxial Diamond Films. *Japanese Journal of Applied Physics*, Volume 29, pp. 824-827.
- Gabrysch, M. et al., 2008. Compensation in boron-doped CVD diamond. *Physica Status Solidi A*, 205(9), pp. 2190-2194.
- Gajewski, W. et al., 2009. Electronic and optical properties of boron-doped nanocrystalline diamond films. *Physical Review B*, 79(4), p. 045206.
- Galimov, E. M., Kudin, A. M. & Skorobogatskii, V. N., 2003. Experimental corroboration of the synthesis of diamond in the cavitation process. *Doklady Physics*, 49(3), pp. 150-153.
- Gheeraert, E., 1992. *Défauts de structure et impuretés dans les couches minces de diamant élaborées par dépôt chimique en phase vapeur*. Grenoble: thèse à l'Université Joseph Fourier.
- Gheeraert, E., Deneuille, A. & Mambou, J., 1999. Influence of diborane on the growth rate and phase stability of diamond films. *Carbon*, 37(1), pp. 107-111.
- Gonon, P., 1993. *Films polycristallins de diamant : dopage au bore à partir de la phase vapeur*. Grenoble: thèse à l'Université Joseph Fourier.
- Gonon, P. et al., 1995. Chemical vapor deposition of B-doped polycrystalline diamond films: Growth rate and incorporation efficiency of dopants.

REFERENCE

- Journal of Applied Physics*, 78(12), p. 360393.
- Goodwin, D. G. & Butler, J. E., 1998. *Handbook of Industrial Diamonds and Diamond Films*. New York: Marcel Dekker.
- Govender, M. G., Rootman, S. M. & Ford, T. A., 2003. An ab initio study of the properties of some hydride dimers. *Crystal Engineering*, 6(4), pp. 263-286.
- Hall, H. T., 1958. Ultrahigh-Pressure Research: At ultrahigh pressures new and sometimes unexpected chemical and physical events occur. *Science*, 128(3322), p. 445.
- Harris, S. J. & Weiner, A. M., 1989. Effects of oxygen on diamond growth. *Applied Physics Letters*, 55(21), pp. 2179-2181.
- Härtwig, J., 2009. *X-ray characterisation of diamond at the ESRF*. Domaine du Mas Blanc, France, 1ere école thématique DIAMANT.
- Haubner, R., Bohr, S. & Lux, B., 1999. Comparison of P, N and B additions during CVD diamond deposition. *Diamond & Related Materials*, 8(2-5), pp. 171-178.
- Hird, J. R. & Field, J. E., 2004. Diamond polishing. *Proceeding of the Royal Society A*, Volume 460, p. 3547-3568.
- Hofmann, S., 1977. Depth Resolution in Sputter Profiling. *Applied Physics*, 13(2), pp. 205-207.
- Hofmann, S., 1994. Atomic mixing, surface roughness and information depth in high-resolution AES depth profiling of a GaAs/AlAs superlattice structure. *Surface & Interface Analysis*, 21(9), pp. 673-978.
- Hofmann, S., 1998. Sputter depth profile analysis of interfaces. *Reports on Progress in Physics*, 61(7), pp. 827-888.
- Hofmann, S. & Schubert, J., 1998. Determination and application of the depth resolution function in sputter profiling with secondary ion mass spectroscopy and Auger electron spectroscopy. *Journal of Vacuum Science & Technology A*, 16(3), pp. 1096-1102.
- Imura, M. et al., 2012. Development of AlN/diamond heterojunction field effect transistors. *Diamond & Related Materials*, Volume 24, pp. 206-209.
- Institute, W. S., 2012. *nextnano3 - next generation 3D nano device simulator*. [Online] Available at: <http://www.nextnano.de> [Accessed 17 02 2012].
- Isberg, J., Hammersberg, J., Twitchen, D. J. & Whitehead, A. J., 2004. Single crystal diamond for electronic applications. *Diamond & Related Materials*, 13(2), pp. 320-324.
- Issaoui, R. et al., 2011. Influence of oxygen addition on the crystal shape of CVD boron doped diamond. *Physica Status Solidi A*, 208(9), pp. 2023-2027.
- Issaoui, R. et al., 2012. Evaluation of freestanding boron-doped diamond grown by chemical vapour deposition as substrates for vertical power electronic devices. *Applied Physics Letters*, 100(12), p. 122109.
- Ito, E., 2007. *Multianvil cells and high-pressure experimental methods, in Treatise of Geophysics, Vol 2*. Amsterdam: G. Schubert ed., Elsevier.
- Johnson, E., 1965. Physical limitations on frequency and power parameters of transistors. *IRE International Convention Record*, pp. 27-34.
- Kajihara, S. A., Antonelli, A. & Bernholc, J., 1991. Nitrogen and potential n-type dopants in diamond. *Physical Review Letters*, 66(15), pp. 2010-2013.

REFERENCE

- Kajihara, S. A., Antonelli, A. & Bernholc, J., 1993. Impurity incorporation and doping of diamond. *Physica B: Condensed Matter*, 185(1-4), pp. 144-149.
- Kamo, M., Sato, Y., Matsumoto, S. & Setaka, N., 1983. Diamond synthesis from gas phase in microwave plasma. *Journal of Crystal Growth*, 62(3), pp. 642-644.
- Kanaya, K. & Okayama, S., 1972. Penetration and energy-loss theory of electrons in solid targets. *Journal of Physics D: Applied Physics*, 5(1), p. 43.
- Kanda, H., 2007. Nonuniform Distributions of Color and Luminescence of Diamond Single Crystal. *New Diamond and Frontier Carbon Technology*, 17(2), pp. 105-116.
- Katagiri, M., Isoya, J., Koizumi, S. & Kanda, H., 2004. Lightly phosphorus-doped homoepitaxial diamond films grown by chemical vapor deposition. *Applied Physics Letters*, 85(26), pp. 6365-6367.
- Kato, H., Futako, W., Yamasaki, S. & Okushi, H., 2004. Homoepitaxial growth and characterization of phosphorus-doped diamond using tertiarybutylphosphine as a doping source. *Diamond & Related Materials*, 13(11-12), p. 2117-2120.
- Kato, H. et al., 2009. Selective Growth of Buried n+ Diamond on (001) Phosphorus-Doped n-Type Diamond Film. *Applied Physics Express*, Volume 2, p. 055502.
- Kato, H. et al., 2012. Diamond bipolar junction transistor device with phosphorus-doped diamond base layer. *Diamond & Related Materials*, Volume 27-28, pp. 19-22.
- Kato, H., Yamasaki, S. & Okushi, H., 2005(a). n-type doping of (001)-oriented single-crystalline diamond by phosphorus. *Applied Physic Letters*, 86(22), p. 222111.
- Kato, H., Yamasaki, S. & Okushi, H., 2005(b). Growth and characterization of phosphorus-doped diamond using organophosphorus gases. *Physica Status Solidi A*, 202(11), pp. 2122-2128.
- Kawano, A. et al., 2010. Superconductor-to-insulator transition in boron-doped diamond films grown using chemical vapor deposition. *Physical Review B*, 82(8), p. 085318.
- Keyes, R. W., 1972. Figure of merit for semiconductors for high-speed switches. *Proceedings of the IEEE*, Volume 60, pp. 222-225.
- Klein, T. et al., 2007. Metal-insulator transition and superconductivity in boron-doped diamond. *Physical Review B. Condensed Matter and Materials Physics*, 75(16), p. 165313.
- Kobayashi, T. et al., 1994. Analytical studies on multiple delta doping in diamond thin films for efficient hole excitation and conductivity enhancement. *Journal of Applied Physics*, 76(3), pp. 1977-1979.
- Kociniewski, T. et al., 2006. n-type CVD diamond doped with phosphorus using the MOCVD technology for dopant incorporation. *Physica Status Solidi A*, 203(12), pp. 3136-3141.
- Kohn, E. & Denisenko, A., 2007. Concepts for diamond electronics. *Thin Solid Films*, 515(10), pp. 4333-4339.
- Koizumi, S. et al., 1997. Growth and characterization of phosphorous doped {111} homoepitaxial diamond thin films. *Applied Physics Letters*, 71(8), p. 1065.
- Koizumi, S., Nebel, C. E. & Nesladek, M., 2008. *Physics and Applications of CVD*

REFERENCE

- Diamond*. Verlag GmbH & Co. KGaA ed. Weinheim: Wiley VCH.
- Koizumi, S., Watanabe, K., Hasegawa, M. & Kanda, H., 2001. Ultraviolet Emission from a Diamond pn Junction. *Science*, 292(5523), pp. 1899-1901.
- Kumagai, K. & Sekiguchi, T., 2009. Sharing of secondary electrons by in-lens and out-lens detector in low-voltage scanning electron microscope equipped with immersion lens. *Ultramicroscopy*, 109(4), pp. 368-372.
- Kumar, A., Pernot, J., Deneuville, A. & Magaud, L., 2008. Ab initio study of boron-hydrogen complexes in diamond and their effect on electronic properties. *Physical Review B*, 78(23), p. 235114.
- Kumar, A. et al., 2011. Boron-deuterium complexes in diamond: How inhomogeneity leads to incorrect carrier type identification. *Journal of Applied Physics*, 110(3), p. 033718.
- Kunze, M. et al., 1999. δ -Doping in diamond. *Carbon*, 37(5), pp. 787-791.
- Kyuregyan, A. S. & Yurkov, S. N., 1989. Room-Temperature Avalanche Breakdown Voltages of P-N Junctions Made of Si, Ge, Sic, Gaas, Gap, and Inp. *Soviet Physics Semiconductors-Ussr*, Volume 23, pp. 1126-1131.
- Lagrange, J.-P., Deneuville, A. & Gheeraert, E., 1998. Activation energy in low compensated homoepitaxial boron-doped diamond films. *Diamond & Related Materials*, 7(9), pp. 1390-1393.
- Lagrange, J.-P., Deneuville, A. & Gheeraert, E., 1999. A large range of boron doping with low compensation ratio for homoepitaxial diamond films. *Carbon*, Issue 37, p. 807-810.
- Lee, N. & Badzian, A., 1997. A study on surface morphologies of (001) homoepitaxial diamond films. *Diamond & Related Materials*, 6(1), pp. 130-145.
- Liang, Q., Harrison, J. G. & Vohra, Y. K., 2008. Modeling of nitrogen/diborane/methane/hydrogen plasma for nanocrystalline diamond growth: Comparison with experimental data. *Diamond & Related Materials*, 17(12), p. 2067-2070.
- Liou, Y. et al., 1990. The effect of oxygen in diamond deposition by microwave plasma enhanced chemical vapor deposition. *Journal of Materials Research*, Volume 5, pp. 2305-2312.
- Liu, J.-L. et al., 2010. Progress of High Frequency and High Output Power FET. *Journal of Inorganic Materials*, 25(9), pp. 897-905.
- Lombardi, E. B., 2009. Boron-hydrogen complexes in diamond: Energy levels and metastable states. *Physica B: Condensed Matter*, 404(23-24), pp. 4525-4528.
- Lombardi, G. et al., 2005. Modeling of microwave discharges of H₂ admixed with CH₄ for diamond deposition. *Journal of Applied Physics*, 98(5), p. 053303.
- Loshak, M. G. & Alexandrova, L. I., 2001. Rise in the efficiency of the use of cemented carbides as a matrix of diamond-containing studs of rock destruction tool. *International Journal of Refractory Metals and Hard Materials*, 19(1), pp. 5-9.
- Ma, J., 2008 PhD thesis. *Exploration of the gas phase chemistry in microwave activated plasmas used for diamond chemical vapour deposition*, Bristol: Thesis submitted to the University of Bristol in accordance with the requirements of the degree of Doctor of Philosophy in the Department of Chemistry, Faculty of Science.

REFERENCE

- Ma, J. et al., 2010. Spectroscopic and Modeling Investigations of the Gas Phase Chemistry and Composition in Microwave Plasma Activated B₂H₆/CH₄/Ar/H₂ Mixtures. *Journal of Physical Chemistry A*, 114(37), p. 10076–10089.
- Makino, T. et al., 2005. Strong Excitonic Emission from (001)-Oriented Diamond P–N Junction. *Japanese Journal of Applied Physics*, Volume 44, pp. 1190-1192.
- Matsui, Y., Matsumoto, S. & Setaka, N., 1983. TEM — electron energy loss spectroscopy study of the diamond particles prepared by the chemical vapour deposition from methane. *Journal of Materials Science Letters*, 2(9), pp. 532-534.
- Matsumoto, S., Sato, Y., Kamo, M. & Setaka, N., 1982. Vapor Deposition of Diamond Particles from Methane. *Japanese Journal of Applied Physics*, Volume 21, pp. L183-L185.
- Matsumoto, S., Sato, Y., Tsustumi, M. & Setaka, N., 1982. Growth of diamond particles from methane-hydrogen gas. *Journal of Materials Science*, 17(11), pp. 3106-3112.
- McMaster, r. M. C. et al., 1995. Dependence of the gas composition in a microwave plasma-assisted diamond chemical vapor deposition reactor on the inlet carbon source: CH₄ versus C₂H₂. *Diamond & Related Materials*, 4(7), pp. 1000-1008.
- Mer-Calfati, C. et al., 2009. High surface smoothing of diamond HPHT (100) substrates. *Physica Status Solidi A*, 206(9), pp. 1955-1959.
- Moran, D. et al., 2011. Processing of 50 nm gate-length hydrogen terminated diamond FETs for high frequency and high power applications. *Microelectronic Engineering*, Volume 88, pp. 2691-2693.
- Morse, J. et al., 2007. Single crystal CVD diamond as an X-ray beam monitor. *Diamond & Related Materials*, 16(4-7), pp. 1049-1052.
- Mortet, V. et al., 2008. Characterization of boron doped diamond epilayers growth in a NIRIM type reactor. *Diamond & Related Materials*, 17(7-10), pp. 1330-1334.
- Nebel, C. E. et al., 2007. Nebel et al. J. Phys. Appl. Phys. 2007. *Journal of Physics D: Applied Physics*, 40(20), pp. 6443-6466.
- Nesládek, M. et al., 2003. N-type P-doped polycrystalline diamond. *Physica Status Solidi A*, 199(1), pp. 77-81.
- Okano, K. et al., 1989. Characterization of Boron-Doped Diamond Film. *Japanese Journal of Applied Physics*, Volume 28, pp. 1066-1071.
- Omnès, F. et al., 2011. Study of boron doping in MPCVD grown homoepitaxial diamond layers based on cathodoluminescence spectroscopy, secondary ion mass spectroscopy and capacitance–voltage measurements. *Diamond & Related Materials*, 20(7), pp. 912-916.
- Ōsawa, E., 2007. Recent progress and perspectives in single-digit nanodiamond. *Diamond & Related Materials*, 16(12), pp. 2018-2022.
- Pal'yanov, N., Sokol, A. G., Borzdov, M. & Khokhryakov, A. F., 2002. Fluid-bearing alkaline carbonate melts as the medium for the formation of diamonds in the Earth's mantle: an experimental study. *Lithos*, 60(3-4), pp. 145-159.
- Pernot, J. et al., 2010. Hall hole mobility in boron-doped homoepitaxial diamond. *Physical Review B*, 81(20), p. 205203.

REFERENCE

- Prelas, M. A., Popovici, G. & Bigelow, L. K., 1997. *Handbook of Industrial Diamonds and Diamond Films*. New York: Marcel Dekker.
- Ralchenko, V. et al., 1999. Quality of diamond wafers grown by microwave plasma CVD: effects of gas flow rate. *Diamond & Related Materials*, 8(2-5), pp. 189-193.
- Rauch, C. J., 1962. Proceedings of the International Conference on the Physics of Semiconductors. In: A. C. Stickland, ed. *The Institute of Physics and the Physical Society*. London: Exeter, p. 276.
- Ri, S.-G. et al., 2002. Misorientation angle dependence of surface morphology in homoepitaxial diamond film growth at a low CH₄/H₂ ratio. *Journal of Crystal Growth*, 235(1-4), pp. 300-306.
- Scarsbrook, G. A. et al., 2006. *DIAMOND TRANSISTOR AND METHOD OF MANUFACTURE THEREOF*. GB, Patent No. WO/2006/117621.
- Schneider, H., Sanchez, J. L. & Achard, J., 2005. The diamond for power electronic devices. *European Conference on Power Electronics and Applications*, 3(1), pp. 1-9.
- Schubert, E. F. & Ploog, K., 1985. The δ -Doped Field-Effect Transistor. *Japanese Journal of Applied Physics*, Volume 24, pp. L608-L610.
- Schubert, E. F., Ploog, K., Fisher, A. & Horikoshi, Y., 1984. *Semiconductor Devices with at Least One Monoatomic Layer of Doping Atoms*. US Patent, Patent No. 4 882 609.
- Shiomi, H., 1995. Pulse-doped diamond p-channel metal semiconductor field-effect transistor. *IEEE Electron Device Letters*, 16(1), pp. 36-38.
- Shiomi, H., 1999. Crystal growth of diamond and its application for semiconductor devices. *Electronics and Communications in Japan (Part II: Electronics)*, 82(7), pp. 68-79.
- Show, Y. et al., 2000. Structural changes in CVD diamond film by boron and nitrogen doping. *Diamond & Related Materials*, 9(3-6), pp. 337-400.
- Silva, F. et al., 2008. Geometric modeling of homoepitaxial CVD diamond growth: I. The {1 0 0}{1 1 1}{1 1 0}{1 1 3} system. *Journal of Crystal Growth*, 310(1-4), pp. 187-203.
- Silva, F., Hassouni, K., Bonnin, X. & Gicquel, A., 2009. Microwave engineering of plasma-assisted CVD reactors for diamond deposition. *Journal of Physics: Condensed Matter*, 21(36), p. 364202.
- Spitsyn, B. V. & Deryagin, B. V., 1980. USSR, Patent No. 339.134.
- Sumida, N. & Lang, A. R., 1981. Cathodoluminescence evidence of dislocation interactions in diamond. *Philosophical Magazine A*, 43(5), pp. 1277-1287.
- Takano, A. et al., 2003. Evaluation of SIMS depth resolution using delta-doped multilayers and mixing-roughness-information depth model. *Applied Surface Science*, Issue 203-204, pp. 294-297.
- Takano, Y. et al., 2005. Superconductivity in polycrystalline diamond thin films. *Diamond & Related Materials*, 14(11-12), pp. 1936-1938.
- Takeuchi, D. et al., 2000. Homoepitaxial diamond films grown by step-flow mode in various misorientation angles of diamond substrates. *Diamond & Related Materials*, 9(3), pp. 231-235.
- Tallaire, A., Kasu, M., Ueda, K. & Makimoto, T., 2008. Origin of growth defects in

REFERENCE

- CVD diamond epitaxial films. *Diamond & Related Materials*, Issue 17, pp. 60-65.
- Teraji, T., 2006. Chemical vapor deposition of homoepitaxial diamond films. *Physica Status Solidi A*, 203(13), pp. 3324-3357.
- Teraji, T. & Ito, T., 2004. Homoepitaxial diamond growth by high-power microwave-plasma chemical vapor deposition. *Journal of Crystal Growth*, 271(3-4), pp. 409-419.
- Teraji, T. et al., 2006. Highly efficient doping of boron into high-quality homoepitaxial diamond films. *Diamond & Related Materials*, 15(4-8), pp. 602-606.
- Teukam, Z. et al., 2003. Shallow donors with high n-type electrical conductivity in homoepitaxial deuterated boron-doped diamond layers. *Nature Materials*, Volume 2, pp. 482-486.
- Thonke, K., 2003. The boron acceptor in diamond. *Semiconductor Science and Technology*, 18(3), p. S20-S26.
- Tokuda, N. et al., 2007. Surfaceroughening of diamond (001) films during homoepitaxial growth in heavy boron doping. *Diamond & Related Materials*, 16(4-7), pp. 767-770.
- Tran Thi, T. et al., 2011. Ultra-smooth single crystal diamond surfaces resulting from implantation and lift-off processes. *Physica Status Solidi A*, 208(9), pp. 2057-2061.
- Tranchant, N. et al., 2012. *Growth of ultra-sharp delta-doped structures using an innovative gas injection system and their characterizations*. Boston, Materials Research Society.
- Tsukioka, K. & Okushi, H., 2006. Hall Mobility and Scattering Mechanism of Holes in Boron-Doped Homoepitaxial Chemical Vapor Deposition Diamond Thin Films. *Japanese Journal of Applied Physics*, Volume 45, pp. 8571-8577.
- Ueda, K. et al., 2006. Diamond FET Using High-Quality Polycrystalline Diamond With f_T of 45 GHz and f_{max} of 120 GHz. *IEEE Electron Device Letters*, 27(7), pp. 570-572.
- Vescan, A., 1997. High-temperature, high-voltage operation of pulse-doped diamond MESFET. *IEEE Electron Device Letters*, 18(5), pp. 222-224.
- Visser, E. P. et al., 1992. Electrical conduction in homoepitaxial, boron-doped diamond films. *Journal of Physics: Condensed Matter*, 4(36), p. 7365.
- Volpe, P.-N., 2009 PhD thesis. *Réalisation de composants unipolaires en diamant pour l'électronique de puissance*. Grenoble: thèse à l'Université Joseph Fourier.
- Volpe, P.-N., Muret, P. & Omnès, F., 2008. Effect of ECR etching conditions of (100)1b diamond substrates on homoepitaxial low boron doped diamond layer quality. *Physica Status Solidi A*, 205(9), pp. 2173-2178.
- Volpe, P.-N. et al., 2010. Extreme dielectric strength in boron doped homoepitaxial diamond. *Applied Physics Letters*, 97(22), p. 223501.
- Volpe, P.-N., Pernot, J., Muret, P. & Omnès, F., 2009. High hole mobility in boron doped diamond for power device applications. *Applied Physics Letters*, 94(9), p. 092102.
- Volpe, P.-N. et al., 2012. Ultra-sharp boron interfaces for delta doped diamond structures. *physica status solidi (RRL) - Rapid Research Letters*, 6(2), pp. 59-61.
- Wade, M., Muret, P., Omnès, F. & Deneuille, A., 2006. Technology and

REFERENCE

- electrical properties of ohmic contacts and Schottky diodes on homoepitaxial layers grown on (100) diamond surfaces. *Diamond & Related Materials*, 15(4-8), pp. 614-617.
- Werner, M. & Locher, R., 1998. Growth and application of undoped and doped diamond films. *Reports on Progress in Physics*, 61(12), p. 1665.
- Werner, M. et al., 1997. The diamond Irvin curve. *Diamond & Related Materials*, 6(2-4), pp. 308-313.
- Wild, C. et al., 1994. Oriented CVD diamond films: twin formation, structure and morphology. *Diamond and Related Materials*, 3(4-6), pp. 373-381.
- Willatzen, M., Cardona, M. & Christensen, N. E., 1994. Linear muffin-tin-orbital and $k \cdot p$ calculations of effective masses and band structure of semiconducting diamond. *Physical Review B*, 50(24), p. 18059.
- Windheim, J. A., Venkatesan, V., Malta, D. M. & Das, K., 1993. Electrical characterization of semiconducting diamond thin films and single crystals. *Journal of Electronic Materials*, 22(4), pp. 391-398.
- Wojewoda, T. et al., 2008. Doping-induced anisotropic lattice strain in homoepitaxial heavily boron-doped diamond. *Diamond & Related Materials*, 17(7-10), p. 1302-1306.
- Yamanaka, S. et al., 1998. High-Quality B-Doped Homoepitaxial Diamond Films using Trimethylboron. *Japanese Journal of Applied Physics*, Volume 37, pp. L1129-L1131.
- Zaitsev, A. M., 2001. *Optical Properties of Diamond*. Berlin: Springer-Verlag.
- Ziegler, J. F., Ziegler, M. D. & Biersack, J. P., 2010. SRIM - The stopping and range of ions in matter. *Nuclear Instruments and Methods in Physics Research, Section B*, 268(11-12), pp. 1818-1823.

ANNEXES

I. FLUID MECHANICS

The aim of this paragraph is to determine the possibility to generate turbulent gas flow in the reactor tube by increasing the total gas flow rate. In the case of the diamond growth, the gas is mainly composed of hydrogen. The “standard” atmospheric pressure (*i.e.* at sea level) is 101 325 Pa. Unlike calculations of losses for liquids (considered as practically incompressible) the loss due to the flow a gaseous fluid (air, gas, steam, etc.) is accompanied by an expansion which results in an increase in flow (*i.e.* the speed), a decrease in the density and an increase in dynamic viscosity.

I.1. Correction of the gas density

The density ρ of the fluid in must be corrected from the reference fluid density according the working pressure and the temperature as followed: $\rho = M_{ref} \cdot \frac{Pb+P}{101325} \cdot \frac{273.15}{275.15+t}$, where:

- M_{ref} = gas density (kg/m³) taken at 0°C and 101325 Pa
- P = gas relative pressure in use (Pa)
- t = gas temperature in use (°C)
- Pb = atmospheric pressure taken at the working altitude (Pa).

In the case of hydrogen, $M_{ref} = 0.0899$ kg/m³.

I.2. Correction of the gas flow

The volumetric flow rate Q_c of the fluid in must be corrected from the setup volumetric flow rate Q (sccm) according the working pressure and the temperature as followed:

$$Q_c = Q \cdot \frac{273.15+t}{273.15} \cdot \frac{101325}{Pb+P}, \text{ where:}$$

- Q_c = the corrected volumetric flow rate (cm³/min) (measured in new conditions)
- Q = the standard volumetric flow rate (cm³/min) (101325 Pa)
- t = gas temperature in use (°C)
- P = gas relative pressure in use (Pa)
- Pb = atmospheric pressure taken at the working altitude (Pa).

I.3. Reynolds number for a pipe

For gas flows in a pipe or a tube, the Reynolds number is generally defined as:

$$Re = \frac{\rho v D_H}{\mu} = \frac{D_H}{\nu} = \frac{Q D_H}{\nu A}, \text{ where:}$$

- D_H is the hydraulic diameter of the pipe; its characteristic travelled length, L, (m)
- Q is the volumetric flow rate (m³/s)
- A is the pipe *cross-sectional* area (m²)
- ν is the mean velocity of the object relative to the fluid (m/s)

- μ is the dynamic viscosity of the fluid (Pa·s or N·s/m² or kg/(m·s))
- ν is the kinematic viscosity (m²/s)
- ρ is the density of the fluid (kg/m³).

The Reynolds Number can be used to determine if the flow is laminar, transient or turbulent. The flow is laminar when $Re < 2300$, transient when $2300 < Re < 4000$, and turbulent when $Re > 4000$.

ρ_{Ref}	μ	Flow	P	Temp.	ρ	Q_{Cor}	U	Re(0,025)
10 ⁻²	10 ⁻⁵	sccm	Torr	°C	10 ⁻³	10 ⁻⁵	m.s ⁻¹	
Kg.m ⁻³	Pa.s				kg.m ⁻³	m ³ .s ⁻¹		
8,99	1,03	200	33	100	2,86	9,74	48,4	10571
8,99	1,03	2000	33	100	2,86	97,4	484,4	105706
8,99	1,03	200	50	100	4,33	6,43	31,9	6977
8,99	1,03	2000	50	100	4,33	64,3	319,7	69766

Table A-1: Determination of Reynolds values

I.4. Position on Moody chart: turbulence regime

The Moody chart or Moody diagram is a graph in non-dimensional form that relates the Darcy friction factor, Reynolds number and relative roughness for fully developed flow in a circular pipe. It can be used for working out pressure drop or flow rate down such a pipe. In our case it allows to estimate the flow behavior.

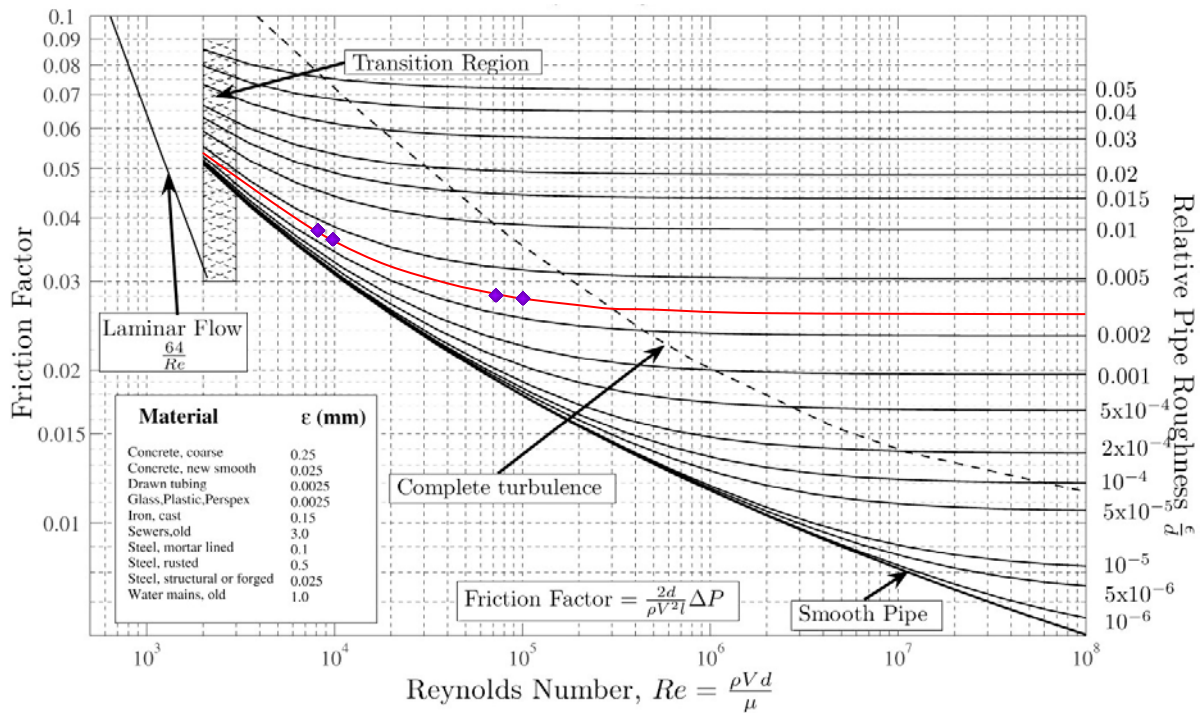


Figure A-1 : Moody diagram applied to flow into cylindrical pipes.

II. MASS-SPECTROMETRY

By the mass-spectrometry system (detailed in Chapter 2), it is possible to follow the gas composition in the reaction chamber, particularly when the etching-back occurs. The figure a-2 illustrates different process steps: 40 min of buffer layer p-- growth followed by 3 min of H₂ rinsing, 1 min of p++ growth, 3 min of H₂ rinsing, 5 min of etch-back, 3 min of H₂ rinsing and 4 min of cap layer p-- growth. Mass-to-charge ratio observed were 44 for CO₂, 32 for O₂, 28 for CO, 27 for B₂H₅, 15 for CH₃.

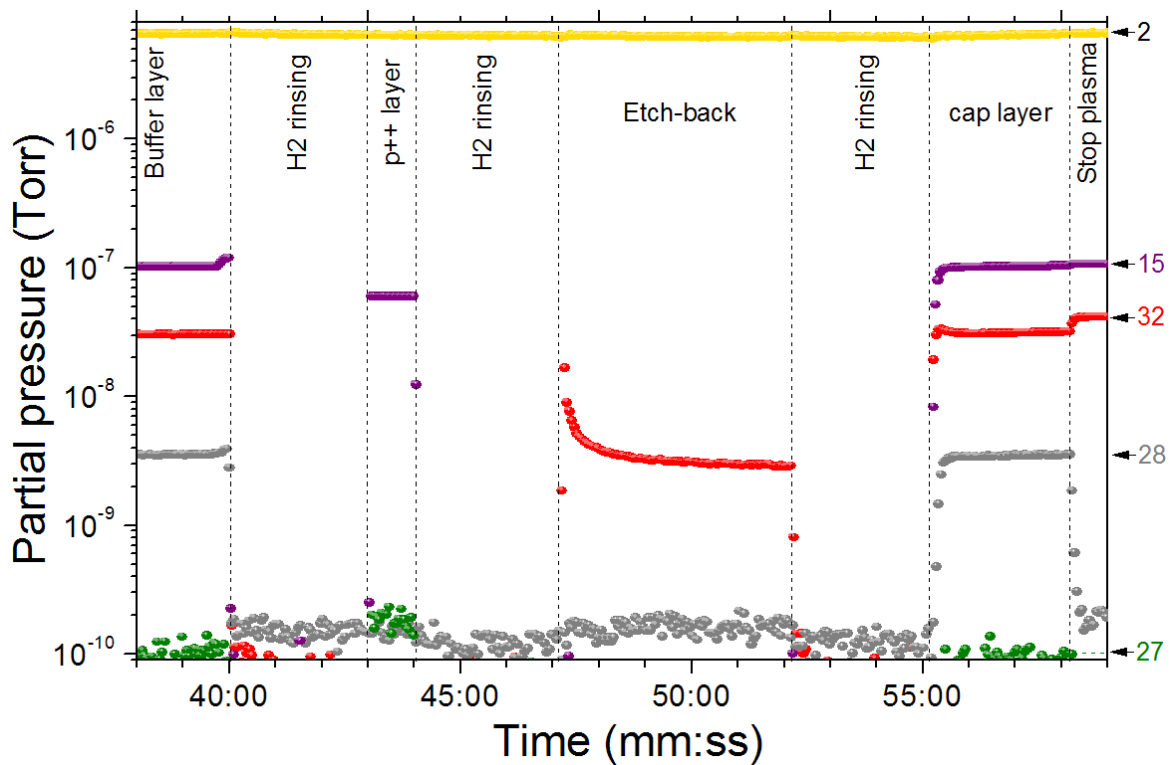


Figure A-2 : Mass-spectrometry of delta-layer growth with etch-back step.

Molecules as CO and CO₂ are generated during the p-- growth from reaction between oxygen and methane. On the figure below, m/z ratio 28 could be attributed to silicon, even if the reactor wall and the sample-holder are made of silicon. The contribution of the silicon in the m/z = 28 is weak; the signal was strong when p-- layers were growing. Molecules like CO, CO₂ and H₂O are detected as products of diamond etching; similar to the combustion products of any carbon-based matter. Based on these mass ratios it is possible, after calibration, to use the mass spectrometer in order to monitor the etching rate.

III. LOW BORON DOPING MEASUREMENT

Oxygen addition in the gas reduces drastically the boron concentration incorporation during the growth. This ability depends of the concentration used. In order to estimate the residual boron doping, sample were analyzed by CL and CV measurements have been performed on p--/p++ structures.

III.1. By CL

CL at 5 Kelvin under low voltage (typ. 5kV) gives information mainly from the last layer growth *i.e.* p--. From Monte-Carlo simulation at 5kV the peak energy from electron is located 100nm below the surface.

The effect of oxygen is illustrated on Figure A-3 , where the intensity of the BE^{TO} is decreasing. On this figure, p-- growth where made with 0.75% of CH_4 . According the relation between the ratio $I(BE^{TO})/I(FE^{TO})$ and boron concentration (Omnès, et al., 2011), the estimation of boron content in p-- layers is given in table a-2.

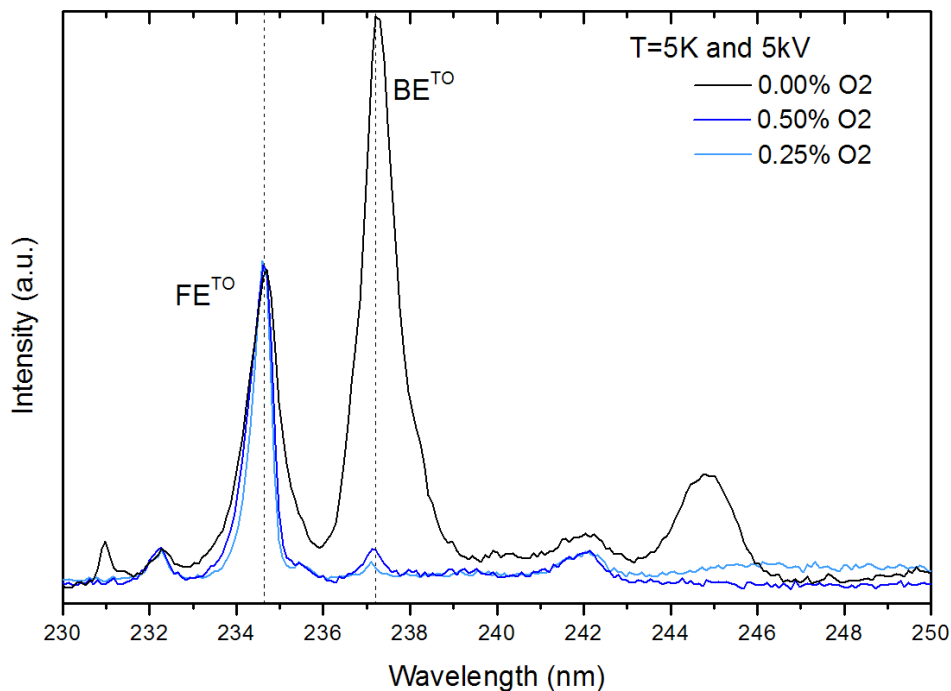


Figure A-3 : CL spectra of p-- layers made with 0.75% of methane and with different oxygen ratio in the gas phase taken at 5 Kelvin under 5 kV.

% CH ₄ /H ₂	% O ₂ /H ₂	I(BE ^{T0})/I(Fe ^{T0})	[B] _{CL} (cm ⁻³) ²⁷
0.75	0	3.17	1.1×10 ¹⁶
0.75	0.25	0.0346	1.2×10 ¹⁵
0.75	0.32	<i>too noisy</i>	-
0.75	0.50	0.0545	1.9×10 ¹⁵

Table A-2 : Boron concentration estimated from CL at 5K, 5kV.

It important to notice that p-- layers are very insulating and the CL intensity decrease during measurement because of charge accumulation at the sample surface (as explained on Chapter 3). This explain why the CL signal for the growth made with 0.32% (O₂/H₂) and 0.75% (CH₄/H₂) is too noisy to be exploited; BE^{T0} intensity is very small and requires several hundreds of seconds to be above the background level and finally appears like a small bump.

III.2. By Capacitance-Voltage (C(V))

One solution to measure the so low boron concentration which cannot be extracted from CL is the capacitance-voltage measurement. A Schottky barrier is deposited on the p-- surface of a p--/p++ structure. By applying a voltage, space charge region is expanding and by measuring the capacitance generated, it is possible to determined N_A-N_D.

Unfortunately μm-thick p-- growth provide defects at the sample surface which are negative for electrical tests (killer defective point), negative the depth profile (roughness) and negative to overgrowth homogeneous p++ layers (flat equipotential). This imposes to realize a large number of small contacts in order to statistically improve the possibly to probe correctly the p-- diamond material.

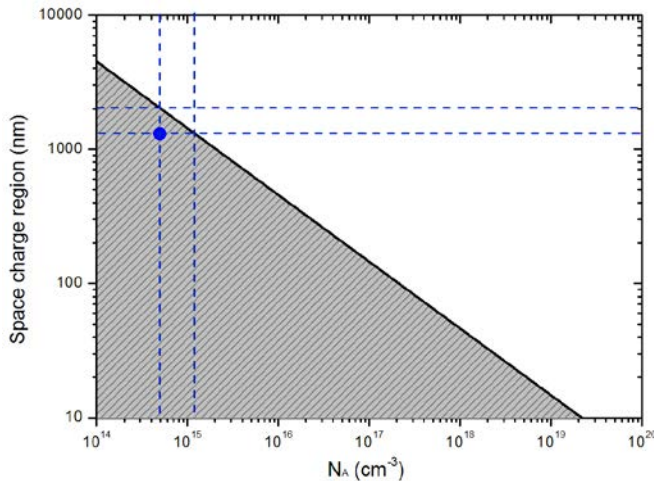


Figure A-4 : Extension of the space charge region dependency with the acceptor concentration

²⁷ [B]_{CL} (cm⁻³) = 3.5×10¹⁶× I(BE^{T0})/I(Fe^{T0}), from (Omnès, et al., 2011)

IV. SURFACE CONTAMINATION DURING P-- GROWTH

We can distinguish two kinds of defects due to contamination: UCs and micro-masking. Surface is easily contaminated during p-- growth. This phenomenon can be a result of the surface charging because of insulation material growth. Diamond crystallite nucleate on the sample hold or silicon particular might be attracting be the growing surface and finally stick at the surface. Because of the lateral growth, these parasites create flat UC or macro-masking.

IV.1. UC

Diamond crystallites appear randomly at the surface and at the top of PH. The Figure A-5 illustrates by HDVSI mode optical profile the covertures of UC on the surface.

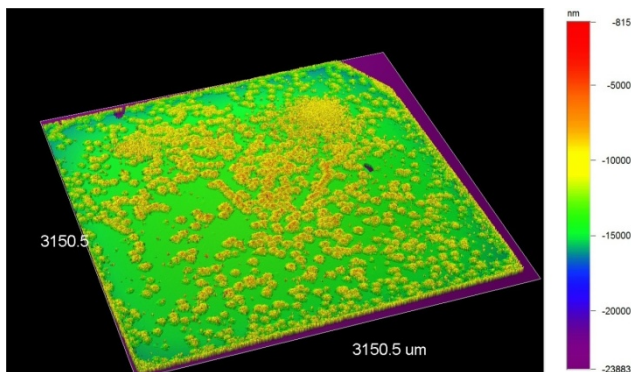


Figure A-5 : HDVSI mode optical profile of p-- layer entirely covered by UCs.

UC are located at the top of PH, on their face and on surface valley. They have the same height and the same diameters. Coalescence of UC is possible and is clear visible by SEM Figure A-6. This let's supposed their coming at the first step of the growth, they sticks at the surface and stars to growth laterally and when they are too closed together, they coalesce.

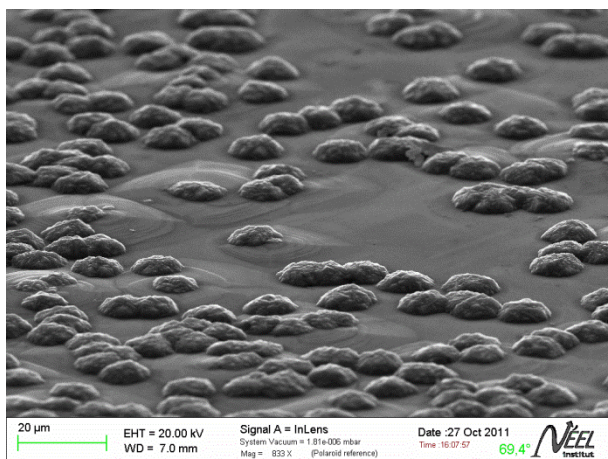


Figure A-6 : SEM picture of p-- surface entirely covered of UCs.

IV.2. Micro-masking

Has been observed when silicon is deposited accidentally on the diamond surface. Silicon is a mask for the growth and because of the lateral growth dominance; the mask is covered on its borders during the growth and shows some cushion shapes. It is also an indirect way to measure the thickness of the growth.

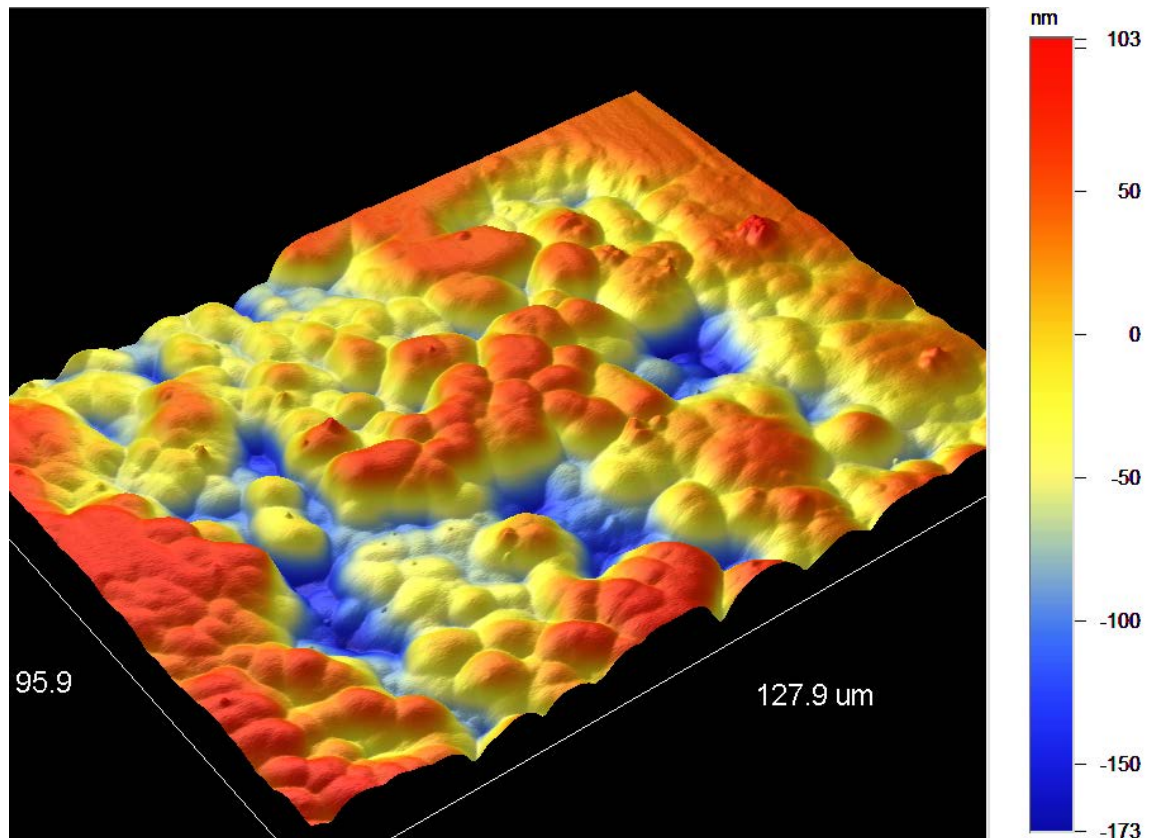


Figure A-7 : Detail of micro-masking on p- lateral growth sample by PSI mode optical profile

V. STRUCTURES ON SAMPLE GROWTH STUDIED

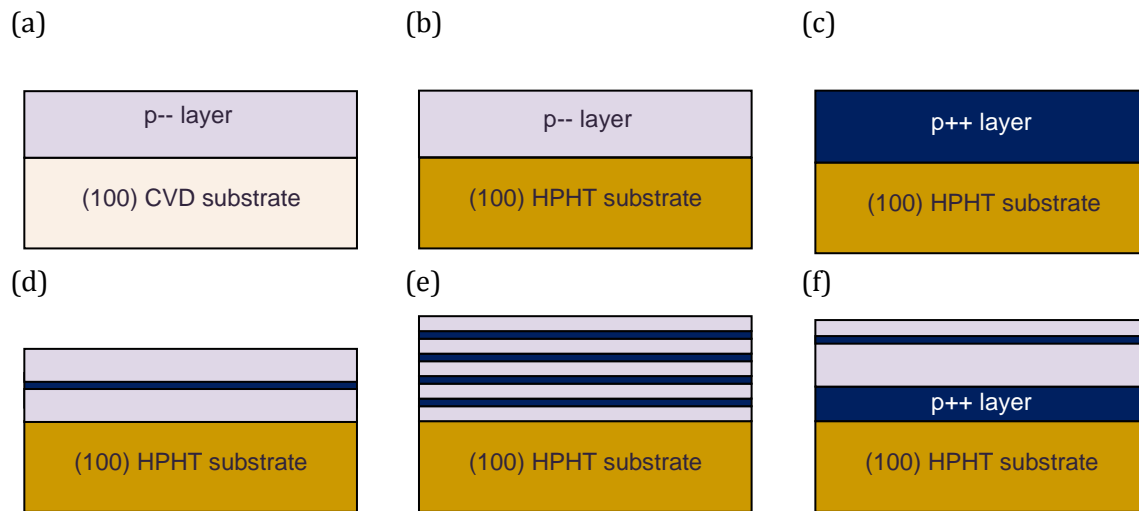


Figure A-8 : structure of sample grown

At first, p-- layers were grown on “as received” CVD substrates (Figure A-8(a)). The surface of “as received” CVD substrates is covered of small holes 15 nm deep in average and few μm in diameter (see chapter 4) which provide anchor point for surface defects generation along the growth. If the p-- is slow enough, it is expected to cover these small holes and to reduce to size of surface defects after overgrowth.

“As received” HPHT substrates are covered by polishing lines and don’t have small holes which be found on CVD substrates (see chapter 4). The overgrown layer kept the same surface morphology during the growth and polishing lines starter points are responsible or defects along the growth. If the p-- growth is slow enough, it is expected to reduce 1D peak-to-valley induces by the substrate polishing and to reduce at the same time the size of defects.

Samples composed of p-- layers overgrown on p++ metallic diamond typ. 300nm thick were realized in order to measure the boron concentration remaining inside the p--layer (Figure A-8(c)). It is expected a boron concentration below $1 \times 10^{15} \text{cm}^{-3}$ and such atoms concentration cannot be determined by SIMS measurement due to the available limit of detection ($1 \times 10^{16} \text{cm}^{-3}$). In consequence, so called “p--/p++” samples were etch by oxygen plasma mixture to performed cylindrical MESA structures (figure A-9) topped with Schottky contact in order to keep equipotential lines parallel vertically inside the p-- studied layer.

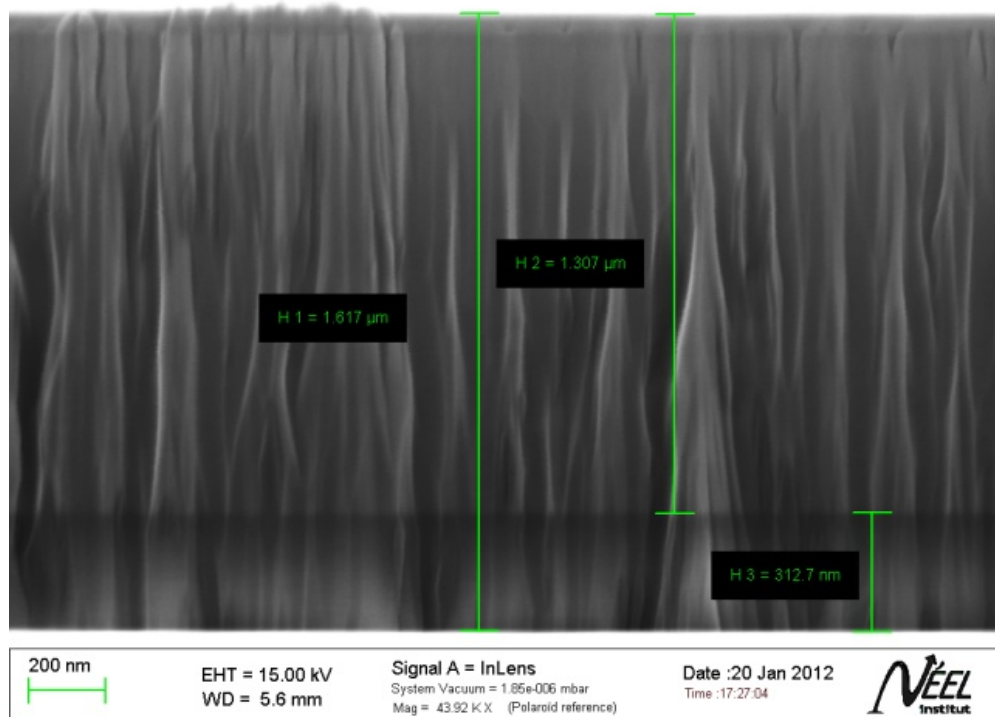


Figure A-9 : 90° tilted SEM views of MESA etching on p--/p++ sample

On the figure A-9, the p++ layer appears darker than the p--. This difference of contrast is very useful to determine the thickness and the growth rate of the p-- layer by a simple measurement on picture taken by SEM.

VI. SUMMARY OF COLOR-PRODUCING DIAMOND DEFECTS NOT RELATED TO DIAMOND TYPE

Several lattice defects contribute to the color of diamond even though they are not involved in the assignment of diamond type. Most of these features selectively absorb light in the visible range of the electromagnetic spectrum to produce color, and they can be seen with a gemological spectroscope or a UV-Vis-NIR absorption spectrometer. These defects are commonly mentioned in the scientific and gemological literature. A brief description of each is given below (from Clark et al., 1979; Collins, 1982, 2001; Zaitsev, 2001; and GIA staff observations).

N3 (415 nm): This defect consists of three nitrogen atoms surrounding a vacancy. In addition to contributing to yellow color in “cape” diamonds, it can also produce blue luminescence in response to longwave UV radiation.

N2 (478 nm): This broad absorption is associated with N3 and is part of the well-known “cape” spectrum in many yellow diamonds. It is also related to nitrogen impurities.

Band A blue (480 nm): This broad band is a defect of unknown origin that commonly produces yellow or orange color in type Ia diamonds. Strong yellow fluorescence is typical of diamonds colored by this mechanism.

H4 (496 nm): This defect consists of four nitrogen atoms separated by two vacancies. It is created when a vacancy migrates through the diamond lattice and combines with a B-aggregated nitrogen impurity. H4 produces yellow color in diamond.

H3 (503.2 nm): This is an uncharged defect consisting of two nitrogen atoms separated by a vacancy [i.e., (N-V-N)₀]. H3 absorption alone creates yellow color, while the defect can also produce green luminescence in response to illumination.

3H (503.5 nm): This is a negatively charged vacancy in the diamond lattice (i.e., V_□). It is intimately related to GR1 and, on rare occasions, absorbs strongly enough to enhance the green color caused by GR1 absorption.

Band A green (550 nm): This broad band is poorly understood and thought to be associated with plastic deformation of the diamond lattice. This is the most common defect that produces pink-to-red color in natural diamonds, but it is also common in brown stones.

NV₀ (575 nm): This defect consists of a nitrogen atom adjacent to a vacancy; it is in a neutral charge state. In combination with the 637 nm defect, the NV₀ center produces pink color in most treated pink diamonds as well as in a few natural pink stones.

595 nm: This band is a nitrogen-related defect of uncertain structure. It is commonly associated with laboratory irradiation and annealing of diamond to produce green, yellow, or pink colors, but it is also present as a weak feature in many natural-color green or yellow diamonds.

NV_□ (637 nm): This defect consists of a nitrogen atom adjacent to a vacancy. This defect is in a negative charge state. In combination with the 575 nm defect, the NV-center produces pink color in most treated pink diamonds as well as a few natural stones.

GR1 (741 nm): This defect is a single, uncharged vacancy in the diamond lattice. It is common in most natural and artificially irradiated type Ia and IIa blue or green diamonds. Although outside the visible spectral range (~400–700 nm), strong absorption by GR1 produces related bands at the red end of the spectrum that result in green or blue color.

H2 (986 nm): This is a negatively charged defect that consists of two nitrogen atoms separated by a vacancy [i.e., (N-V-N)_□]. It is closely related to H3 and is commonly cited as evidence for HPHT treatment in type Ia diamonds. Occasionally, H2 (and related broad band absorptions) can be so intense that the combination of H3 and H2 produces a strong green body color.

ABSTRACT

The aim of this PhD thesis was to better understand the boron delta-doping of diamond over building a new Microwave Plasma Chemical Vapour Deposition reactor prototype. We succeed to grow step by step heavy on low, and more original, low on heavy boron-doped layers of (100)-oriented diamond in the same process and without stopping the plasma. We also settled growth parameters for a growth rate slow enough to get nanometre-thick homoepitaxial films with boron doping jumps over several orders of magnitude, called delta-doping. We demonstrated the presence of super-sharp interfaces, after optimized in situ etching, by joint Secondary Ion Mass Spectrometry and Scanning Tunneling Electron Microscopy at High-Angle Annular Dark Field analysis. Finally superlattices with abrupt boron doping levels have been grown; they show satellite peaks of X-ray diffraction representative of a super-period.

RESUME

Dans ce projet de thèse, qui s'appuie sur l'optimisation d'un réacteur de croissance du diamant et la construction d'un prototype, nous avons démontré l'épitaxie par étapes de couches de diamant, orientées (100), lourdement dopées au bore sur des couches de dopage plus faible dans le même processus, sans arrêter le plasma. Plus original, nous avons démontré la situation inverse. Nous présentons aussi des croissances assez lentes pour l'épitaxie de films d'épaisseur nanométriques avec de grands sauts de dopage, appelé delta-dopage. L'accent a été porté sur le gain en raideur des interfaces. Nous démontrons la présence d'interfaces fortement abruptes, issues de gravures in-situ optimisées, par une analyse conjointe en spectrométrie de masse à ionisation secondaire et en microscopie électronique en transmission à balayage en champ sombre annulaire aux grands angles. Des super-réseaux de dopages abrupts montrent des pics satellites de diffraction X typiques de la super-période.